



HAL
open science

Ocean Wave Rectifier water canal

Rémi Carmigniani

► **To cite this version:**

Rémi Carmigniani. Ocean Wave Rectifier water canal. Fluids mechanics [physics.class-ph]. Université Paris-Est, 2017. English. NNT : 2017PESC1049 . tel-01743826

HAL Id: tel-01743826

<https://pastel.hal.science/tel-01743826>

Submitted on 26 Mar 2018

HAL is a multi-disciplinary open access archive for the deposit and dissemination of scientific research documents, whether they are published or not. The documents may come from teaching and research institutions in France or abroad, or from public or private research centers.

L'archive ouverte pluridisciplinaire **HAL**, est destinée au dépôt et à la diffusion de documents scientifiques de niveau recherche, publiés ou non, émanant des établissements d'enseignement et de recherche français ou étrangers, des laboratoires publics ou privés.



École Doctorale SIE

Laboratoire d'Hydraulique Saint-Venant

Thèse

Présentée pour l'obtention du grade de DOCTEUR
DE L'UNIVERSITE PARIS-EST

par

Rémi Carmigniani

Canal redresseur de vagues

Spécialité : Mécanique des Fluides

Soutenue le 14 décembre 2017 devant un jury composé de :

Président du jury	Pr. Vincent Rey	(Université du Sud-Toulon-Var, France)
Rapporteur	Pr. Dick Yue	(M.I.T., USA)
Rapporteur	Dr. Denys Dutykh	(Université de Savoie, France)
Examineur	Pr. David Le Touzé	(Ecole Centrale de Nantes, France)
Examineur	Dr. Gaële Perret	(Université du Havre, France)
Directeur de thèse	Dr. Damien Violeau	(EDF R&D & LHSV, France)
Co-encadrant de thèse	Pr. Morteza Gharib	(Caltech, USA)



Thèse effectuée au sein du **Laboratoire d'Hydraulique Saint-Venant**
de l'Université Paris-Est
6, quai Watier
BP 49
78401 Chatou cedex
France

Résumé

Comment générer des courants à partir des vagues ? En s'inspirant de la nature et particulièrement des pompes à impédance, deux systèmes permettant de pomper avec des vagues sont étudiés : la pompe à résonance et les vagues au dessus d'une plaque submergée. Dans cette étude, l'origine de l'écoulement est reliée au terme de transport de masse des vagues dans la couche de surface. Il correspond à la quantité de masse déplacée par les vagues entre la crête et le creux au cours d'une période. Ce terme peut-être amplifié par des changements de bathymétrie et par résonance. Cela permet de créer des zones d'aspiration et donc de générer un courant. Le problème est modélisé par une simple description linéaire potentielle. Un modèle avec dissipation est aussi présenté afin de prendre en compte les effets de dissipation dus au déferlement et au frottement visqueux. Le modèle est comparé à des expériences et des simulations. Il permet de prédire les fréquences intéressantes et la dynamique globale. Ceci permet de comprendre l'origine d'un phénomène de pompage par vague, mais aussi de dimensionner le système à partir d'une théorie simple.

Mots-clé:

Pompe à vagues, transport de masse, méthode SPH, dissipation, méthode des expansions, modes propres.

Ocean Waves Rectifiers: Toward a
Novel Way to Harvest Waves Energy

Abstract

How to generate currents from water waves? Inspired by nature original way of pumping in the embryonic heart, two wave pumps are studied in the present thesis: the resonance wave pump directly inspired by the Liebau's pump and the waves above a submerged plate pump. The origin of the observed circulation is linked to the wave mass transport term: it corresponds to the amount of mass advected by the waves in the surface layer. The latter is the domain between the crest and the trough of the waves and is a part of the flow that is not always submerged. It is possible to amplify this surface term by resonance and by varying the bathymetry. The latter enables to generate local suction toward the surface layer and leads to mean circulation. The problem is described using a simple potential theory and a dissipative model is proposed to take into account wave dissipation due to friction and wave breaking. The simplified model is compared to experiments and simulations in both cases. It provides a simple framework to predict the pumps behavior: the interesting frequency range and the strength of the flow. It is also a tool for the design of real life applications.

Keywords:

Wave pumping, Wave mass transport, SPH method, Wave dissipation, Eigen expansion function method.

Acknowledgments

Where to start? There are a lot of people I would like to thank in leading me toward this achievement. Probably the first person, I have to thank is Pr. Sidney Nagel at University of Chicago who motivated me to pursue this path. He was a great mentor and wonderful person to meet. Pr. Christophe Clanet is also in my mind as he is the first person who inspired me to do research and I am really excited to work with him in the future. All this would of course not have been possible without Pr. Mortesa Gharib at Caltech. He is among the most talented person I have ever met and I really look forward to working with him in the future as I do think it will be mutually beneficial. I was also lucky to meet in my life Pr. Michel Benoit who trusted me from the start and enabled me to do this PhD. Pr. Damien Violeau is also one of the pillar of this work and I am really thankful for his mentoring in the last two years of my thesis when he took me as a PhD student after Pr. Benoit had to leave for Marseilles. He is a wonderful researcher and a great PI. Pr. Benoit and Pr. Violeau were instrumental in my success/research during these three years and I cannot thank them enough.

I would also like to thank Dr. Morgan Grivel, Dr. Chris ρ (Roh, as I like to write it out) who were greatly helpful and amazing friends during my journeys to Caltech. You guys are the best and I really hope we will have a chance to hang out in the future. I also want to mention Kelly Mauser who I have known for quite a long time and count among my dearest friends. I want to thank my best friend Kyle Costenbader and my amazing girlfriend Elsa Lustig who supported me in the difficult times during these three years. A special acknowledgment to my parents and sister Julie who took the time to read part of my thesis even-though they did not know much about the subject.

I also want to express gratitude to the good friends I made during this thesis Alex Ghaitanellis, Adrien Bourgoïn, Roberto Frau, Sofiane Martel, Alexis Herrault, Antoine Joly, Agnes Leroy, Marine Le Gal, Sara Pavan, and Virgine Hergault. You all mean a lot to me. What is a thesis without its jury? And this is why I would like to finish by thanking all of them: Gaële Perret, Dick Yue, Vincent Rey, David Le Touzé, and Denys Dutykh for their time, suggestions to correct the manuscript and the wonderful discussion we had during the defense. I was tense at the beginning as it might be expected but you really made it a wonderful time. Thank you a lot for everything and I really hope we will have opportunities to collaborate in the future.

To Masha: my wonderful dog!

Contents

Introduction	1
1 Wave theory	9
1.1 Water waves: definition and description	10
1.1.1 Water waves: definition	10
1.1.2 Governing equations and boundary conditions at the surface	12
1.2 Potential approximation	16
1.3 Linear wave theory	19
1.3.1 Linear dispersion relation and linear wave profile	19
1.3.2 Wave energy, wave energy flux and power	22
1.3.3 Stokes drift and wave mass transport	24
1.3.4 Eigenfunction expansion matching method	28
1.4 Waves and mean flow interaction	38
1.4.1 Second order potential theory and mean flow	38
1.4.2 General wave-mean flow Eulerian equations	40
1.4.3 Interaction stress tensor and wave mass transport calculation	42
1.5 Non-linearity, dissipation and wave breaking	45
1.5.1 Non-linear waves and dispersion relation	45
1.5.2 Maximum wave amplitude and wave breaking thresholds	47
1.5.3 Dissipative dispersion relation	49
1.5.4 Wave mass transport in the roller	54
2 The Resonance Wave Tank	57
2.1 Introduction: Resonance and pumping	58
2.2 Experimental setup and measurement techniques	59

2.2.1	Setup and dimensions	59
2.2.2	Data acquisition	61
2.3	Flow rate under the submerged plate and resonance characteristics	62
2.3.1	Reference configuration	62
2.3.2	Effects of other parameters on the flow rate	72
2.4	Potential model of the resonance wave pump	79
2.4.1	Linear potential model without dissipation	79
2.4.2	Adding dissipation	80
2.5	Mass flux above the submerged plate	85
2.5.1	PIV measurements above the submerged plate	86
2.5.2	2D Numerical simulations:	92
2.6	Efficiency and potential applications	95
3	Waves above a submerged plate	99
3.1	Introduction: From breakwater studies to a pump	100
3.2	Potential model for the WASP	101
3.2.1	General equations	102
3.2.2	Wave mass transport above the plate	103
3.2.3	Wave mass transport and dissipation	109
3.2.4	Oscillations under the submerged plate and dissipation	114
3.3	2D-SPH simulations	115
3.3.1	SPH numerical wave tank	116
3.3.2	Validations	120
3.3.3	Wave harmonic amplitude and set-down	127
3.3.4	Wave mass flux and mass transport	129
3.3.5	Varying incident wave height and frequency	133
3.4	3D-SPH simulation	135
	Conclusions and future work	139
	Bibliography	142
	Appendices	157

A Gerstner's waves	159
A.1 Deep water trochoidal theory	160
A.2 Mean horizontal Eulerian mass flux of Gerstner's waves	164
A.3 Compared Mass flux theory and simulations	166
B Boundary Layers Effects and Wave Mass Transport	169
C Solver <i>Mathematica</i> waves generated by plunger	175
C.1 Linear dispersion relation for waves	176
C.2 Projection Calculations	177
C.3 Solver	177
C.4 Convergence tests	178
C.4.1 Convergence of the wave amplitude	179
C.4.2 Decay of the coefficients absolute value	179
D Proof of mean flow kinematic boundary condition	181
E Higher orders Stokes waves theory and Non-linear dispersion relation	185
E.1 Second order wave theory	186
E.2 Third order wave theory	188
E.3 Approximation of the non-linear dispersion relation	188
F Lamb's viscous waves	191
F.1 Solution for a wave	192
F.2 Dispersion relation and approximation	194
G Potential flow of viscous fluid	195
H Viscous potential flow	199
H.1 Case of no-slip condition:	200
H.2 Case of slip condition:	203
H.3 Discussions	203
I Optimal Sponge Layer for water waves numerical models	207
I.1 Introduction	208

I.2	Waves absorption by energy penalisation: General formulation	210
I.2.1	Equations of motions and Bernoulli's equations	210
I.2.2	Perturbation method and sponge layer equations	211
I.3	2D applications with constant depth	213
I.3.1	Linear two dimensional equations and sponge layer functions	213
I.3.2	Sponge layer functions	214
I.3.3	Finite element solver and SPH model	215
I.3.4	Sponge layer prediction and optimal for fixed Ω	220
I.3.5	Sponge layer prediction as a function of Ω	223
I.4	3D application	225
I.5	Conclusion	227
J	Dissipation above a shelf	231
K	Smoothed Particle Hydrodynamics	237
L	Error calculation and Raw data	243
L.1	Error Calculation	244
L.2	Data tables	247
M	Experiment of WASP at Le Havre	251
M.1	Experimental protocol	252
M.2	Experimental results	253
M.3	Numerical simulations	254
N	Experimental trials of 3D RWT	259

List of Figures

1	Annual mean wave power density and direction.	2
2	Schematic diagram of Allison's peristaltic pump.	4
3	Peristaltic and impedance pumps diagram.	5
4	Wave rectifiers designed studied.	7
1	Wave theory	9
1.1	Wave train aerial picture	11
1.2	Sketch of restoring forces.	12
1.3	Two-phase problems	12
1.4	Wave trains and notations.	18
1.5	Linear wave dispersion relation.	21
1.6	First ten wavenumbers for Airy waves for $\Omega = 1$ in the complex plane.	22
1.7	Definition of emergence time.	26
1.8	Piston wave maker.	30
1.9	Velocity profiles at the piston-type wave maker in the linear theory.	31
1.10	Plunger wave maker.	32
1.11	Plunger wave maker theoretical ratio of wave amplitude over the piston stroke.	35
1.12	Reflection/Transmission at a step.	36
1.13	Wave mass transport variation at a step.	37
1.14	Non-linear dispersion relations with $K = kd$ for a wave steepness $KA = 0.25$	47
1.15	Trajectories of the first two wavenumbers with viscosity for $\Omega = 1$	52
1.16	Dissipation with Reynolds number.	52
1.17	Velocity in a breaker and roller area.	54

2 The Resonance Wave Tank	57
2.1 Original closed loop impedance pump.	58
2.2 Resonance wave tank and main notations.	60
2.3 Transient response for different forcing frequencies.	64
2.4 Influence of initial conditions on the RWT.	66
2.5 Frequency response for different forcing frequencies.	67
2.6 Periodic flow rate for four frequencies.	68
2.7 Mean and first harmonic velocity profiles.	69
2.8 Mean, first and second harmonic flow rate as a function of frequency.	70
2.9 Surface envelope for different frequencies.	71
2.10 Non-dimensional first harmonic and mean flow rate for different strokes amplitude.	73
2.11 Absolute mean flow rate as a function of the stroke amplitude.	74
2.12 Non-dimensional mean flow rate for different plunger lengths and two stroke amplitude.	75
2.13 Non-dimensional first harmonic and mean flow rate for different water depths.	77
2.14 Non-dimensional first harmonic and mean flow rate for different opening heights.	78
2.15 Sketch of a U-tube oscillator.	78
2.16 Domain decomposition of the RWP	80
2.17 Non-dimensional first harmonic and mean flow rate with EFE and EFE NI models.	81
2.18 Wave mass transport in the RWT with EFE NI.	83
2.19 Sketch of the wave mass transport effect on the mean flow for $f_0 = 1.60$ Hz.	84
2.20 Sketch of the wave mass transport effect on the mean flow for $f_0 = 1.20$ Hz.	84
2.21 Mean flow rate with stroke amplitude with EFE NI.	85
2.22 Mean flow rate with plunger position with EFE NI.	86
2.23 Flow rate and velocity profiles in PIV window (5).	87
2.24 Velocity field zones (2) and (3) during upward plunger stroke.	88
2.25 Velocity field zones (2) and (3) during downward plunger stroke.	89
2.26 Experimental mean mass flux above the submerged plate.	91
2.27 Transient regime flow rate simulations compared to experimental results.	92

2.28	Numerical mean mass flux fields above the submerged plate (OpenFOAM).	93
2.29	Numerical mean mass flux fields above the submerged plate (Sphynx).	94
2.30	Compared simulations and model wave mass transport.	95
2.31	Resonance wave tank applications.	96
3	Waves above a submerged plate	99
3.1	Average circulation at breakwater.	100
3.2	Domain decomposition of the WASP	102
3.3	Wave mass transport at the origin of wave pumping.	103
3.4	Evolution of the wave mass transport and energy flux, according to EFE method.	104
3.5	Evolution of the wave mass transport and energy flux, according to EFE method.	105
3.6	Wave mass transport profiles.	106
3.7	FEM and EFE wave mass transport and divergence profiles.	107
3.8	FEM solution for the potential mean flow equations and flow repartition.	107
3.9	Wave mass transport profiles and dissipation for different Λ_p for $L_p = 1$ and $D_p = 1/6$.	110
3.10	Sketch of the two possible kinds of mean flow in the waves above submerged plate problem with dissipation.	111
3.11	Wave mass transport with dissipation for $D_p = 1/6$ and $L_p = 1$ with EFE NI.	112
3.12	Wave mass transport profiles and dissipation for $\Lambda_p = 0.65$ for $L_p = 1$ and $D_p = 0.1$.	113
3.13	Wave mass transport with dissipation for $D_p = 0.1$ and $L_p = 1$.	113
3.14	Amplitude of oscillations under the submerged plate with EFE NI method.	114
3.15	Sketch of the numerical wave tank.	116
3.16	Wave generation and reflection in SPH.	118
3.17	Sketch of the AWAS- η principle.	119
3.18	Validation AWAS in the SPH simulations.	119
3.19	Non-dimensional incident wave amplitude, transmission and reflection coefficients in the case of Brossard <i>et al.</i> [16]	121
3.20	Murakami <i>et al.</i> 's case. Flow rate under the submerged plate in SPH.	123

3.21	Vorticity in SPH simulation of waves above a submerged plate (Murakami <i>et al.</i> 's case).	126
3.22	Murakami <i>et al.</i> 's case. Mean velocity under the submerged plate in the SPH simulations, linear models and experiment.	127
3.23	Wave harmonic amplitude in the SPH simulations (Murakami <i>et al.</i> 's case).	128
3.24	Mean water level in the SPH simulations (Murakami <i>et al.</i> 's case).	129
3.25	Water elevation detection during breaking in the SPH simulations.	129
3.26	Mean mass flux around the submerged plate in the SPH simulation (Murakami <i>et al.</i> 's case).	130
3.27	Zoom of the mean mass flux around the submerged plate in the SPH simulation (Murakami <i>et al.</i> 's case).	130
3.28	Mean mass flux around the submerged plate in SPH simulation after 5 waves (Murakami <i>et al.</i> 's case).	131
3.29	Wave mass transport in the surface layer in the SPH simulations and the models (Murakami <i>et al.</i> 's case).	132
3.30	Instantaneous wave mass transport maximum and mean flow rate in the SPH simulation (Murakami <i>et al.</i> 's case).	132
3.31	Murakami <i>et al.</i> 's configuration with varying incident wave height and frequency.	134
3.32	3D SPH simulation of waves above a submerged plate (whole tank).	135
3.33	3D SPH simulation of waves above a submerged plate (zoom).	136
3.34	Flow rate under the submerged plate in 3D SPH (Murakami <i>et al.</i> 's case).	137
3.35	Wave amplitude in 3D SPH.	137
3.36	Incident and reflected wave amplitude in 3D SPH.	138
3.37	Wave energy converter general problem.	140
A Appendix A: Gerstner's waves		159
A.1	Free surface profiles of Gerstner's waves of different steepness.	164
A.2	Mean mass flux Eulerian profiles for Airy and Gerstner's waves (with $ka_w = 0.1$).	166
A.3	Numerical wave flumes	166
A.4	Incident wave amplitude and reflection coefficient in the SPH wave flume.	167
A.5	SPH-simulated Gerstner-like wave profiles	168

B	Appendix B: Boundary Layers Effects and Wave Mass Transport	169
B.1	Boundary layer horizontal velocity profiles in linear waves	172
C	Appendix C: Solver waves generated by plunger	175
C.1	Error wave amplitude generated by a plunger	179
C.2	Coefficients J_n of the wave generated by a plunger	180
C.3	Coefficients C_n of the wave generated by a plunger	180
D	Appendix D: Mean flow kinematic boundary condition	181
E	Appendix E: Higher orders Stokes waves theory and Non-linear dispersion relation	185
E.1	Non linearity effect on the wave number for short, intermediate and long waves.	189
F	Appendix F: Lamb's viscous waves	191
G	Appendix G: Potential flow of viscous fluid	195
H	Appendix H: Viscous potential flow	199
H.1	Trajectories of the wavenumber with viscosity for $\Omega = 1$	202
H.2	Trajectories of the wavenumber with viscosity for $\Omega = 1$	204
H.3	Effect of viscous dissipation on the real part of the wavenumber for $\Omega = 1$	205
H.4	Effect of viscous dissipation on the imaginary part of the wavenumber for $\Omega = 1$	206
I	Appendix I: Optimal Sponge Layer	207
I.1	Different type of sponge layer functions in the absorbing domain ($\Xi = (X - X_0)/(X_{max} - X_0)$). The different colours denote different power coefficients n_B	215
I.2	Sketch of the wave fume.	216

- I.3 Instantaneous velocity field in the SPH simulation for $x_{SL} = 2\lambda$ with $n_B = 3$, $B_{max} = 0.5$. The shaded region shows the sponge layer domain. The density plot shows the horizontal velocity rescaled by the linear surface velocity $u_s = a_{inc}\omega \coth kd$. The red line shows the shape of the sponge layer used. 217
- I.4 SPH simulations (black solid lines) time evolution of the reflection and incident wave amplitude measured using Goda & Suzuki two probes method at the centre of the physical tank for $n_B = 3$, $B_{max} = 0.5$ and $x_{SL} = 2\lambda$. The red dashed lines show the linear sponge layer model solution of eq.I.3.2 found using the FEM. 217
- I.5 SPH simulations surface envelope for a power sponge layer of length $x_{SL} = 2\lambda$ with $n_B = 3$, $B_{max} = \{0.5, 5, 32\}$ 218
- I.6 SPH simulations surface first harmonic amplitude for a power sponge layer of length $x_{SL} = 2\lambda$ with $n_B = 3$, $B_{max} = \{0.5, 5, 32\}$. The red dashed lines show the linear sponge layer model eq.I.3.2 solved with FEM. 219
- I.7 Reflection coefficient measured from SPH simulations (symbols) for different power sponge layer functions compared to the present linear sponge layer model of eq.I.3.2 solved with FEM (continuous lines). The sponge layer length is fixed to $x_{SL} = 2\lambda$ 219
- I.8 Reflection coefficient measured from SPH simulations (symbols) for different sponge layer lengths using the power sponge layer with $n_B = 3$, compared to the present linear sponge layer model of eq.I.3.2 solved with FEM (continuous lines). 220
- I.9 Reflections coefficient contour plot obtained with FEM for different n_B values for power sponge layer for $\Omega \approx 1.17$. The red contours outline the iso reflection of 1% and 2%. The blue points show the value obtains for a threshold of 5% using the Golden section search algorithm and the white line the minimum reflection starting once the reflection is below 5%. The green point in the first figure shows the expected reflection for the first free mode for a sponge layer of non-dimensional length 0.5 and $B_{mean} = 0.6$ for the dominant first harmonic. 222
- I.10 Reflection coefficient measured from SPH simulations (symbols) for a sponge layer of length $x_{SL} = 0.5\lambda$ with $n_B = 1$, compared to the present linear sponge layer model of eq.I.3.2 solved with FEM (continuous line). 223

- I.11 Effect of varying the angular frequency and sponge layer strength on the reflection coefficient for a power sponge layer with $n_B = 3$ and $X_{SL} = 1$. Compared SPH-based simulation (symbols) and FEM-based solutions of the linear theory (solid lines) results of the reflection coefficient for a fixed $B_{mean} = 0.36$ (in gray) and for the optimal value of B_{mean} found using the Golden section search algorithm and the FEM solver (in black). Figure I.12 shows the optimal sponge layer strength values as a function of Ω for the black points and line. 224
- I.12 Evolution of the optimal value of B_{mean} with the angular frequency Ω for power sponge function with $n_B = 3$ and $X_{SL} = 1$. The black line is found using the Golden section search algorithm to find the minimum of reflection. The gray horizontal line shows the value found in the limit of deep water waves. The diamonds show the value used in the SPH simulations. The reflection coefficients are plotted in figure I.11. 225
- I.13 Top view of the 3D SPH numerical wave flume. The shaded gray region represent the sponge layer. The dotted line shows the sampled line for the water surface elevation. 226
- I.14 3D SPH simulation wave tank at the end of the simulation. The shaded region shows the sponge layer domain. The density plot shows the horizontal velocity rescaled by the linear surface velocity $u_s = a_{inc}\omega \coth kd$ 227
- I.15 3D SPH simulation wave amplitude and phase along the lines $y = \{1/4, 1/2, 3/4\} \ell$ in blue, black and red respectively (see dashed lines in figure I.13). The phase is evaluated using the measured wavenumber $k = 9.54 \text{ m}^{-1}$ different from the theoretical one $k_0 = 10.0 \text{ m}^{-1}$. The vertical color lines show the beginning of the sponge layer at the different positions. The amplitude and phase are identical in the physical part. 228
- I.16 Example of mesh used in the FEM for $dx = \lambda/50$. The mesh is refined near the free surface. 229
- I.17 Convergence test: error on the value of the reflection coefficient for power sponge layer with $n_B = 3$ and $B_{max} = 0.5$. The dashed line shows the resolution used for the contour plots. 229
- I.18 Convergence test: reflection coefficient for power sponge layer with $n_B = 3$ as a function of B_{mean} for different mesh resolution. The red curve shows the resolution used for the contour plots. 230

J Appendix J: Dissipation above a shelf 231

- J.1 Convergence of the dissipative models for wave at a step. 234

J.2	Wave mass transport jump above the shelf and dissipative models.	235
K	Appendix K: The SPH method	237
K.1	Sketch of a fluid portion in SPH.	239
L	Appendix L: Error and Data	243
L.1	Instantaneous flow rate with uncertainties.	245
L.2	Mean, first and second harmonic flow rate as a function of frequency.	246
M	Appendix M: Experiment of WASP at Le Havre	251
M.1	Sketch of the experimental tank.	252
M.2	Experimental time evolution incident and reflected wave amplitude.	254
M.3	Experimental time evolution of the flow rate under the plate.	255
M.4	Compared SPH and experimental flow rate.	255
M.5	Velocity magnitude in the SPH simulations.	256
M.6	FFT of the SPH simulation flow rate.	256
N	Appendix N: Experimental trials of 3D RWT	259
N.1	3D RWT experimental setup.	260
N.2	90° wedge deflector.	261
N.3	Straight inclined wall.	261
N.4	Curved wall.	262

List of Tables

1	Wave theory	9
1.1	Physical properties of air, fresh water and sea water with salinity 35‰. . .	16
2	The Resonance Wave Tank	57
3	Waves above a submerged plate	99
3.1	Simulation parameters for waves above a submerged plate.	122
3.2	Simulation and models results for waves above a submerged plate (Murakami <i>et al.</i> 's case).	124
A	Appendix A: Gerstner's waves	159
B	Appendix B: Boundary Layers Effects and Wave Mass Transport	169
C	Appendix C: Solver waves generated by plunger	175
D	Appendix D: Mean flow kinematic boundary condition	181
E	Appendix E: Higher orders Stokes waves theory and Non-linear disper- sion relation	185
F	Appendix F: Lamb's viscous waves	191
G	Appendix G: Potential flow of viscous fluid	195

H	Appendix H: Viscous potential flow	199
I	Appendix I: Optimal Sponge Layer	207
I.1	Predicted power sponge layers range of B_{mean} to get less than 5% reflection for different wave length (extremes value) and value at which the minimum is reached (center). The number in red shows minimum for which the predicted reflection is below 2%.	223
I.2	Table values of B_{mean} for different sponge layer functions with minimum reflection. The values are listed if the predicted reflection is below 5% and in red if below 2%. The results are found using the Golden section search algorithm.	226
J	Appendix J: Dissipation above a shelf	231
K	Appendix K: The SPH method	237
L	Appendix L: Error and Data	243
L.1	Estimated uncertainties ranges.	245
L.2	Experimental configurations A to B.	247
L.3	Experimental configurations C to E.	247
L.4	Raw data Experiment A.	248
L.5	Raw data Experiment B: vary the stroke amplitude.	248
L.6	Raw data Experiment C: vary the plunger length, $s_0 = 0.69$ cm.	249
L.7	Raw data Experiment C: vary the plunger length, $s_0 = 1.16$ cm.	249
M	Appendix M: Experiment of WASP at Le Havre	251
M.1	Simulation results for waves above a submerged plate case compared to the experimental data.	255
N	Appendix N: Experimental trials of 3D RWT	259

Nomenclature

Abbreviations

BLR	Boundary layer resolved
EFE	Eigenfunction expansion (linear potential method without dissipation)
EFE Full	Eigenfunction expansion dissipation model
EFE NI	Eigenfunction expansion not incompressible (simplified dissipation model)
FFT	Fast Fourier transform
fps	Frame per seconds
LES	Large eddy simulation
PIV	Particle image velocimetry
RWT	Resonance wave tank
SPH	Smoothed particle hydrodynamics
VOF	Volume of fluid
WASP	Waves above a submerged plate
WEC	Wave energy converter

Dimensional quantities

μ	Dynamic viscosity	$(\text{kg}\cdot\text{m}^{-1}\cdot\text{s}^{-1})$
ν	Kinematic viscosity	$(\text{m}^2\cdot\text{s}^{-1})$
ρ	Density	$(\text{kg}\cdot\text{m}^{-3})$
σ	Surface tension	$(\text{N}\cdot\text{m}^{-1})$
ζ	Adiabatic index	

c_0	Speed of sound at 1 bar	$(\text{m} \cdot \text{s}^{-1})$
g	Gravitational acceleration	$(\text{m} \cdot \text{s}^{-2})$
p	Kinematic pressure	$(\text{kg} \cdot \text{m}^{-1} \cdot \text{s}^{-2})$
$p_* = p + \rho g z$	Excess pressure	$(\text{kg} \cdot \text{m}^{-1} \cdot \text{s}^{-2})$
$\mathbf{u} = (u, v, w)$	Velocity vector	$(\text{m} \cdot \text{s}^{-1})$
φ	Scalar velocity potential	$(\text{m}^2 \cdot \text{s}^{-1})$
\mathbf{f}_d	Volumetric dissipative forces	$(\text{kg} \cdot \text{m}^{-2} \cdot \text{s}^{-2})$
λ	Wavelength	(m)
ω	Wave angular frequency	$(\text{rad} \cdot \text{s}^{-1})$
a	Wave amplitude	(m)
d	Water depth	(m)
f	Wave frequency	(Hz)
h_w	Wave height	(m)
k	Wavenumber	(m^{-1})
T	Wave period	(s)
ϕ	Flow rate	$(\text{cm}^2 \cdot \text{s}^{-1})$
$c_\varphi = \omega/k$	Phase velocity	$(\text{m} \cdot \text{s}^{-1})$
$c_g = \omega/k$	Group velocity	$(\text{m} \cdot \text{s}^{-1})$
$\boldsymbol{\pi} = p_* \mathbf{u}$	Energy flux or excess pressure work	$(\text{kg} \cdot \text{s}^{-3})$
$\mathbf{M}^w = \rho \overline{\int_{\eta}^{\eta} (u, v)^T dz}$	Wave mass transport	$(\text{kg} \cdot \text{m}^{-1} \cdot \text{s}^{-2})$

Non-Dimensional quantities and numbers

$\mathcal{R} = (gd^3/\nu^2)^{1/2}$	Wave Reynolds number
$Bo = \rho g \lambda^2 / \sigma$	Bond number
$Ma = U_{max} / c_0$	Mach number
$Re = \rho u_0 L / \mu$	Reynolds number
$Ro = af\lambda/\nu = ReSt$	Roshko number

$St = af/u_0$ Strouhal number

Resonance wave tank notations

$\delta x_{R/L}$ Opening lengths.....(cm)

d Water depth above the submerged plate..... (cm)

$d_o = d_{tot} - d - t_{sp}$ Opening height under the submerged plate (cm)

d_p Plunger mean draft (cm)

d_{tot} Total water depth (cm)

f_0 Plunger stroke frequency (cm)

l_c Plunger center location from lateral wall (cm)

l_p Plunger half length.....(cm)

l_{sp} Submerged plate length (cm)

l_t Tank length (cm)

l_w Tank width (cm)

s_0 Plunger stroke amplitude (cm)

t_{sp} Submerged plate thickness (cm)

$\bar{\phi}$ Instantaneous mean flow rate ($\text{cm}^2 \cdot \text{s}^{-1}$)

ϕ Instantaneous flow rate ($\text{cm}^2 \cdot \text{s}^{-1}$)

$\phi^{(0)}$ Asymptotic mean flow rate ($\text{cm}^2 \cdot \text{s}^{-1}$)

$\phi^{(1)}$ Asymptotic first harmonic flow rate ($\text{cm}^2 \cdot \text{s}^{-1}$)

ϕ_1 Instantaneous first harmonic flow rate ($\text{cm}^2 \cdot \text{s}^{-1}$)

β_{wb} Wave breaking threshold.....

$\mathcal{R}_{init} = \sqrt{gd^3/\nu_{init}^2}$ Model initial dissipation Reynolds' number.....

ν_{init} Model initial dissipation viscosity ($\text{m}^2 \cdot \text{s}^{-1}$)

Simulation parameters

α Mixture scalar function in OpenFOAM (cm)

δx Grid resolution in OpenFOAM (cm)

$c_{SPH} \approx 10\sqrt{gd}$	Numerical speed of sound in SPH method	$(\text{m} \cdot \text{s}^{-1})$
h_{SPH}	Smoothing length in SPH method	(cm)
r_{SPH}	Particle size in SPH method	(cm)
Waves above submerged plate notations		
d	Water depth before the submerged plate	(cm)
d_p	Water depth above the submerged plate	(cm)
l_p	Submerged plate half length	(cm)
t_p	Submerged plate thickness	(cm)
$D_p = d_p/d$	Immersion ratio	
$L_p = l_p/d$	Length to depth ratio	
$T_p = t_p/d$	Thickness to depth ratio	
$\lambda = 2\pi/k_0$	Wave length in the water depth d	(m)
$\lambda_p = 2\pi/k_0^p$	Wave length in the water depth d_p	(m)
$\Lambda_p = 2l_p/\lambda_p$	Non-dimensional wave length above the plate	
ω	Incident wave angular frequency	$(\text{rad} \cdot \text{s}^{-1})$
$\Omega = \omega\sqrt{d/g}$	Non-dimensional incident wave angular frequency	$(\text{rad} \cdot \text{s}^{-1})$
$A = a_{inc}/d$	Non-dimensional incident wave height	
a_{inc}	Incident wave height target	(cm)
$K_0 = k_0d$	Principal non-dimensional wave number evaluated with respect to d in the water depth d	
$K_0^p = k_0^p d$	Principal non-dimensional wave number evaluated with respect to d in the water depth d_p	
a_{SPH}	Incident wave height measured in the simulations	(cm)
$\phi_I = a_{inc}\omega/k_0$	Characteristic wave flow rate	
$\varpi_I = a_{inc}\omega \cosh[k_0(d - d_p)]/\delta_\nu \sinh k_0d$	Characteristic vorticity at the plate	(s^{-1})
$M_I = \rho^{1/2}a_{inc}^2\omega \coth k_0d$	Incident wave mass transport	$(\text{kg} \cdot \text{m}^{-1} \cdot \text{s}^{-1})$
$u_I = a_{inc}\omega/k_0d$	Characteristic wave velocity	$(\text{m} \cdot \text{s}^{-1})$

Introduction

L'énergie des vagues est une source d'énergie renouvelable peu ou pas exploitée à ce jour [161]. Elle reste la source d'énergie renouvelable la plus chère comparée aux autres ressources renouvelables. Avec près de 2TW de puissance disponible [65, 138], son potentiel représente pas moins de 10% de la puissance nécessaire pour subvenir à la demande énergétique mondiale actuelle : un challenge et une opportunité pour la France et les États-Unis d'Amérique qui se partagent les deux plus grandes zones exclusives marines.

D'un point de vue historique, le premier système d'extraction d'énergie des vagues a été proposé et breveté par le Français Pierre-Simon Girard et son fils en 1799. Depuis, de nombreux systèmes ont été proposés par la communauté scientifique et des entrepreneurs. Les énergies houlomotrices restent cependant chères. Pour réduire leur coût, il est envisagé de les coupler avec des systèmes déjà existants et d'étendre leurs activités [50].

Dans cette étude, il est proposé d'utiliser l'énergie des vagues afin de générer ou d'amplifier des courants. Il s'agit donc de rectifier l'énergie oscillante des vagues et de la transformer en courant continu.

Dans la nature, deux types de pompes utilisant les vagues sont remarquables : les pompes péristaltiques et les pompes à impédance. Les premières ne tirent pas avantage de la possibilité de faire entrer le système en résonance, contrairement aux secondes. Les pompes à impédance se retrouvent dans le développement du coeur embryonnaire, faisant de ce type de pompe le meilleur rapport "qualité/prix" pour la nature. Elles sont très simples à concevoir. Elles se composent d'un tube flexible où les vagues se propagent et d'un tube rigide refermant le système. Les ondes sont générées par une compression périodique à une position excentrée sur le tube flexible. Un écoulement se met en place lorsque la période d'excitation est proche d'une période propre de la pompe.

Dans cette thèse, en s'inspirant des pompes à impédance, on propose d'étudier deux types de pompes à vagues : la pompe à résonance dans un bassin fermé et, les vagues au-dessus d'une plaque submergée en bassin infini. Dans les deux cas, il est montré comment les propriétés des vagues permettent de générer un écoulement autour d'une plaque submergée qui sépare la colonne d'eau en une partie "flexible" (à surface-libre) et une partie "rigide" (sous la plaque).

Wave energy context and challenges

Ocean waves represent a tremendous source of renewable energy but an expensive one [161]. Waves originate from the wind local forcing at the water interface (see section 1.1). As wind comes from uneven solar heating (generating temperature gradient), ocean waves can essentially be seen as condensed form of the solar energy. Wave energy accounts for the major part of the energy content of the ocean [15]. It is estimated that the worldwide wave power capacity reaching the world coastlines is of the order of 2TW [65, 138]. This represents no less than 10% of the total world energy consumption (of the order of 18 TW [2]), a vast, yet untapped, reservoir of renewable energy. A particularly interesting challenge for countries like France and the United States of America which own the two largest exclusive economic zone (EEZ) in the world (11,691,000 km² and 11,351,000 km², respectively [1]).

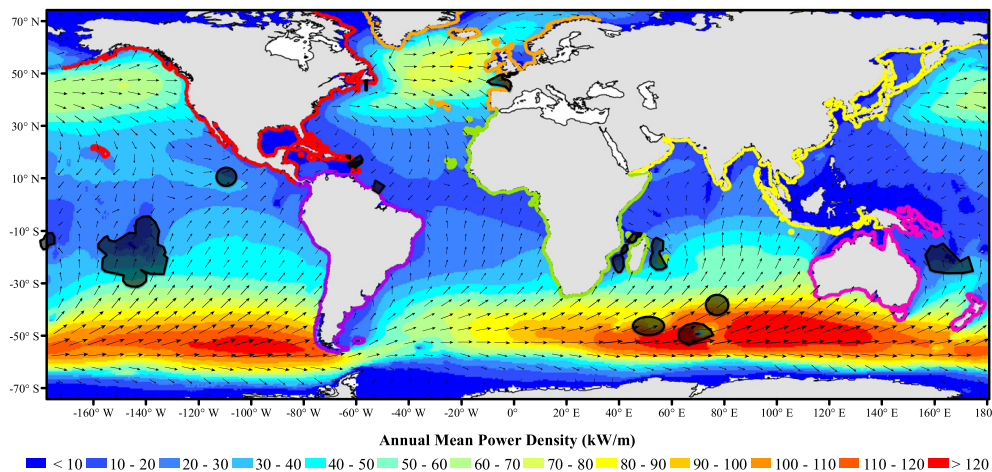


Figure 1: Annual mean wave power density and mean best direction of wave energy flux. The color lines show the boundary delimitation used to estimate the shore wave power capacity. Figure adapted from [65] (with permission). The shaded black regions show the EEZ of France approximative localization.

Historically the first concept of wave energy converter (WEC) was proposed and patterned by the Frenchmen Girard Pierre-Simon and his son in 1799 [57]. It corresponds mostly to the idea of what is now called a point absorber [43]. Since then, plethora of concepts have been proposed by researchers and inventors worldwide (see [38, 45, 160] for reviews of WECs). The oil crisis in the 1970s gave a boost to the development of WECs. Unfortunately, as of today, the wave energy is currently the most expensive form of power available on the planet [161] (see [145] for an illustration of the approximative cost of WECs energy). This high cost is due mostly to the challenges the wave energy power industry has to tackle [45, 159]: how to extract the energy? how to make the device resistant to extreme events? how to minimize the environmental consequences? how to optimize the system?

For instance, it is quite common to target off-shore wave energy as the wave energy is more abundant there. Nevertheless, it is more challenging to bring the energy back to the consumer and the wave energy is less well organized out-there¹. Furthermore, the WEC has to be fixed to the sea bed somehow and the design resistant to the extreme waves: two difficult tasks to achieve at once. An idea to reduce the cost for this kind of WEC is to couple them with off-shore structures such as aquaculture facilities [50]. On the other hand, on-shore systems have less energy reaching them as waves lose energy when travelling in shallower water. In the same time waves come to die on the shore reducing the environmental impact the energy extraction has. This also enables to kill two birds with one rock: protect the shore and extract the energy. Sharing the installation cost between the shore-protection and the energy harvesting is definitely an attractive opportunity (see [50] for other strategies on cost-sharing opportunities). A popular system for this is the oscillating water column (OWC) [42, 44, 105], which can be inserted in harbour protecting breakwater. In this WEC, a chamber open at the bottom to the sea communicates with the atmosphere above via a duct. As the waves oscillate in the chamber, the air is pushed out and in. The energy is extracted by the mean of a turbine (a Wells turbine in general). Another advantage of such a device is that the energy converter (namely the turbine) is not in direct contact with the ocean. Nevertheless, this device requires to be partially emerged and thus is not suitable for coastline protection, while it is quite suited for harbour breakwaters. Submerged WECs are thus of interest (eg. the wave carpet [4]). Unfortunately most of the energy is located in the near surface region where wave breaking is likely to happen as most WECs relies on some kind of resonances to be efficient [145].

In the present work, it is suggested to transform the global wave energy (potential and kinematic) into a current from which the energy can be extracted in a “safer” region. Oscillatory flows are less interesting than steady unidirectional flows from an energy point of view. The goal is thus to use the wave properties (interaction with obstacles) to generate uniform currents or to “rectify” the waves: pumping with water waves and designing ocean wave rectifiers. The generation of steady currents is interesting for wave energy harvesting as: a) it is easy to extract energy efficiently from uniform currents, b) it can be coupled with already existing larger scale currents (from tide for instance) such that to amplify them locally, c) currents can be used for other wave energy applications: water desalination (for reverse osmosis) or water cooling. The question left to answer is: how to generate currents with water waves or waves in general?

¹At the origin, waves are formed irregularly (in a storm region) and as they travel they tend to reorganize in groups of rather uniform frequency, called “wave trains” (see figure 1.1 in chapter 1 as an illustration). The waves basically transport the energy of the storm on long distance with little dissipation and the different speed makes the waves reorganize in coherent groups as they travel long distances.

Pumping with waves in nature

The ocean provides the wave source and the goal is to transform part or all of the wave oscillatory energy into a mean current from which the energy can be extracted or used for some of the applications listed before. Ocean waves can generate mean circulation and an example is the longshore currents. The wave breaking occurring in the surf-zone near the shoreline with an incident angle induces an exchange of momentum with the mean flow [94].

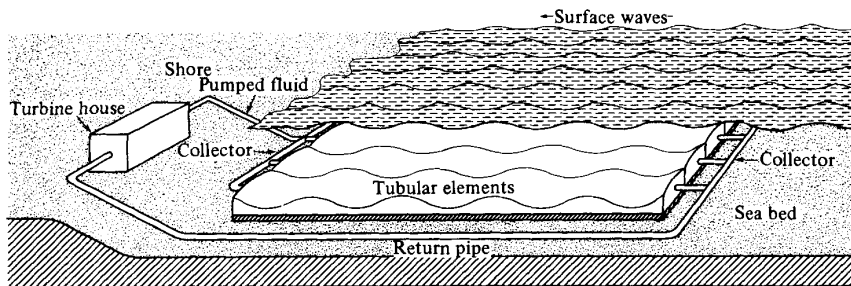


Figure 2: Schematic diagram of Allison’s peristaltic pump [5, 95] (extracted from [5] with permission).

Ocean waves also generate currents near the sea floor through what is called “acoustic streaming”². This led to the study of a kind of “peristaltic” pump (see figure 3-a) by Allison [5] and Longuet-Higgins [95] (see figure 2). This device is quite similar to the wave carpet idea of Alam [4]. A deformable membrane at the sea floor extracts the energy of the waves. The membrane separates the ocean medium from the fluid in the peristaltic pump. The water waves push the membrane down between two wave crests and block fluid between these two points. As the waves travel, the fluid in the pump is forced to travel in the wave direction generating pumping. This is sketch with a single compression point in figure 3-a. This device is quite interesting as peristaltic pumps are a kind of pump that one can find in different living examples: intestines for instance use this principle. In the intestines, the muscles (*muscularis propria*) play the roles of the water waves. But peristaltic pumps do not take advantage of resonances. From a biological point of view, the peristaltic pumps are actually quite complex to design. Imagine the complexity it would require to create such a pump with muscle rings around a cylindrical membrane: the muscles would need to contract successively in a organized fashion to generate the desired wave shape on the surface of the membrane³. Nature is an interesting library of ideas and when it comes to pumping with periodic excitations and waves, peristaltic is only one of the solution it found.

²See discussion in section 1.3.3 and appendix B.

³In the case of the intestines, two layers of muscles are involved: an inner layer organized in circular rings fashion and an outer layer arranged longitudinally.

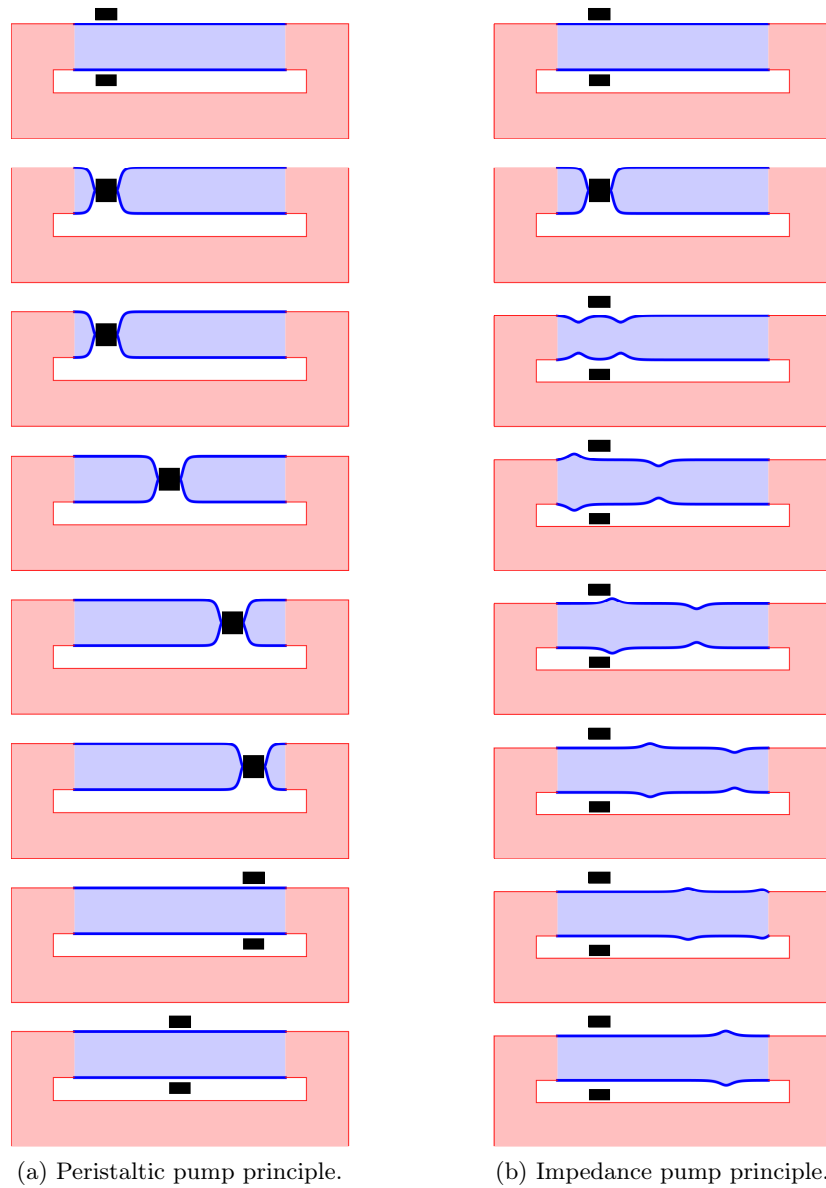


Figure 3: Peristaltic and impedance pumps diagram. The shaded blue region represents the flexible membrane, while the shaded red one represents rigid tubes.

When looking at the early stage of life one can observe another way nature came up with a technique to pump using a periodic excitation and wave properties. That is in the development of the embryonic heart. A blood flow is crucial for the well development of the embryonic heart. In the human embryo, the first beats and the blood circulation start well before the heart, with its chambers and valves to ensure unidirectional flow, is formed. The flow starts around the day 22 of the embryo development, while the heart is fully functional after 50-60 days [48]. At the beginning the blood flow is driven by impedance pumping [49] and not by peristaltic pumping as previously described. Forouhar et al. [49]

showed this by studying the development of the heart of a zebrafish. They showed that the blood velocity of the embryo was not linearly linked to the heart frequency, as it would be for a peristaltic pump. The impedance pumps are thus the way nature pumps at “low capital cost”⁴. It is quite simple to design with a mind experiment with muscle rings and a flexible tube: one just needs to place the muscles at an off-centered position on the flexible tube and then contract the tubes at a constant pace. Experimentally this means just giving electrical shocks to the muscles. When the pace (or contraction frequency) matches a natural frequency of the device a unidirectional flow arises. A sketch of the impedance pump with a flexible tube is shown and compared to the peristaltic pump in figure 3. The black squares represent an actuator which for the impedance pump just needs to be contracted while for the peristaltic pump it needs to be translated too. The flexible tube (shaded blue) is connected at its extremities to more rigid tubes represented in solid red (which can form a closed loop as sketched here). For the impedance pump, it is the wave dynamics that is responsible for the observed pumping. The cycle sketched in figure 3 repeats.

The goal of this research is to use and explain the idea of the impedance pumping to pump with water waves. The flexible membrane does not appear as a good strategy as it is prone to failure and would increase the capital cost. Instead, the water surface is proposed to be used as the “flexible membrane”. A prototype was proposed by Meier [112] and Gharib. In this concept, the pump involved the circulation around a submerged plate in a closed tank. This device is studied in details in chapter 2. The circulation around the submerged plate due to the wave action is not without link to another WECs that was proposed following the studies of submerged breakwater by Dick [36]: waves above a submerged plate. This is studied in the chapter 3. Interestingly, the concept of impedance pumping and waves above a submerged were both studied in the 1960’s: one inspired by biological observation of embryos and another one to reduce breakwater capital cost. They are now linked in the present thesis. In both cases, the waves generate a circulation around a submerged structure which acts like a separation between a the water surface or “flexible domain” and a “rigid domain” (see figure 4).

Outline of this work

The present manuscript is organized as follows: in the chapter 1, a general review of wave properties is given and the main theoretical background required to model the physics of the two problems of wave pumping is presented. In particular, the eigenfunction expansion (EFE) matching method is reviewed and the wave mass transport is defined. It is also outlined in a simple example that the wave mass transport can vary locally due to variation

⁴Where it is considered here that the capital cost of nature is the time required to get a functional device.

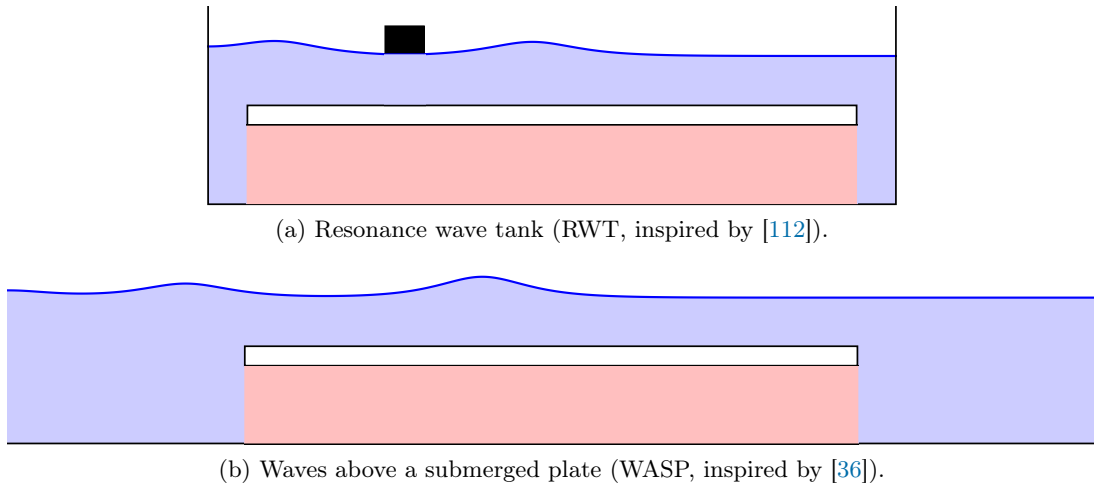


Figure 4: Wave rectifiers designed studied in the present thesis and inspired by Meier [112] and Dick [36] works. The color outlined similarity to the peristaltic and impedance pump of figure 3: the flexible equivalent part in blue (free surface domain) and rigid equivalent part in red (under the submerged plate).

of the water depth. A dissipation model is proposed to capture wave dissipation due to breaking or friction, which is useful in resonance cases mostly. The additional mass transported during breaking is also discussed.

Then the concept proposed by Meier [112] is studied experimentally and theoretically (see figure 4-a). It will be shown that the wave pump works near special frequencies that through the linear description are identified as resonance frequencies (in accordance with previous studies on impedance pump). Using the dissipative model presented in the first chapter, the direction and the magnitude of the flow can be fairly guessed by looking at the wave mass transport variation of the generated waves. Through a numerical analysis, it is shown that the flow is mostly due to the surface wave mass transport term. For the first time, a clear description of the physical origin of the circulation is thus provided for the free-surface impedance pump.

The system proposed by Meier [112] appeared while studying it, similar to another conceptual idea of WECs studied in the 1960s by Dick [36]: waves above a submerged plate (see figure 4-b). In the third chapter of this thesis, the waves above a submerged plate problem is revisited in the light of the previous findings. The description to understand the physics of the wave pump of Meier [112] is thus applied to the breakwater device. It is found that the circulation observed by Dick [36] while studying breakwater appears to have the same origin as the flow in the free surface impedance pump of Meier [112]. The waves above a submerged plate are thus in some sense a kind of impedance pump.

In summary in this thesis, a new way to harvest energy from waves is proposed and takes advantage of the waves-induced current. It is simply linked to the waves properties which

can lead to local variation of the wave mass transport (and can be evaluated by simple linear theory). This surface flow can be amplified locally using the waves interaction properties and generate currents which can be used for different WECs applications such as energy harvesting, water desalination or cooling and even water sport (applications are discussed in conclusion).

The chapters 2 and 3 are independent and can be read separately. The chapter 1 material is used in all the other chapters. The thesis comes also with numerous appendices which aim to provide more details and discussions. Appendix A presents a review of Gertsner's wave theory and is an alternative model to the Airy's wave theory used in the rest of the manuscript. The theory is compared to simulations using the SPH method. Appendix B is a review of the boundary layer effects on the mean flow. Appendix C provides an example of coded solver of linear wave problem and shows the convergence rate of the method. Appendix D details the calculation of the important boundary condition for the mean flow equations of section 1.4.2. Appendix E shows the equations for the second and third order wave theory along with a derivation of the non-linear dispersion relation. Appendices F to H look at viscous wave theories. They show other existing viscous dissipation models and also discussed the wavenumbers evolution with viscosity. Appendix I provides in the form of a submitted article a discussion on the design of optimal wave absorption sponge layers for numerical modeling of water waves. It is not discussed in the core of the thesis as it is not essential to the wave pumping discussion though it is used in chapter 3 and appendices A and M. Appendix J justifies the simplification of the model presented in section 1.5.3 for wave dissipation by the mean of an example. Appendix K provides a quick overview of the SPH method used for the numerical modeling of water waves. The thesis is not on SPH development. Appendix L details the error calculations in the experiments of chapter 2 and provides tables of experimental results of the flow rate measurements. Appendix M presents a new experimental observation of wave pumping around a submerged plate along with numerical simulation of this case. Last, appendix N show 3D prototypes tested in laboratory of the resonance wave pump of chapter 2.

Chapter 1

Wave theory

Dans ce chapitre, les différents outils théoriques utilisés dans le reste de la thèse sont présentés. Dans un premier temps une définition de la notion de vagues est donnée. La thèse s'intéresse principalement aux ondes monochromatiques, c'est-à-dire avec une seule fréquence. Les équations et les conditions aux limites associées sont données et commentées. L'approximation d'écoulement potentiel est introduite et la théorie linéaire est rappelée. En particulier, on montre que les vagues déplacent de la masse dans leur direction de propagation dans une couche de surface correspondant à la zone décrite par la surface libre. On appelle cela le transport de masse des vagues. Pour résoudre les équations potentielles linéaires dérivées, on présente un outil mathématique basé sur les expansions en mode propre et on donne des exemples d'application. L'interaction entre le champ de vagues et l'écoulement moyen induit est ensuite discutée. En particulier, l'accent est mis sur l'importance du transport de masse des vagues sur l'écoulement moyen. On rappelle les effets des non-linéarités sur la longueur d'onde et la taille maximale de vague ou la limite de déferlement. Un modèle de dissipation est proposé pour appliquer de la dissipation dans les zones où les vagues dépassent la taille limite de déferlement. Enfin, on rappelle l'estimation de la masse additionnelle transportée lors du déferlement dans les rouleaux.

Abstract

This chapter provides an overview of the different theoretical tools used to study waves throughout the rest of the thesis. First, a general definition of water waves is given. The focus here is on periodic gravity waves. The general governing equations and boundary conditions are given and discussed. Then, the potential flow assumption is applied and the linear theory reviewed. It is shown that waves transport mass in their direction of propagation in the surface layer, which corresponds to the region covered by the surface during a period. This is called the wave mass transport. A mathematical tool to solve the linear potential problem, called eigenfunction expansion (EFE) matching method, is presented and applied to simple problems for illustration. In particular, the case of a wave train at a step enlightens the possible variation of the mass transport and the induced currents. The interaction of the rapidly oscillating wave field with a mean current is then discussed. It is observed that the variation of the wave mass transport acts like a source term to the mean flow equations. The effect of non-linearities on the dispersion relation are discussed and the maximum wave height, or wave breaking threshold, are reviewed. When waves reach this threshold dissipation is important. A model to represent wave dissipation is therefore presented. It involves only one dissipative term on the kinematic boundary condition¹. A simplification of the model is proposed (EFE NI). Last, the additional wave mass transported during wavebreaking in the rollers is discussed.

1.1 Water waves: definition and description

1.1.1 Water waves: definition

Ocean waves are unsteady deformations of a water-atmosphere interface subject to gravitational forces which propagate through the water medium. They are called *gravity waves*. The competition between inertia and gravity (the *restoring force*) leads to the surface oscillation. There are two other main families of waves on the surface of an incompressible fluid defined by their restoring force: Coriolis waves (a large scale process due to the rotation of the Earth) and capillary waves (a short scale process due to surface tension forces).

In this thesis, the main focus is on periodic gravity waves. The waves are considered close to monochromatic and are generated by an oscillatory body (paddle, piston). In open ocean, this is equivalent to waves generated by wind stress (disturbing force) in the far ocean and travelling long distance toward the shore. As it will be shown in the coming sections, gravity waves are dispersive and thus, even though the generation can be unsteady and chaotic (like in storms), as the waves travel they reorganize in wave groups or trains of similar frequencies and reach the coast in the form of regular wave trains. Figure 1.1 shows

¹Other models are discussed in appendices F to H.

a photograph of a wave train at Ventura Point on February 24th 2016 (courtesy of the great work of @WoodyWavesWoodWorth, professional surf photographer) as an illustration of the regularity of waves on the shore. This is an exceptional configuration which shows an extremely regular event.



Figure 1.1: Aerial of Ventura Point showing a wave train (February 24th 2016). Photo taken from Instagram account @WoodyWavesWoodWorth, with permission.

Different theories can be developed to describe the behavior of the surface depending mainly on the magnitude of the surface variation of amplitude compared to the characteristic length of the deformation. It is important in any theoretical description to establish a limit of validity between the different theories. For instance, consider the domain of applicability of gravity and capillary waves. In both cases inertia forces are compensated by a pressure force (or restoring force, due to the gravitational acceleration or surface tension) that tries to empty the crest of the wave. In the figure 1.2, λ represents the so-called *wavelength* of the surface deformation. One can also define the *wavenumber* $k = 2\pi/\lambda$.

The gravity force is the dominating restoring force over the capillary force if:

$$\left| \frac{\nabla P_g}{\nabla P_c} \right| \propto \frac{\rho g}{\sigma k^2} \gg 1 \quad (1.1.1)$$

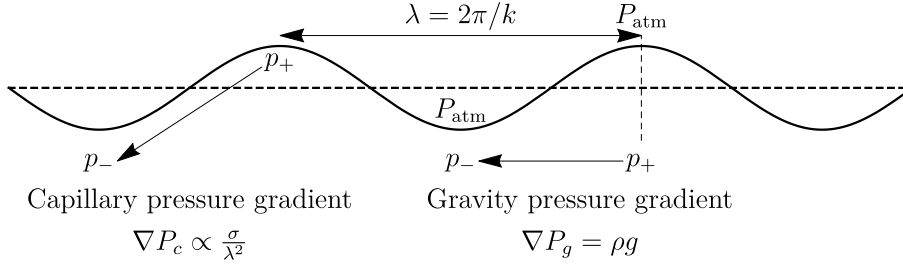


Figure 1.2: Capillarity and gravity spring forces due to pressure variation.

where g the gravitational acceleration, ρ the fluid density, σ is the surface tension and the subscript c (g) refers to capillary (gravity, respectively) and ∇P is the pressure gradient associated to these forces. One can define the *Bond number* :

$$Bo = \frac{\rho g}{\sigma k^2}. \quad (1.1.2)$$

For ocean waves, $\lambda \approx 10 - 100$ m, $\rho \approx 10^3$ kg.m³ and $\sigma \approx 70 \cdot 10^{-3}$ N.m⁻¹. Hence, the typical order of magnitude of the Bond number in water wave problems is $Bo \approx 3.5 \times 10^5 - 10^7$ and thus surface tension can be neglected. In the experimental part of this thesis, the wavelengths are smaller than in the ocean (on the order of 25 cm to 1 m), but the Bond number stays significantly larger than unity allowing the same approximations ($Bo \approx 10^2 - 10^3$). One can also compare the inertia forces with the capillary forces (gravity forces) to define the *Weber number* (*Froude number*).

1.1.2 Governing equations and boundary conditions at the surface

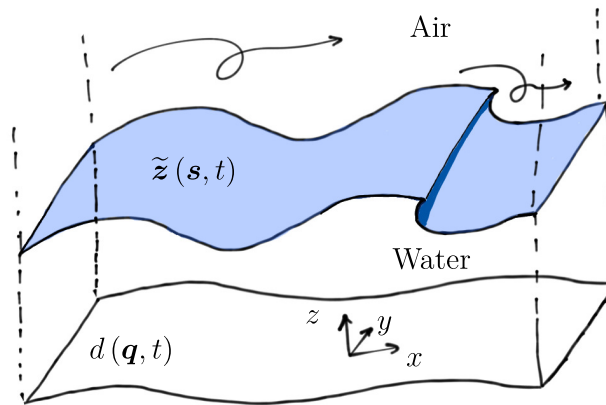


Figure 1.3: Two-phase problem: the air-water interface is defined by a parametric function $\tilde{z}(\mathbf{s}, t)$ and the sea-bed by $d(\mathbf{q}, t)$.

Water wave dynamics is a two-phase problem and is mathematically complex to describe. There exists no exact solution per say to this problem thus approximations have to be

made. Consider the general problem sketched in figure 1.3: a water and an air phase separated by an interface (or surface) described by the parametric function

$$\tilde{\mathbf{z}}(\mathbf{s}, t) = \begin{pmatrix} \eta_x(\mathbf{s}, t) \\ \eta_y(\mathbf{s}, t) \\ \eta_z(\mathbf{s}, t) \end{pmatrix}, \quad (1.1.3)$$

where \mathbf{s} is a parametric vector and t is the time. This general formulation allows the description of wave breaking. The seabed is defined by a function $d(\mathbf{q}, t)$, where \mathbf{q} is another parametric vector. Under the Navier–Stokes hypotheses², the water phase is governed by the following set of equations:

$$\begin{cases} \partial_t \rho + \nabla \cdot (\rho \mathbf{u}) = 0, \\ \partial_t \mathbf{u} + (\mathbf{u} \cdot \nabla) \mathbf{u} = -\frac{1}{\rho} \nabla p + \mathbf{g} + \frac{1}{\rho} \nabla \cdot \bar{\bar{\tau}} + \mathbf{f}_d \end{cases} \quad (1.1.4)$$

where \mathbf{u} is the velocity vector, p is the pressure, \mathbf{g} is the gravitational acceleration (assumed constant), \mathbf{f}_d represents extra volume forces (which can be the Coriolis or centrifugal acceleration or, for the purpose of modeling or numerical dissipation, a friction type force, see appendix I), and $\bar{\bar{\tau}}$ is the Stokes' stress tensor:

$$\bar{\bar{\tau}} = \mu \left(\nabla \mathbf{u} + \nabla \mathbf{u}^T - \frac{2}{3} (\nabla \cdot \mathbf{u}) \bar{\bar{I}} \right), \quad (1.1.5)$$

and μ is the fluid dynamic viscosity, and $\bar{\bar{I}}$ is the identity matrix. These equations are called the *Navier–Stokes* equations and are written for a compressible fluid. Water is a compressible fluid [86]. The *Tait–Murnaghan* equation of state can be considered:

$$p = \frac{\rho_0 c_0^2}{\zeta} \left[\left(\frac{\rho}{\rho_0} \right)^\zeta - 1 \right], \quad (1.1.6)$$

where $\zeta \approx 1 - 7$ is an adiabatic index, c_0 and ρ_0 are the speed of sound and the density at the reference pressure of 1 bar³. For water, the value of the speed of sound is typically of the order of $c_0 \approx 1500$ m/s at 20° [34, 67, 86] (see table 1.1). It is thus common to consider the fluid as incompressible. A criteria for incompressibility is commonly defined as the *Mach* number:

$$Ma = \frac{U_{max}}{c_0}, \quad (1.1.7)$$

where U_{max} is the maximum speed in the fluid. For ocean gravity water waves, the wave maximum velocities are of the order of the meter per second thus the incompressible

²Air and water are considered to be continuous media.

³This is used for numerical modeling with a lower speed of sound in the SPH method.

approximation is valid. The set of equations eq.1.1.4 becomes

$$\begin{cases} \nabla \cdot \mathbf{u} = 0, \\ \partial_t \mathbf{u} + (\mathbf{u} \cdot \nabla) \mathbf{u} = -\frac{1}{\rho} \nabla p + \mathbf{g} + \frac{1}{\rho} \nabla \cdot \bar{\boldsymbol{\tau}} + \mathbf{f}_d \end{cases} \quad (1.1.8)$$

and the stress tensor becomes the Stokes' stress tensor:

$$\bar{\boldsymbol{\tau}} = \mu (\nabla \mathbf{u} + \nabla \mathbf{u}^T). \quad (1.1.9)$$

It is common in wave problems, to neglect the viscosity based on the comparison of the convective and viscous terms of the previous equations (in the absence of turbulence):

$$\frac{|\rho(\mathbf{u} \cdot \nabla) \mathbf{u}|}{|\mu \Delta \mathbf{u}|} \propto \frac{\rho h_w \omega}{2\mu k} = \frac{af\lambda}{\nu} = Ro = StRe \quad (1.1.10)$$

is the *Roshko* number, where $h_w = 2a$ is the wave height and a the wave amplitude, $\omega = 2\pi f$ is the wave angular frequency, f the frequency, and $\nu = \mu/\rho$ is the kinematic viscosity, $St = af/u_0$ is the *Strouhal number*, $Re = u_0\lambda/\nu$ is the *Reynolds number* and u_0 a characteristic velocity. For ocean waves, a typical wave period is 15 seconds and the wave height is about a meter, the kinematic viscosity of fresh water at 20° is $1.01 \times 10^{-6} \text{ m}^2 \cdot \text{s}^{-1}$, and sea-water at 20° with absolute salinity of 35 g/kg is $1.06 \times 10^{-6} \text{ m}^2 \cdot \text{s}^{-1}$ [135], thus $Ro \approx 7 \times 10^5$ which justifies this approximation (see table 1.1). An inviscid fluid, or one without viscous effects, is called an *ideal* or *perfect fluid*⁴.

These equations are completed by boundary conditions. At the sea-bed, the condition for a viscous fluid is a no-slip condition:

$$\mathbf{u} = \mathbf{w}_{SB}, \quad (1.1.11)$$

where \mathbf{w}_{SB} is the velocity of the sea bed (for instance for the study of earthquakes). For the case of an ideal fluid, the condition is relaxed to a simple slip condition or no-through flow condition:

$$\mathbf{u} \cdot \mathbf{n}_{SB} = \mathbf{w}_{SB} \cdot \mathbf{n}_{SB}, \quad (1.1.12)$$

where \mathbf{n}_{SB} is the normal (oriented inward). In the rest of this thesis, the sea bed is fixed, *i.e.* $\mathbf{w}_{SB} = \mathbf{0}$.

For water wave problems, the challenging boundary is the air-water interface (called the surface for now) as it is both an unknown and a boundary. There are two equations to describe its dynamics. Two jump conditions can be written from the transport theorem of

⁴Through misuse of language the flow is sometimes referred to as ideal flow, while an ideal fluid is by definition a fluid without viscosity: that is $\mu = 0$.

the mass and momentum conservation:

$$\begin{cases} \llbracket \rho (\mathbf{u} - \mathbf{w}_{FS}) \rrbracket \cdot \mathbf{n} = 0, \\ \llbracket p \rrbracket \mathbf{n} - \llbracket \bar{\tau} \rrbracket \cdot \mathbf{n} + \rho (\mathbf{u} - \mathbf{w}_{FS}) \cdot \mathbf{n} \llbracket \mathbf{u} \rrbracket = \sigma \mathbf{n} (\nabla \cdot \mathbf{n}) - \nabla_s \sigma, \end{cases} \quad (1.1.13)$$

where \mathbf{w}_{FS} is the surface velocity, \mathbf{n} is the normal to the surface (the convention is from the water to the air), $\llbracket a \rrbracket = a_{water} - a_{air}$ denotes the jump of a at the interface and ∇_s is the surface gradient operator:

$$\nabla_s \sigma = \nabla \sigma - \mathbf{n} (\mathbf{n} \cdot \nabla \sigma). \quad (1.1.14)$$

In the rest of this thesis, the surface tension is neglected as the Bond number is large.

As the two fluid are assumed to be immiscible, the first boundary condition simplifies to

$$\mathbf{u} \cdot \mathbf{n} = \mathbf{w}_{FS} \cdot \mathbf{n}, \quad (1.1.15)$$

and \mathbf{u} refers here to the water (or air) phase velocity. It is called the *kinematic boundary condition*. This condition simply states that there is no mass transfer through the interface.

The second boundary condition is called the *dynamic boundary condition*⁵. The dynamic boundary condition is at the center of the study of wind wave generation and link the air flow to the water phase enabling momentum exchange [76, 115, 132]. In this thesis, the air flow is assumed to be “at rest”, which amounts to assuming that air friction on the water is negligible (that is $|\bar{\tau}_{air} \cdot \mathbf{n}| \ll |\bar{\tau}_{water} \cdot \mathbf{n}|$).

Under this assumption, the dynamic condition becomes

$$p_{water} \mathbf{n} - \bar{\tau}_{water} \cdot \mathbf{n} = p_{air} \mathbf{n}. \quad (1.1.16)$$

From now on, p_{air} will be called p_{atm} for atmospheric pressure, and the subscript *water* will be dropped as only the water phase is considered. The surface is now referred to as a *free surface* (meaning free of stress). For an ideal fluid, the boundary condition is thus simply the continuity of pressure:

$$p = p_{atm}, \text{ at the free surface.} \quad (1.1.17)$$

For a general fluid, it is important to outline that the dynamic boundary condition does not imply the continuity of pressure at the free surface, the term $\mathbf{n} \cdot \bar{\tau}_{water} \cdot \mathbf{n} \neq 0$ in general. In summary, the general equations in the water phase for wave problems under the incom-

⁵Note that this condition does not include volume forces and in particular the dissipative force of the form \mathbf{f}_d .

	air 0°C	fresh water 20°C	sea water (35‰) 20°C
ρ (kg · m ⁻³)	1.293	998.2	1024.8
μ (kg · m ⁻¹ · s ⁻¹)	1.72×10^{-5}	1.0081×10^{-3}	1.0838×10^{-3}
ν (m ² · s ⁻¹)	1.37×10^{-5}	1.0099×10^{-6}	1.0576×10^{-6}
c_0 (m · s ⁻¹)	331.45	1483	1514

Table 1.1: Physical properties of air, fresh water and sea water with salinity 35‰.

pressible fluid assumption are

$$\begin{cases} \nabla \cdot \mathbf{u} = 0, \\ \partial_t \mathbf{u} + (\mathbf{u} \cdot \nabla) \mathbf{u} = -\frac{1}{\rho} \nabla p + \mathbf{g} + \frac{1}{\rho} \nabla \cdot \bar{\boldsymbol{\tau}} + \mathbf{f}_d, \end{cases} \quad (1.1.18)$$

with boundary conditions at the sea bed

$$\mathbf{u} = \mathbf{0} \quad (1.1.19)$$

and at the free surface

$$\begin{cases} \mathbf{u} \cdot \mathbf{n} = \mathbf{w}_{FS} \cdot \mathbf{n}, \\ p\mathbf{n} - \bar{\boldsymbol{\tau}} \cdot \mathbf{n} = p_{atm}\mathbf{n}. \end{cases} \quad (1.1.20)$$

In the next section, these equations are considered in the potential framework. It is thus assumed that there exists a scalar potential function φ such that: $\mathbf{u} = \nabla\varphi$. It is also further assumed that the surface can be described as a function of the horizontal coordinates:

$$\tilde{\mathbf{z}}(x, y, t) = \begin{pmatrix} x \\ y \\ \eta(x, y, t) \end{pmatrix}. \quad (1.1.21)$$

This implies that no rolling or wave breaking are considered in this description. These approximations are frequently performed in wave theories and provide important features of water waves. It will also be shown in the next chapters that they can be used to explain the major physical aspects of current generation by waves.

1.2 Potential approximation

The motion of an incompressible, ideal fluid with no additional dissipation is now considered to be potential with a free surface $z = \eta(x, y, t)$. It is further assumed that there is

no pressure fluctuation in the air phase, $p_{atm} = 0$, and the sea-bed is uniform, $d = \text{cst}$.

The flow being potential, there exists a scalar function φ called the scalar velocity potential such that $\mathbf{u} = \nabla\varphi$. Using the mathematical property

$$(\mathbf{A} \cdot \nabla) \mathbf{A} = \frac{1}{2} \nabla (|\mathbf{A}|^2) - \mathbf{A} \times (\nabla \times \mathbf{A}), \quad (1.2.1)$$

and $\nabla \times \nabla a = \mathbf{0}$ (where a is a scalar function) and applying it to the velocity vector in the momentum equation with no dissipation, yields Bernoulli's equation:

$$\partial_t \varphi + \frac{1}{\rho} p + gz + \frac{1}{2} |\mathbf{u}|^2 = \text{cst}(t) = 0, \quad (1.2.2)$$

where the constant is dropped⁶. This equation is also valid for a viscous potential flow since then $\Delta \mathbf{u} = \Delta \nabla \phi = \mathbf{0}$ [77](see appendix G).⁷

Using Bernoulli's equation eq.1.2.2 and the dynamic condition at the surface eq.1.1.17, one can link the surface deformation η to the scalar potential at the disturbed interface

$$\partial_t \varphi + g\eta + \frac{1}{2} |\mathbf{u}|^2 = 0, \quad \text{at } z = \eta. \quad (1.2.3)$$

The kinematic boundary condition eq.1.1.15 for potential flow, becomes

$$\partial_t \eta + \partial_x \eta \partial_x \varphi + \partial_y \eta \partial_y \varphi = \partial_z \varphi. \quad (1.2.4)$$

Taking the total derivative of eq.1.2.3 and using eq.1.2.4, one can derive an equation that is only an expression of the velocity potential at the disturbed free surface:

$$\partial_{t,t} \varphi + g \partial_z \varphi + \partial_t (|\mathbf{u}|^2) + \frac{1}{2} \mathbf{u} \cdot \nabla (|\mathbf{u}|^2) = 0, \quad \text{at } z = \eta(x, y, t). \quad (1.2.5)$$

This equation can be practical to use in some cases as it depends only on the scalar potential φ evaluated at the free surface (recall $\mathbf{u} = \nabla\varphi$) [172].

The system of equation to be solved is

$$\begin{cases} \Delta \varphi(x, y, z, t) = 0 & (x, y, z) \in]-\infty, +\infty[^2 \times]-d, \eta[, \\ \partial_{t,t} \varphi + g \partial_z \varphi + \partial_t (|\mathbf{u}|^2) + \frac{1}{2} \mathbf{u} \cdot \nabla (|\mathbf{u}|^2) = 0 & \text{on } z = \eta(x, y, t), \\ \partial_t \varphi + g\eta + \frac{1}{2} |\mathbf{u}|^2 = 0 & \text{on } z = \eta(x, y, t), \\ \partial_z \varphi = 0 & \text{on } z = -d, \end{cases} \quad (1.2.6)$$

⁶ It is an arbitrary constant of time which can be omitted by simply redefining φ . This does not affect the velocity field.

⁷ It is two different hypothesis to assume the fluid ideal and the flow potential. There is no mathematical contradiction in assuming the fluid viscous and the flow potential. The general Bernoulli's equation does not require the fluid to be inviscid as long as the flow is potential.

where the first equation corresponds to the mass conservation and is called *Laplace's equation* and the third equation enables reconstruction of the free surface from the velocity potential directly. Note however that it is more intuitive to keep the kinematic boundary condition and Bernoulli's equation when looking at the mean flow equations (see sect.1.4). This system of equations is used in this chapter to study water waves. It is assumed that the waves are monochromatic from now on, and thus a wave angular frequency ω is defined. The waves are also characterized by their wavelength λ or their wavenumber $k = 2\pi/\lambda$ and their amplitude a (see figure 1.4). For non-symmetric waves, the amplitude is still defined as half the trough to crest vertical distance.

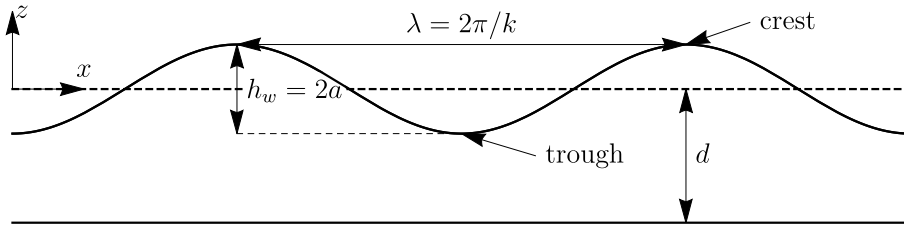


Figure 1.4: Wave trains and notations. The black curve shows the instantaneous surface at the origin of time.

It is convenient, when looking at the general properties of waves in constant water depth, to work in a non-dimensional framework. The following non-dimensional variables are therefore defined:

$$\begin{aligned} (X, Y, Z) &= (x, y, z) / d, \quad \mathcal{T} = t\sqrt{g/d}, \quad K = kd, \quad \Omega = \omega\sqrt{d/g}, \\ A &= a/d, \quad \tilde{Z} = \eta/d, \quad \Phi = \varphi/\sqrt{gd^3}. \end{aligned} \quad (1.2.7)$$

The system of eq.1.2.6 in non-dimensional form becomes

$$\left\{ \begin{array}{ll} \Delta\Phi(X, Z, \mathcal{T}) = 0 & (X, Y, Z) \in]-\infty, +\infty[^2 \times]-1, \tilde{Z}[, \\ \partial_{\mathcal{T}, \mathcal{T}}\Phi + \partial_Z\Phi + \partial_{\mathcal{T}}(|\mathbf{U}|^2) + \frac{1}{2}\mathbf{U} \cdot \nabla(|\mathbf{U}|^2) = 0 & \text{on } Z = \tilde{Z}(X, Y, \mathcal{T}), \\ \partial_{\mathcal{T}}\Phi + \tilde{Z} + \frac{1}{2}|\mathbf{U}|^2 = 0 & \text{on } Z = \tilde{Z}(X, Y, \mathcal{T}), \\ \partial_Z\Phi = 0 & \text{on } Z = -1, \end{array} \right. \quad (1.2.8)$$

and here $\mathbf{U} = \nabla\Phi$ is the non-dimensional velocity. Note that the non-dimensional form of the surface kinematic boundary condition is

$$\partial_{\mathcal{T}}\tilde{Z} + \partial_X\Phi\partial_X\tilde{Z} + \partial_Y\Phi\partial_Y\tilde{Z} = \partial_Z\Phi \quad \text{on } Z = \tilde{Z}(X, Y, \mathcal{T}). \quad (1.2.9)$$

This system is still too complex to be solved analytically, thus additional assumptions have to be made. It is assumed that the waves are weakly non-linear and thus one can expand

the wave functions around an undisturbed solution:

$$\begin{cases} \tilde{Z} = \left\{ \tilde{Z}^{(1)} + \epsilon \tilde{Z}^{(2)} + \epsilon^2 \tilde{Z}^{(3)} + O(\epsilon^4) \right\}, \\ \Phi = \epsilon \left\{ \Phi^{(1)} + \epsilon \Phi^{(2)} + \epsilon^2 \Phi^{(3)} + O(\epsilon^4) \right\}. \end{cases} \quad (1.2.10)$$

where $\epsilon = |KA|$ is a small parameter and the superscripts (i) refer to the expansion term order, (0) being the undisturbed solution, (1) the first harmonic term and so on and so forth.

In the next section, this expansion is used to simplify the system of eq.1.2.8. It is further assumed that the flow is two dimensional, *i.e.* the flow is assumed to be invariant through y translations with zero y velocity component (y is defined in figure 1.3 and is from now on the out-of-plane direction).

1.3 Linear wave theory

The flow is considered two dimensional. Injecting the perturbation development of eq.1.2.10 into the system of equations eq.1.2.8 and retaining only the first order terms, one can find the famous linear potential equations for water waves:

$$\begin{cases} \Delta \Phi^{(1)}(X, Z, \mathcal{T}) = 0 & (X, Z) \in]-\infty, +\infty[\times]-1, 0[, \\ \partial_{\mathcal{T}, \mathcal{T}} \Phi^{(1)} + \partial_Z \Phi^{(1)} = 0 & \text{on } Z = 0, \\ \partial_{\mathcal{T}} \Phi^{(1)} + \tilde{Z}^{(1)} = 0 & \text{on } Z = 0, \\ \partial_Z \Phi^{(1)} = 0 & \text{on } Z = -1, \end{cases} \quad (1.3.1)$$

This set of equations are referred to as the *Airy wave theory* [3] or sometimes as the Stokes I theory [148] (for more information on the origin of the water waves theory, see [28]).

The linearized version of Bernoulli's equation eq.1.2.2 is

$$\partial_{\mathcal{T}} \Phi^{(1)} + P^{(1)} + Z = 0, \quad (1.3.2)$$

and allows the pressure to be solved for.

1.3.1 Linear dispersion relation and linear wave profile

Consider the progressive waves solution of the system eq.1.3.1 of the form

$$\left\{ \Phi^{(1)}, \tilde{Z}^{(1)} \right\} = \Re \left[\left\{ F^{(1)}(Z), A \right\} e^{i(\Omega \mathcal{T} - KX)} \right]. \quad (1.3.3)$$

It is easy to find after basic algebra the well-known first order scalar potential function (in complex notation):

$$F^{(1)}(Z) = \frac{iA\Omega}{K \sinh K} \cosh [K(1 + Z)], \quad (1.3.4)$$

and the dispersion relation relating K to Ω :

$$\Omega^2 = K \tanh K. \quad (1.3.5)$$

The latter equation has an infinite (but countable) number of solutions: there are two real solutions and a countable number of imaginary solutions (see section 1.3.4 for the mathematical properties). Consider for now the real solutions. It is obvious that if K is solution then $-K$ is solution. They correspond to forward and backward travelling waves respectively. In the rest of this section, forward travelling waves are considered.

In the limit $K \rightarrow 0$, corresponding to *long waves* or *shallow water waves*, the dispersion relation reduces to

$$K = \Omega. \quad (1.3.6)$$

On the other hand, in the limit $K \rightarrow \infty$, corresponding to *short waves* or *deep water waves*, the dispersion relation reduces to

$$K = \Omega^2. \quad (1.3.7)$$

The dispersion relation eq.1.3.5 cannot be solved analytically for all values of Ω . To find the values of the wavenumbers for a given angular frequency Ω , a *Newton-Raphson* algorithm is used and initialized with the approximate solution given by Chamberlain and Porter [23]:

$$K \approx \Omega^2 \left\{ 1 - \frac{4 \left[15 - (15 + 30\Omega^2 + 30\Omega^4 + 5\Omega^6 - 10\Omega^8 + 2\Omega^{10}) e^{-2\Omega^2} \right]}{15 \left[2\Omega^2 + \sinh 2\Omega^2 - 4(1 - (\Omega^2 + 1) e^{-2\Omega^2}) \right]} \right\}^{-1/4}. \quad (1.3.8)$$

The wavenumber as a function of the angular frequency is plotted in figure 1.5 with the different approximations (short waves, long waves theories and the approximation of Chamberlain and Porter). It appears graphically that the short wave theory is valid for $\Omega \leq 0.3$ and the long wave theory for $\Omega \geq 1.7$.

The dispersion relation of eq.1.3.5 also have an infinite (countable) number of complex solution which corresponds to evanescent modes (as the waves have to be bounded in a physical world). If it is assumed that $K = -iA_n$ (note the use of $-i$ such that A_n is positive, which corresponds to an evanescent mode for a forward travelling wave), then the dispersion relation is

$$\Omega^2 = -A_n \tan A_n. \quad (1.3.9)$$

The dimensional counterpart is defined as α_n .

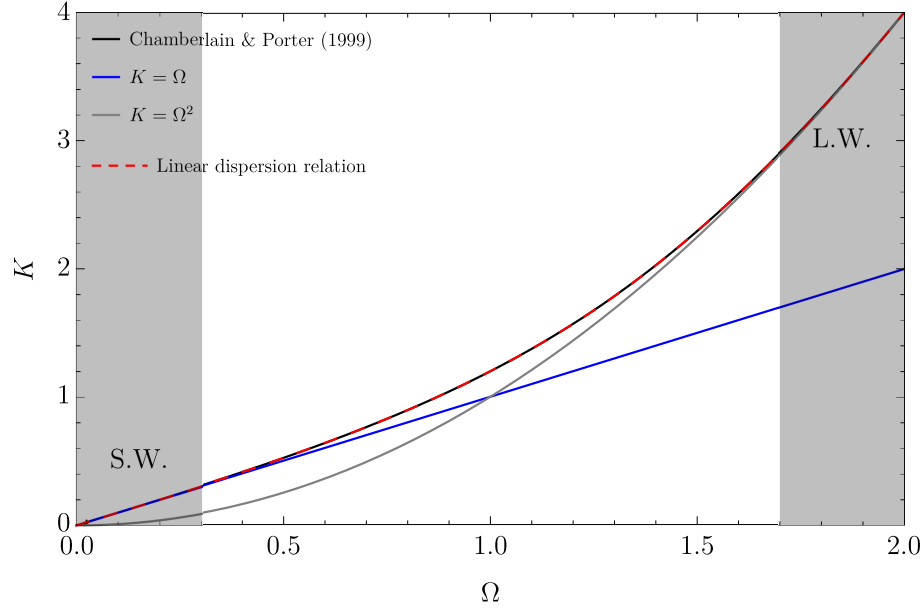


Figure 1.5: Linear wave dispersion relation between K and Ω compared with short waves (SW), long waves (LW) theories and the approximation of Chamberlain and Porter (see eq.1.3.8).

Chamberlain and Porter [23] also provided an approximation for A_n and a scheme to converge towards the solution. Their approximate solution is used as an initialization in the Newton–Raphson algorithm:

$$A_n \approx \pm \left(n\pi - \frac{\pi}{2} \tanh \left(\frac{2\Omega^2}{n\pi^2} \right) \right), \quad (1.3.10)$$

where $n \in \mathbb{N}^*$. Figures 1.6 shows the first ten solutions of the dispersion relation in the complex plane (the first one being the travelling mode and the other nine the decaying modes sorted by value of the evanescent term) for $\Omega = 1$, *i.e.* intermediate waves. The general form is always the same. The travelling mode is on the real axis and the evanescent modes are on the imaginary axis.

The first order kinematic pressure plus the equilibrium pressure, or excess wave pressure⁸, is readily found using the first order linearized Bernoulli's expression 1.3.2:

$$\begin{aligned} P_*^{(1)} = P^{(1)} + Z &= -\partial_{\mathcal{T}}\Phi \\ &= \Re \left\{ A \frac{\cosh[K(1+Z)]}{\cosh K} e^{i(\Omega\mathcal{T}-KX)} \right\} \end{aligned} \quad (1.3.11)$$

⁸Sometimes called *dynamic pressure* which is a misuse of language as the dynamic pressure is $e_k = \rho|u|^2/2$ or the kinetic energy per unit volume.

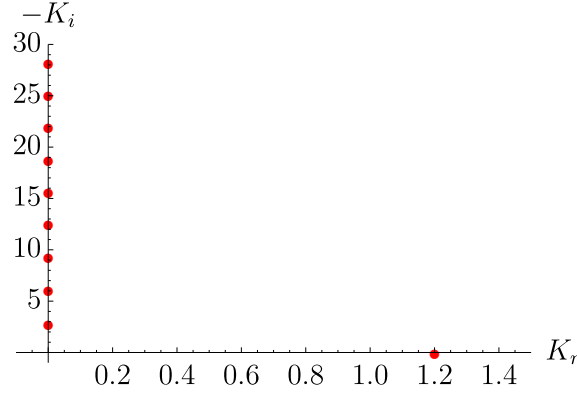


Figure 1.6: First ten wavenumbers for Airy waves for $\Omega = 1$ in the complex plane.

1.3.2 Wave energy, wave energy flux and power

As they travel, waves transport energy in two forms: potential and kinetic energies. The kinetic energy per unit volume, e_k , is by definition

$$e_k = \frac{\rho}{2} |\mathbf{u}|^2, \quad (1.3.12)$$

or in non-dimensional form:

$$E_k = \frac{e_k}{\rho g d} = \frac{1}{2} |\mathbf{U}|^2. \quad (1.3.13)$$

Substituting the expression of the velocity potential, yields

$$E_k = \frac{A^2 \Omega^2}{4} \Re \left\{ \operatorname{csch}^2 K e^{2i(\Omega T - K X)} + \cosh(2K(1 + Z)) \operatorname{csch}^2 K \right\}, \quad (1.3.14)$$

where the following property of complex multiplication is used:

Proposition 1. *Let $a(\mathcal{T})$ and $b(\mathcal{T})$ be two real functions of time such that:*

$$a(\mathcal{T}) = \Re \{ A e^{i\Omega \mathcal{T}} \}, \text{ and } b(\mathcal{T}) = \Re \{ B e^{i\Omega \mathcal{T}} \},$$

where A and B are two complex numbers. Then:

$$a(\mathcal{T}) \times b(\mathcal{T}) = \frac{1}{2} \Re \{ A \times B e^{2i\Omega \mathcal{T}} + A \times B^* \},$$

where the star denotes the complex conjugate.

Integrating over the water depth and keeping only the second order terms yields the instantaneous kinetic energy per unit area:

$$\mathcal{E}_k = \int_{-1}^{\tilde{Z}} E_k \, dZ = \frac{A^2 \Omega^2}{4} \Re \left\{ \operatorname{csch}^2 K e^{2i(\Omega T - K X)} + \frac{\coth K}{K} \right\}. \quad (1.3.15)$$

Integrating over a wave period, one can define the mean kinetic energy per unit area ⁹:

$$\overline{\mathcal{E}_k} = \frac{1}{\mathfrak{T}} \int_0^{\mathfrak{T}} \mathcal{E}_k d\mathcal{T} = \frac{1}{4} A^2, \quad (1.3.16)$$

where \mathfrak{T} is the non-dimensional wave period: $\mathfrak{T} = T\sqrt{g/d} = 2\pi/\Omega$. Similarly the potential energy per unit volume, e_p , is defined as

$$e_p = \rho g z, \quad (1.3.17)$$

and in non-dimensional form:

$$E_p = Z. \quad (1.3.18)$$

Integrating over the water depth and keeping only the second order terms:

$$\mathcal{E}_p = \int_{-1}^{\tilde{Z}} E_p dZ = \frac{1}{2} (\tilde{Z}^2 - 1). \quad (1.3.19)$$

The potential energy is defined up to a constant. Taking the reference as the potential energy of the fluid at rest and averaging over a wave period:

$$\overline{\Delta\mathcal{E}_p} = \frac{1}{4} A^2 \quad (1.3.20)$$

For Airy waves, the mean total energy of a wave per unit area is thus evenly distributed between potential and kinetic energy and

$$\overline{\mathcal{E}_{tot}} = \frac{1}{2} A^2, \quad (1.3.21)$$

or in dimensional form:

$$\overline{\varepsilon}_{tot} = \frac{1}{2} \rho g a^2. \quad (1.3.22)$$

The mean energy of a wave per unit area is thus proportional to the square of its wave amplitude under the present approximation (linear waves).

For wave energy purposes, it is common to define the flux of wave energy across a vertical plane. This corresponds to the amount of energy that reaches a certain point, *e.g.* a wave energy converter. The energy flux is equal to the work done by the excess of pressure (see [111]):

$$\boldsymbol{\pi} = p_* \mathbf{u}, \quad (1.3.23)$$

or in non-dimensional form:

$$\boldsymbol{\Pi} = P_* \mathbf{U}. \quad (1.3.24)$$

⁹Unit length along a wave crest and along the wave direction of propagation.

For linear waves, keeping the first non zero order terms simplifies this expression to

$$\mathbf{\Pi}^{(1)} = P_*^{(1)} \mathbf{U}^{(1)}. \quad (1.3.25)$$

Using the excess wave pressure expression given in eq.1.3.11 and the potential velocity of eq.1.3.4 and averaging over a wave period (retaining only the second order terms), yields

$$\bar{\mathcal{F}} = \overline{\int_{-1}^{\bar{Z}} \Pi_X dZ} = \frac{1}{2} \frac{\epsilon_{tot}}{K} \frac{\Omega}{K} \left(1 + K \frac{1 - \tanh^2 K}{\tanh K} \right), \quad (1.3.26)$$

or in dimensional form:

$$\bar{\mathfrak{F}} = \frac{1}{2} \frac{\epsilon_{tot}}{k} \frac{\omega}{k} \left(1 + kd \frac{1 - \tanh^2 kd}{\tanh kd} \right) \quad (1.3.27)$$

Thus the non-dimensional energy velocity propagation is

$$C_g = \frac{1}{2} \frac{\Omega}{K} \left(1 + K \frac{1 - \tanh^2 K}{\tanh K} \right), \quad (1.3.28)$$

which is equal to the group velocity: $C_g = \partial\Omega/\partial K$. In dimensional form:

$$c_g = \frac{1}{2} \frac{\omega}{k} \left(1 + kd \frac{1 - \tanh^2 kd}{\tanh kd} \right), \quad (1.3.29)$$

1.3.3 Stokes drift and wave mass transport

Another interesting feature of Airy water waves is the transport of mass or drift. This was first noticed by Stokes [148]. In his introduction, Stokes stated:

“There is one result of a second approximation which may possibly be of practical importance. It appears that the forward motion of the particles is not altogether compensated by their backward motion ; so that, in addition to their motion of oscillation, the particles have a progressive motion in the direction of propagation of the waves.”

1.3.3.1 Lagrangian mean velocity

In this paragraph, the proof based on Stokes [148] is given. Consider a material point $\mathbf{X}_0 = (X_0, Z_0)$ at an initial time such that the surface at this particular position is at the undisturbed height 0. It is always possible to find such an abscissa for an infinite wave train. Then the particle velocity at a later time is equal to the velocity of the fluid at this position and time:

$$d_{\mathcal{T}} \mathbf{X} = \mathbf{U}(\mathbf{X}(\mathcal{T}), \mathcal{T}) \quad (1.3.30)$$

where the upright $d_{\mathcal{T}}$ refers to the Lagrangian derivative. The particle position can be expanded similarly to eq.1.2.10:

$$\mathbf{X}(\mathcal{T}) = \mathbf{X}_0 + A\mathbf{X}^{(1)}(\mathcal{T}) + A^2\mathbf{X}_2(\mathcal{T}) + \dots \quad (1.3.31)$$

Substituting the velocity expression of eq.1.3.4 into eq.1.3.30 and keeping the first order terms yields

$$d_{\mathcal{T}}\mathbf{X} \approx \Re \left\{ \frac{A\Omega}{\sinh K} \begin{pmatrix} \cosh [K(1 + Z_0)] \\ i \sinh [K(1 + Z_0)] \end{pmatrix} \right\} e^{i\Omega\mathcal{T}}, \quad (1.3.32)$$

so at the first order the particle follows an ellipsoid in a clockwise direction:

$$A\mathbf{X}^{(1)}(\mathcal{T}) = \Re \left\{ \frac{A}{\sinh K} \begin{pmatrix} -i \cosh [K(1 + Z_0)] \\ \sinh [K(1 + Z_0)] \end{pmatrix} e^{i\Omega\mathcal{T}} \right\}, \quad (1.3.33)$$

Expanding to the next order:

$$d_{\mathcal{T}}\mathbf{X} \approx \mathbf{U}(X_0, Z_0, \mathcal{T}) + A\nabla\mathbf{U}(X_0, Z_0, \mathcal{T}) \cdot \mathbf{X}^{(1)}. \quad (1.3.34)$$

Using the proposition 1, it is easily found that

$$\begin{aligned} A\nabla\mathbf{U}(X_0, Z_0, \mathcal{T}) \cdot \mathbf{X}^{(1)} = \Re \left\{ \frac{A^2K\Omega}{2\sinh^2 K} \begin{pmatrix} -1 \\ 0 \end{pmatrix} e^{2i\Omega\mathcal{T}} \right\} \\ + \frac{A^2K\Omega}{2\sinh^2 K} \begin{pmatrix} \cosh [2K(1 + Z_0)] \\ 0 \end{pmatrix} \end{aligned} \quad (1.3.35)$$

The first term on the righthand side can be omitted as it requires the development of the second order wave theory to take into account the complete second harmonic terms. The second term corresponds to the drift mentioned by Stokes [148]. The *Stokes drift* is defined as this Lagrangian velocity:

$$\mathcal{U}_D = \frac{1}{2}(AK)^2 C_{\varphi} \frac{\cosh [2K(1 + Z)]}{\sinh^2 K}, \quad (1.3.36)$$

where $C_{\varphi} = \Omega/K$ is the phase velocity. In dimensional form, the Stokes drift is

$$U_D = \frac{1}{2}(ak)^2 c_{\varphi} \frac{\cosh [2k(d + z)]}{\sinh^2 kd}. \quad (1.3.37)$$

The total wave mass transport can be defined from this Lagrangian velocity:

$$\mathcal{M}_{tot}^w = \int_{-1}^0 \mathcal{U}_D dZ = \frac{1}{2}A^2\Omega \coth K, \quad (1.3.38)$$

and in dimensional form:

$$M_{tot}^w = \frac{1}{2} \rho a^2 \omega \coth kd, \quad (1.3.39)$$

and corresponds to the amount of mass transported by the wave per unit wave crest on the total water depth.

1.3.3.2 Eulerian mean mass flux

Another way of looking at the effect of the waves on the mass transport is to look at the mean Eulerian velocity. In the linear theory, it is obvious that in the interior (core, or always submerged part) of the flow, the mean Eulerian velocity is nil. In the surface layer, sometimes called the “splash zone” [118], $-A < Z < A$, the emergence effects have to be taken into account. Yet the velocity in the linear theory is defined only in the region $-1 < Z < 0$. It is therefore assumed that the velocity can be analytically continued to the free surface.

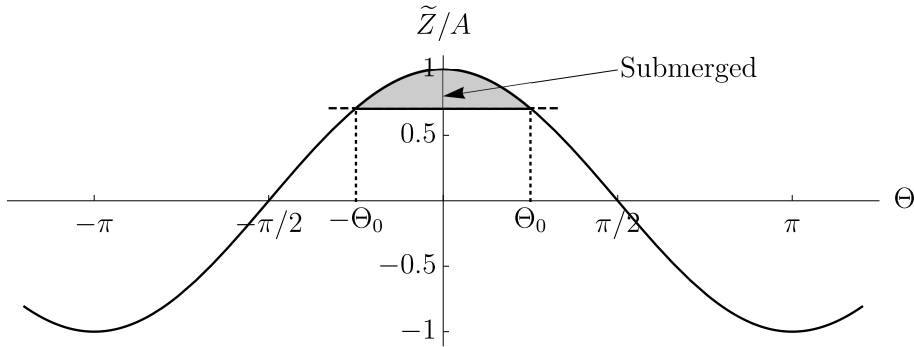


Figure 1.7: Surface variation of a linear wave with emergence time. The shaded gray region shows the emergence time.

It is improper from a two-phase point of view to talk about mean Eulerian velocity as the velocity in air is not zero and actually larger than in the water phase [11]. This problem can be alleviated by considering instead the mass flux $\rho \mathbf{u}$ as it appears in the original kinematic condition at the surface (eq.1.1.13). Then invoking the fact that the air density is three orders of magnitude smaller than that of water, the mass flux from the air can be neglected. The density thus works like a mask on the mass flux.

Consider a point such that $-A \leq Z \leq A$, the point is in the water phase if

$$Z \leq \tilde{Z}(\Theta), \quad (1.3.40)$$

where $\Theta = \Omega \mathcal{T} - KX$. Solving and retaining the first order terms:

$$\cos \Theta \geq \cos \Theta_0 = \frac{Z}{A}. \quad (1.3.41)$$

Thus the submergence occurs between $-\Theta_0$ and Θ_0 on a period taken between $-\pi$ and π (see figure 1.7). The mean value of the Eulerian horizontal mass flux is

$$\begin{aligned} u_E(Z) = \overline{U(Z)} &= \frac{1}{2\pi} \int_{-\Theta_0}^{\Theta_0} U(0, Z, \mathcal{T}(\Theta)) \, d\Theta \\ &\approx \frac{1}{2\pi} \int_{-\Theta_0}^{\Theta_0} \frac{A\Omega}{\sinh K} \cosh K \cos \Theta \, d\Theta \\ &\approx \frac{A\Omega}{\pi \sinh K} \sqrt{1 - \left(\frac{Z}{A}\right)^2} \cosh K, \end{aligned} \quad (1.3.42)$$

where the first non-zero order terms are retained. The wave mass transport is defined from the Eulerian velocity as

$$\mathcal{M}^w = \int_{-A}^A u_E(Z) \, dZ = \frac{1}{2} A^2 \Omega \coth K, \quad (1.3.43)$$

which is exactly the result found using the Lagrangian development of Stokes [148] as there is no mass transported in the core in the Eulerian point of view. Note that here the subscript *tot* is not used as this term corresponds to the mass transport in the surface layer only.

It is interesting to see that the two points of view (Eulerian and Lagrangian) are drastically different. If the Lagrangian point of view is usually legion in the wave community, in the rest of the thesis the Eulerian point of view is preferred.

In the Eulerian point of view, the wave mass transport is a surface phenomenon restricted to the surface layer (or “splash zone”) which corresponds to the region covered by the instantaneous surface. In the limit of infinitesimal waves, it can be regarded as a surface current.

The wave mass transport can also be defined as

$$\mathcal{M}^w = \overline{\int_0^{\tilde{Z}^{(1)}} U^{(1)}(Z, \mathcal{T}) \, dZ} \approx \overline{\tilde{Z}^{(1)} U^{(1)}|_{Z=0}}, \quad (1.3.44)$$

which yields the same expression as found earlier with the Eulerian and Lagrangian development. Recall that it is assumed that the velocity can be analytically continued to the surface.

The important feature of the Eulerian drift is the net forward mass flux in the surface layer. As mass has to be conserved overall, a variation of the mass travelling in this surface must be transferred to the interior of the flow. This is key to the rest of this thesis. A more general proof of this simple principle is given in section 1.4 where the waves and mean flow interaction are reviewed.

1.3.3.3 Comments and remarks on the mass flux

In a closed experimental facility the mass flux over a water column should be zero ($M_{tot}^w = 0$). Thus the mass travelling in the surface layer must be compensated by the same amount travelling in the opposite direction in the interior of the flow (called “return flow” or “undertow flow”). The distribution of this interior flow is unknown *a fortiori*. There exist theories of water waves without mass transport. The most famous one is Gerstner’s wave theory. This theory was originally developed by Gerstner [54] in 1802. It is the first theory of waves that was proposed, and it is an exact solution to the Euler’s equations (eq.1.1.18 without viscosity) for infinite water depth. This theory is reviewed in more detail in appendix A.

The Lagrangian drift velocity is obviously zero for Gerstner’s waves but the Eulerian drift velocity is not, as proven by Moe and Arntsen [118] and shown in appendix A. It has a strong backward velocity just under the wave crest, and there is a similar mass flux in the surface layer as in Airy’s waves. The total mass transport, M_{tot}^w , is zero on a water column but one can still define the wave mass transport in the surface layer, M^w . The two mean Eulerian profiles are compared in figure A.2 in appendix A for deep water waves. The wave mass transport in the surface layer is the same for both the Airy’s and Gerstner’s waves. This quantity is therefore an intrinsic property of water waves. Unfortunately, this theory is valid only in deep water. Even though there exist shallow water models [53], none are, up to the author’s knowledge actual solution of the Euler’s equations. In the appendix A it is shown that only in deep water do such waves satisfy the continuity equation.

The surface layer should not be confused with the boundary layers at the free surface and sea bed. They can also influence the mean total mass flux. For instance, Russell and Osorio [143] observed drift profiles and reported positive drift near the sea bed. This is due to friction at the wall and can be compared to *acoustic streaming*. It can be shown that friction at the wall induces a streaming velocity independent of the viscosity in the direction of propagation of the waves (see appendix B). Longuet-Higgins [95] used this effect to study Allison’s peristaltic pump [5] and found a 5/2 amplification of the total wave mass transport, M_{tot}^w of eq.1.3.39.

1.3.4 Eigenfunction expansion matching method

In this paragraph, a method to solve linear water wave problems (system of eq.1.3.1, the index (1) are dropped for brevity as only first order terms are considered here), that will be used in the next chapters, is presented. The method is called the *eigenfunction expansion matching method* (hereafter called EFE). Details on the mathematical technique can be found in various textbooks, such as Linton and McIver [90]. It takes advantage of the *Sturm-Liouville theory*. Indeed, one can show that the system of equations eq.1.3.1 can be solved using a *regular* Sturm-Liouville ordinary differential equations (S-L ODE) where

the negative square of the wavenumbers are called the *eigenvalues* and the functions of the form of eq.1.3.4 are called *eigenfunctions*. Then the system

$$\begin{cases} F_n''(Z) + L_n F_n'(Z) = 0, \\ F_n'(-1) = 0, \\ -\Omega^2 F_n(0) + F_n'(0) = 0, \end{cases} \quad (1.3.45)$$

is a regular S-L ODE and the pairs $\{L_n, F_n\}$ are non-trivial solutions. The L_n are all simple, real, countable and can be ordered. The index n corresponds to the ranking of the ordered eigenvalues L_n , and F_n is the associated eigenfunction (which is proportional to $F^{(1)}$). The smallest eigenvalue $L_0 < 0$ corresponds to travelling waves (in the positive and negative directions). The eigenfunctions are *orthogonal* and form a *basis* of functions solution of the problem; that is to say, every solution functions can be decomposed in series of these functions, and the series converges in the mean-square sense.

Hence, a solution to the system in eq.1.3.1 can be written in the form

$$\Phi^{(1)} = \Re \left\{ \Phi_{\mathbb{C}}^{(1)} e^{i\Omega\mathcal{T}} \right\}, \quad (1.3.46)$$

where $\Phi_{\mathbb{C}}$ is a complex function:

$$\Phi_{\mathbb{C}}^{(1)} = \sum_{n \in \mathbb{N}} (C_n^+ e^{-iK_n X} + C_n^- e^{iK_n X}) F_n(Z). \quad (1.3.47)$$

Here, K_0 corresponds to the travelling modes and $K_{n>0}$ to the evanescent modes (see section 1.3), which are all solutions to the dispersion relation eq.1.3.5, $F_n = \cosh [K_n (1 + Z)]$ and

$$\langle F_i | F_j \rangle_{-1}^0 = \int_{-1}^0 F_i(Z) F_j(Z) dZ = \delta_{i,j} \frac{2K + \sinh 2K}{4K}, \quad (1.3.48)$$

where $\delta_{i,j}$ is the *Kronecker delta*, and the $\{C_n^{\pm}\}_{n \in \mathbb{N}}$ are complex coefficients that depend on the nature of the problem. The coefficients with a plus (minus) sign correspond to forward (backward) travelling wave solutions (respectively).

As an illustration of this method, three simple problems are considered: the generation of waves by a piston and by a plunger, and the wave reflection and transmission at a step. These first two problems will be of interest in the next chapters and show how to use this method in general. The last example shows an interesting feature of waves often omitted in similar studies.

1.3.4.1 Wave generation by a piston

The wave generation by a piston problem is well-known, and one of the first solution was given by Biesel and Suquet [12] in 1951. A solution can also be found in [90] in section

2.2.1. The goal here is to illustrate the method. The solution proposed here is done using non-dimensional notation.

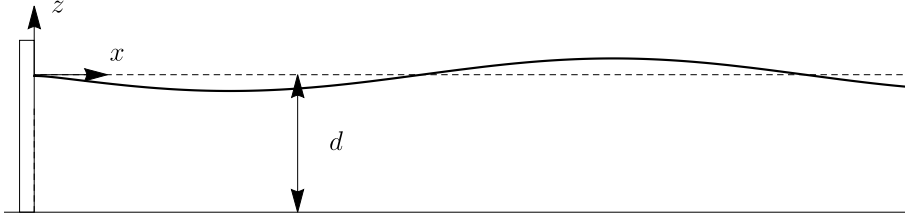


Figure 1.8: Piston wave maker notations.

Consider a semi-infinite domain of fluid with uniform depth: $\mathcal{D}_f = \{(X, Z) \in \mathbb{R}^+ \times [-1, 0]\}$. At the origin of the domain a piston-type wave maker is controlled in surge motion with a non-dimensional amplitude of oscillations $S_0 = s_0/d$ (where recall d is the dimensional water depth) at angular frequency Ω . Figure 1.8 shows a sketch of such a wave maker. It generates waves that propagate to infinity. The paddle velocity is assumed to be uniform along the vertical coordinate:

$$U_P(\mathcal{T}) = S_0 \Omega \sin \Omega \mathcal{T}, \quad (1.3.49)$$

or using complex notations:

$$U_P(\mathcal{T}) = \Re \{ -i S_0 \Omega e^{i \Omega \mathcal{T}} \}. \quad (1.3.50)$$

It is also further assumed that the linear theory assumptions hold.

In the water phase, a solution of the form of eq.1.3.47 is sought. As the domain is limited to positive X , the $C_{n \in \mathbb{N}}^- = 0$. This is also called the *radiation condition*: the solution has to be bounded and all the waves are outgoing. It can be written as

$$\Phi_C^{(1)} \rightarrow \frac{i A \Omega}{K \sinh K} e^{-i K X} \cosh [K (Z + 1)], \quad X \rightarrow +\infty. \quad (1.3.51)$$

At the paddle, the condition is a Neumann condition on the scalar velocity field:

$$\partial_X \Phi_C^{(1)} = -i S_0 \Omega, \quad \text{on } X = 0. \quad (1.3.52)$$

Using the orthogonality of the eigenfunctions:

$$-i K_n C_n^+ \frac{2K_n + \sinh 2K_n}{4K_n} = -i S_0 \Omega \int_{-1}^0 F_n(Z) dZ, \quad (1.3.53)$$

and after some calculus, it yields

$$C_n^+ = \frac{4 S_0 \Omega \sinh K_n}{K (2K_n + \sinh 2K_n)}. \quad (1.3.54)$$

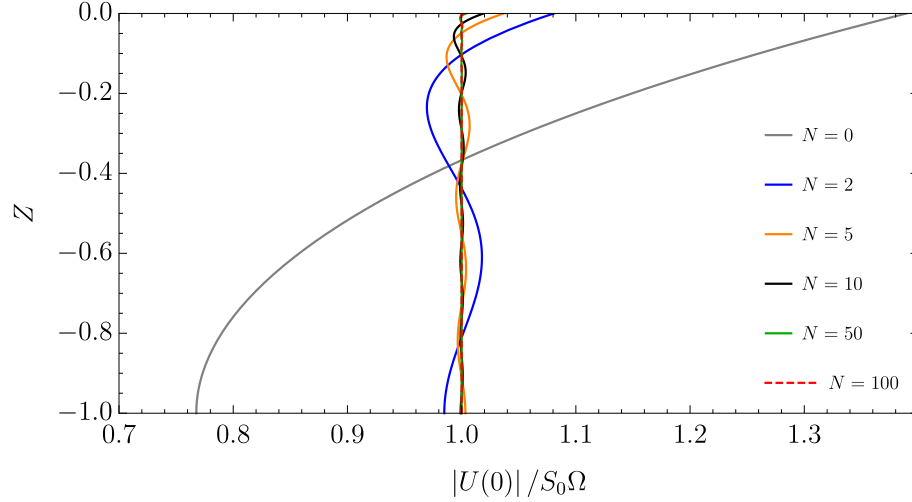


Figure 1.9: Velocity profiles at the piston-type wave maker in the linear theory using the expansion method for different numbers of modes for $\Omega = 1$.

Figure 1.9 shows the horizontal velocity profiles for different numbers of modes for $\Omega = 1$. The velocity profiles converge toward the uniform profile as N is increased.

The wave amplitude and phase of the generated waves are found using eq.1.3.4 and eq.1.3.54:

$$A = -i \frac{4S_0 \sinh^2 K}{2K + \sinh 2K}, \quad (1.3.55)$$

where $K = K_0$ is the travelling mode. Note that the velocity of the paddle and the surface elevation are thus in phase.

In experiments, it is generally the wave amplitude that is the control parameter, thus the useful expression is the paddle stroke as a function of the target wave height $H = 2|A|$:

$$S_0 = H \frac{2K + \sinh 2K}{8 \sinh^2 K}. \quad (1.3.56)$$

1.3.4.2 Wave generation by an oscillating rectangular plunger

The wave generation by an oscillating plunger was also mentioned as a way of generating waves by Biesel and Suquet [12] in 1951. Here the plunger is controlled in heave motion only. Zheng et al. [173] also considered the sway and roll motions.

Consider an infinite domain of fluid with uniform depth: $\mathcal{D}_f = \{(X, Z) \in \mathbb{R} \times [-1, 0]\}$. At the origin of the domain a rectangular plunger of width $2L = 2l/d$ is controlled in heave motion with a non-dimensional amplitude of oscillations $S_0 = s_0/d$ at a angular frequency Ω . The mean draft of the plunger is $D_p = d_p/d$ and is assumed to be strictly positive here. Figure 1.10 shows a sketch of the domain with the notations. The problem to solve here

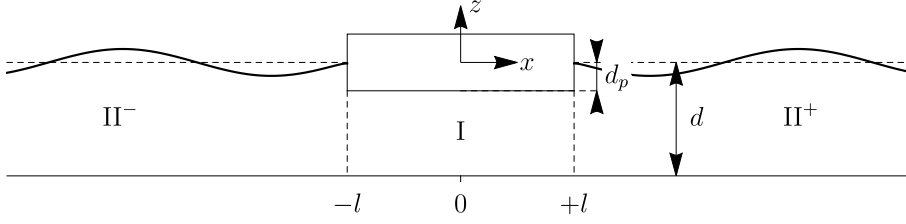


Figure 1.10: Plunger wave maker: domain decomposition and notations.

is for linear waves:

$$\begin{cases} \Delta \Phi_{\mathbb{C}}^{(1)} = 0, & \text{for } (X, Z) \in \mathcal{D}_f, \\ \partial_Z \Phi_{\mathbb{C}}^{(1)} = 0, & \text{at } Z = -1, \\ \partial_Z \Phi_{\mathbb{C}}^{(1)} = S_0 \Omega, & \text{at } Z = -D_p, \text{ and } X \in [-L, L], \\ \partial_X \Phi_{\mathbb{C}}^{(1)} = S_0 \Omega, & \text{at } Z \in [-D_p, 0], \text{ and } X = \pm L, \\ \partial_Z \Phi_{\mathbb{C}}^{(1)} - \Omega^2 \Phi_{\mathbb{C}}^{(1)} = 0, & \text{at } Z = 0, \end{cases} \quad (1.3.57)$$

where $\Phi^{(1)} = \Re \left\{ \Phi_{\mathbb{C}}^{(1)} e^{i\Omega \mathcal{T}} \right\}$ with the radiation condition:

$$\Phi_{\mathbb{C}}^{(1)} \rightarrow \frac{iA^{\pm}\Omega}{K \sinh K} e^{\mp iKX} \cosh [K(Z+1)], \quad X \rightarrow \pm\infty. \quad (1.3.58)$$

In order to complete the description of the problem, the behavior of the solution near the vicinity of the corners of the paddle (singular points) needs to be specified. Consider a small fluid region near one of these corners. Define cylindrical coordinates (r, θ) with the origin at the corner of interest such that the sides correspond to $\theta = 0$ and $\theta = 3\pi/2$. The boundary conditions on the walls are for the trivial problem (with no forcing), $\partial_{\theta} \Phi = 0$ on the $\theta = 0$ and $\theta = 3\pi/2$. The solution must therefore satisfy $\Phi \sim c + r^{2/3} \cos \frac{2\theta}{3}$ as $r \rightarrow 0$, where c denotes a constant. This implies that the velocity diverges near these corners:

$$\nabla \Phi = \mathcal{O} \left(r^{-1/3} \right) \quad \text{as } r \rightarrow 0. \quad (1.3.59)$$

This property will be helpful in evaluating the speed of convergence of the coefficients.

The problem is decomposed into three domains: I, under the paddle and II^{\pm} , for the free surface domains. In domain I, the scalar potential is of the form:

$$\begin{aligned} \Phi_{\mathbb{C},\text{I}}^{(1)} = S_0 \Omega \frac{(Z+1)^2 - X^2}{2(1-D_p)} + (G_0 X + J_0) P_0(Z) \\ + \sum_{n \in \mathbb{N}^*} \left(G_n e^{-B_n(X+L)} + J_n e^{B_n(X-L)} \right) P_n(Z), \end{aligned} \quad (1.3.60)$$

where the first term corresponds to the source terms and enables to satisfy the velocity

condition at the plunger:

$$\partial_Z \Phi_{\text{C,I}}^{(1)}(Z = -D_p) = S_0 \Omega. \quad (1.3.61)$$

The other terms are solutions of the trivial problem with a fixed plunger:

$$\begin{cases} \Delta \Phi_{\text{C,I}}^{(1)} = 0, \\ \partial_Z \Phi_{\text{C,I}}^{(1)}(Z = \{-1, -D_p\}) = 0, \end{cases} \quad (1.3.62)$$

and then:

$$P_n = \cos [B_n (Z + 1)] \quad \text{and} \quad B_n = \frac{n\pi}{1 - D_p}, \quad (1.3.63)$$

where $\{P_n\}$ forms also an orthogonal basis by the S-L ODE property.

In the domains II^\pm , the solutions are of the form:

$$\Phi_{\text{C,II}^\pm}^{(1)} = \sum_{n \in \mathbb{N}} C_n^\pm e^{\mp i K_n (X \mp L)} F_n(Z), \quad (1.3.64)$$

where the radiation condition is used. The coefficients $\{C_n^\pm, G_n, J_n\}_{n \in \mathbb{N}}$ are unknown and must be solved for.

By symmetry of the problem, it is clear that $\Phi_{\text{C}}(X) = \Phi_{\text{C}}(-X)$ and thus $C_n^+ = C_n^-$, $G_0 = 0$, and $G_n = J_n$. The coefficients are then found by forcing the continuity of the scalar potential and its normal derivative at the interface of domains I-II $^\pm$:

$$\begin{cases} \Phi_{\text{C,II}^+}^{(1)}(X = \pm L) = \Phi_{\text{C,I}}^{(1)}(X = \pm L), & \text{for } Z \in [-1, -D_p] \\ \partial_X \Phi_{\text{C,II}^+}^{(1)}(X = \pm L) = \begin{cases} 0, & \text{for } Z \in [-D_p, 0] \\ \partial_X \Phi_{\text{C,I}}^{(1)}(X = \pm L), & \text{for } Z \in [-1, -D_p] \end{cases} \end{cases} \quad (1.3.65)$$

This corresponds to continuity of the normal velocity and pressure at the interface of each domain. Projections are then used in the following manner:

- project the velocity equations using the basis functions of the largest vertical section (here the basis functions of domain II)¹⁰,
- project the scalar potential equations using the basis functions of the smallest domain.

This leads to:

$$\begin{aligned} -i K_n C_n^+ \langle F_n | F_n \rangle_{-1}^0 &= -\frac{S_0 \Omega}{1 - D_p} L \langle 1 | F_n \rangle_{-1}^{-D_p} \\ &+ \sum_{j \in \mathbb{N}^*} J_j (1 - e^{-2B_j L}) B_j \langle P_j | F_n \rangle_{-1}^{-D_p}, \end{aligned} \quad (1.3.66)$$

¹⁰ Note that this enables to enforce the no-through flow conditions at the plunger in one single projection.

$$\begin{aligned} \sum_{j \in \mathbb{N}} C_j^+ \langle F_j | P_n \rangle_{-1}^{-D_p} &= \frac{S_0 \Omega}{1 - D_p} \frac{1}{2} \left\langle (Z + 1)^2 - L^2 | P_n \right\rangle_{-1}^{-D_p} \\ &+ \delta_{0,n} J_0 \langle 1 | P_n \rangle_{-1}^{-D_p} + (1 - \delta_{0,n}) J_n (1 + e^{-2B_n L}) \langle P_n | P_n \rangle_{-1}^{-D_p} \end{aligned} \quad (1.3.67)$$

This expression is an infinite number of linked equations and cannot be solved analytically. The expansion is limited to N terms in each domain. This reduces the problem to $2N$ equations for the $2N$ unknowns: $\{C_n, J_n\}_{n \in [0, N-1]}$. The solution is found by numerically solving this systems of equations. Here, the function *NSolve* of *Mathematica* [75] is used (see code in appendix C). The coefficients can be scaled by $S_0 \Omega$ without loss of generality. Using the singularity expressed in eq.1.3.59 and a Mellin transform [104] one can show that

$$\sum_{n=1}^{\infty} n^{-2/3} e^{-nx} \sim \Gamma(1/3) x^{-1/3} \text{ as } x \rightarrow 0^+, \quad (1.3.68)$$

it follows that

$$C_n^{\pm} = O\left(n^{-5/3}\right), J_n = O\left(n^{-5/3}\right) \text{ as } n \rightarrow \infty. \quad (1.3.69)$$

This is shown in appendix C where a code in *Mathematica* is provided.

The figure 1.11 shows the ratio of the wave amplitude over the piston stroke as a function of the wave angular frequency for this kind of plunger using 10-term and 50-term expansions for $D_p = 0.2$ and $L = 1.5$ (which corresponds to the experiments presented in chapter 2) and also 10-term expansions for $D_p = 0.1$ and $D_p = 0.5$ for $L = 1.5$ and $D_p = 0.2$ for $L = 2$. The wave amplitude is linear with Ω for long waves: $A_{\infty} \sim S_0 L \Omega$. There is a resonance effect which mostly depends on the draft D_p . Then high frequency attenuation appears. The behavior is similar to a spring-mass system as pointed out by Rytkönen and Granholm [144].

1.3.4.3 Wave transmission and reflection at a step

Consider the reflection and transmission of a wave train travelling from a domain of constant depth d and encountering an abrupt change of depth $d_s (< d)$, see figure 1.12). Lamb [82] first solved this problem in the limit of long waves. This approximation supposes that the vertical acceleration is neglected, which is clearly incorrect in the vicinity of the step. Bartholomeusz [9] solved this problem rigorously and validated the results of Lamb [82] in the limit of long waves. The scattering of waves by a submerged finite step was investigated theoretically by Takano [152] and Mei and Black [109]. Massel [106] extended the solution to the second order and looked at the generation of higher harmonics.

In this example, the linear theory is solved using the expansion method. The mass transport is evaluated and found to increase due to the abrupt change in water depth.

The water depth d is taken as the reference depth and the non-dimensional depth above

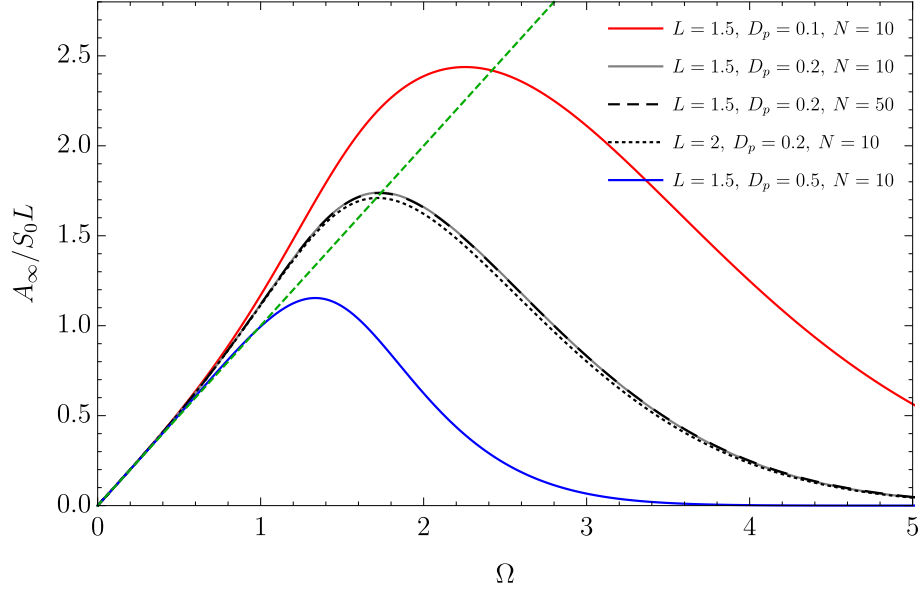


Figure 1.11: Plunger wave maker theoretical ratio of wave amplitude over the piston stroke as a function of the angular frequency for different L , D_p and N . The red (gray, blue) line shows the amplitude of the wave as a function of the angular frequency for $L = 1.5$ and $D_p = 0.1$ (0.2 , 0.5 , respectively). The maximum wave size and angular frequency at which it happens are inversely proportional to the draft. The black dashed line shows a 50-term expansion. The results are similar to the gray line with 10-term expansion, showing convergence (they are on top of each other, see appendix C for more details on convergence). The dotted black curve shows the effect of varying the plunger width. The green dashed line shows the asymptotic shallow water limit: $A_\infty = S_0 L \Omega$.

the step is defined as $D_s = d_s/d < 1$. The problem to solve can be stated as

$$\begin{cases} \Delta \Phi_{\mathbb{C}}^{(1)} = 0, & \text{for } (X, Z) \in]-\infty, 0] \times [-1, 0] \cup [0, +\infty[\times, [-D_s, 0] \\ \partial_Z \Phi_{\mathbb{C}}^{(1)} = 0, & \text{at } Z = -1, X < 0 \text{ and } Z = -D_s, X > 0, \\ \partial_X \Phi_{\mathbb{C}}^{(1)} = 0, & \text{at } X = 0, -1 < Z < -D_s \end{cases} \quad (1.3.70)$$

where $\Phi^{(1)} = \Re \left\{ \Phi_{\mathbb{C}}^{(1)} e^{i\Omega \mathcal{T}} \right\}$ with radiation conditions:

$$\begin{cases} \Phi_{\mathbb{C}}^{(1)} \rightarrow \frac{iA\Omega}{K_0 \sinh K_0} (e^{-iK_0 X} + R e^{iK_0 X}) \cosh [K_0 (Z + 1)], & X \rightarrow -\infty, \\ \Phi_{\mathbb{C}}^{(1)} \rightarrow \frac{iA\Omega}{K_0^s \sinh K_0^s D_s} T e^{-iK_0^s X} \cosh [K_0^s (Z + D_s)], & X \rightarrow +\infty, \end{cases} \quad (1.3.71)$$

where K_0 (K_0^s) is the non-dimensional wavenumber in the domain of water depth d (d_s). The dispersion relation over the step can be written as

$$\Omega^2 = K^s \tanh (K^s D_s). \quad (1.3.72)$$

The description of the problem is completed similarly to the previous ones in the vicinity

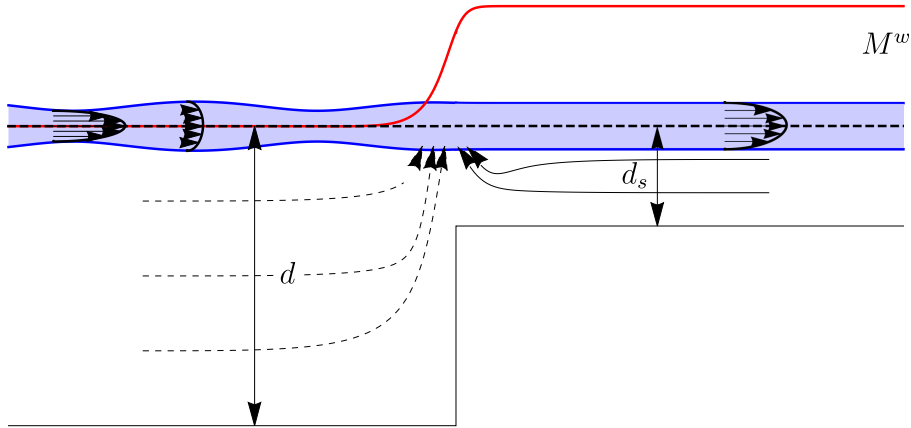


Figure 1.12: Reflection/Transmission at a step: notations and outline of the increase in wave mass transport due to the abrupt change in depth. The blue shaded region shows the surface layer and the red curve the amount of mass travelling in the surface layer based on the linear theory. The mass transport increase above the submerged plate for intermediate waves leads to a suction upward in the mean flow in the vicinity of the step. This is represented by the arrows (dashed and continuous arrows).

of the step corner. The velocity diverges similarly to eq.1.3.59. The method of resolution is identical to the previous section. The problem is decomposed in two domains (before and after the step):

$$\begin{aligned}\Phi_{\text{C,I}}^{(1)} &= \frac{iA\Omega}{K_0 \sinh K_0} e^{-iKX} F_0(Z) + \sum_{n \in \mathbb{N}} C_n^- e^{iK_n X} F_n(Z), \quad \text{for } X < 0 \\ \Phi_{\text{C,II}}^{(1)} &= \sum_{n \in \mathbb{N}} C_n^+ e^{-iK_n^s X} F_n^s(Z), \quad \text{for } X > 0\end{aligned}\quad (1.3.73)$$

where $[K_n, F_n]_{n \in \mathbb{N}}$ ($[K_n^s, F_n^s]_{n \in \mathbb{N}}$) are the eigenvalues and eigenfunctions in the domain of water depth d (d_s). The problem is then solved by matching the velocities and pressure at the interface. The projection strategy is the same as mentioned earlier (see the *Mathematica* code for the plunger as an example in appendix C).

It is well-known that the flux of energy is conserved in such a configuration in the linear theory. A less frequently mentioned result concerns the wave mass transport. The general trend is sketched by the red solid line in figure 1.12. The amount of mass travelling in the surface layer increases above the step. This means that there must be a transfer of mass between the surface layer and the interior of the flow near this point. The transfer can be either from the shoreside (shallow side) to the surface layer (sketched by the solid line arrows) or from the seaside (deep side) to the surface layer (sketched by the dashed line arrows) or both, depending on the boundary conditions at $X = \pm\infty$. A probable scenario is that globally in the deep side there is no mass transport and on the shore side the waves will break on a beach and the excess of mass transport will circulate around in the shoreside as sketched by the solid line arrows. Figure 1.13 shows the effect of varying the

frequency and the water depth on the wave mass transport variation, $\Delta\mathcal{M} = \mathcal{M}_{\text{II}} - \mathcal{M}_{\text{I}}$, for different step heights. A positive value means an increase in wave mass transport as shown in figure 1.12. The results are obtained with a 10-term expansion. The wave mass transport increases for long waves and tends to zero for short waves. The first result is sketched in figure 1.12. The maximum value near the long wave limit ($\Omega \rightarrow 0$) is also inversely proportional to the water depth. The fact that the variation of mass transport tends to zero as $\Omega \rightarrow \infty$ is not surprising as one would expect the step to have few effects as the wavelength becomes small (limit of deep water, the step is barely noticeable for the short waves). The wave mass transport variation systematically changes sign as the angular frequency is increased. This is a more astonishing result. There exists a critical frequency at which the effect is reversed. The value at which the sign changes is inversely proportional to the depth ratio D_s . It appears that this value is near $\Omega\sqrt{D_s} = 1$ in the limit $D_s \rightarrow 0$.

In the next section the equations of exchange between the surface layer and the interior are derived.

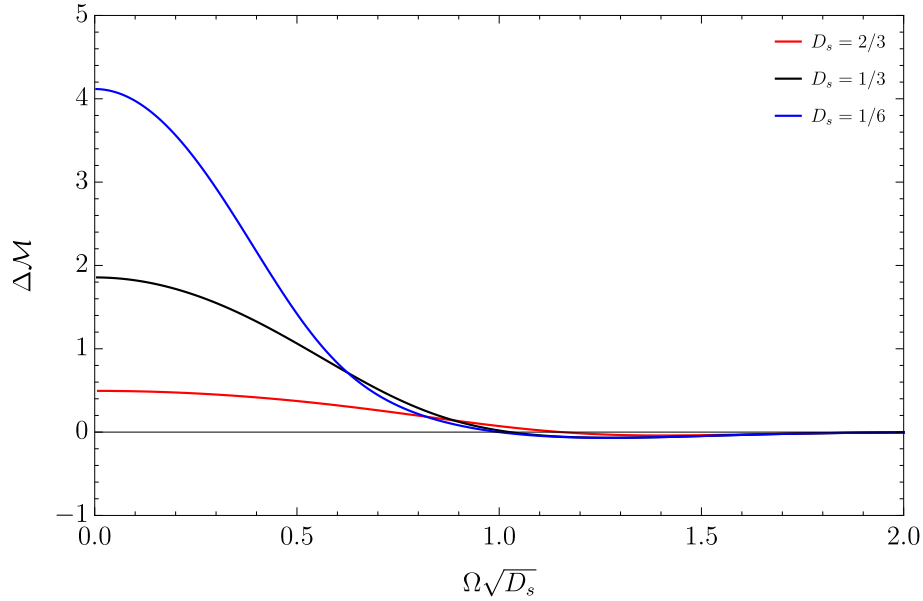


Figure 1.13: Wave mass transport variation at a step (based on the linear theory) as a function of the non-dimensional frequency above the step. The variation is measured as the difference between the mass transport over the step and the one on the seaside and is non-dimensionalized by the incident mass transport. A positive value means an increase in the wave mass transport over the step as shown in figure 1.12. A value of zero means that there is no variation. The red (black, blue) shows the variation of $\Delta\mathcal{M} = \Delta M/M_{inc}$ for $D_s = 2/3$ ($1/3$, $1/6$).

1.4 Waves and mean flow interaction

In this section, a review of the interaction of waves with larger scale motions such as mean current is provided. This will be of importance in the next chapters.

The effect of a mean current on a wave train was studied by Whitham [169, 170] in 1967 using an elegant Lagrangian approach. The presence of the mean current affects the wavenumber in particular. The effect of complex current with shear was studied by Dalrymple [30].

Here, the effect of the wave field on the mean flow is considered. In particular, the focus is on how a wave field can affect and/or generate a current. It was already shown before that waves, as described by the theory of Stokes, transport mass (Stokes drift). It was outlined that in the Eulerian point of view the mean current was concentrated in the surface layer. In this section, using the Eulerian point of view, the equations for the mean flow are derived.

In the first part, the Stokes theory of potential wave is derived to the second order. It is thus assumed that the mean flow is also potential. The potential theory leads to a single wave field term acting on the potential mean flow through the divergence of the wave mass transport. Another boundary condition enables one to deduce the effect of the wave train on the mean water surface elevation.

In the second part, a more general point of view is taken [66]. This development use a method similar to Reynolds averaging in turbulence and is called the interaction stress representation. Another representation is called the vortex-force representation [29] which arose to explain the Langmuir circulations. They are formally equivalent and are compared in [83]. In the present representation, the mean flow equations are derived from the general Euler's equations of motion for an ideal fluid. It appears then that the wave field interacts with the mean flow through two terms: once more the wave mass transport and a new term called the interaction stress tensor. This latter term is the local analog to the radiation stress tensor introduced by Longuet-Higgins and Stewart [98] in 1960. It plays a role in the generation of longshore current for instance [94]. These two source terms of mean flow are evaluated for the case of a linear Stokes wave train, a dissipated Stokes wave train and for standing waves.

1.4.1 Second order potential theory and mean flow

In this section, the calculations of the previous section are pursued and non-dimensional notations are used. The potential theory is now extended to the second order in 2D. Keeping the second order terms in the system of equations eq.1.2.8 leads to the second

order system:

$$\left\{ \begin{array}{ll} \Delta\Phi^{(2)}(X, Z, \mathcal{T}) = 0 & (X, Z) \in]-\infty, +\infty[\times]-1, 0[, \\ \partial_{\mathcal{T}}\tilde{Z}^{(2)} - \partial_Z\Phi^{(2)} = -\partial_X(U^{(1)}\tilde{Z}^{(1)}) & \text{on } Z = 0, \\ \partial_{\mathcal{T}}\Phi^{(2)} + \tilde{Z}^{(2)} = -\tilde{Z}^{(1)}\partial_{\mathcal{T},Z}\Phi^{(1)} - \frac{1}{2}|U^{(1)}|^2 & \text{on } Z = 0, \\ \partial_Z\Phi^{(2)} = 0 & \text{on } Z = -1. \end{array} \right. \quad (1.4.1)$$

The kinematic boundary condition at the surface is used here instead of original second equation eq.1.2.5, which, when retaining second order terms, is

$$\partial_{\mathcal{T},\mathcal{T}}\Phi^{(2)} + \partial_Z\Phi^{(2)} = -\tilde{Z}^{(1)}\partial_Z(\partial_{\mathcal{T},\mathcal{T}}\Phi^{(1)} + \partial_Z\Phi^{(1)}) - \partial_{\mathcal{T}}(|U^{(1)}|^2) \quad \text{on } Z = 0. \quad (1.4.2)$$

The latter is convenient when deriving the second harmonic terms in the potential theory (see for instance [162] eq.3.11-3.13, or appendix E) but the chosen formulation is more adapted to the mean flow description.

Due to the influence of the first order solution on the second order equations, it is clear that the second order term is composed of oscillatory terms at a frequency of 2Ω and time-independent terms. This section focuses on the latter. The time-independent terms are defined by the superscript $(2, 0)$. Time-averaging the system of equations eq.1.4.1 leads to the system of equations for the mean scalar potential:

$$\left\{ \begin{array}{ll} \Delta\Phi^{(2,0)}(X, Z, \mathcal{T}) = 0 & (X, Z) \in]-\infty, +\infty[\times]-1, 0[, \\ \partial_Z\Phi^{(2,0)} = \partial_X\mathcal{M}^w & Z = 0, \\ \partial_Z\Phi^{(2,0)} = 0 & Z = -1, \end{array} \right. \quad (1.4.3)$$

where $\mathcal{M}^w = \overline{U^{(1)}\tilde{Z}^{(1)}}$ is just the mean mass transport as defined in eq.1.3.44. This boundary condition physically means that the variation of the mass transport in the surface layer is compensated by an equal flux through the undisturbed surface. If the wave mass transport increases, from the mean flow point of view, it looks like there is a sink at the surface (see figure 1.12). It is important to outline that if the wave field is constant and thus M^w is constant, then there is no potential mean flow with this theory. In particular, in the case of a standing wave, the wave mass transport is constant and nil. Indeed, in that situation, the potential is

$$\Phi_{\mathcal{C}}^{(1)} = \frac{iA\Omega}{K \sinh K} \cosh[K(1+Z)] \{e^{-iKX} + e^{+iKX}\}, \quad (1.4.4)$$

and

$$\tilde{Z}_{\mathcal{C}}^{(1)} = A \{e^{-iKX} + e^{+iKX}\}, \quad (1.4.5)$$

and it turns out that $\partial_X \Phi_C^{(1)} \tilde{Z}_C^{(1)*}$ is an imaginary number¹¹.

The remaining boundary condition in the system of equations eq.1.4.1 yields the effect of the wave on the mean surface elevation:

$$\tilde{Z}^{(2,0)} = -\overline{\tilde{Z}^{(1)} \partial_{T,Z} \Phi^{(1)}} - \frac{1}{2} \overline{|\mathbf{U}^{(1)}|^2} \quad \text{on } Z = 0, \quad (1.4.6)$$

For the case of a forward travelling wave train, after simple algebra, the well-known wave second order *set-down* is obtained:

$$\tilde{Z}^{(2,0)} = -\frac{A^2 K}{2 \sinh 2K}. \quad (1.4.7)$$

For the case of a standing wave, the expression becomes:

$$\tilde{Z}^{(2,0)} = -\frac{A^2 K}{\sinh 2K} + \frac{A^2 K}{\tanh 2K} \cos 2KX. \quad (1.4.8)$$

Thus the mean water level is set-down by the contribution of each wave train and fluctuates due to their interaction. The mean water level is higher at the antinodes (set-up) and similarly lower at the nodes (set-down).

In the next section, a more general set of equations for the mean flow is derived.

1.4.2 General wave-mean flow Eulerian equations

The development is based on the paper of Hasselmann [66] in 1971. He derived the mean-flow equations by averaging the Eulerian equations of motion with the appropriate boundary conditions. In this section, dimensional notations are used and the equations are not restricted to two dimensions for now. Consider the motion of an ideal homogeneous fluid of constant depth d with a free surface $z = \eta(x, y, t)$. The system of equations of eq.1.1.18 for an inviscid fluid with the boundary conditions eq.1.1.19 and eq.1.1.20 is

$$\begin{cases} \nabla \cdot \mathbf{u} = 0, & -d \leq z \leq \eta, \\ \partial_t \mathbf{u} + (\mathbf{u} \cdot \nabla) \mathbf{u} + \frac{1}{\rho} \nabla p_* = 0, & -d \leq z \leq \eta, \\ p_* - \rho g \eta = 0, & \text{at } z = \eta, \\ \partial_t \eta + (\mathbf{u} \cdot \nabla_s) \eta - w = 0, & \text{at } z = \eta, \\ w = 0, & \text{at } z = -d, \end{cases} \quad (1.4.9)$$

where $\mathbf{u} = (u, v, w)$ is the velocity, $p_* = p + \rho g z$ is the excess pressure and $\nabla_s = (\partial_x, \partial_y)$. Similarly to turbulence theory, it shall be considered that the flow can be decomposed in a rapidly oscillating wave field $\tilde{\mathbf{u}}, \tilde{\eta}$ such that $\overline{\tilde{\mathbf{u}}} = \mathbf{0}$, $\overline{\tilde{\eta}} = 0$, and a mean flow $\bar{\mathbf{u}}$ with a mean water elevation $\bar{\eta}$, which varies slowly with respect to time. Averaging the system

¹¹See proposition 1.

of equations eq.1.4.9 and applying the boundary condition to the mean surface elevation $z = \bar{\eta}$, the equations become

$$\begin{cases} \nabla \cdot \bar{\mathbf{u}} = 0, & -d \leq z \leq \bar{\eta}, \\ \partial_t \bar{\mathbf{u}} + (\bar{\mathbf{u}} \cdot \nabla) \bar{\mathbf{u}} + \frac{1}{\rho} \nabla p_m = \nabla \cdot \bar{\bar{\tau}}^{int}, & -d \leq z \leq \bar{\eta}, \\ p_m - \rho g \bar{\eta} = 0 & \text{at } z = \bar{\eta}, \\ \partial_t \bar{\eta} + (\bar{\mathbf{u}} \cdot \nabla_s) \bar{\eta} - \bar{w} = -\frac{1}{\rho} \nabla_s \mathbf{M}^w & \text{at } z = \bar{\eta}, \\ \bar{w} = 0 & \text{at } z = -d, \end{cases} \quad (1.4.10)$$

where p_m is defined as the mean pressure in the absence of the wave field ($\bar{p} = p_w + p_m$, where p_w is the wave contribution to the mean pressure field), $\bar{\bar{\tau}}^{int}$ is called the *interaction stress tensor*, defined as

$$\bar{\bar{\tau}}^{int} = - \begin{pmatrix} \overline{\tilde{u}^2} + \frac{1}{\rho} p_w & \overline{\tilde{u}\tilde{v}} & \overline{\tilde{u}\tilde{w}} \\ \overline{\tilde{v}\tilde{u}} & \overline{\tilde{v}^2} + \frac{1}{\rho} p_w & \overline{\tilde{v}\tilde{w}} \\ \overline{\tilde{w}\tilde{u}} & \overline{\tilde{w}\tilde{v}} & \overline{\tilde{w}^2} + \frac{1}{\rho} p_w \end{pmatrix}, \quad (1.4.11)$$

(it is composed of the *Reynolds stresses* and wave contribution to the mean pressure), and \mathbf{M}^w is the *wave mass transport* as already discussed earlier and defined by Hasselmann [66] as

$$\mathbf{M}^w = \rho \overline{\int_{\bar{\eta}}^{\eta} (u, v)^T dz}. \quad (1.4.12)$$

Note that it is a plane vector and it is on the total horizontal velocities¹² component $(u, v)^T$ (note the superscript T refers here to the transpose operator). The kinematic boundary condition

$$\partial_t \bar{\eta} + (\bar{\mathbf{u}} \cdot \nabla_s) \bar{\eta} - \bar{w} = -\frac{1}{\rho} \nabla_s \mathbf{M}^w \quad \text{at } z = \bar{\eta}, \quad (1.4.13)$$

is readily equivalent to the boundary condition found in the potential theory (see eq.1.4.3). The proof of this boundary condition is given in appendix D.

The wave field thus interacts with the mean flow through two source terms: a force given by the divergence of the interaction stress tensor and a mass flux due to the divergence of the wave mass transport \mathbf{M}^w .

The system of equations eq.1.4.10 is valid for any kind of “wave field”. The only assumption made by Hasselmann [66] is that the flow field could be continued analytically to the mean surface $\bar{\eta}$ for $\tilde{\eta} < 0$, which is when the mean position of the surface is above the free surface. Like in turbulence under the so-called Reynolds-averaging process, the system is not closed and other equations need to be prescribed to describe the wave field $\tilde{\mathbf{u}}, \tilde{\eta}$. In this thesis, the focus is on the wave field induced mean flow. It is thus assumed that the mean flow is a consequence of the wave field and the back interaction is neglected.

¹²Mean flow velocity plus rapidly oscillating wave field velocity in the surface layer.

1.4.3 Interaction stress tensor and wave mass transport calculation

The theory is applied to simple cases. First the case of a linear wave train is evaluated. The impact of dissipation is also estimated. Finally the case of standing waves is analyzed.

1.4.3.1 Linear travelling wave

In the case of linear waves, as described in the previous section, the interaction stress tensor and the wave mass transport can be rigorously evaluated. The wave field contribution to the mean pressure is readily found using the argument of vertical flux of momentum developed by Longuet-Higgins and Stewart [97]. The mean flux of vertical momentum, that is $p_w + \overline{\rho \tilde{w}^2}$ must be enough to support the weight of the water above it, hence $p_w = -\overline{\rho \tilde{w}^2}$. The interaction stress tensor for 2D linear wave field of the form of section 1.3 (with no dissipation) is then

$$\bar{\tau}^{int} = \frac{a^2 g k}{\sinh 2kd} \begin{pmatrix} -1 & 0 & 0 \\ 0 & \sinh^2 [k(z+d)] & 0 \\ 0 & 0 & 0 \end{pmatrix}, \quad (1.4.14)$$

and thus the divergence reduces to zero. After expanding with respect to $\tilde{\eta}$, the wave mass transport becomes:

$$\mathbf{M}^w = \rho \left(\overline{\tilde{u} \tilde{\eta}}, 0 \right) + \partial_z \bar{\mathbf{u}}|_{z=\tilde{\eta}} \overline{\tilde{\eta}^2}. \quad (1.4.15)$$

Neglecting the second term which can be assumed to be at least a third order term, it just becomes the now well-known mass transport

$$\mathbf{M}^w = \frac{1}{2} \rho a^2 \omega \coth kd \begin{pmatrix} 1 \\ 0 \end{pmatrix}, \quad (1.4.16)$$

and thus the divergence is also zero. It is also interesting to look at the mean stress acting on the surface layer defined by

$$\bar{\tau}^{sl} = - \overline{\int_{\tilde{\eta}}^{\eta} \begin{pmatrix} u^2 + \frac{1}{\rho} p & uv \\ uv & v^2 + \frac{1}{\rho} p \end{pmatrix} dz}, \quad (1.4.17)$$

and for linear waves simplifies to

$$\bar{\tau}^{sl} = -g \overline{\tilde{\eta}^2} \mathbb{I} = -\frac{1}{2} g a^2 \mathbb{I}, \quad (1.4.18)$$

where here \mathbb{I} denotes the identity matrix. Note this mean stress as defined here is homogeneous to a surface tension. The surface shear stress, $\boldsymbol{\tau}_s$, acting on the mean surface is then found by taking the divergence of the surface layer mean stress $\bar{\tau}^{sl}$. For the present

case, it is once more zero.

1.4.3.2 Adding dissipation: a model for wave-breaking

Assume now that the wave amplitude slowly varies with the horizontal coordinate $a \rightarrow a(x)$ where $|a'(x)| \ll 1$. If the expression is directly injected in the expression of the velocity, the continuity is not satisfied anymore. To avoid this, assume for now $a(x) = a_0 e^{-\alpha x}$, where $\alpha \in \mathbb{R}$. To satisfy the continuity, rewrite the scalar potential in the following way:

$$\varphi^{(1)} = \frac{a_0 \omega}{\kappa \sinh \kappa d} \cosh [\kappa (d + z)] e^{i(\omega t - \kappa x)}, \quad (1.4.19)$$

where $\kappa = k - i\alpha$ is the apparent wavenumber. Then, $\Delta\varphi^{(1)} = 0$. It is assumed that $\alpha \ll k$ and also $\alpha d \ll 1$. Re-evaluating the interaction stress tensor yields

$$\bar{\bar{\tau}}^{int} \approx \frac{a_0^2 g k}{\sinh 2kd} e^{-2\alpha x} \begin{pmatrix} -1 & 0 & -\alpha(z+d) \\ 0 & \sinh^2 [k(z+d)] & 0 \\ -\alpha(z+d) & 0 & 0 \end{pmatrix}. \quad (1.4.20)$$

Adding dissipation leads to an additional vertical shear stress. Taking the divergence and retaining only the first order terms in αd , yields

$$\nabla \bar{\bar{\tau}}^{int} \approx \frac{a_0^2 g k}{\sinh 2kd} \begin{pmatrix} \alpha \\ 0 \\ 0 \end{pmatrix}, \quad (1.4.21)$$

and identifying the terms $-a_0 \alpha e^{-\alpha x} \approx a'(x)$, gives

$$\nabla \bar{\bar{\tau}}^{int} \approx \frac{a g k}{\sinh 2kd} \begin{pmatrix} -a'(x) \\ 0 \\ 0 \end{pmatrix}. \quad (1.4.22)$$

The mean water level variation can be found using the dynamic boundary condition $p_m = \rho g \bar{\eta}$, which yields

$$\partial_x \bar{\eta} \approx -a'(x) \frac{a k}{\sinh 2kd}. \quad (1.4.23)$$

If $a'(x) < 0$, corresponding to wave dissipation due to internal frictions or wave breaking, the mean water level increases. This corresponds to the *set-up*. On the contrary, if $a'(x) > 0$, the wave amplitude increases, the water level decreases: *set-down*. This development is valid in the case where k and d are held fixed. For variable k and d , the depth averaged developments of Longuet-Higgins and Stewart [96] yield simpler results. A model to evaluate suitable values of $\alpha \approx a'(x)/a(x)$ is discussed in the next section. The wave mass transport is not modified but a varies, leading to exchange of mass between the

interior and the surface layer.

The surface shear stress is

$$\boldsymbol{\tau}_s = -ga a'(x) \mathbf{e}_x, \quad (1.4.24)$$

where \mathbf{e}_x is the unit vector in the wave direction propagation. When $a'(x) < 0$, the shear stress on the surface is thus in the same direction as the wave “pushing” the mean flow in this direction.

1.4.3.3 The case of standing waves

Consider now a standing-wave field. As mentioned in section 1.4.1, the wave mass transport term is exactly zero. After some basic algebra, the interaction stress tensor yields

$$\bar{\bar{\tau}}^{int} = 2\bar{\tau}_{sw}^{int} + \frac{a^2 g k}{\sinh 2kd} \begin{pmatrix} 2c_2 \cos 2kx & 0 & s_2 \sin 2kx \\ 0 & 2s \cos 2kx & 0 \\ s_2 \sin 2kx & 0 & 0 \end{pmatrix}, \quad (1.4.25)$$

where $\bar{\tau}_{sw}^{int}$ is the interaction stress tensor of a single wave given by eq.1.4.14, $s = \sinh [k(d+z)]$, $c_2 = \cosh [2k(d+z)]$, $s_2 = \sinh [2k(d+z)]$. The interaction stress tensor divergence is

$$\nabla \cdot \bar{\bar{\tau}}^{int} = \frac{a^2 g k^2}{\sinh 2kd} \begin{pmatrix} -2c_2 \sin 2kx \\ 0 \\ 2s_2 \cos 2kx \end{pmatrix}. \quad (1.4.26)$$

Assuming steady mean flow, the pressure is given by

$$p_m = gk \frac{a^2 k^2}{\sinh 2kd} \cos 2kx \cosh [2k(d+z)]. \quad (1.4.27)$$

The mean water level is found by setting $z \rightarrow 0$ and using the dynamic boundary condition:

$$\bar{\eta} = gk \frac{a^2 k^2}{\tanh 2kd} \cos 2kx. \quad (1.4.28)$$

The surface shear stress is:

$$\boldsymbol{\tau}_s = 2ga^2 k \sin(2kx) \mathbf{e}_x. \quad (1.4.29)$$

The surface shear acts here like surface tension on the mean water level pushing water away from the mean water level crest to fill the trough. This leads to circulation cells of typical size $\lambda/4$ and might influence the mean flow on typical scales of the order of $\lambda/2$ [21]¹³.

¹³This is similar to the cascade of energy in turbulence.

1.5 Non-linearity, dissipation and wave breaking

In the previous section, the notion of wave dissipation was introduced to outline the set-up and a form of mass transfer from the surface layer to the interior of the flow of a wave train. In this section, a model of wave dissipation and its effect on the wavenumbers are discussed. This section first discusses the limit of validity of the linear theory developed so far. In all the previous sections no comments were made on the maximum amplitude a wave can achieve. It was always assumed that the waves were small compared to any quantity. When this is no longer the case, the Taylor series of eq.1.2.10 should be expanded to higher order. In the present study, the goal is not to achieve a higher order description of the model but to already get the most information from the linear theory. Yet the linear theory might lead to unacceptable predictions such as tremendously large waves amplitude (for instance in the next chapter, the amplitude will be infinite at resonance). In reality, the wave amplitude is limited by wave breaking. This goes against the initial assumption of no rolling surface. Nonetheless, the motion considered is always periodic and thus it will be instructive to represent this complex wave breaking through a dissipative term. But then when should dissipation be added and to what amount? The goal of this section is to address these questions.

First the effect of increasing wave size on the dispersion relation is discussed. It will be pointed out in particular that increasing the wave amplitude leads to a reduction of the apparent wavenumber (or equivalently an increase in the wavelength), at fixed wave period. Consequently the wave speed is increased by non-linearity. If the wave size is further increased, the waves will eventually break. Wave breaking thresholds are discussed for the case of travelling waves and in the more complex case of standing waves on a constant water depth. The latter will be of interest in the applications where reflections are large. To capture the wave breaking in the linear potential theory, a dissipation model is proposed in the framework of potential flow: potential wave dissipation¹⁴. The dissipation in the roller is modeled by a surface dissipation term in the kinematic boundary condition. The effect of adding this dissipation force on the wavenumbers is also discussed. The dissipative potential model leads to a reduction of the wavenumber (thus similar to the non-linearity effects). The effect of wave breaking on the wave mass transport is discussed briefly.

1.5.1 Non-linear waves and dispersion relation

As wave amplitude becomes larger, the potential theory should be extended to higher orders. The goal here is not to derive the potential theory to arbitrary order. Fenton [46] derived a fifth order wave theory for Stokes waves. Some effects of wave non-linearities have been mentioned earlier: wave mass transport and set-down. Another important effect

¹⁴Other models are discussed in appendices F, G, H and I.

to the present discussion is the one of the wave amplitude on the dispersion relation. This can be elegantly found using the variational approach of Luke [101] and Whitham [169] or by expanding the potential theory up to the third order¹⁵. The non-linear dispersion relation is readily derived in the absence of mean current:

$$\omega^2 = gk \tanh kd \left\{ 1 + k^2 a^2 \frac{9 - 10 \tanh^2 kd + 9 \tanh^4 kd}{8 \tanh^4 kd} \right\}, \quad (1.5.1)$$

or in non-dimensional form:

$$\Omega^2 = K \tanh K \left\{ 1 + K^2 A^2 \frac{9 - 10 \tanh^2 K + 9 \tanh^4 K}{8 \tanh^4 K} \right\}. \quad (1.5.2)$$

Expanding the non-linear dispersion relation near the linear solution, one can see that non-linearity tends to decrease the wavenumber (or increase the wavelength). This leads to a slight increase in the phase velocity ($c_\varphi = \omega/k$), in agreement with the comment of Goda [58] who noticed that the wave celerity is slightly higher than predicted by the linear theory near breaking. The non-linear dispersion relation of eq.1.5.1 diverges for $kd \rightarrow 0$:

$$\omega^2 = gk^2 d \left\{ 1 + \frac{9}{8} \left(\frac{a}{d} \right)^2 (kd)^{-2} \right\}, \quad kd \rightarrow 0, \quad (1.5.3)$$

which shows, as pointed out by Kirby and Dalrymple [81], the severe restriction on a/d as depth becomes small. The formulation is considered valid as long as *Ursell* number is “small”:

$$U_r = \frac{a}{k^2 d^3} < O(1). \quad (1.5.4)$$

Below this threshold the Stokes theory is not valid and the waves are better described by the *cnoidal wave theory*¹⁶. This is outside the scope of the present subject. The dispersion relation in shallow water is better described by Hedges’ empirical formulation [68]:

$$\omega^2 = gk \tanh (kd + ka). \quad (1.5.5)$$

It will be pointed out that the Stokes non-linear dispersion relation can be corrected to be valid in both wave regimes as proposed empirically by Kirby and Dalrymple [81]:

$$\omega^2 = gk \tanh [k(d + f_1 a)] \left\{ 1 + f_2 k^2 a^2 \frac{9 - 10 \tanh^2 kd + 9 \tanh^4 kd}{8 \tanh^4 kd} \right\}, \quad (1.5.6)$$

where $f_1 = (kd / \sinh kd)^4$ and $f_2 = \tanh^5 kd$. Their formulation is based on the asymptotic regime behaviors.

¹⁵Here, the expansion was carried up to the second order for the mean flow, the second and third orders are given in appendix E.

¹⁶ See appendix E for a discussion on the Ursell number.

The different dispersion relations are compared in figure 1.14, where the ratio of the phase velocity with the deep water phase velocity is plotted against the non-dimensional wavenumber $K = kd$ for $KA = ka = 0.25$. The model of Kirby and Dalrymple [81] nicely avoids the singularity of Stokes dispersion and matches the dispersion for cnoidal waves. In all the cases the dispersion relation shows an increase in the apparent wavelength compared to the linear theory and equivalently a faster wave celerity.

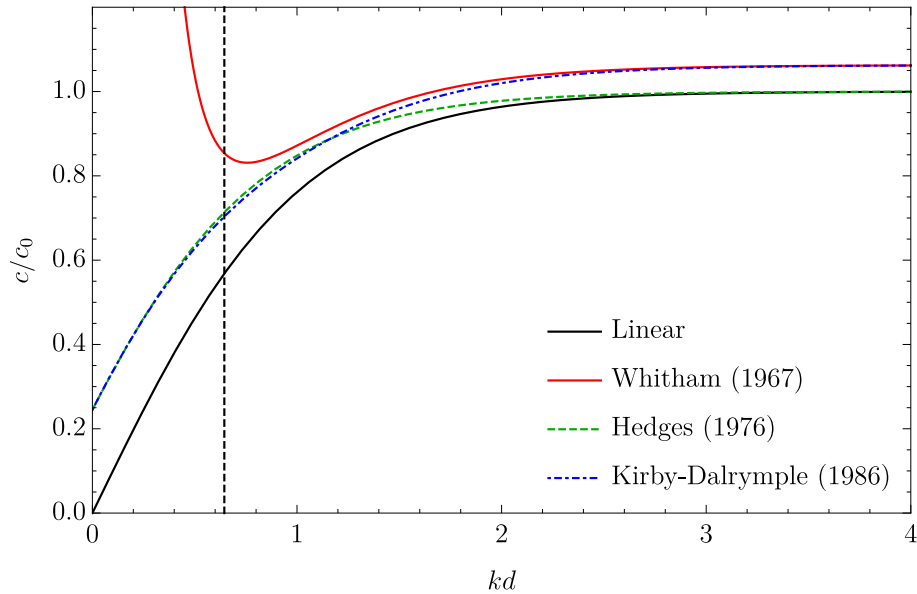


Figure 1.14: Non-linear dispersion relations with $K = kd$ for a wave steepness $KA = 0.25$. The celerity is non-dimensionalized by the deep water celerity $c_0 = g/\omega$. The different models correspond to the linear theory (black solid line, eq.1.3.5), the Stokes non-linear theory (red solid line, eq.1.5.1), Hedges' cnoidal empirical theory (green dashed line, eq.1.5.5) and the model of Kirby and Dalrymple [81] (blue dot-dashed line, eq.1.5.6). In all the cases, the non-linear dispersion shows an increase in the phase velocity. The vertical dashed line shows the breaking wave threshold from [113] (the waves are predicted to break below this threshold of K).

1.5.2 Maximum wave amplitude and wave breaking thresholds

If the wave train continues increasing in amplitude the waves will start breaking. Breaking occurs when the maximum downward acceleration exceeds gravity. Another way to state this is to say that waves will break when the crest travels faster than the phase velocity. In any case, this leads to the upper band of wave breaking:

$$a_{wb} < \frac{\tanh kd}{kd} d, \quad (1.5.7)$$

where the subscript wb is for “wave breaking”. Miche [113] provided a more accurate value using Stokes theory:

$$h_{wb} \approx \beta_{Miche} \frac{\tanh kd}{kd} d, \quad (1.5.8)$$

where $\beta_{Miche} = 2\pi \times 0.142 \approx 0.89$, which yields $h_{wb} \approx 0.89d$ for long waves, a value in good agreement with the observation of Munk [119] for solitary waves but slightly overestimated. The value of 0.89 is based on the maximum theoretical deep water wave steepness limit of Michell [114]. A recent model of wave breaking was proposed by Liu et al. [92] and links the breaking threshold to the wavenumber through the implicit equation :

$$0.69 = \left(1.21 - \frac{3.30}{2\pi} kh_{wb} \right) \left(1.48 - 0.54 \frac{h_{wb}}{d} \right) \frac{gh_{wb}}{c_{wb}}, \quad (1.5.9)$$

where c_{wb} is the non-linear celerity at the breaking threshold. Liu et al. [92] used the dispersion relation of Hedges [68] for c_{wb} . For more information about the wave breaking thresholds, one can refer to the recent review of Robertson et al. [141].

For standing waves, the studies on the breaking threshold are more sparse. Penney and Price [129] put forward an argument that the highest wave should have a sharp angle of 90° . In their calculation done for deepwater, they found that the maximum wave height was, from crest to trough:

$$h_{wb} \approx 0.218\lambda, \quad kd \gg 1. \quad (1.5.10)$$

This was verified experimentally by Taylor [153]. Above that height, the downward acceleration at the crest exceeds gravity based on the fifth order expansion for deepwater waves of Penney and Price [129]. Expanding this similarly to the work done by Miche [113], it is proposed that in the presence of standing waves, the wave breaking threshold is

$$h_{wb} \approx \beta_{SW} \frac{\tanh kd}{kd} d, \quad (1.5.11)$$

where $\beta_{SW} \approx 1.37$.

In the rest of this thesis, a wave breaking threshold of the form

$$h_{wb} \approx \beta_{wb} \frac{\tanh kd}{kd} d, \quad (1.5.12)$$

is used, where β_{wb} is a wave breaking non-dimensional parameter and $0 < \beta < 2$ by eq.1.5.7, in the case of simple travelling waves with small or no reflection it should be near 0.88 and in the case of large expected reflection the value of β_{wb} should be near 1.37, which is a bit less than twice the previous threshold, based on the previous discussions. Note that Carmigniani et al. [21] used in their model a factor 2×0.88 instead of 1.37.

Wave breaking is not allowed in the potential description developed here as surface rolling is not considered. To model the wave breaking, dissipative terms are considered in the

potential description.

1.5.3 Dissipative dispersion relation

The goal here is to keep the wave size below the breaking onset described in the previous paragraph in the linear potential predictions. For instance consider the previous case of the waves above the step (see section 1.3.4.3). On the seaside, the incident wave might be correctly described by the linear potential theory. Yet, the linear prediction can predict an unphysical wave size at the step. This will lead to wave-breaking in nature. To account for this, breaking wave regions are considered as regions of strong dissipation. To that extent, dissipative forces are considered and their effect on the dispersion relation reviewed. The description is limited to a dissipative term on the kinematic boundary condition. This term is intended to model the dissipation due to surface rolling¹⁷. Note that it can also be used to model other sources of dissipation (such as sea-bed friction, but requires some tuning to get the proper dissipation rate, see section 3.3.2.1).

The present potential wave dissipation model can be compared to three other potential wave dissipation models based on viscosity: the potential flow of viscous fluid (PVF) by Funada and Joseph [52], Joseph and Wang [78] (see appendix G), which recognises the fact that a fluid can be viscous and potential ; the viscous potential flow (VPF) description developed by Dutykh and Dias [41] (see appendix H), where the equations are corrected to take into account the effect of vorticity and thus are closer to the last model of viscous waves of Lamb [82] (see appendix F), where the wave equations are derived from the linearized Navier–Stokes equations. All three models assume that the surface displacement is negligible compared to the viscous boundary layer at the surface, or in the limit of creeping flow. Another model consists in adding a fictitious linear dissipation of the form $\mathbf{f}_d = -\rho\beta\mathbf{u}$ as done by Le Méhauté [84] (this is discussed along with the case of variable β for wave absorption in [20] and appendix I).

In the present description, the kinematic free-surface condition (see eq.1.2.4) is modified to:

$$\partial_t\eta + \partial_x\varphi\partial_x\eta - 2\nu\partial_{x,x}\eta = \partial_z\varphi, \quad \text{at } z = \eta, \quad (1.5.13)$$

where ν is a dynamic viscosity. The new term is similar to the one found when considering the effect of the rotational part of the flow on the potential equations [41]. It tends to flatten the surface deformations.

Using the previously defined non-dimensional notations and the linear wave assumption,

¹⁷It presents one big advantage over considering the case of potential flow of viscous fluid (see appendix G), which is that the matching condition between two domains remains the continuity of the velocity and pressure (or equivalently the continuity of the scalar velocity and its derivative).

the system to solve becomes

$$\begin{cases} \Delta\Phi = 0 & (X, Y, Z) \in]-\infty, +\infty[^2 \times]-1, \tilde{Z}[, \\ \partial_{\mathcal{T}}\Phi + \tilde{Z} = 0 & \text{on } Z = 0, \\ \partial_{\mathcal{T}}\tilde{Z} - \frac{2}{\mathcal{R}}\partial_{X,X}\tilde{Z} = \partial_Z\Phi & \text{on } Z = 0, \\ \partial_Z\Phi = 0 & \text{on } Z = -1, \end{cases} \quad (1.5.14)$$

where \mathcal{R} is called wave Reynolds number:

$$\mathcal{R} = \sqrt{\frac{gd^3}{\nu^2}}. \quad (1.5.15)$$

One can write a boundary condition that depends only on the scalar potential at the free surface of the form

$$\partial_{\mathcal{T},\mathcal{T}}\Phi + \partial_Z\Phi + \frac{2}{\mathcal{R}}\partial_{Z,Z,\mathcal{T}}\Phi = 0, \quad \text{on } Z = 0, \quad (1.5.16)$$

where the continuity equation is used to replace the double derivation with respect to X by a derivation with respect to Z .

Then, it yields the new function $F^{(1)}$ defined similarly to eq.1.3.4

$$F^{(1)}(Z) = \frac{iA\Omega}{K \sinh K} \left(1 - i\frac{2K^2}{\Omega\mathcal{R}} \right) \cosh [K(1 + Z)], \quad (1.5.17)$$

and the dispersion relation eq.1.3.5 becomes

$$\Omega^2 \left(1 - i\frac{2K^2}{\Omega\mathcal{R}} \right) = K \tanh K, \quad (1.5.18)$$

or in dimensional form

$$\omega^2 \left(1 - i\frac{2\nu k^2}{\omega} \right) = gk \tanh kd. \quad (1.5.19)$$

Note that this is the same dispersion relation as the one found in the case of potential flow of viscous fluid, where the dissipation is limited to the dynamic boundary condition (see appendix G).

In the limit of small viscosity (*i.e.* $\mathcal{R} \rightarrow \infty$), one can show that

$$K \xrightarrow{\mathcal{R} \rightarrow \infty} K_0 \left(1 - i\frac{2K_0^2}{\Omega\mathcal{R}} \frac{\sinh 2K_0}{2K_0 + \sinh 2K_0} \right), \quad (1.5.20)$$

where K_0 is the solution of the undamped linear dispersion relation eq.1.3.5. For forward propagating waves, *i.e.* $K_0 > 0$, the imaginary part in eq.1.5.20 leads to a dissipation in the direction of the wave propagation without affecting the real part at the first order (the apparent wavelength is unchanged). Compared to the case of viscous potential flow (see

appendix H), there is a factor of two difference. In practice, this leads to a difference of a factor of one half on the Reynolds' number.

For the evanescent modes ($K_0 = -iA_n$, with $A_n > 0$), dissipation leads to modes with negative real parts and thus waves propagating in the opposite direction to the dominant mode. Recall that the evanescent terms are used in the eigenfunction expansion method for matching conditions¹⁸.

For a fixed observer looking at the waves propagating on the surface, the amplitude will appear to diminish as the waves travel and the coefficient of dissipation at first order is simply the imaginary part of eq.1.5.20. In the literature, the dissipation is frequently given as a function of time in the form

$$\partial_t a = -\frac{a}{\tau_d}, \quad (1.5.21)$$

where a is the wave amplitude and τ_d is the characteristic dissipation time. It means that the observer is travelling with the wave and the wavelength is fixed. The velocity at which the observer shall be travelling is the group velocity. Then, from the previous development, the characteristic time of dissipation is readily found by multiplying the imaginary part of the expression of K in eq.1.5.20 by the group velocity expression of eq.1.3.28:

$$T_d = \frac{\mathcal{R}}{K_0^2}, \quad (1.5.22)$$

or in dimensional form:

$$\tau_d = \frac{1}{\nu k_0^2}. \quad (1.5.23)$$

This value is different from the one found by Lamb [82] by a factor of 1/2. The reason for this discrepancy is the fact the viscous shear at the free surface is neglected here¹⁹.

Expanding to the next order: $K = K_0 + K_1 + K_2 + O(1/\mathcal{R}^3)$, yields the second order correction:

$$K_2 = -2 \left(\frac{2K_0^2}{\Omega \mathcal{R}} \right)^2 \frac{K_0 \sinh^2 2K_0 (K_0 (1 + \Omega^2) + \sinh 2K_0)}{(2K_0 + \sinh 2K_0)^3}. \quad (1.5.24)$$

At the second order, viscous dissipation leads to a reduction of the apparent wavenumber or equivalently and increase in the wavelength. This means that from this point of view of fixed frequency of waves, the wave speed (or phase velocity) is increased with dissipation for all values of the wave frequency.

Typical trajectories of the wavenumbers as the viscosity is increased are shown in figure 1.15 for $\Omega = 1$. The color gradient indicates the variation of the Reynolds number. It appears that for $\mathcal{R} < 50$, the travelling mode starts to degrade: the real and imaginary

¹⁸ Note that the Sturm-Liouville theory does not apply anymore and thus the modes are no longer orthogonal.

¹⁹ See the discussion on the dispersion relation of viscous waves for creeping flow in appendix F and the viscous potential correction in appendix H.

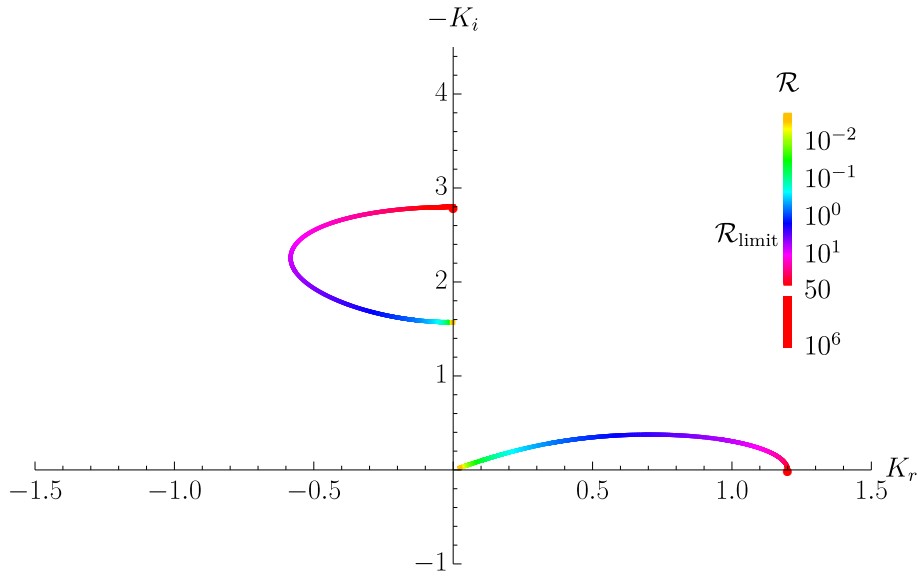


Figure 1.15: Trajectories of the first two wavenumbers (the forward travelling mode and the first evanescent mode) with viscosity for $\Omega = 1$ for the dispersion relation eq.1.5.18. The color indicates the value of the Reynolds number (or the inverse of the viscosity).

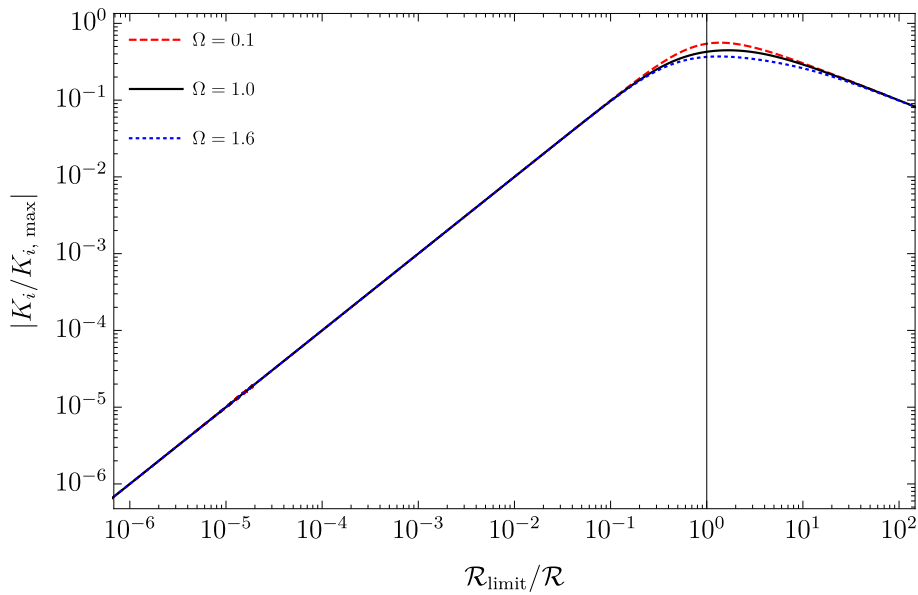


Figure 1.16: Dissipation with Reynolds number for different wave frequencies. The curves are collapsed using eq.1.5.27 and 1.5.26.

parts go to zero²⁰. One can thus readily estimate the trend of the dominant mode as

²⁰This is not the case for viscous waves of Lamb, where only the real part goes to zero but the dissipation is constant.

$\mathcal{R} \rightarrow 0$ by simply assuming $|K| \rightarrow 0$. This leads to

$$K \xrightarrow{\mathcal{R} \rightarrow 0} (1 - i) \frac{\sqrt{\Omega \mathcal{R}}}{2}, \quad (1.5.25)$$

and thus equating the imaginary parts to the limit $\mathcal{R} \rightarrow \infty$ of eq.1.5.20, a definition for a limit Reynolds number is found:

$$\mathcal{R}_{limit} = \frac{K_0^2}{\Omega} \left(\frac{4 \sinh 2K_0}{2K_0 + \sinh 2K_0} \right)^{2/3}. \quad (1.5.26)$$

This enables one to find an estimate of the maximum dissipation one can achieve:

$$|K_{i,max}| = K_0 \left(\frac{\sinh 2K_0/2}{2K_0 + \sinh 2K_0} \right)^{1/3}. \quad (1.5.27)$$

Using these definitions, the imaginary part can be rescaled (see figure 1.16) and the curves for different wave frequencies collapsed. Note that the real part starts to vary for larger \mathcal{R} values.

The limit Reynolds number defined in eq.1.5.26 can be compared to dissipation of energy in breaking waves models. Battjes and Janssen [10] scaled the power dissipated by a breaking wave using mass and momentum conservation across a bore and found that the dissipation per unit mass $D \propto 1/4gh_w^3/Td$ in shallow water. If it is compared to the dissipation due to a viscous model as proposed here, then $D \propto \nu s^2$ where $s \propto 1/T$ is the scalar rate of strain. It comes that $\nu \propto 1/4gh_w^3T/d^2$ or using the non-dimensional notations, $\mathcal{R}_{limit} \propto 2\Omega/(\pi H_w^3)$. In the limit of shallow water, eq.1.5.26 yields $\mathcal{R}_{limit} \propto 2^{2/3}\Omega$. Comparing the two scalings, one can define a wave breaking threshold: $H_w = 2^{1/9}/\pi^{1/3} \approx 0.74$ which compares well with the previous thresholds of 0.89 mentioned above.

The new wavenumbers found with the present dispersion relation enable one to define new eigenfunctions. There is, exactly like in the potential case, a countable amount of these modes. They are not orthogonal to each other, and more modes are thus required to solve the complex linked problem with an eigenfunction expansion matching method between two or more domains²¹. As the full dissipative problem (hereafter called EFE Full) is too computationally expensive²² compared to the potential case without dissipation (EFE), a simplification (called EFE NI, for not incompressible) is used. The effect of the dissipation is limited to the propagative terms, such that in an expansion

$$\Phi_{\mathbb{C}} = C_0^{\pm} e^{\pm iK_0 X} \cosh [K_0 (Z + 1)] + \sum_{n \in \mathbb{N}^*} C_n^{\pm} e^{-iK_n X} \cosh [K_n (Z + 1)], \quad (1.5.28)$$

²¹ A Gram-Schmidt process could be applied to make the set of eigenfunctions orthogonal but this complexifies the evaluation of the horizontal velocities.

²²To solve the 10-term expansion problem, one needs 0.6 seconds with the EFE and 30 seconds with the EFE Full. EFE Full does not also converge as fast making 10-term expansion not sufficient.

in the original potential model (EFE), the wavenumber K_0 is changed to its dissipative complex value $K_0^{\mathcal{R}}$ in the exponential only:

$$\Phi_{\mathbb{C}} = C_0^{\pm} e^{\pm i K_0^{\mathcal{R}} X} \cosh [K_0 (Z + 1)] + \sum_{n \in \mathbb{N}^*} C_n^{\pm} e^{-i K_n X} \cosh [K_n (Z + 1)]. \quad (1.5.29)$$

This enables one to recover the orthogonal property of the eigenfunctions and takes into account the wave dissipation during propagation. The drawback is that the propagative terms do not verify the Laplace equation (thus the name). In [21] another model was proposed (called EFE Limited) where the term in $\cosh [K_0 (Z + 1)]$ was replaced by $\cosh [K_0^{\mathcal{R}} (Z + 1)]$, which enables one to conserve the incompressibility by verifying the Laplace equation but leads to divergence of the surface horizontal velocity at the interface between two domains. This is due to the slow convergence of the coefficients of the projection of $\cosh [K_0^{\mathcal{R}} (Z + 1)]$ in the original base $\{\cosh [K_n (Z + 1)]\}_{n \in \mathbb{N}}$ when the dissipation is strong. Thus the continuity of Φ and $\partial_X \Phi$ cannot be enforced at the same time at this point. Besides these Gibbs-like phenomena, the results are quite similar for intermediate and shallow water waves with the two simplified models. So the results found in [21] are not affected by this change of theory. The difference between the EFE Full, EFE Limited and EFE NI models is discussed in an example in appendix J.

1.5.4 Wave mass transport in the roller

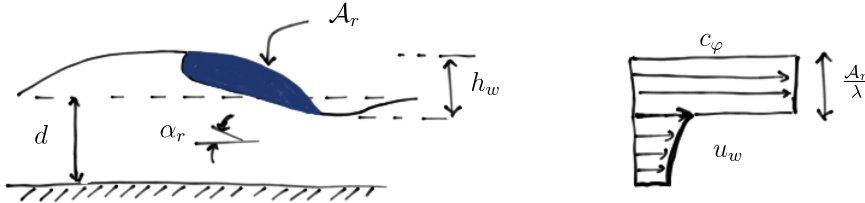


Figure 1.17: Velocity in a breaker and roller area. Sketched inspired from the figure 3 of Svendsen [151].

Consider for now a monochromatic wave train without reflection. When wave breaking occurs, the wave mass transport is increased. This is due to the turbulence that is generated near the surface. A volume of water with area per unit wave crest noted \mathcal{A}_r rushes down the front face of the wave as sketched in figure 1.17. At first approximation, this volume moves at the wave phase velocity c_φ . This generates an extra mass transport:

$$M_r = \rho_r c_\varphi \frac{\mathcal{A}_r}{\lambda}, \quad (1.5.30)$$

where ρ_r is the density of the roller. The density of the roller is in general less than the density of the water because of the air entrainment that occurs during breaking, “white

water". The percent of air entrained was estimated by Longuet-Higgins and Turner [99] to be at most 15–20%. This is not always negligible but without loss of generality this can be compensated by a reduction of the adequate amount of the area \mathcal{A}_r . The area of the roller can be estimated using an analogy with a straight walled diffusor [32], which leads to:

$$\mathcal{A}_r = \frac{h_w^3}{4d \tan \alpha_r}, \quad (1.5.31)$$

where α_r is the angle of the wave/roller interface. Svendsen [151] estimated the roller area using the experimental results of Duncan [39] and found $\mathcal{A}_r \approx 0.9 \times h_w^2$, where recall h_w is the wave height. This is equivalent to eq.1.5.31 if one uses the wave breaking threshold in shallow water $h_w = \beta_{wb}d$ and defines $\alpha_r = \arctan(\beta_{wb}/3.6)$. When using the breaking threshold of Miche [113], one finds $\alpha_r \approx 13.9^\circ$. This value compares well with the ones of Lippmann et al. [91] and Deigaard [32]. Applying the approximation of Svendsen [151] to the evaluation of the roller mass transport for a monochromatic wave train, it comes

$$M_r \approx 0.9 \frac{h_w^2}{T} \quad (1.5.32)$$

where T is the wave period. In non-dimensional form, the wave mass transport in the roller becomes:

$$\mathcal{M}_r \approx 0.6A^2\Omega. \quad (1.5.33)$$

Comparing to the stokes wave mass transport it comes:

$$\frac{\mathcal{M}_r}{\mathcal{M}^w} = 1.2 \tanh K, \quad (1.5.34)$$

which leads to a maximum increase $\mathcal{M}_r = 1.2\mathcal{M}^w$. This development is carried for a unidirectional travelling wave train. When the wave field is the superposition of wave travelling in opposite direction, it is not clear how this term should be evaluated. It is thus not well adapted for the case with high-reflection. This is an important effect though to keep in mind in the next chapters and it will be used to improve the predictions of the wave mass transport in breaking waves in chapter 3.

Conclusion

In this chapter, the different theoretical tools used in the rest of the thesis were presented. The description of waves was intentionally limited to the first order as it will be shown it already enables one to understand the main physical aspects of the wave pumping. The important parameter to be measured is the wave mass transport as it allows the exchange of mass between the surface layer and the interior of the flow to be predicted and thus the generation of current to be deduced as illustrated in the case of waves at a step. In

the coming chapter, the case of the resonance wave tank (RWT) is studied in detail. The eigenfunction expansion method along with the dissipation model and the wave breaking threshold are used.

Chapter 2

The Resonance Wave Tank

Dans ce chapitre, une première application du principe de transfert de masse entre la couche de surface et l'intérieur du fluide est présentée. Le système est appelé la pompe à résonance de vagues. Il s'inspire des pompes à impédance, ou pompes de Liebau qui les a mises en évidence. Un nouveau concept est présenté. Les pompes à impédance classiques font intervenir en général des tubes plastiques. Ici ils sont remplacés par une simple surface libre. Le système est étudié expérimentalement dans un premier temps. La théorie linéaire standard développée dans le chapitre précédent est ensuite utilisée et met en évidence le caractère de résonance du système. L'ajout de la dissipation au modèle permet en plus de prédire de façon robuste la direction de l'écoulement. Le rôle du transport de masse dans la couche de surface est mis en évidence à travers des expériences et des simulations 2D. La plupart des résultats de ce chapitre a été publiée dans [21]. On propose des pistes d'applications de ce cas à l'extraction d'énergie des vagues.

Abstract

In the previous chapter, it was outlined that waves can generate current through mass transfer between the *surface layer* and the *bulk* part of the flow (or interior). In this chapter, a first application of this principle to generate current is proposed. It is called the *Resonance Wave Pump* (RWP). The idea is similar and inspired by the well-known Impedance Pump, also called Liebau's pump in honour of Liebau [87] who was the first to illustrate the principle of pumping with this mechanism. A novel application of the Liebau's pump with no flexible tubings is presented here and studied experimentally in details for the first time. The proposed linear model with dissipation enables to capture all characteristics of the pump and predicts the pumping regimes qualitatively. Experimental measurements of the velocity field near the free surface along with simulations are used to validate the model. The role of wave mass transport in the pumping mechanism is outlined. Several points developed in this chapter led to the publication of [21].

2.1 Introduction: Resonance and pumping

To exploit the mass transport ability to generate currents, one needs to recognize that mass transport is a second order term and is therefore usually negligible. In order to make it predominant, it is possible to make use of the resonance property of waves. In a closed basin excited at natural or resonance frequencies the amplitude can become dramatically large even though the original excitation is small. The *impedance pump* is a particular kind of pump that is based on the resonance properties of waves [8] (see introduction). It is a promising technique for producing or amplifying a net flow for both macro- and micro-scale devices [70]. It does not require any special valves or impellers.

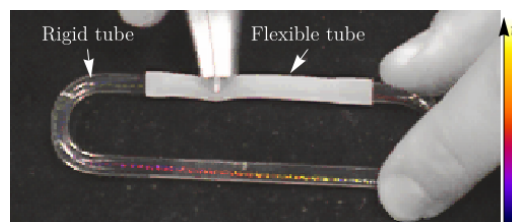


Figure 2.1: Original closed loop impedance pump. The white section corresponds to the flexible tube and is connected to a glass tube. An actuator excites the surface of the flexible tube (at 2 Hz here) and generates a unidirectional flow counter-clockwise here. The particles are colored with time (scale on the right). Picture adapted from a video of Hickerson and Gharib.

This valveless resonance pump is usually composed of a flexible tube connected at its two extremities to more rigid tubes (hereafter called rigid tubes) in a closed loop [14, 88, 112, 125, 140] (see figure 2.1) or open loop [87, 140, 158] (in the case of open loop pump the rigid

tubes are connected to reservoirs). The flexible tube is excited at an off-centered position by a pincher. Waves propagate on the flexible membrane and their complex reflection-transmission with the rigid tubes leads to pumping when the excitation is near natural frequencies¹.

Meier [112] suggested studying the case of a free-surface Liebau pump. He proposed possible applications for wave energy harvesting. The goal of this chapter is to study this novel kind of impedance pump with free-surface in details. First, the experimental setup is presented, then different relevant parameters are varied to see their influence on the pump ability to generate a current. The first sets of experimental results solely focus on the flow rate measurement under the submerged plate. Using the previous chapter theoretical results, a potential model is proposed and it is shown that pumping² occurs near resonance frequencies. Unfortunately, the linear theory leads to a standing wave solution and as pointed out in the previous chapter, the mass transport is zero for standing waves. Adding dissipation to the model enables to alleviate this issue and capture the direction of pumping through a simple two-parameters model. The model is then compared to both experiments and numerical simulations to have a qualitative and quantitative assessment of the role of mass transport in the pumping mechanism.

2.2 Experimental setup and measurement techniques

2.2.1 Setup and dimensions

The resonance wave pump along with notations is sketched in figure 2.2. The resonance wave tank is a simple rectangular tank with a rectangular-submerged plate spanning the width of the tank (out of plane direction), with a plunger wave maker. The tank as well as the submerged plate are made of plexiglass.

The tank length is $l_t = 77.4 \pm 0.1$ cm and its width is $l_w = 25 \pm 0.1$ cm (out of plane direction in figure 2.2). The total water depth, d_{tot} , denotes the vertical distance between the undisturbed water surface and the bottom of the tank.

The submerged plate is horizontal. Small rectangular holders fixed to the wall of the tank are used to support the plate and help with calibration and alignment. Their obstructions (less than 1.2 cm in width) are small when compared to the tank width, thus their effects on the flow are negligible. The calibration blocks used to set the opening lengths and heights were 3D printed using the MAKEiT Pro-M/L of the *TechLab* at *Caltech* (allowing a submillimetric accuracy). The depth of the submerged plate, d , represents the distance between the undisturbed surface and the upper part of the submerged plate. The sub-

¹They can also be called resonance frequencies. Sometimes they are wrongly-called resonant frequencies, which is improper as being resonant is not an attribute of a fixed frequency [73].

²Pumping means here the time-averaged (called also mean) flow rate being none zero.

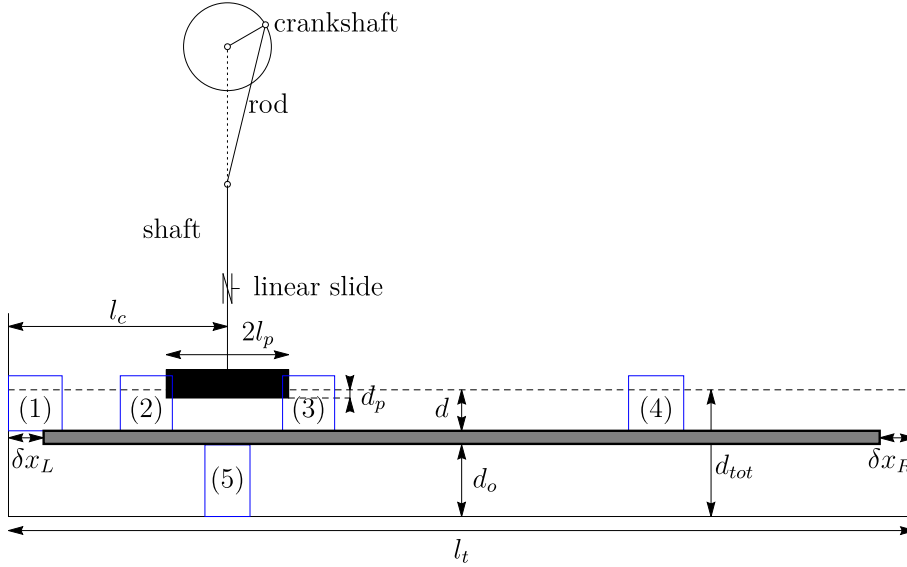


Figure 2.2: Resonance wave tank and main notations. The illustration presents the tank of length l_t , the submerged plate (shaded in gray) of thickness $t_{sp} = d_{tot} - d - d_o$, the plunger at its mean position (shaded in black), the motion controller and the position of the undisturbed water surface (dashed line). Important parameters are shown: the main depth for wave propagation (d), the openings length ($\delta x_{R/L}$), the plunger length ($2l_p$), the plunger mean draft (d_p), the plunger center location (l_c), and the opening height of water under the submerged plate (d_o). The blue rectangles numbers 1 to 5 show the sections where PIV measurements are performed.

merged plate length is fixed to $l_{sp} = 71.4 \pm 0.1$ cm. The bottom of the submerged plate leaves an opening height d_o under the submerged plate where the water can recirculate. To hold the submerged plate fixed under wave action, special semi-circular grooves were cut out on the sides of the submerged plate touching the lateral walls. Surgical rubber tubings fill the grooves and are emptied using a syringe when positioning the plate. Once the selected position is achieved the tubes are pressurised and stopcocks are used to maintain the pressure. In addition clamps are used to compress the lateral walls. Waterproof tape³ was carefully added on the sides of the submerged plate touching the tank walls to further ensure a leakproof connection.

To generate the waves at the free surface, a plunger type wave maker of length $2l_p$ and thickness t_p is used. It spans almost the full width of the tank. Similarly to the impedance pumps with flexible tubings, the plunger is off-centered. Its mean draft is d_p . The distance between the left wall of the tank and the center of the plunger is denoted l_c . To control the plunger motion, a simple stepper motor along with a crankshaft and rod are used. To avoid rotations two additional shafts are used and blocked in translations. This system transforms the rotational motion of the stepper motor into reciprocating translation. The

³Atomik waterproof hatch tape.

rod is about 10 times longer than the crankshaft. The length of the crankshaft directly controls the amplitude of the plunger motion. The deviation of the plunger from its mean position is denoted $s(t)$. The motor rotates at a constant rotational velocity. The transformed motion is a quasi-sinusoidal translation ($s(t) \approx s_0 \cos(2\pi f_0 t)$).

In the present study, the different plunger parameters: length, stroke amplitude, position and forcing frequencies are varied. The effects of modifying the water depth above the submerged plate as well as the height of the recirculation section are also quantified. The other parameters are kept constant and their values are justified in section 2.3.1.

2.2.2 Data acquisition

In all experiments, two cameras are used to capture the data simultaneously.

A first camera (Imperx IPX-2M30-L or Nano sense MKIII with a Tamron SP with a Vivitar 28-85 mm lens) is used to record the Particle Image Velocimetry (PIV) videos. The Nano sense MKIII has a large sensor and enables recording at a higher frame rate. It is primarily used for the PIV measurements near the free surface where the velocities will be large. The different regions where PIV measurements were performed are depicted in figure 2.2.

The water is seeded with silver-coated hollow ceramic spheres of typical diameter $100 \mu\text{m}$ and specific averaged density of 1.10 g/cc (Conduct-O-Fil AG-SL150-30-TRD). To keep only buoyant particles, the water used to fill the tank was seeded with particles about 24 hours prior to the experiment in separate buckets. Only water away from the surface and the bottom of the buckets was used to fill the tank. To illuminate the particles, a continuous 1W 532 nm green laser (Wicked Laser) and cylindrical lens are used to create a laser sheet. A green filter was aligned with the camera to avoid light pollution. The PIV data are analyzed using the open source code MATLAB PIVlab [154, 155]. The code enables sub-pixel accuracy.

The flow being an oscillatory flow, the velocity in some instance can get small. To improve the PIV measurement in the instance of low velocities, frame rate adaptation is implemented. This is made easily possible since in all the data acquisition made here a continuous laser and a constant frame rate is used. When a characteristic particle displacement in the PIV is less than a threshold value of pixel/frame (the threshold used here is 0.8 pixel/frame taking advantage of the sub-pixel accuracy) a frame is skipped up to a maximum predefined frame jump (here a maximum jump of 3 is used).

A second camera (Nikon 1 S1 or AW1 with lens 1 Nikkor 11-27.5 mm f/3.5-5.6) is used to record the entire resonance wave tank. The laser used for the PIV also illuminates the surface. For certain cases, in addition to the laser, a white projector was used with a red filter to illuminate the plunger and record its stroke. The green filter on the PIV camera limits the pollution induced on the PIV. The motion of the plunger was recorded. The

frame rate of the second camera is always set to 60 frame per second (fps). This camera is not used for quantitative measurement of the surface elevation but for a qualitative visualization of wave dynamics generated by the plunger.

The two cameras are not synchronized numerically.

2.3 Flow rate under the submerged plate and resonance characteristics

2.3.1 Reference configuration

In this section, the total water and submerged plate depth are held fixed to $d_{tot} = 10.82 \pm 0.05$ cm and $d = 3.5 \pm 0.05$ cm. In this first test, the ratio of the water depth above the submerged plate and the tank length, $d/l_t \approx 4.5$ %, is comparable to the ratio of the inner radius to tube length in impedance pump studies [8, 112, 140]. The free surface plays the role of the flexible membrane here. The waves are gravity waves⁴ while in the case of impedance pumps of the classic type, the restoring force is the elastic force of the flexible tube. The opening height under the submerged plate is $d_o = 6.2 \pm 0.1$ cm. The section under the submerged plate is equivalent to the rigid tubes. The connection between the two sections is made through two openings at the tank extremities.

The submerged plate is centered and horizontal: $\delta x_R = \delta x_L = 3.0 \pm 0.1$ cm. The openings length $\delta x_{R/L}$ are rather unique to the present free-surface pump. For the classic pump, the connection between the flexible tube and the rigid tube is made through a no-surface-displacement boundary condition. This is not possible for the free surface pump. The wall at the two extremities have a no-through condition. This leads to a different behavior of waves when reflecting. On a no-displacement condition the reflection of a crest leads to a trough while for a no-through the crest stays a crest. In this chapter, the case of small openings is considered $\delta x_{R/L}/\lambda \approx 0.02 - 0.1$. The limit $\delta x_{R/L}/\lambda \rightarrow \infty$ will lead to the study of waves above a submerged plate in open ocean [61, 63, 120, 134, 162] and is the subject of the next chapter.

For now the plunger length is $2l_p = 10.5 \pm 0.05$ cm and $t_p = 2.54 \pm 0.1$ cm and is held fixed at $l_c = 18.7 \pm 0.1$ cm. Note that the center of the plunger (playing the role of the “pincher”) is such that $l_c/l_t \approx 25\%$, which is similar to previous study of impedance pumps of the Liebau type with flexible tubings [8, 112, 140]. The mean draft of the plunger is chosen such that the plunger is at the free-surface in its upper position for the stroke amplitude $s_0 = 0.69 \pm 0.05$ cm (reference stroke here). Its thickness is selected such that the plunger is not completely immersed for the largest amplitude $s_0 = 1.16$ cm. For now, only the

⁴ With the present water depth and range of frequencies, the Bond number is about $Bo \approx 300 - 3000$ and thus the surface tension can be neglected in first approximation.

frequency is varied between 0.3 and 1.8 Hz.

Referring to the previous chapter, the wave phase velocity is:

$$c = \frac{\omega_0}{k(\omega_0)}, \quad (2.3.1)$$

where $\omega_0 = 2\pi f_0$ is the angular frequency and k the wave number verifying the dispersion relation:

$$\omega_0^2 = gk \tanh(kd). \quad (2.3.2)$$

Solving for the frequency range of the experiment, the wave speed is between 0.54 and 0.59 m/s. A wave travels through the entire tank in about 1.4 s (or a frequency of 0.7 Hz). The frequency range thus encompasses the natural resonance frequencies of the tank. The lower band of 0.3 Hz is chosen to avoid seeing parasitic stepper motor motion and also to have a large enough flow to be measured. The upper band is bounded by 3D effects (lateral sloshing). The width of the tank l_w gives the expected first symmetric transversal resonance frequency:

$$f_1 = \sqrt{\frac{g}{2\pi l_w} \tanh \frac{2\pi d}{l_w}} \approx 2 \text{ Hz} \quad (2.3.3)$$

above the submerged plate.

In the coming paragraph, the flow rate is measured under the plate near region (5) (see figure 2.2) for different frequencies.

2.3.1.1 Instantaneous flow rate measurements

In this section, four frequencies are considered $f_0 = \{0.6, 1.00, 1.20, 1.60\}$ Hz (see experiment A in table L.2). The data are obtained using the Imperx IPX-2M30-L camera. The image resolution is 680×325 and the data are recorded at 60 fps for 90 seconds. To improve the measurements when the velocity is small, the code used is allowed to skip up to three frames (thus reducing the frame rate down to ≈ 20 fps). This is performed when the displacement vector is less than 0.8 pixel/frame.

PIV measurements enable to have access to the instantaneous velocity field, $\mathbf{u}(x_i, z_j)$, where x_i and z_j are the position of the PIV grid centers. The PIV velocities are then integrated using the trapezoidal rule to define an instantaneous flow rate per unit width at each horizontal velocity profiles:

$$\phi_i = \int_0^{d_o} u(x_i, z) dz, \quad (2.3.4)$$

where zero denotes the bottom of the tank and d_o the opening height. Data points are missing at the walls. A no-slip velocity is assumed at each walls. The different flow rates, ϕ_i , are averaged to reduce the errors due to the PIV method and 3D effects. The result is

denoted $\phi(t)$. The error can be estimated and is detailed in appendix L. The flow rate is considered positive if the flow is going from left to right under the submerged plate (see figure 2.2 for convention).

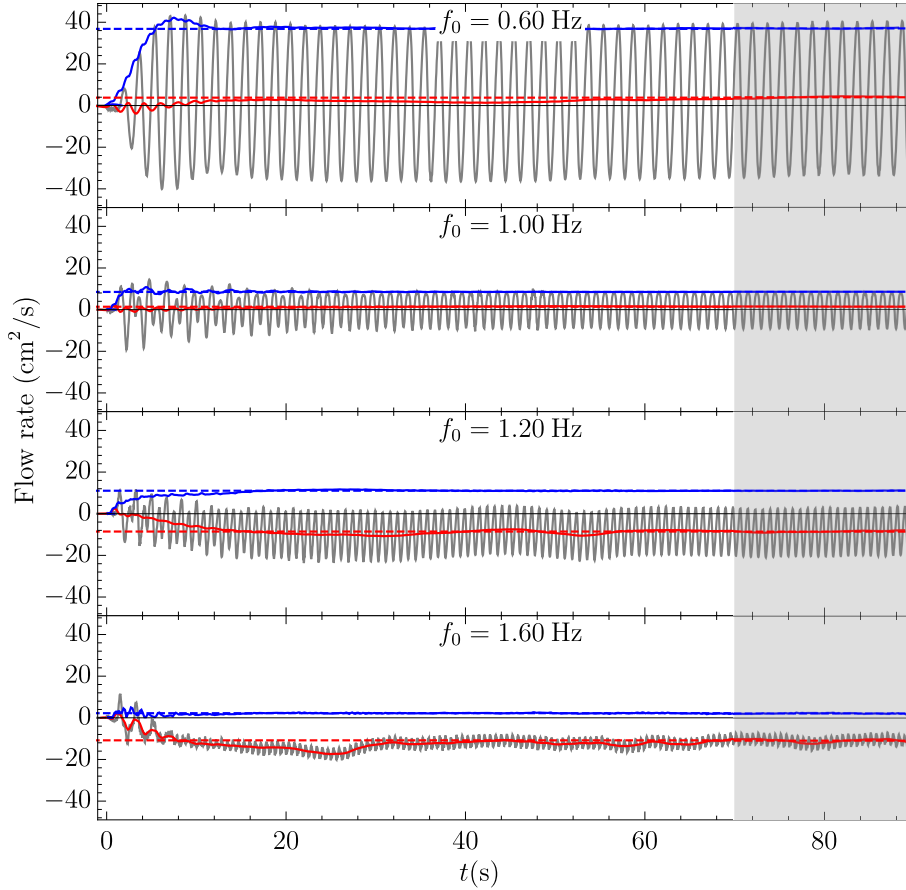


Figure 2.3: Transient response for different forcing frequencies for $2l_p = 10.5 \pm 0.05$ cm, a fixed stroke amplitude $s_0 = 0.69$ cm and fixed plunger position $l_c = 18.7 \pm 0.1$ cm. The gray solid lines show the instantaneous flow rate measured from the PIV data assuming no-slip conditions at the walls, the red (blue) solid line is the instantaneous mean (first harmonic) flow rate as defined by eq.2.3.6 (eq.2.3.5, respectively). The dashed lines represent the mean value of the mean and first harmonic flow rate in the last 20 seconds. The asymptotic mean flow rates are 3.53 ± 0.5 , 1.40 ± 0.4 , -8.6 ± 0.5 and -10.8 ± 0.7 $\text{cm}^2 \cdot \text{s}^{-1}$ for $f_0 = 0.60$, 1.00, 1.20 and 1.60 Hz, respectively.

The instantaneous first harmonic flow rate⁵ is defined as:

$$\phi_1 = \frac{1}{T} \left| \int_{t-T}^{t+T} e^{i\omega_0 t} \phi(t) dt \right|, \quad (2.3.5)$$

⁵ Note that there is no factor of $2T$ here as the amplitude is calculated for the two harmonics $\pm i\omega_0$.

where $\omega_0 = 2\pi f_0$, and the mean flow rate is defined as:

$$\bar{\phi}(t) = \frac{1}{2T} \int_{t-T}^{t+T} \phi(t) dt. \quad (2.3.6)$$

Both are displayed in figure 2.3 as the solid blue and red lines, respectively. The integrals are once more approximated using the trapezoidal rule. Two wave periods are used in both definitions. No noticeable variations are observed when varying the number of periods from 1 to 4.

Here, the experiments start with a tank at quasi-rest. The plunger starts and leads to oscillations under the submerged plate. In all cases after a transient regime, the instantaneous flow rate reaches a periodic regime, hereafter called asymptotic regime. At a frequency $f_0 = 0.60$ Hz, the pump behaves like an underdamped oscillator as it can be seen by the overshoot of the first harmonic flow rate compared to its asymptotic value. The oscillations are relatively large compared to the other selected frequencies. There is a slightly positive mean flow rate that is achieved at the end. At a frequency $f_0 = 1.00$ Hz, the oscillations are much smaller. A weak mean flow rate in the positive direction can be identified. For $f_0 = 1.20$ Hz, the pump has an interesting behavior similar to the one of efficient frequencies of Liebau impedance pump. The flow rate reaches an asymptotic pulse flow regime after 20 s. In this regime, the flow rate oscillates between zero and a negative value with a significant bulk component of about $-10 \text{ cm}^2 \cdot \text{s}^{-1}$. Note here that the mean and first harmonic flow rates reach an asymptotic regime near the same time but the slope of the first harmonic is steeper than the mean one. This seems to suggest that the mean flow is a consequence of the oscillations. At a frequency $f_0 = 1.60$ Hz, the flow becomes unidirectional with small oscillations compared to the mean component: it is rectified. Oscillations at lower frequency can be observed on the mean component. The time required to reach an asymptotic regime depends mostly on the frequency. From experimental observations, one needs to wait about 20 wave periods before reaching the asymptotic regime for the mean flow.

To check that the initial conditions do not affect the asymptotic regime, a test was performed with a disturbed tank and the frequency of the plunger was switched to a first frequency where a positive mean flow rate was expected ($f_0 = 1.00$ Hz) and then to one where the mean flow rate is expected to be negative ($f_0 = 1.60$ Hz). The results are displayed in figure 2.3 and compared to the measurement found when starting from a tank at rest. This suggests that the regimes observed are independent of initial conditions.

From now on, the transient regime is not considered anymore and the flow rates are measured directly in the asymptotic regime. In all cases the data are taken after the plunger has been running for at least a minute and sample for 20 seconds.

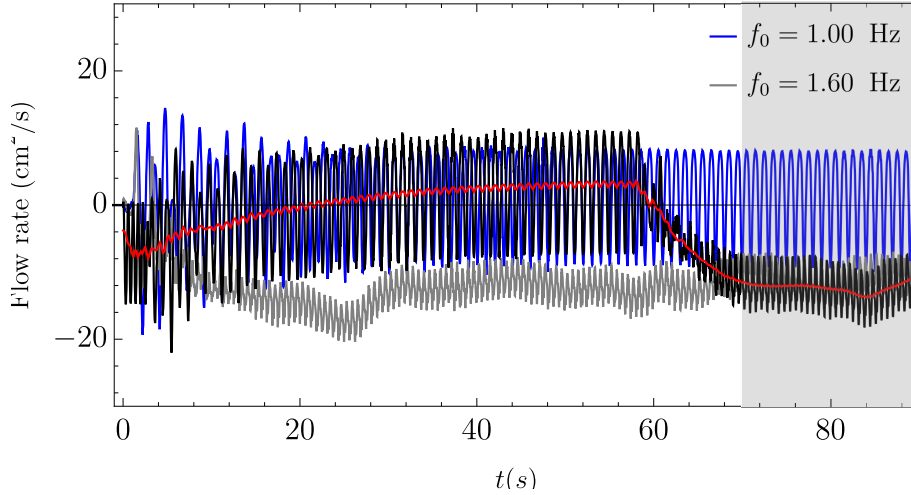


Figure 2.4: Influence of initial conditions on the RWT for $2l_p = 10.5 \pm 0.05$ cm, a fixed stroke amplitude $s_0 = 0.69$ cm and fixed plunger position $l_c = 18.7 \pm 0.1$ cm. The black curve shows the disturbed case, the gray and blue curves the undisturbed cases with constant forcing frequency. The red curve is the filtered curve of the instantaneous flow rate of the disturbed experiment. For the disturbed case, the tank is first randomly agitated then the plunger is forced to oscillate at a frequency $f_0 = 1.00$ Hz. After a minute the frequency of the plunger is switched to $f_0 = 1.60$ Hz.

2.3.1.2 Frequency signature of the flow rate

To see the frequency signature of the flow, Fast Fourier Transform (FFT) analysis is applied to instantaneous flow rate samples during the last 20 seconds of the previous set of data. The sample time size is fixed to capture the low frequency oscillations at the highest frequencies and such that the resolution of the FFT is $df = 0.05$ Hz. The results are displayed in figure 2.5. A peak is clearly visible at each forcing frequency harmonics $n \times f_0$ where $n = 0, 1, 2, \dots$. In addition, the asymptotic mean and first harmonic flow rate averaged during the last 20 seconds (named hereafter $\phi^{(0)}$ and $\phi^{(1)}$) are displayed with their uncertainties in gray circles.

From now on, it is thus assumed that the flow rate under the submerged plate can be decomposed such that:

$$\phi \underset{t \rightarrow \infty}{\equiv} \phi^{(0)} + \phi^{(1)} \cos(\omega_0 t + \theta^{(1)}) + \phi^{(2)} \cos(2\omega_0 t + \theta^{(2)}) + \dots, \quad (2.3.7)$$

where the superscripts (i) refers to the order of the harmonics decomposition⁶.

Figure 2.6 shows the flow rate in the asymptotic regime plotted on a single period. The initial phase is chosen such that the flow rate is maximum at the origin of time. It is

⁶Notation can also be compared to the expansion decomposition of chapter 1, and the (0) will be shown to be quite close to the (2, 0) terms.

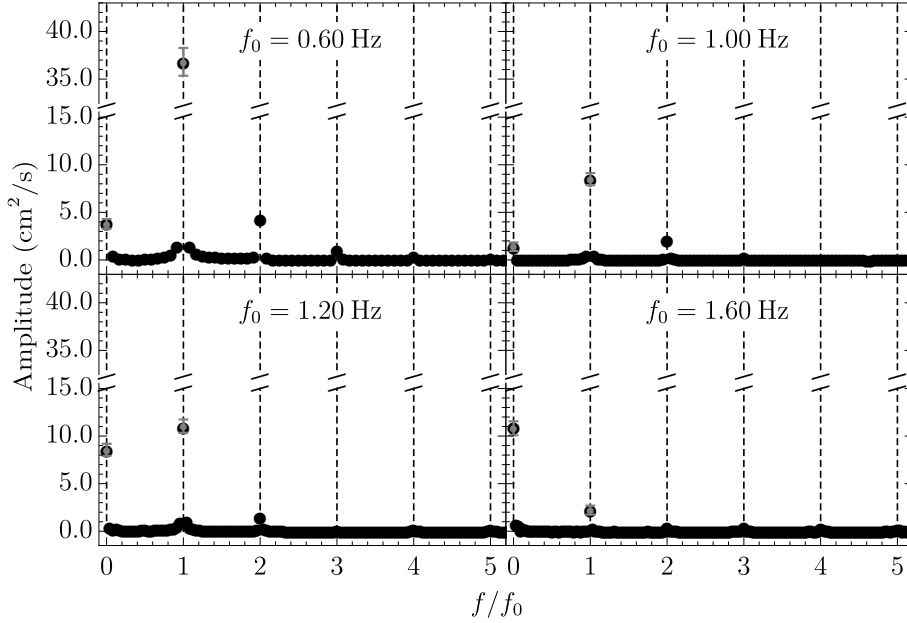


Figure 2.5: Frequency response for four frequencies with $2l_p = 10.5 \pm 0.05$ cm, a fixed stroke amplitude $s_0 = 0.69$ cm and fixed plunger position $l_c = 18.7 \pm 0.1$ cm. The results are obtained by performing a FFT of the flow rate during the last 20 seconds for the different frequencies f_0 (0.60, 1.00, 1.20 and 1.60 Hz respectively). The dashed lines show the different harmonics nf_0 where $n = 0, 1, 2, \dots$. The gray points are obtained by averaging the instantaneous mean and first harmonic flow rate during the last 20 seconds. The calculation of the error bars is detailed in appendix L.

readily seen that in all cases the development up to the second harmonic is sufficient to capture the flow rate dynamics. For all cases, the amplitude of the second order harmonic is no more than 24% of the amplitude of the first harmonic. The maximum is found for the frequency $f_0 = 1.00$ Hz. At this frequency, the second order and the first order are almost in opposition of phase, leading to sharper trough and flatter crest. Near this frequency second order effects are noticeable. For the case $f_0 = 1.20$ Hz, the ratio of the amplitude of the second order harmonic over the first one is about 13%.

2.3.1.3 Velocity profiles under the submerged plate

In this section, the velocity profiles under the submerged plate in the asymptotic regimes are evaluated. Note that the PIV window covers a length of about 15 cm under the submerged plate in the current experiment (called experiment A in table L.2). The instantaneous velocity profiles are averaged along the horizontal direction. The mean velocity profiles are then evaluated by time averaging all vertical components. The first harmonic velocity profile is evaluated similarly to $\phi^{(1)}$. The different profiles are displayed in figure 2.7. The first harmonic velocity profiles appear to be rather constant along the vertical

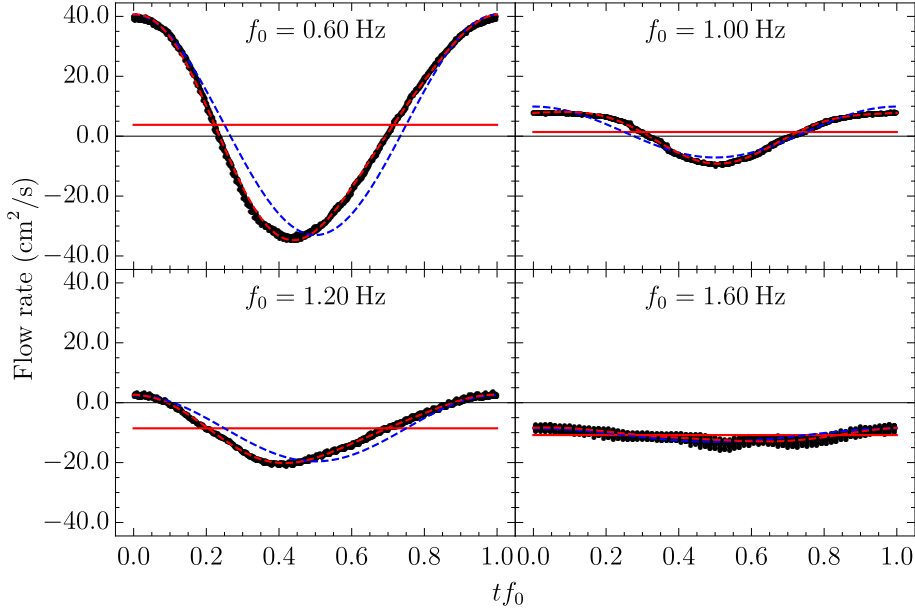


Figure 2.6: Periodic flow rate for four frequencies with $2l_p = 10.5 \pm 0.05$ cm, a fixed stroke amplitude $s_0 = 0.69$ cm and fixed plunger position $l_c = 18.7 \pm 0.1$ cm. The figures show the flow rate plotted in the shaded gray time window of figure 2.3 collapsed on a single period. The red solid line shows the mean flow rate, the blue (red) dashed line is the development of eq.2.3.7 up to the first (second) harmonic.

direction. Slip boundary conditions are thus acceptable to describe the oscillatory part of the flow. This will be done in section 2.4 in the linear potential model.

2.3.1.4 Flow rate frequency response

In the previous section, the flow rate was analyzed for four distinct frequencies and it appears that the flow behaves drastically differently from one frequency to another. This outlines the non-linear response of the system. In this section the forcing frequency response is measured experimentally. The mean, first and second harmonic asymptotic flow rates $\phi^{(0)}$, $\phi^{(1)}$ and $\phi^{(2)}$ are evaluated for three independent experiments⁷. Figure 2.8 shows the frequency response averaged on the three set of data (see appendix L for the three sets separately). It is observed that the mean, second and first harmonic flow rate vary significantly with the forcing frequency. The mean flow rate is stronger near abrupt changes in the first harmonic, near what appears to be resonances. These results are quite similar to the observations made in previous works done with micro-scale impedance pumps [8, 70, 112]. It is interesting even with a drastically different scale and the absence of compliant tubes; the resonance mechanism still provides a pumping action. The second

⁷An independent experiment means here that the tank was fully emptied, the submerged plate removed and resettled between each experiments. This shows the biased on the experiment configuration.

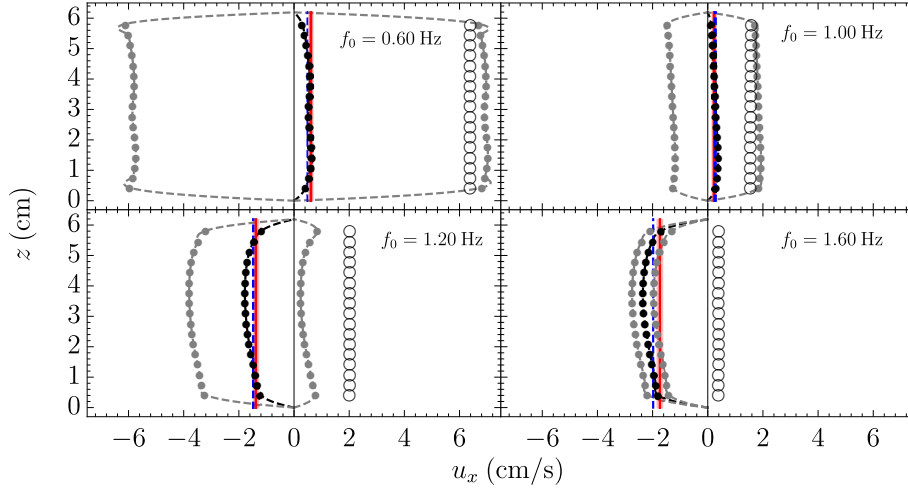


Figure 2.7: Mean and first harmonic velocity profiles for four frequencies with $2l_p = 10.5 \pm 0.05$ cm, a fixed stroke amplitude $s_0 = 0.69$ cm and fixed plunger position $l_c = 18.7 \pm 0.1$ cm. The black solid circles are obtained by time averaging the velocity at each cells and averaging horizontally. The opened circles are obtained by evaluating the amplitude of the first harmonic. These profiles are roughly linear. The gray filled circles are the mean velocity plus/minus the first harmonic. The dashed lines are interpolation of the data with no slip conditions at the wall. The vertical red line and the shade around it shows the mean velocity with the uncertainties.

harmonic amplitude does not appear to play a significant role.

Five regions can be identified where pumping is significant. The first one is near the frequency $f_0 = 0.60$ Hz. The mean velocity is positive, but the oscillations are large. The second region is near $f_0 = 0.70$ Hz. This region does not have a significant mean flow rate but it can be clearly identified. The mean flow rate is negative and oscillations are less important. Note that when looking at the amplitude of oscillations, one can not clearly identify a resonance near this frequency. It will be shown however that this is indeed a resonance frequency by the mean of the linear theory. In the range $f_0 = 1.00 - 1.15$ Hz, there is a region where the mean flow is positive and the oscillations are 2 to 3 times larger. The next region is near the frequency $f_0 = 1.20$ Hz. In that part the flow is a pulse flow. The region is wider than the previous one. From there the mean flow is always negative. The last region starts near $f_0 = 1.60$ Hz. The oscillations are highly damped now and the flow is fully rectified, which amounts to saying that the pump transforms a pulsating excitation (the plunger motion) into a continuous flow.

To better understand the pumping mechanism, the second camera is now used to look qualitatively at the surface envelope.

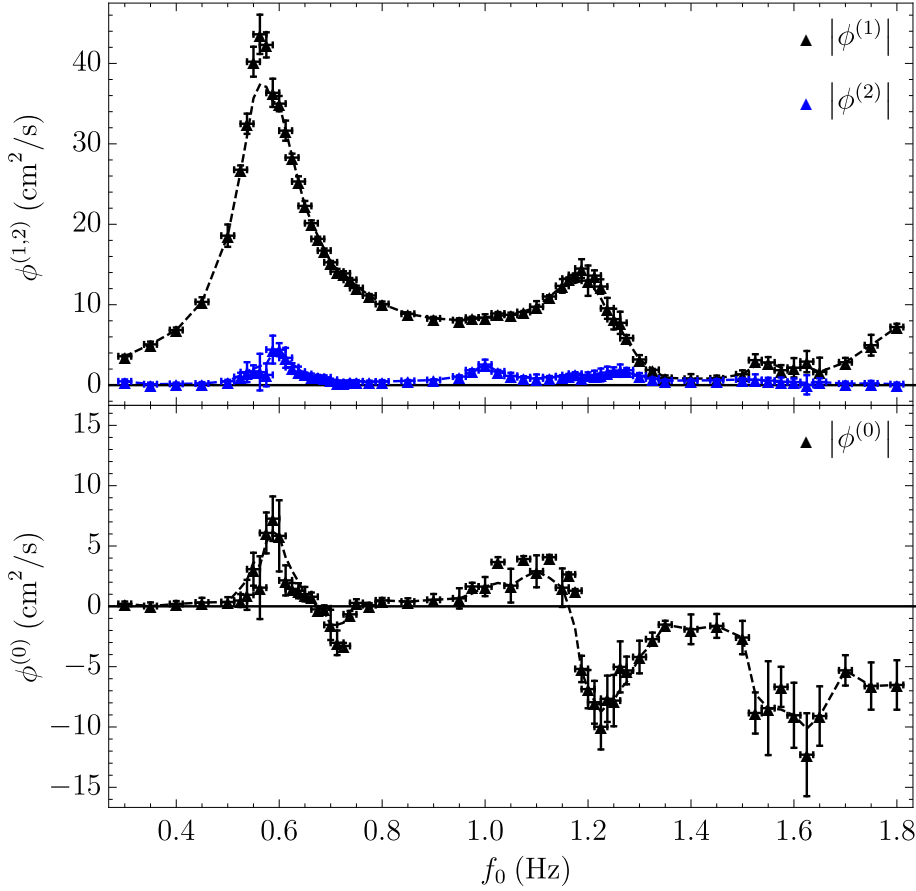


Figure 2.8: Mean, first and second harmonic flow rate as a function of frequency with $2l_p = 10.5 \pm 0.05$ cm, a fixed stroke amplitude $s_0 = 0.69$ cm and fixed plunger position $l_c = 18.7 \pm 0.1$ cm. The points show the average of three independent experiments. The black dashed line is the mean of the three experiments linear interpolation functions. The experiment is reproducible (see figure L.2 to see the three experiments separately).

2.3.1.5 Mean flow rate and surface envelopes

In this section, six representative forcing frequencies are used: one near the five interesting regions of pumping and one near $f_0 = 0.80$ Hz, where the pumping is not significant. The Nikon camera is used to visualize the surface envelope. The results are obtained by taking the standard deviations of the picture frames on 5 wave periods. The results are displayed in figure 2.9. The surface envelope outlines wave features such as nodes and antinodes. The vertical dashed lines in the figure show the theoretical position of the nodes and antinodes found by solving a linear potential equivalent problem (see section 2.4). In this paragraph, when the mean flow is negative (positive) under the submerged plate, the mean flow is said to circulate clockwise (counter-clockwise, respectively).

For $f_0 = 0.60$ Hz, the surface envelope is wider on the left side of the plunger than on the

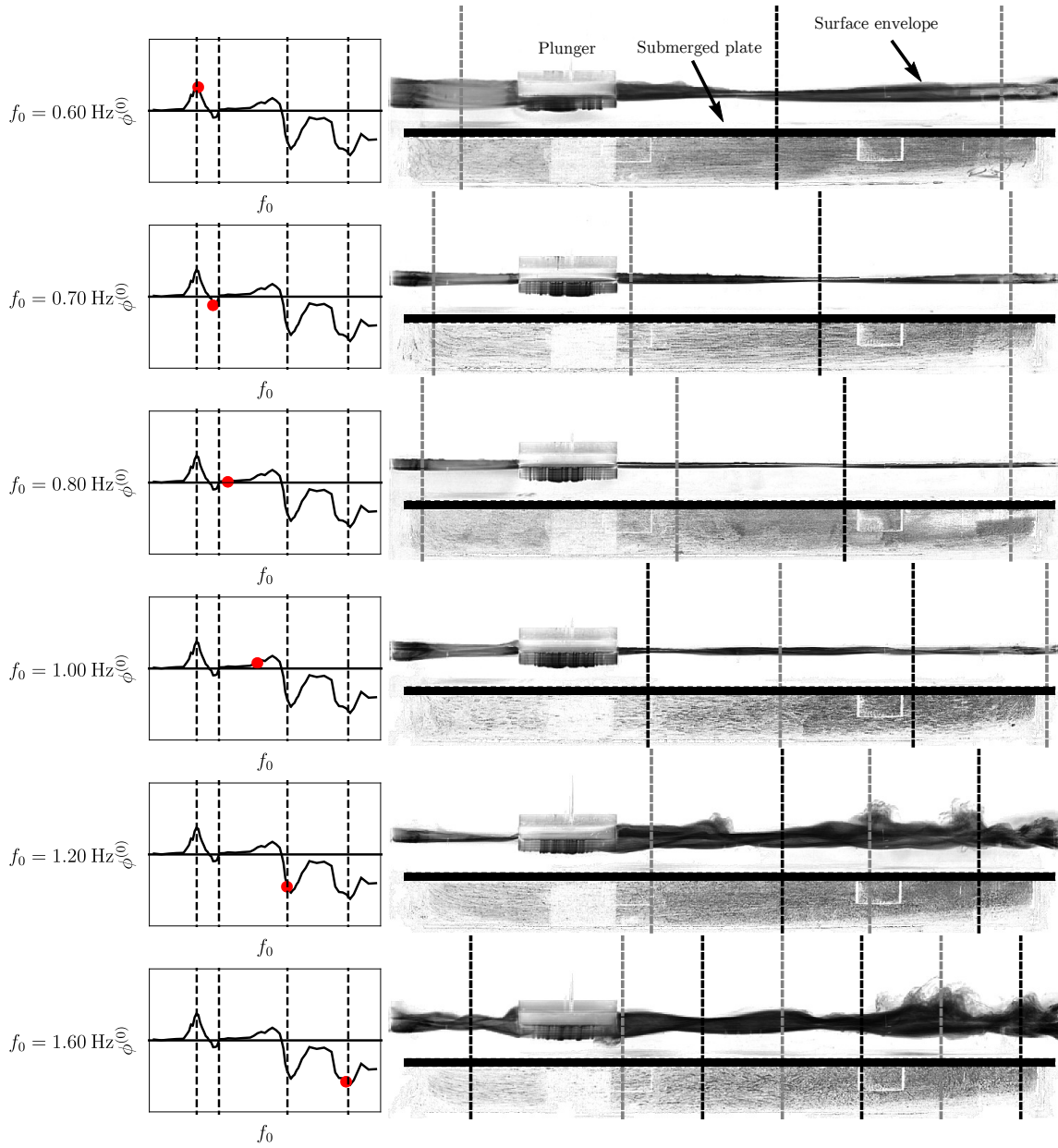


Figure 2.9: Surface envelope for different frequencies with $2l_p = 10.5 \pm 0.05$ cm, a fixed stroke amplitude $s_0 = 0.69$ cm and fixed plunger position $l_c = 18.7 \pm 0.1$ cm. Six characteristic free-surface envelopes are shown. The graph on the left shows the mean flow rate and the red point the corresponding value for the frequency of this row. A negative value means that the mean flow circulates clockwise (toward the left under the submerged plate). On the right, the picture is obtained by taking the standard deviation of 5 wave periods sampled at 60 fps. The result is the envelope of the surface elevation. Under the submerged plate, PIV particles are visible and some streamlines can be observed. The gray (black) dashed lines give the position of the antinodes (nodes) found by solving the linearized problem of section 2.4.1.

right side. From the set-down eq.1.4.8, this means that one should expect a lower mean water surface on the left side than on the right side of the plunger. Consequently a suction is expected to compensate the difference of water level between both sides of the plunger. A flow is thus going from the right side toward the left side above the submerged plate creating a counter-clockwise circulation (or positive flow rate under the submerged plate). As can be seen, the wave features (nodes and anti-nodes) are shifted to the left due to the mean flow in that direction above the submerged plate.

For f_0 between 0.70 and 1.00 Hz, the surface is rather placid. The amplitudes are once more noticeably larger on the left side of the plunger for $f_0 = 1.00$ Hz. Therefore as expected a counterclockwise circulation is measured. For $f_0 = 0.70$ Hz, the surface amplitudes on both sides are close to each other. For this case, almost an entire wavelength fits on the left side. Therefore the tank is close to the first wave resonance on this side. For $f_0 = 0.80$ Hz the surface envelope is almost completely flat on the right side of the plunger and the amplitude is a bit larger on the left thus the small positive mean flow rate can be justified with a similar argument.

For $f_0 = 1.20$ and 1.60 Hz, the surface envelope shows breaking and travelling waves features on the right side of the plunger and two and three wavelength fits on that side, respectively. For $f_0 = 1.20$ Hz, the first breaking wave feature appears between the position of the first antinode and node of the linear wave theory. The wave breaks toward the right, suggesting that the mass transported in the surface layer is in this direction.

For $f_0 = 1.20$ and 1.60 Hz, there are two other wave breaking points near the right hand wall aligned with a linear-predicted antinode and node. The latter can be interpreted as a second order response. Strong non-linear effects are expected for these cases. These “turbulent” sections suggest that the mean pressure should be lower near the right wall. Therefore suction can be expected toward this region. Gravity limits suction from under the submerged plate and therefore the circulation induced is also clockwise.

The surface envelope figures outline the importance of the wave dynamics. It is clear that the pulse flow regime and rectified regime near $f_0 = 1.20$ and 1.60 Hz are linked to the wave breaking. Other parameters are varied before discussing a model to better understand the physics.

2.3.2 Effects of other parameters on the flow rate

In this section other experimental parameters are now varied separately. First the effect of varying the stroke amplitude on the mean and first harmonic flow rate is discussed. It appears that the oscillations have a relative linear response with stroke amplitude. This comforts the linear description of the next section. It also appears that the mean flow rate evolves close to quadratically with the forcing frequency up to saturation point, then

linearly. Secondly, the plunger length is varied for two strokes amplitude. It appears that it is possible to achieve a mean flow rate close to optimal, which amounts to saying that the mean flow rate is almost equal to the fluid displaced by the plunger at each stroke⁸. Thirdly, the water depth is varied. It seems that the pump works better when the water depth is relatively small. Lastly, the opening width is varied and affects the first resonance. The position of the plunger is discussed in section 2.4.1.

2.3.2.1 Stroke amplitude

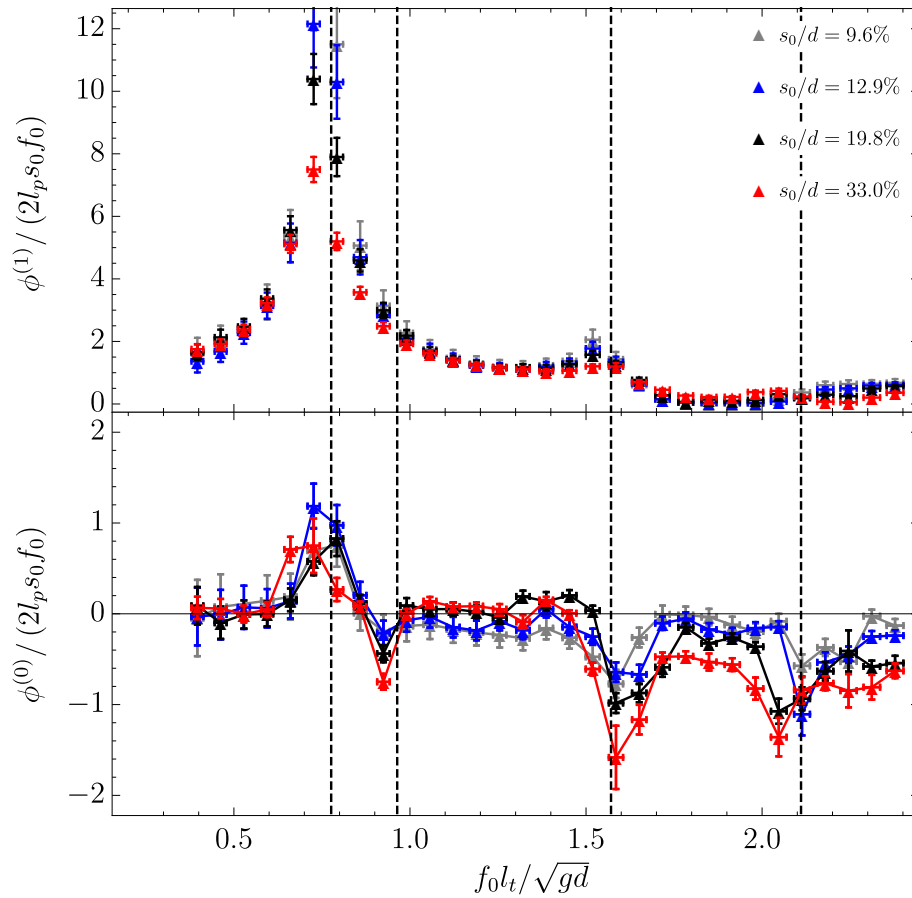


Figure 2.10: Non-dimensional first harmonic and mean flow rate for different strokes amplitude with $2l_p = 10.5 \pm 0.05$ cm and fixed plunger position $l_c = 18.7 \pm 0.1$ cm. For the first harmonic flow rate (top figure) there are small variations observed while varying the stroke amplitude: it appears more damped near the resonance frequencies. For the mean flow rate, increasing the amplitude results in higher non-dimensional flow rates (thus efficiency) near the resonance frequencies. The vertical dashed lines show the resonance frequencies found using the linear theory of section 2.4.1.

⁸This corresponds to the efficiency of the peristaltic pump. Recall here the flow rate is evaluated with no-slip at the walls.

The configuration is similar to the one previously described (see table L.2 for more details on the configuration which corresponds to experiment B). The stroke amplitude is varied. The results correspond to a single set of experiments recorded for 20 seconds in the asymptotic regime. The data are taken all the same day to avoid bias from the plunger position, water depth and opening heights. The flow rate is also non-dimensionalized by half the rate of volume displaced by the plunger (volume times the frequency) as suggested by Thomann [156] and Hickerson and Gharib [70] and done in Avrahami's computational work [8]. The frequency is non-dimensionalized by multiplying it by the ratio of the tank length over the shallow water wave speed. The latter corresponds to the time a wave takes to approximatively travel an entire tank length.

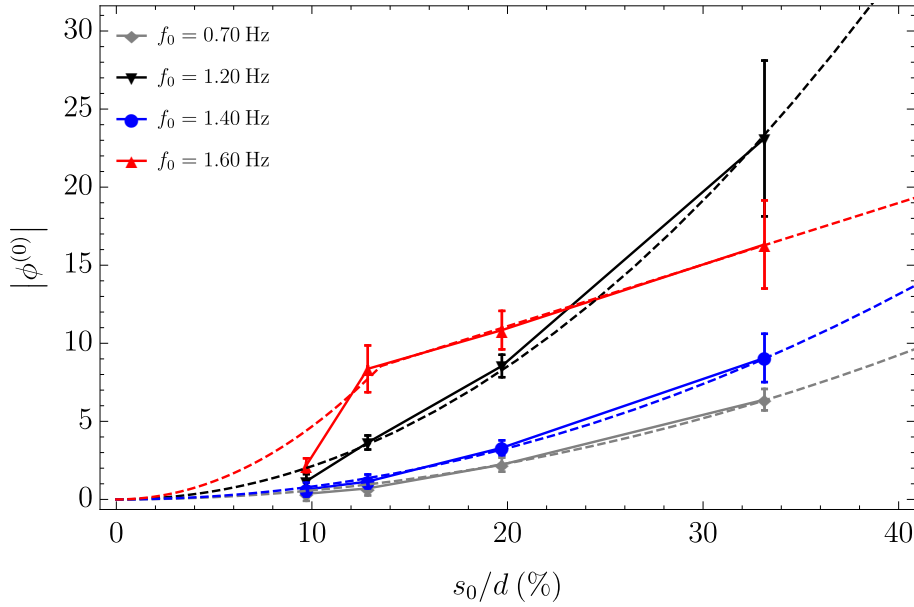


Figure 2.11: Absolute mean flow rate as a function of the stroke amplitude for different forcing frequencies with $2l_p = 10.5 \pm 0.05$ cm and fixed plunger position $l_c = 18.7 \pm 0.1$ cm. For most cases, the mean flow rate is proportional to the square of the stroke amplitude $|\phi^{(0)}| \propto s_0^2$. For the frequency $f_0 = 1.60$ Hz, the mean flow rate first increases quasi-quadratically with the stroke amplitude then slows down to quasi-linearly with the stroke amplitude.

The measured non-dimensionalized mean and first harmonic flow rate are shown in figure 2.10. The first harmonic is relatively well collapsed showing that the response is close to linear with the stroke amplitude. One can notice that the first harmonic is more damped as the wave amplitude increases in particular near the resonance frequency 1.20 Hz (or non-dimensional frequency 1.59). The mean flow rate curves do not collapse. Increasing the stroke amplitude leads in most cases to an increases of the non-dimensional mean flow rate, thus suggesting faster than first order response to the stroke amplitude. One can notice that the frequency range where pumping is important also increases with the stroke amplitude near the resonances (outlined by the vertical dashed lines). To better

understand the effect of the stroke on the mean flow rate, figure 2.11 shows the absolute mean flow rate as a function of the stroke amplitude for four frequencies.

For the case $f_0 = 0.70$ Hz, the mean flow rate increases quasi-quadratically with the stroke amplitude. For the case $f_0 = 1.20$ Hz, there is a similar trend if the first data point is ignored. For the case $f_0 = 1.40$ Hz, the mean flow rate is almost zero for the smallest amplitude (this frequency is in between two resonance frequencies) and when the stroke amplitude increases, it suddenly starts to increase quadratically with the stroke amplitude. For the last frequency ($f_0 = 1.60$ Hz), the flow rate does not follow the general trend. The flow rate continues to increase with the stroke amplitude but at a slower rate (almost linearly).

2.3.2.2 Plunger length

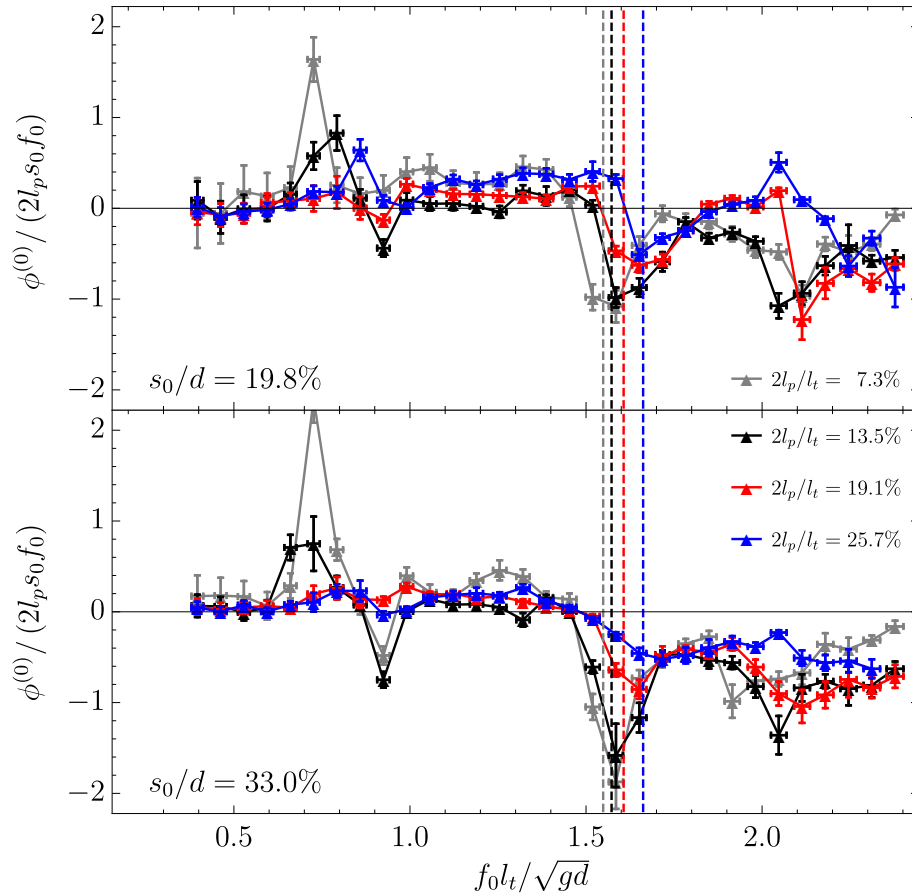


Figure 2.12: Non-dimensional mean flow rate for different plunger lengths and two strokes amplitude with fixed plunger position $l_c = 18.7 \pm 0.1$ cm. The peak value near the non-dimensional frequency 1.6 is near the optimal of 2 and the amplitude of oscillation is about 1.4 for the case $2l_p/l_t = 7.3\%$. The vertical dashed lines show the resonance frequencies found using the linear theory of section 2.4.1 equivalent to the case $f_0 = 1.20$ Hz of the reference experiment.

The plunger length is now varied while its center position is kept fixed ($l_c = 18.7 \pm 0.1$ cm, see experiment C in table L.3). Similarly to the previous section the data are non-dimensionalized. The results are shown in figure 2.12 for two strokes amplitude. The larger plunger covers more than a quarter of the tank length while the shortest one represents about 7% of its length.

For all the cases, increasing the amplitude increases the efficiency measured here as the non-dimensional mean flow rate. For the largest plunger, this effect is a bit diminished as one can expect saturation to be reached faster (as observed for the frequency $f_0 = 1.60$ Hz in the previous section). As one can expect, the resonance frequencies increase with the plunger length. This is because the free-surface length is reduced and higher frequencies are therefore needed to obtain similar wave patterns. It is also noticeable that the smallest plunger yields the highest non-dimensional mean flow rate. The peak value near the non-dimensional frequency 1.6 is near the optimal of 2 and the amplitude of oscillation is about 1.4. This means that for this experimental case, the mean flow rate is almost equivalent to transporting the same volume as the one displaced by the plunger for each stroke.

2.3.2.3 Water depth

The water depth above the submerged plate is now varied with fixed d_o (see experiment D in table L.3). The results are displayed in figure 2.13. The amplitude of oscillations are more important as the water depth is reduced. The curves do not collapse due to the non-linearity of the dispersion relation. For the mean flow rate, the pump works better when the water depth is less important. For the deepest case, the pumping regions are barely noticeable.

2.3.2.4 Recirculation section height

The opening height is now varied keeping the water depth above the submerged plate constant (see experiment E in table L.3). The results are shown in figure 2.14. The effect on the mean flow rate is not so important, while the amplitude of oscillations increases as the opening height increases in the range of non-dimensional frequency above 0.8. The dependance is close to linear suggesting that the first harmonic is proportional to the opening heights in this range. The first resonance before this range appears to have shifted: the resonance frequency increases with the opening height. This resonance is similar to a U-tube oscillator or simple harmonic oscillator. Indeed, consider the non-constant width U-tube oscillator sketched in figure 2.15. Applying the conservation of energy, one can estimate the simple harmonic oscillation angular frequency to be

$$\omega_0 \approx \sqrt{\frac{2g}{2l_a + a l_t / d_o}}, \quad (2.3.8)$$

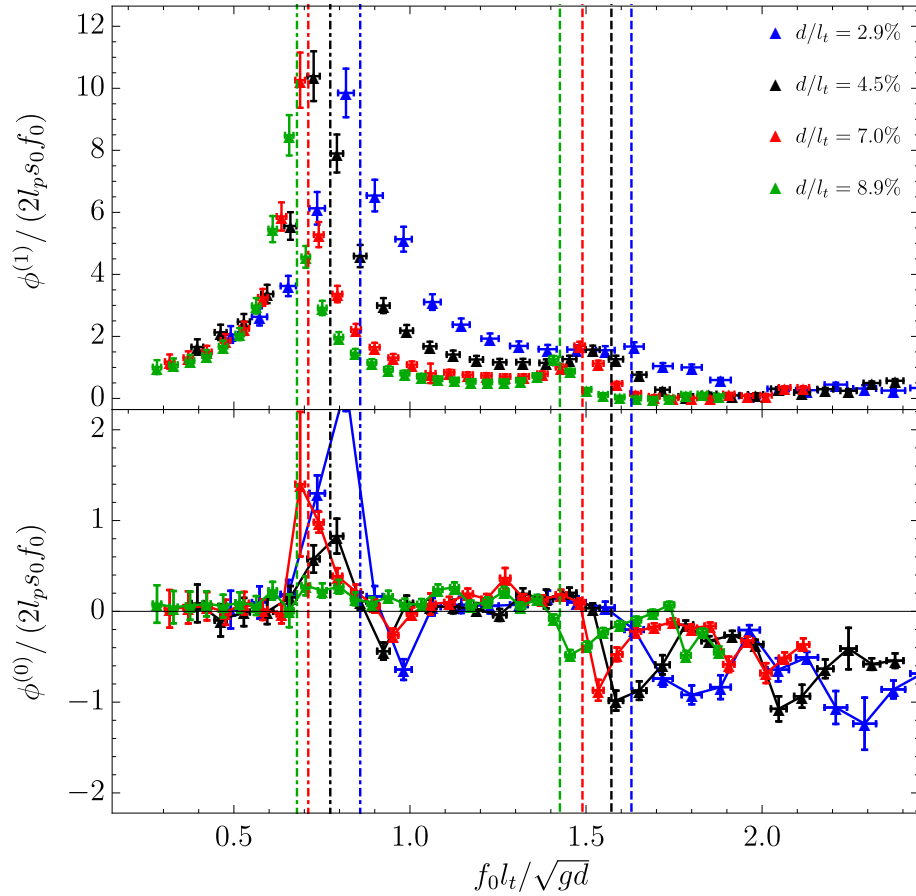


Figure 2.13: Non-dimensional first harmonic and mean flow rate for different water depths. The first harmonic is damped as the water depth increases. The pump works better when the water depth is less important (around 5%). The vertical dashed lines show the resonance frequencies found using the linear theory of section 2.4.1 equivalent to the case $f_0 = 1.20$ Hz of the reference experiment. The vertical dot-dashed lines show the simple harmonic resonance frequencies found using the linear theory of section 2.4.1 equivalent to the case $f_0 = 0.60$ Hz of the reference experiment.

where a is the cross section in the two sections in contact with air of length l_a , and d_o is the variable section of length l_t . If one fixes the lengths and varies d_o it is clear that an increase in d_o leads to a smaller denominator and thus a larger harmonic.

From these experiments, it was shown that near special frequencies the resonance wave pump exhibits interesting behavior: a significant mean flow rate is observed and the system behaves like a pump. In previous studies of such pumps (with flexible tubes), these special frequencies are identified as resonance frequencies. They can be measured experimentally by looking at the response of the system to a step impulse [112]. Hickerson and Gharib [70] noted that their pump resonates at a frequency corresponding to the rate at which a single wave would travel half of the elastic tube length at wave speed. In the present case, this

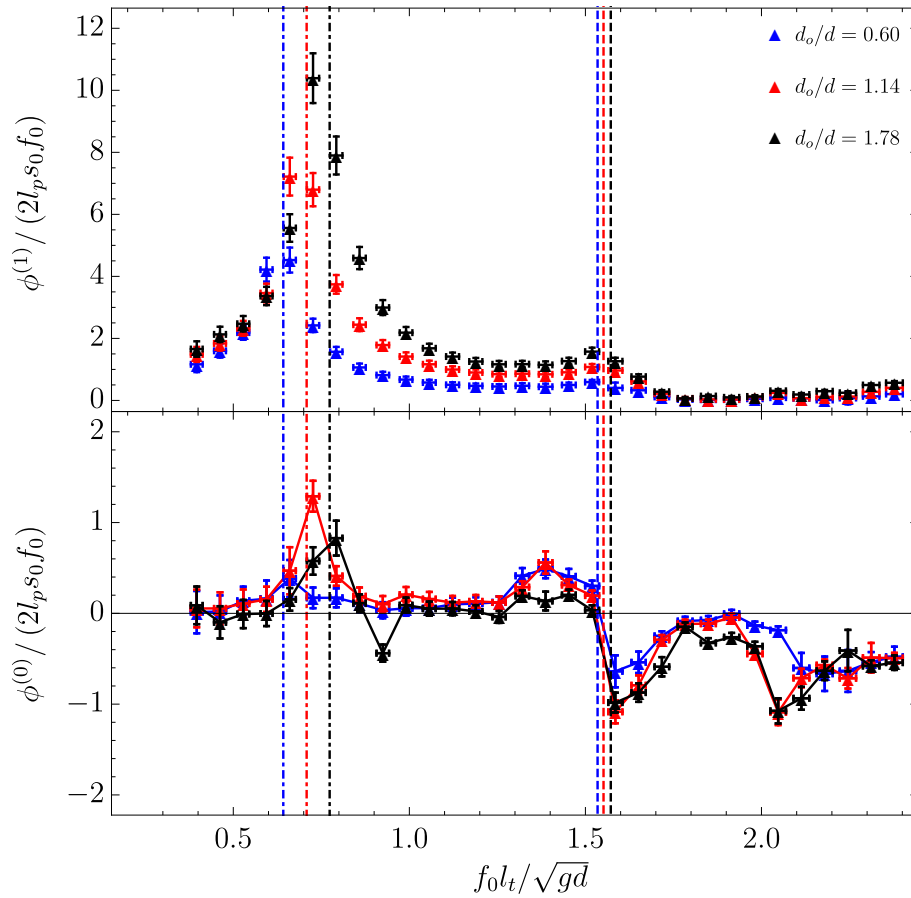


Figure 2.14: Non-dimensional first harmonic and mean flow rate for different opening heights. The vertical dashed lines show the resonance frequencies found using the linear theory of section 2.4.1 equivalent to the case $f_0 = 1.20$ Hz of the reference experiment. The vertical dot-dashed lines show the simple harmonic resonance frequencies found using the linear theory of section 2.4.1 equivalent to the case $f_0 = 0.60$ Hz of the reference experiment. The first harmonic is amplified as the opening height is increased between the two outline resonance frequencies.

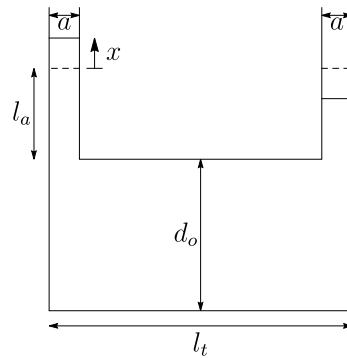


Figure 2.15: Sketch of a U-tube oscillator.

gives $f_H \approx 1.5$ Hz. In the resonance wave pump case, one can take advantage of the linear wave theory of waves to analytically evaluate the resonance frequencies precisely. In the next section, a potential theory approach is described and a dissipative model is proposed to qualitatively characterize the pump dynamics.

2.4 Potential model of the resonance wave pump

2.4.1 Linear potential model without dissipation

In this section, the results of the first chapter are used to describe the resonance wave pump physics. For now, the wave breaking phenomenon outlined in section 2.3.1.5 is ignored. It is assumed that the problem can be described using a linear potential theory. Although, the goal of this theoretical part is to predict the mean flow, it is assumed that the oscillatory part is large compared to it. This is indeed the case above the submerged plate. The main assumption made here is that the mean flow is a consequence of the wave dynamics.

Non-dimensional notations introduced in section 1.2.7 are used. The reference water depth is d above the submerged plate. Only the first order terms are considered and the problem is solved using the eigenfunction expansion (EFE) matching method of section 1.3.4.

The problem for linear waves to be solved can be written as:

$$\left\{ \begin{array}{ll} \Delta \Phi_{\mathbb{C}}^{(1)} = 0, & \text{for } (X, Z) \in \mathcal{D}_f, \text{ (Laplace equation)} \\ \partial_Z \Phi_{\mathbb{C}}^{(1)} = 0, & \text{at } Z = \{-1, -D_{sp}\}, X \in]-X_L, X_R[, \text{ (sub. plate impermeability)} \\ \partial_X \Phi_{\mathbb{C}}^{(1)} = 0, & \text{at } X = \{-X_L, X_R\}, Z \in]-D_{sp}, -1[, \text{ (sub. plate impermeability)} \\ \partial_Z \Phi_{\mathbb{C}}^{(1)} = 0, & \text{at } Z = -D_{tot}, X \in]-L_L, L_R[, \text{ (sea bed impermeability)} \\ \partial_Z \Phi_{\mathbb{C}}^{(1)} = S_0 \Omega, & \text{at } Z = -D_p, \text{ and } X \in [-L_p, L_p], \text{ (plunger control)} \\ \partial_X \Phi_{\mathbb{C}}^{(1)} = S_0 \Omega, & \text{at } Z \in [-D_p, 0], \text{ and } X = \pm L_p, \text{ (plunger control)} \\ \partial_Z \Phi_{\mathbb{C}}^{(1)} = \Omega^2 \Phi_{\mathbb{C}}^{(1)}, & \text{at } Z = 0, \text{ (free surface condition)} \end{array} \right. \quad (2.4.1)$$

where $\Phi^{(1)} = \Re \left\{ \Phi_{\mathbb{C}}^{(1)}(X, Z) e^{i\Omega\tau} \right\}$, \mathcal{D}_f is the fluid domain and all the distance are non-dimensionalized by the water-depth d . Similarly to the plunger of section 1.3.4.2, there are singularities at the corners. The tank is cut in 6 rectangular domains (numbered from I to VI as shown in figure 2.16) and a 10-term expansion is used in each of them. This number of terms was found sufficient in the present applications, as computations with a larger number of terms did not exhibit any significant difference in the results.

This linear theory enables to evaluate the first harmonic oscillatory flow rate under the submerged plate. The flow rate is non-dimensionalized by half the rate of volume displaced by the plunger. The results are displayed in figure 2.17 (black solid line). The top graph shows the first harmonic response. It is now clear that pumping occurs in the vicinity

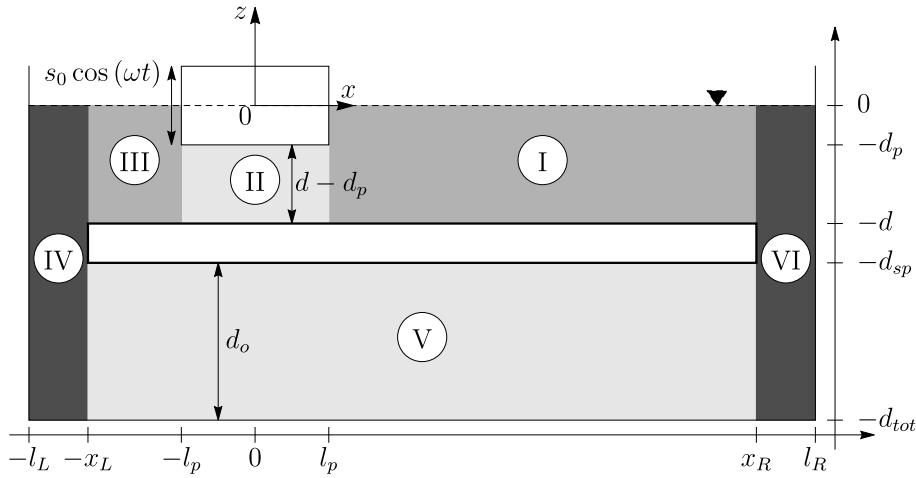


Figure 2.16: Domain decomposition for the Resonance wave pump.

of resonances. There the first harmonic response found experimentally is damped due to non-linearity effects such as wave breaking. Near these points, the assumption of non-rolling surface is not valid. The linear theory already provides important information for the design of such pumps. It enables to predict rather accurately the regions of interest (see all the vertical dashed lines in the figures of the previous section). A similar method could be applied to the case of flexible tubings. The main difference being the free-surface boundary condition. The drawback of this linear theory is that it provides almost no information on the mean flow rate, even if one expands the theory to the next order: neither qualitatively nor quantitatively. That is because, as pointed out in the section 1.4 the only source terms for the mean flow are the wave mass transport and the interaction wave mass transport. The first one is identically zero as the solution of the present problem is obviously a standing wave. The second plays a role on typical distances of the order of $\lambda/2$, where λ is the wavelength. For the case $f_0 = 0.6$ Hz, $\lambda/2 \approx 45$ cm which might be used to explain qualitatively the circulation using the argument of the wave set-down. Nevertheless for the case $f_0 = 1.2$ Hz, $\lambda/2 \approx 24$ cm and these structures won't have a significant role in the mean circulation.

As the linear theory is not valid near the resonances, it is proposed to add dissipation to the model in particular near these peaks.

2.4.2 Adding dissipation

From the linear theory, it appears that the pump works near resonance frequencies. Unfortunately the linear theory is not valid near these frequencies as the waves amplitude predicted from a finite stroke excitation becomes infinite. To extend the range of validity of the potential model, the results of the potential wave dissipation section (see section 1.5.3) are used. The dissipation is modeled through a kinematic viscosity term ν_s in the

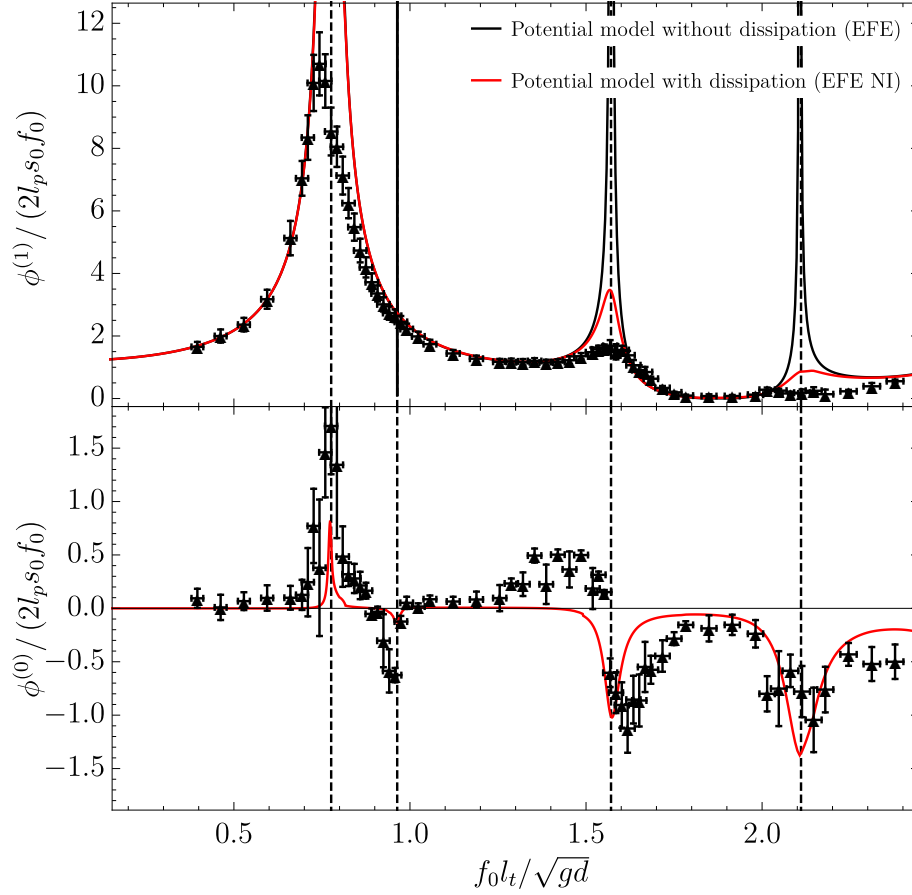


Figure 2.17: Non-dimensional first harmonic and mean flow rate with EFE and EFE NI models for a plunger of length $2l_p = 10.5$ cm and a fixed stroke amplitude $s_0 = 0.69$ cm. The black continuous line in the top figure is obtained by solving the linear potential theory without dissipation and the red one with the present dissipative model with $\nu_{\text{init}} = 8 \times 10^{-4} \text{ m}^2 \cdot \text{s}^{-1}$ and $\beta_{wb} = 2 \times 0.88$. The dashed vertical line shows the position of the resonances.

surface kinematic condition. For the sake of simplicity here the dissipation is fixed to a constant in all the surface domains (that is domains I, III, IV and VI in figure 2.16), and the dissipation is limited to the propagative terms (EFE NI).

The value of ν_s in the present model is selected empirically such that the wave amplitude found with the dissipation is less than a defined wave breaking threshold (see section 1.5.2). Here the value $\beta_{wb} = 2 \times 0.88$ is used.

To solve the problem for a given frequency and stroke amplitude, a bisection search algorithm is implemented to find the viscosity ν_s at which the wave breaking criterium is reached. In terms of non-dimensional viscosity, $1/\mathcal{R}$, the solution is searched in an interval bounded by a user-defined initial value $1/\mathcal{R}_{\text{init}}$ and the maximum viscosity $1/\mathcal{R}_{\text{limit}}$ found in eq.1.5.26⁹. This enables the use of the approximative formula eq.1.5.20 and eq.1.5.24 to

⁹Note that $\mathcal{R}_{\text{limit}} < \mathcal{R}_{\text{init}}$ and the value $\mathcal{R}_{\text{limit}}$ is not actually reached in all the examples.

evaluate the first wave number in the dissipative regions. To increase the efficiency of the numerical method, a one-term expansion is used for the bisection search and the value of ν_s found is used to solve the problem with a 10-term expansion. Note that if with the initial dissipation viscosity the maximum wave amplitude is below the wave breaking criterium, the dissipation is fixed to this initial user defined value.

In summary, the present model involves only two parameters: the wave breaking threshold, which can be justified by the discussion in section 1.5.2 and the initial viscosity $\nu_{\text{init}} = 8 \times 10^{-4} \text{ m}^2 \cdot \text{s}^{-1}$ (or $\mathcal{R}_{\text{init}} \approx 25$)¹⁰.

Figure 2.17 shows the non-dimensional first harmonic and mean flow rate found with this model for $S_0 = s_0/d = 19.8\%$ (red solid line) compared to the linear potential theory without dissipation (solid black line) and the experimental results (up-triangles). Adding the dissipation, even with this large initial viscosity, weakly influences the predicted amplitude of oscillation ($\phi^{(1)}$) away from the resonance frequencies. The first harmonic is significantly damped near the resonance frequencies, similarly to experimental observations¹¹.

The wave mass transport is not identically zero in the cases with dissipations. Figure 2.18 shows wave mass transport profiles for 3 different frequencies. A positive (negative) wave mass transport means that there is a net mass flux toward the right (left, respectively) in the surface layer.

For the frequency $f_0 = 1.60 \text{ Hz}$, the wave mass transport is negative (positive) on the left (right) side of the plunger (respectively). On the right side of the plunger, the wave mass transport first increases: there must be a suction upward to “fill” the surface layer mass flux. After the position $x/l_p \approx 1.2$, the wave mass transport starts to decrease. The wave mass transport is transferred back to the interior of the flow. A similar dynamics is visible on the other side of the plunger. This is sketched on the tank visualization of figure 2.19. The wave mass transport absolute value appears to be stronger on the right than on the left side; a clockwise circulation is therefore expected in the tank. A recirculating on the left side of the plunger can be expected due to the negative wave mass transport on that side¹².

For $f_0 = 1.20 \text{ Hz}$, the wave mass transport is positive on both sides of the plunger. This seems more efficient as there should be no recirculation on the left side of the plunger. The

¹⁰ This value is twice the one in the original paper [21] as the formula in eq.(3.36) was with a four coefficient in the paper and not with a two coefficient as in eq.1.5.20 here. Thus, the parameters are equivalent to the one used in Carmigniani et al. [21] though the problem was solved using EFE Limited in the paper and here with EFE NI. This is justified in appendix J. $\mathcal{R}_{\text{limit}} \in [0.21, 6]$ for the frequency range considered here.

¹¹The model first harmonic over-estimates the amplitude of oscillations. To match the experiments, one can select a $\beta_{wb} = 0.88$ but then the mean flow rate will be smaller and this value is not consistent with standing waves problem. An improvement would be to take into account also the roller mass transport and make a dissipation coefficient per region and per wave direction.

¹² It is observed in the numerical simulations, see section 2.5.2 and see also [17] for longer time observation.

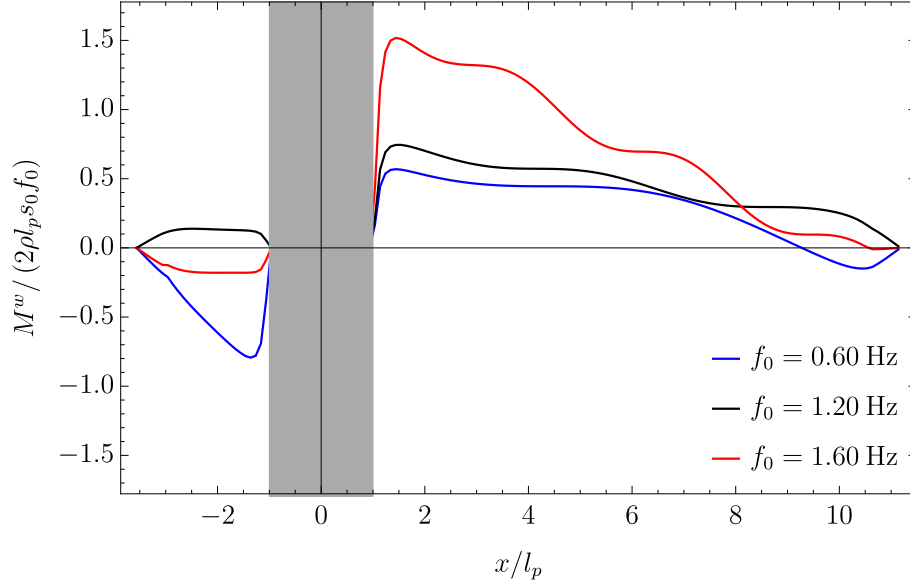


Figure 2.18: Wave mass transport in the resonance wave tank with EFE NI for different frequencies for a forcing amplitude $S_0 = s_0/d = 19.8\%$. The gray shaded area outlines the position of the plunger. Note that for the frequency $f_0 = 1.20$ Hz, the wave mass transport is positive on both sides of the plunger. The curves are obtained using the present dissipative model with $\nu_{\text{init}} = 8 \times 10^{-4} \text{ m}^2 \cdot \text{s}^{-1}$ and $\beta_{wb} = 2 \times 0.88$.

dynamics of the pumping in the tank is sketched in figure 2.20.

The mean flow rate can be roughly estimated as minus the sum of these values. The results as a function of frequency is plotted in the bottom figure 2.17. The model correctly predicts the direction of the observed flow. The values of ν_{init} and β_{wb} affect the maximum absolute mean flow rate reached and also the frequency ranges for which the mean flow rate becomes significant around the resonances. The direction of the flow near the resonances was not found to be influenced by the choice of these parameters in all tests performed.

Recall the wave mass transport is a quadratic term in wave amplitude. Thus one can expect the mean flow rate to vary quadratically with the forcing stroke amplitude s_0 (as observed experimentally, see figure 2.11). This will be the case at constant ν_s . When the wave amplitude is at the wave breaking threshold the dissipation viscosity ν_s will also increase with the stroke amplitude leading to saturation or even decay of the non-dimensional flow rate. Figure 2.21 shows the predicted mean flow rate as a function of the stroke amplitude for $f_0 = 1.20$ Hz, $f_0 = 1.40$ Hz and $f_0 = 1.60$ Hz. In all cases, the mean flow rate first increases quadratically with the forcing stroke amplitude until it reaches a value at which dissipation increases and the mean flow rate starts to increase with a linear trend (see the case $f_0 = 1.60$ Hz and $f_0 = 1.20$ Hz).

The model can also be used to find the optimal plunger position for a given forcing frequency. For $f_0 = 1.20$ Hz and $f_0 = 1.60$ Hz, the predicted mean flow rate is plotted as a

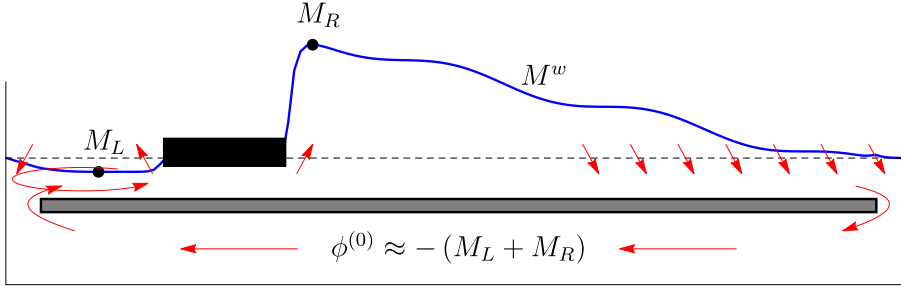


Figure 2.19: Sketch of the wave mass transport effect on the mean flow for $f_0 = 1.60$ Hz. The solid blue line shows the wave mass transport with a positive value if the curve is above the undisturbed free surface (horizontal black dashed line). The extrema are noted M_L and M_R on the left and right side. The mean flow rate under the submerged plate is roughly estimated as minus the sum of these values.

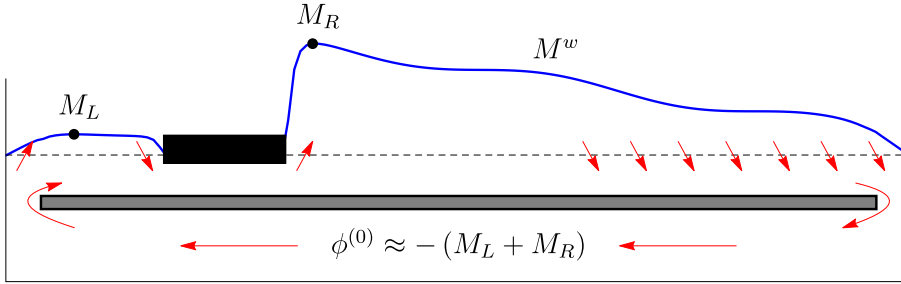


Figure 2.20: Sketch of the wave mass transport effect on the mean flow for $f_0 = 1.20$ Hz. The solid blue line shows the wave mass transport with a positive value if the curve is above the undisturbed free surface (horizontal black dashed line). The extrema are noted M_L and M_R on the left and right side. The mean flow rate under the submerged plate is roughly estimated as minus the sum of these values.

function of the plunger position $\mathcal{O}_p = L_t/2 - L_c$ in figure 2.22. When this parameter is zero the plunger is at the center of the wave tank (and thus there is no mass flux). The position selected for the experiments is close to the optimal one for these frequencies.

The model shows only one part of the whole story. It shows how important the wave mass transport is in the pumping mechanism but ignores the role of the interaction stress tensor which also participates to the mean flow rate dynamics, mostly on the scale of $\lambda/2$. It also ignores the additional wave mass transport coming from the wave rolling when wave breaks (as visible in figure 2.9 for $f_0 = 1.20$ Hz). It is however convenient thanks to its simplicity. The wave mass transport role is equivalent to the conservation of mass principle while the interaction stress tensor shows the role of the conservation of momentum. On top of this, turbulence and the effect of the mean flow rate on the wave dynamics should be added to capture all the physics. The model as presented here enables to understand how the pumping occurs in the resonance wave pump. It predicts

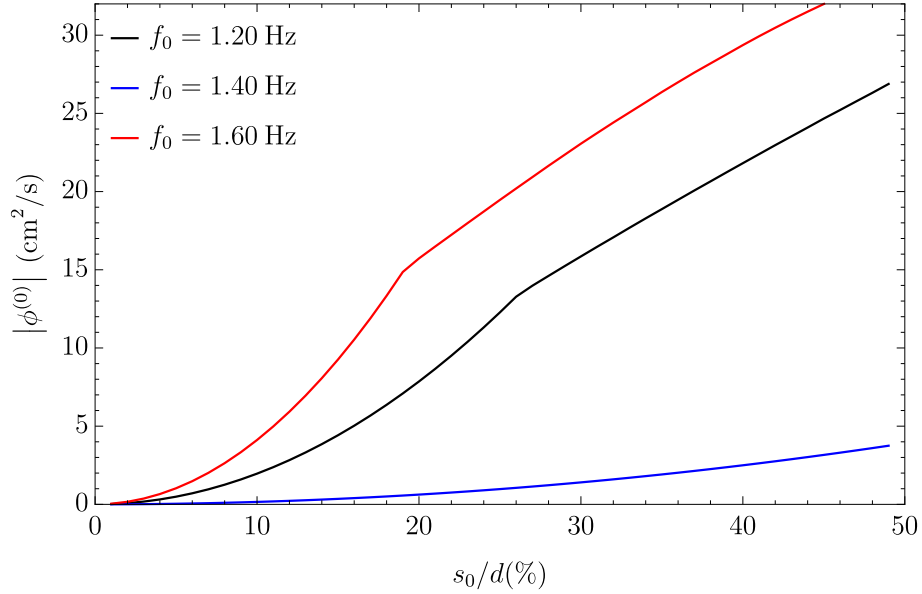


Figure 2.21: Mean flow rate with stroke amplitude with EFE NI for different frequencies with the present EFE NI dissipative model with $\nu_{\text{init}} = 8 \times 10^{-4} \text{ m}^2 \cdot \text{s}^{-1}$ and $\beta_{wb} = 2 \times 0.88$. The model predicts the same trends as the experiment observations.

the evolution of the wave mass transport and shows in particular quite different behaviors for the cases $f_0 = 1.20$ Hz and $f_0 = 1.60$ Hz. To verify the importance of the wave mass transport in the pumping mechanism, PIV measurements above the submerged plate and simulations using two numerical methods are now discussed.

2.5 Mass flux above the submerged plate

In this section, the PIV measurements of the flow above the submerged plate are first described. The experiments are limited to small sections of the tank and small stroke amplitude to avoid wave breaking which prevents data acquisition near the surface. To have a global view of the tank in the case of wave breaking, two numerical methods are used to simulate the tank: the open source OpenFOAM “interDynFOAM” solver [35, 123, 167] and the Smoothed Particle Hydrodynamics solver *Sphynx* [47, 107, 108] (see appendix K for more details). The first method is a Volume of Fluid method, while the second is a Lagrangian method and is more adapted to the case of large surface deformation. The numerical methods are validated by comparing the flow rate measured under the submerged plate and used to see the mean mass flux above the submerged plate.

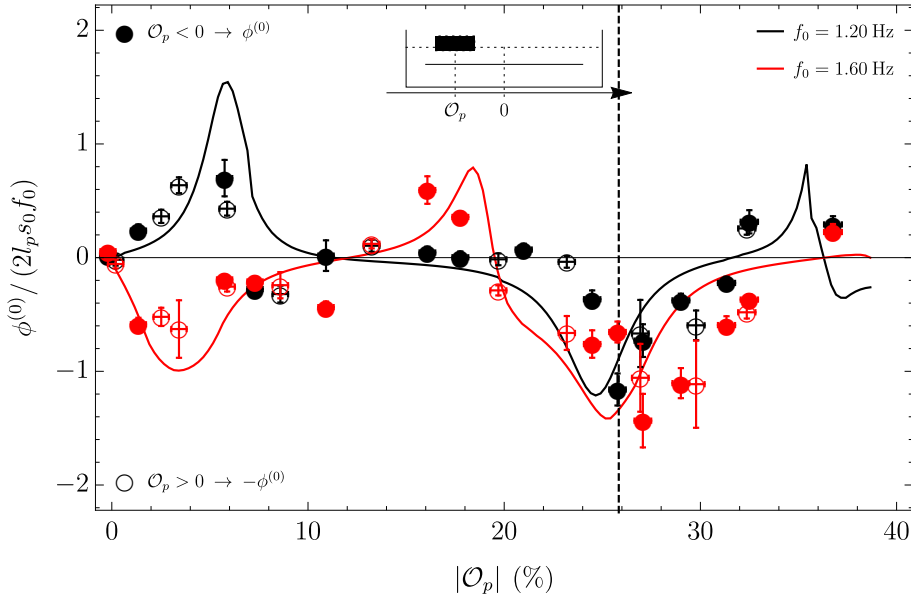


Figure 2.22: Mean flow rate with plunger position with EFE NI for two different frequencies: compared experiments (points) and dissipative model with $\nu_{\text{init}} = 8 \times 10^{-4} \text{ m}^2 \cdot \text{s}^{-1}$ and $\beta_{wb} = 2 \times 0.88$ (solid lines). The filled circles show experimental measurements with the plunger off-centered to the left (as in previous experimental cases) and the empty circles show the plunger on the right side. The off-centered position is given with respect to the center of the tank $\mathcal{O}_p = L_t/2 - L_c$. The model predicts the same trends as the experiment observations in most cases. The vertical dashed line shows the position used in all the other experiments. It is closed to optimal for these two frequencies.

2.5.1 PIV measurements above the submerged plate

A similar set-up to the one described before is used (corresponding to experiment A in table L.2). In this subsection the stroke amplitude is reduced to $s_0 = 0.34 \text{ cm}$ to avoid wave breaking which would blur the free surface as well as prevent PIV measurements near the surface and therefore in the surface layer. The frequency is fixed to $f_0 = 1.2125 \text{ Hz}$. At this frequency, the pump is near resonance but no wave breaking occurs.

The NanoSence MKIII camera is mounted with a Tamron 90mm lens and records videos at 400 fps for 10 seconds. The camera is moved to four different positions above the submerged plate (see figure 2.2 and zones (1) to (4)). The visualization zones are $4.5 \times 6.0 \text{ cm}$ and have a resolution of 164 pixel/cm. The experiment is run twice per visualization zone. Prior to recording the data, the pump runs for at least 1 minute and 30 seconds such that the system reaches an asymptotic regime. The sample is then cut in 30 phases evenly distributed over one stroke period. For each phase, 13 sets of two images spaced by $1/400 \text{ s}$ for each experiments are recorded. The results of each phase are averaged on 13 periods ($T = 1/f_0$) and the mean mass flux fields are obtained by averaging the 30 phases over the two experimental sets. The obtained velocity field resolution is 10 vectors/cm.

The standard deviation of the velocity field is also obtained this way. The camera is not synchronized with the plunger. The origin of time is chosen arbitrarily in the next sections. The PIV is performed near the free surface. All pixels above the surface are masked out to run the PIV. The surface might be difficult to detect automatically in all cases. The detection is performed manually which justifies the limitation to 30 phases in the data while the videos were recorded at 400 fps with a continuous laser.

The flow rate under the submerged plate for this case has a mean value of $-3.1 \pm 0.05 \text{ cm}^2 \cdot \text{s}^{-1}$ where the fluctuation represents the difference between the two experiments. Figure 2.23 shows the mean velocity profile averaged between the two experiments and the flow rate over a period for the two experiments separately. The configuration is close to a resonance. A clockwise circulation occurs similarly to the case $f_0 = 1.20 \text{ Hz}$ of the reference configuration. The origin of time $t/T = 0$ is defined here as the moment the flow rate hits a maximum. The flow rate is above the mean value for $t/T \approx 0.48$. This means that the flow rate is close to a sine function of time under the submerged plate with a small second order contribution.

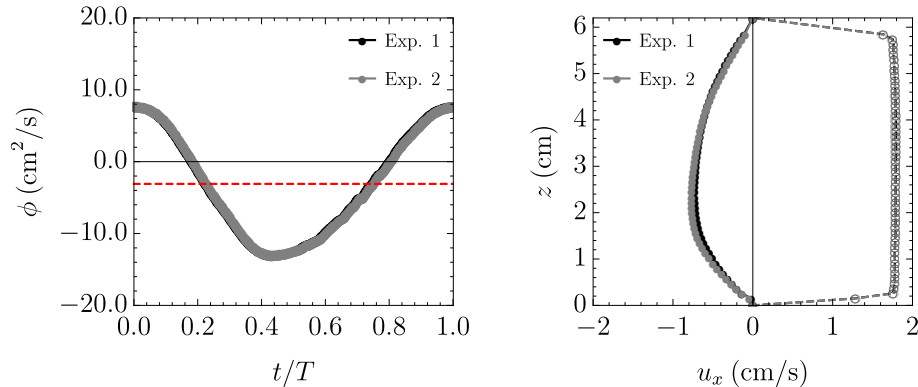


Figure 2.23: Flow rate (left) and velocity profiles (right) in PIV window (5) (see figure 2.2).

Consider for now the instantaneous velocity near the plunger in visualization zones (2) and (3) of figure 2.2 in the asymptotic regime. The phase origin is defined as the moment the plunger is at its lowermost position. Figure 2.24 (figure 2.25) shows the velocity field at six instances in an upward (downward) plunger stroke (respectively). The red solid line represents the instantaneous free-surface position. The plunger is represented by the black rectangles. The plunger is non-dimensionally located between -1 and 1 . The quiver plots show only a quarter of the vectors for the sake of clarity. The figures show a single experimental set averaged on the 13 wave periods at 10 different plunger stroke instances. Recall that the left side of the plunger corresponds to a shorter tank region. It appears here that this short section acts like a reservoir for the left side. The water accumulates slowly on that side during the downward motion (figure 2.25). The upward motion is similar to a “gate opening”. The accumulated potential energy is suddenly released.

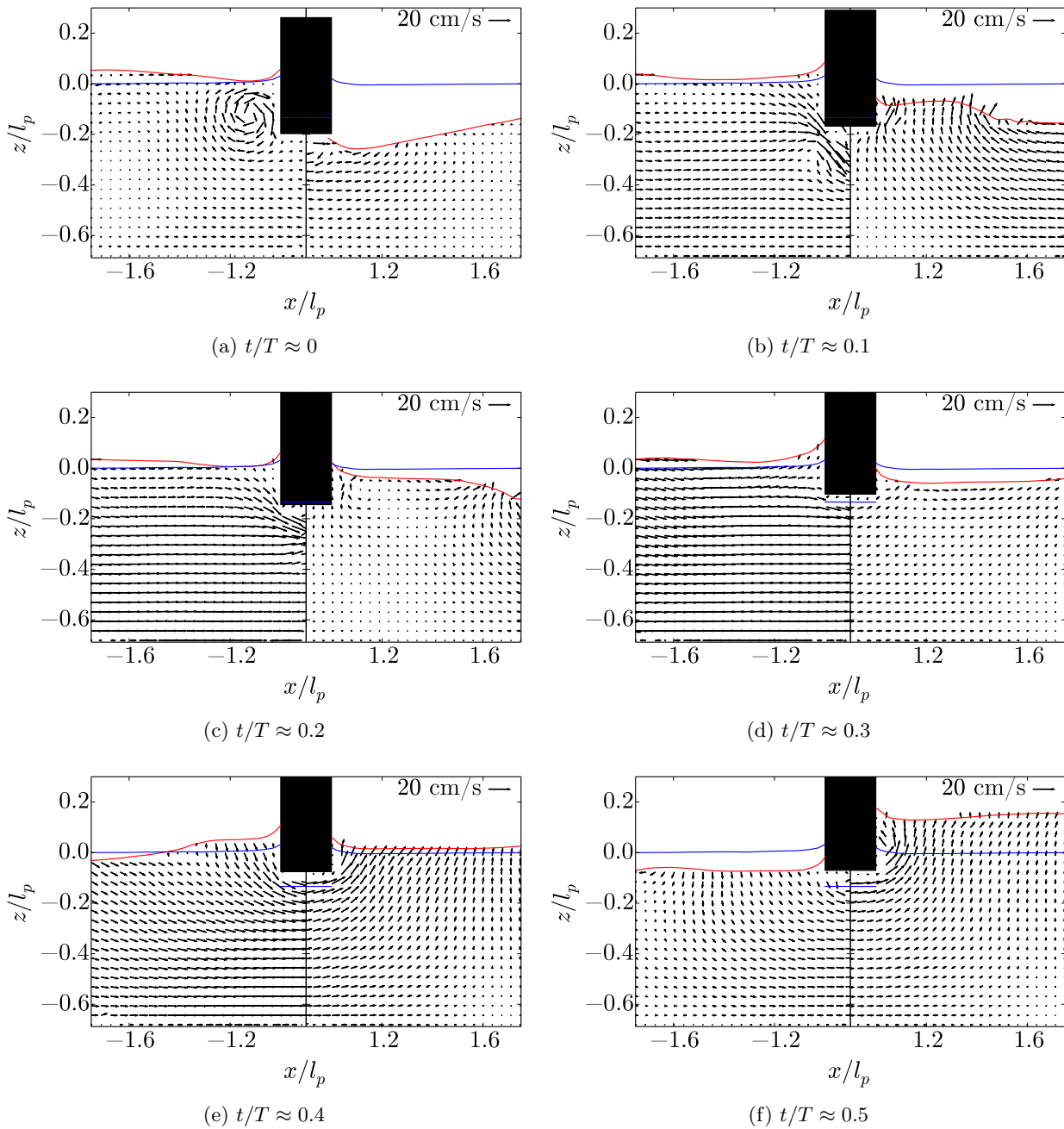


Figure 2.24: Velocity field zones (2) and (3) (see figure 2.2) during upward plunger stroke for $f_0 = 1.2125\text{Hz}$ at six equally spaced instances. The red solid line represents the instantaneous free-surface position and the blue solid line the position of the undisturbed free surface with the plunger position at its mean draft.

During the upward part of the stroke (figure 2.24), the excess of water on the left side of the plunger is discharged to the right. Note that if the tank was at rest and the plunger was moving up, one should expect the flow to be towards the plunger (suction). Here the flow is from the left to the right (or clockwise when looking at the circulation around

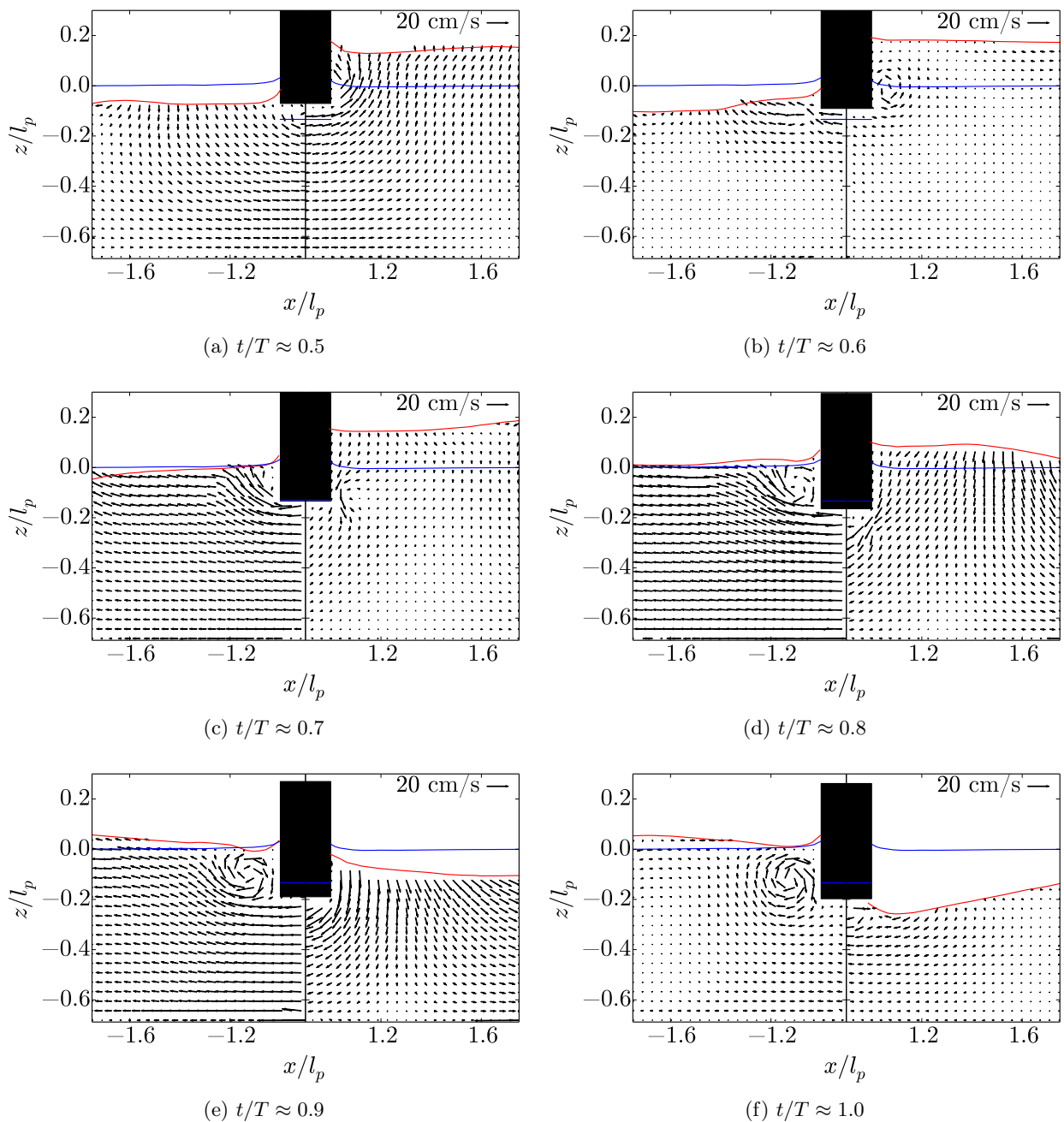


Figure 2.25: Velocity field zones (2) and (3) (see figure 2.2) during downward plunger stroke for $f_0 = 1.2125$ Hz at six equally spaced instances. The red solid line represents the instantaneous free-surface position and the blue solid line the position of the undisturbed free surface with the plunger position at its mean draft.

the submerged plate). This is similar to a gate opening, releasing the excess of potential energy to the right side. A traveling wave is generated on the right side of the plunger and the water level continues to rise. The wave is clearly visible in the instance $t/T \approx 0.1$ and

$t/T \approx 0.2$, where it can be seen travelling to the right (away from the plunger). This will generate a forward mass transport in the surface layer, as can be seen when looking at the mean mass flux.

During the downward motion (figure 2.25), the circulation is reversed. The excess of water on the right is going to the left but the motion of the plunger limits this transfer. In the case of a tank starting at rest with a plunger moving down, one should expect the flow to travel away from the plunger. During an entire stroke (figures 2.24 and 2.25), the surfaces on each side of the plunger are out-of-phase. This leads to an optimal transfer of mass and an amplified wave on the right side.

Averaging the flow on the 30 phases for the two sets of experiments gives the mean mass Eulerian flux field¹³ (figure 2.26 (a-d)). The mean mass flux is defined as $\rho\mathbf{u}$. In the part of the flow always in water, there is no difference between the mean mass flux and the mean velocity fields. In the “splash zone”, the density acts like a mask (it corresponds to the region bounded by the red solid lines in figures 2.26). It is striking to see that the mean mass flux is not zero and there is a net current. Figure 2.26 (a,b) shows the mean mass flux near the plunger.

On the left side of the plunger (figure 2.26-a), there are two recirculation cells: one near the plunger (in the surface layer) and a second one in the opposite direction near position $(-1.5, -0.15)$. There is a net mass flux toward the right at the edge of the plunger. In the surface layer the mass flux changes sign. It is to the right at position $(-1.1, -0.15)$ and in the opposite direction at $(-1.5, -0.10)$. This is different from the prediction model which suggests a mass flux toward the right for this frequency (see figure 2.20).

On the right side of the plunger (figure 2.26-b), there is a noticeable mass flux in the surface layer and almost no flux in the interior. Once more there are two recirculation cells near the plunger. At the right edge of this domain, the flow is almost only in the surface layer.

In visualization zone (1) (figure 2.26-c), near the left edge of the submerged plate outlined by the dashed vertical line, there is a flux of mass travelling from under the submerged plate all the way up to the surface layer. The wave mass transport is thus toward the plunger there. Since in the zone (2) localized forward there was a mass flux in the opposite direction, one can expect a change of sign in between position $x/l_p = -2.8$ and $x/l_p = -1.7$. The positive mass flux in the surface layer near the wall is similar to the model prediction for this frequency.

In visualization zone (4) (figure 2.26-d) the flow is spread between the surface layer and the interior of the flow. The mass flux originally in the surface layer at the end of zone (3) (see figure 2.26-b) dived inside the interior of the fluid. In these experimental results, one can observe the mean mass flux and assess the fact that the dominant part of the flow

¹³ The velocity field in air is masked during the PIV. As the velocity in air is not zero, it is incorrect to talk of mean Eulerian velocity field. To account for this the mean mass Eulerian flux field is defined.

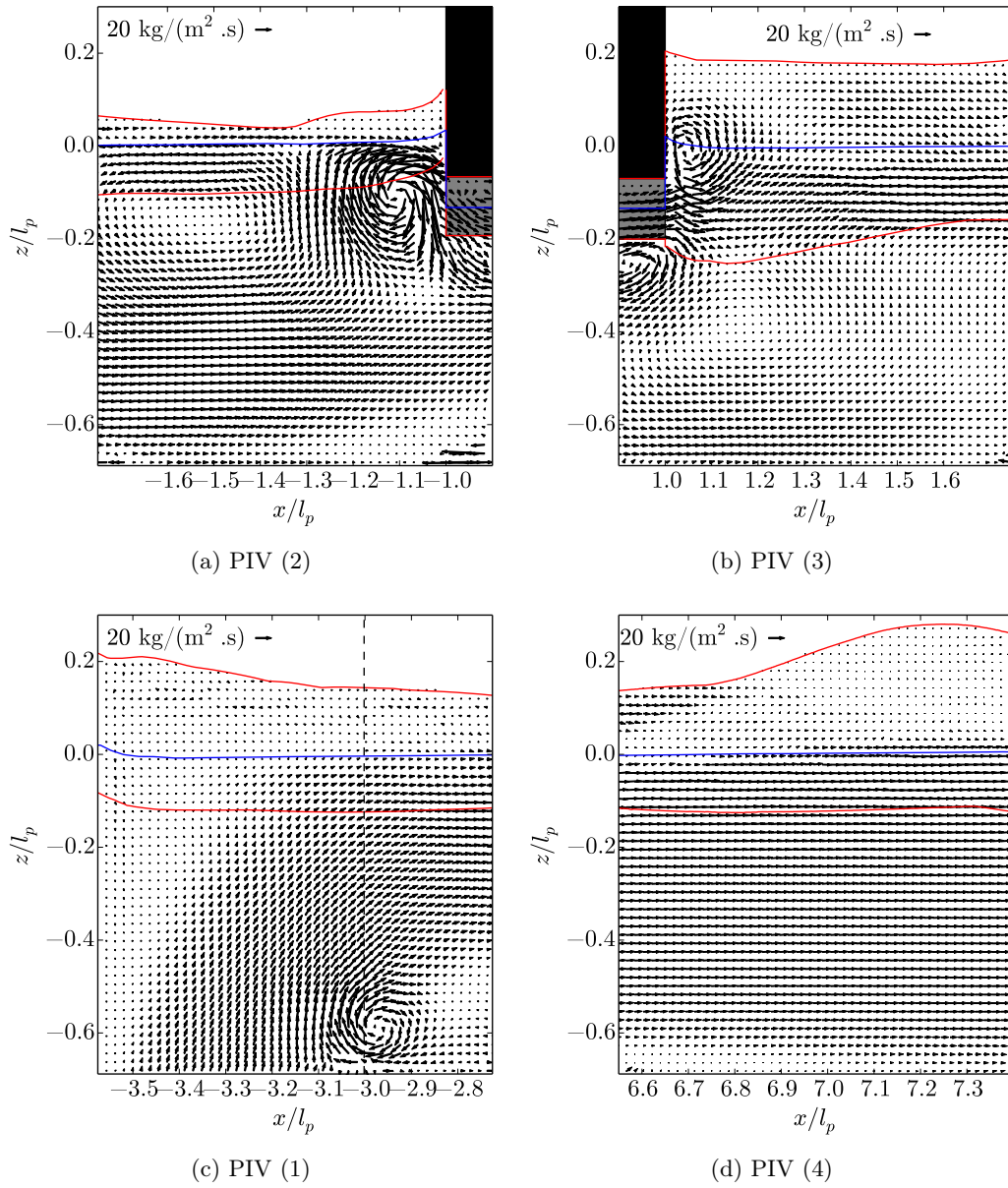


Figure 2.26: Experimental mean mass flux fields above the submerged plate in PIV zones (1) to (4) for $f_0 = 1.2125$ Hz (see figure 2.2). The blue solid line represents the undisturbed free surface with the plunger at its mean draft position. The red solid line depicts the surface layer defined as the domain between the maximum and minimum surface elevation at a given horizontal position. The fluid domain spanned by the plunger is represented by the shaded gray rectangle.

comes from the surface dynamics. The wave mass transport is therefore an important part of the pumping mechanism. The recirculation cells at the edge of the plunger are due to vortex shedding at the corners and the large circulation cells visible in the interior of the

fluid come from the effect of the interaction wave tensor. Next, the resonance wave tank is studied numerically to have a more detailed description of the mean mass flux dynamics above the submerged plate.

2.5.2 2D Numerical simulations:

In this section, two numerical methods are used to simulate the resonance wave tank for the two frequencies $f_0 = 1.20$ Hz and $f_0 = 1.60$ Hz and the stroke amplitude $s_0 = 0.69$ cm (configuration corresponds to experiment A in table L.2): the open source finite element code OpenFOAM with the built-in “interDyMFOAM” solver and the SPH EDF in-house code Sphynx.

The first one is a VOF (volume of fluid) method and the plunger is controlled through mesh deformations. The air and water phases are simulated. The interface is not directly tracked here. Instead a mixture scalar function called α is used and advected. It is equal to 1 in water and 0 in air. The resolution for this simulation is $\delta x = 0.1$ cm.

It is compared to the SPH (smoothed particle hydrodynamics) method, which is a Lagrangian method with particle size $r_{SPH} = h_{SPH}/2 = 0.05$ cm, where h_{SPH} is the smoothing length. The SPH code is weakly compressible and an artificial speed of sound of $c_{SPH} = 11$ m/s is used¹⁴. More details about this method are provided in appendix K.

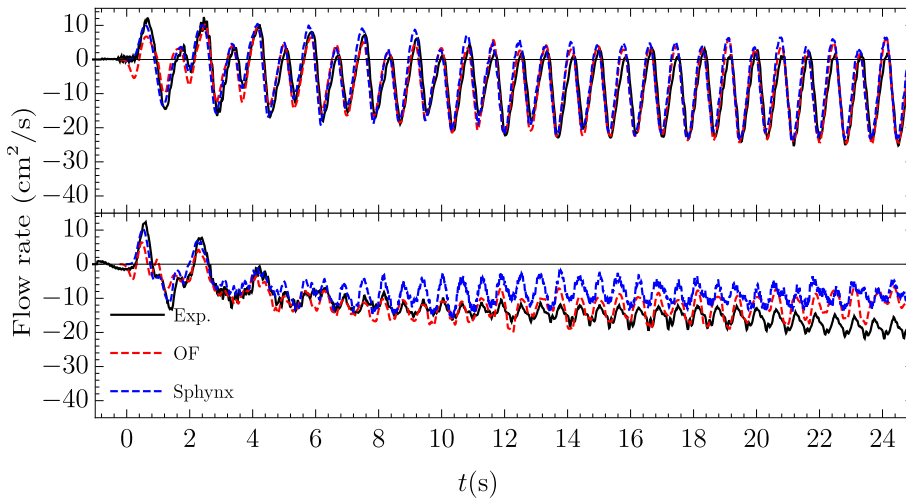


Figure 2.27: Transient regime flow rate simulations compared to experimental results.

First, the transient regime of the flow rate under the submerged plate between the two numerical methods are compared to the experimental results for the cases $f_0 = 1.20$ Hz and $f_0 = 1.60$ Hz in figure 2.27. Both methods capture the transient regime for these two cases. Note that the OpenFOAM simulations starts with the plunger at the mean draft position. As the code uses mesh deformation, it seems more adequate to starts from the

¹⁴This represents approximatively $10\sqrt{gd_{tot}}$ and should thus ensure that the flow is quasi incompressible.

mean position of the plunger, such that the mesh deformation is symmetric with respect to its initial position. The SPH method simulations and the experiments are started with the plunger in the uppermost position. The SPH method correctly captures the plunger start-up. Afterward, the two methods converge toward an asymptotic regime. For the case $f_0 = 1.6$ Hz, the SPH method and VOF method lead to a weaker pumping after 25 sec. The dynamic difference between the two methods can be due to the incompressibility of the SPH method which leads to a shift of the resonance frequencies as discussed in Carmigniani et al. [18].

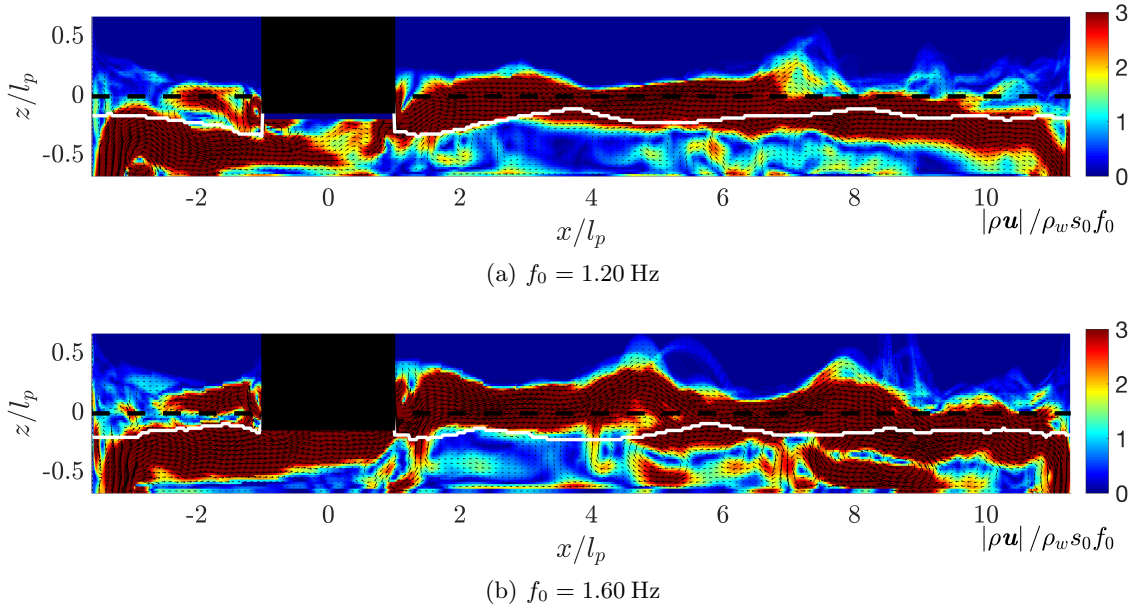


Figure 2.28: Numerical mean mass flux fields above the submerged plate using the VOF method (OpenFOAM) for $f_0 = 1.20$ Hz and $f_0 = 1.60$ Hz. The horizontal black dashed line shows the position of the undisturbed free surface. The white solid line delimits the lower bound of the surface layer.

In both methods, after 20 seconds (or more than 15 wave periods) a quasi-asymptotic regime is reached. The mean mass flux is evaluated for the last 4 wave periods sampled on 101 phases¹⁵.

In the VOF method, the mean mass flux is evaluated as $\rho_w \bar{\alpha} \bar{\mathbf{u}}$, where recall α denotes the mixture scalar function. The surface layer is obtained by looking at $\bar{\alpha}$. In the surface layer the data varies strictly between 1 and 0. The lower bound of the surface layer is defined as the position where the mean value of $\bar{\alpha} < 0.95$. Figure 2.28 shows the results of the mean mass flux above the submerged plate using the VOF method.

In the SPH method Marrone et al. [103]’s method is used with a threshold of 0.55 to track

¹⁵ The mean wave mass flux found is not in completely steady state but no significant changes of trend are found when running the simulation longer (over 120 seconds with VOF method, see [17]). To reach 25 seconds of simulation, one needs to run the SPH method for about 7 days against 2 days using the VOF method. The VOF simulations were run on 9 CPU’s and the SPH on a single GPU.

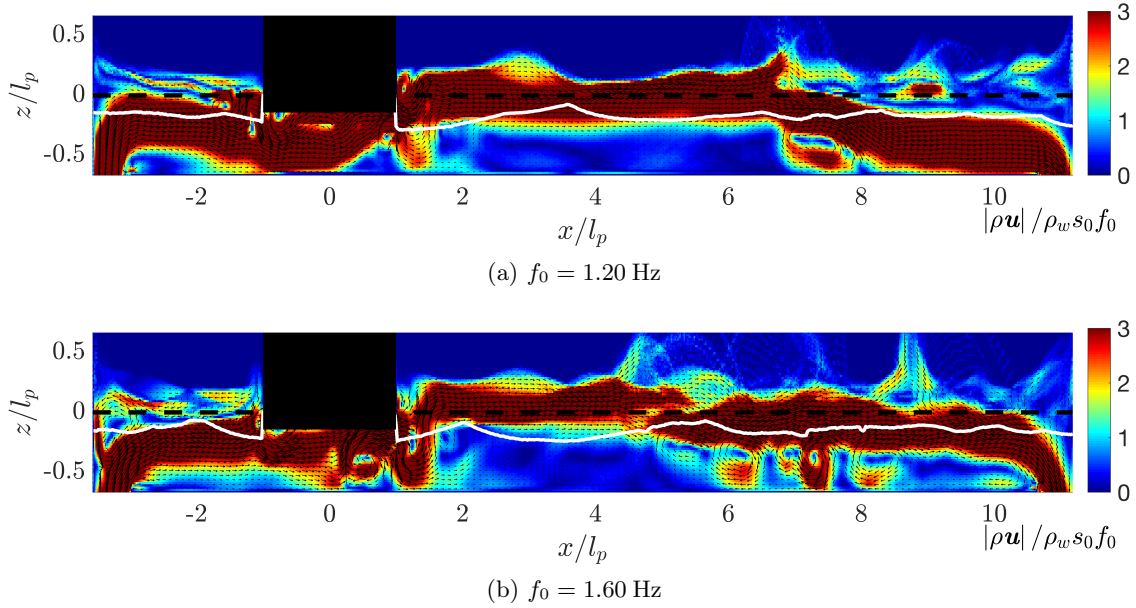


Figure 2.29: Numerical mean mass flux fields above the submerged plate using the SPH method (Sphynx) for $f_0 = 1.20$ Hz and $f_0 = 1.60$ Hz. The horizontal black dashed line shows the position of the undisturbed free surface. The white solid line delimits the lower bound of the surface layer.

the position of the surface particles. The mean mass flux is an Eulerian quantity. The simulation domain is decomposed in boxes of size $h_{SPH} \times h_{SPH}$ ¹⁶. The mass flux at a given time is defined as the mean value of $\rho_w \mathbf{u}$ of the fluid particles in this box. In a box completely submerged there should be about 4 particles. Figure 2.29 shows the results of the mean mass flux above the submerged plate using the SPH method.

In both methods and for both frequencies, one can notice that the mass flux is primarily localized in the surface layer (above the white solid line) between positions $x/l_p = 2$ and $x/l_p = 5 - 6$ on the right side of the plunger (depicted by the black rectangle). It then dives to go under the submerged plate pass the position $x/l_p = 10$. In the SPH method, for the case $f_0 = 1.20$ Hz, the mass flux is almost completely localized under the surface layer pass the position $x/l_p = 7$.

On the left side of the plunger, the two methods predict quite similar behaviors. For the case $f_0 = 1.20$ Hz the mass flux goes all the way up to the surface layer. Note that the case $f_0 = 1.20$ Hz is near the frequency presented in the experimental section on the wave mass transport (see section 2.5.1) and that in the experiment the mass flux is also going all the way up to the surface layer for this frequency. For $f_0 = 1.60$ Hz, a recirculation cell starts to appear on that side. For the SPH method, this is less marked as the mean flow rate is not as strong potentially because of the compressibility effects (see discussion in [18]). Nonetheless in both methods the wave mass flux is mostly toward the left in the

¹⁶This justifies the difference of the resolution between the two simulations.

surface layer on that side.

The results are also quite similar near the plunger for both numerical methods as well as the experiment. In all the cases on the left side of the plunger, there is a clockwise vortex near the plunger and a counterclockwise further to the left. Similar observations are possible on the right side. Recall that the experiment is conducted with a smaller stroke amplitude which explains the difference in position compared to the surface layer of these structures.

The wave mass transport is further measured in the simulations and compared to the previous dissipative model. The results are shown in figure 2.30. There is a good qualitative agreement with the quite simple linear dissipative model proposed in the previous section. In the VOF method, the simulations are run for over 120 seconds and the wave mass transport measured (see orange lines in figures 2.30). There are no drastic changes of behavior (see [17]). The main evolution is on the left side of the plunger for the case $f_0 = 1.60\text{Hz}$ due to the full formation of the recirculation cell. This confirms the importance of the wave mass transport in the pumping mechanism and validates the model. Note that the model is quite powerful considering its simplicity.

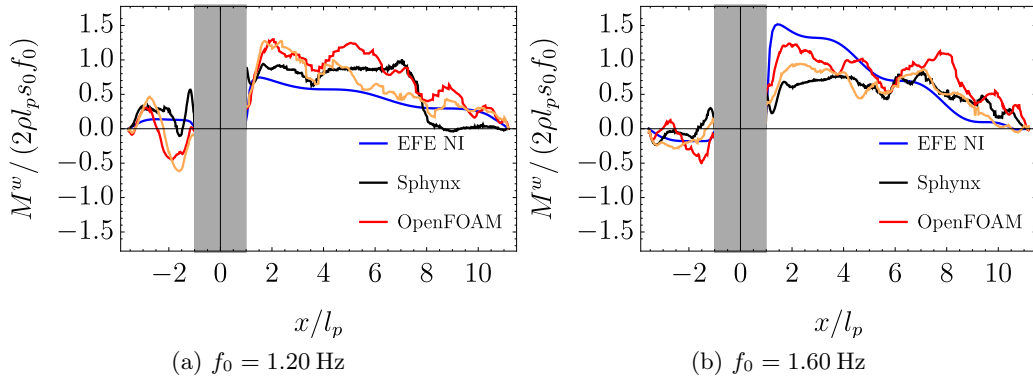


Figure 2.30: Compared simulations and model wave mass transport. The blue solid line corresponds to the linear potential wave dissipation model of section 2.4.2 (EFE NI). The black (red, orange) solid line corresponds to the Sphynx (OpenFOAM, OpenFOAM after 120 s as reported in [17]) simulations. The wave mass transport is obtained by integrating the wave mass flux above the bottom surface layer (white lines in figures 2.29 and 2.28).

2.6 Efficiency and potential applications

The efficiency of the resonance wave pumping to generate currents can be evaluated using the wave mass transport property. One needs first to define the equivalent waves that would be required to power the pump. In the present proof of concept the waves are generated by a plunger. The generation of waves by a plunger is studied in section 1.3.4.2.

In the regime studied in this chapter, $\Omega = 2\pi f_0 \sqrt{d/g} < 0.75$, which means that the wave amplitude of the two waves generated by the plunger in an infinite tank is $a \approx l_p s_0 \omega / \sqrt{dg}$. If one considers that these two waves travelling away from the plunger comes from a single incident wave, the mass transport of this incident¹⁷ wave is then

$$M_I \approx \rho l_p^2 s_0^2 \frac{k}{d} \omega. \quad (2.6.1)$$

Recall that the wave mass transport is evaluated per unit crest. The tank width, l_w , corresponds in the present to the unit crest of the waves travelling away from the paddle. For the case $f_0 = 1.20$ Hz, $2l_p = 5.7$ cm and $s_0 = 0.69$ cm, the incident wave mass transport is thus $M_I/\rho \approx 1.11 \text{ cm}^2 \cdot \text{s}^{-1}$. When compared to the measured flow rate under the tank (see table L.6 of appendix L), $\phi^{(0)} = -5.05 \pm 0.74 \text{ cm}^2 \cdot \text{s}^{-1}$, this means the pump amplifies the incident wave mass transport by a factor 4.5. For the case $2l_p = 10.5$ cm, the factor is closer to 2.5 for this frequency.

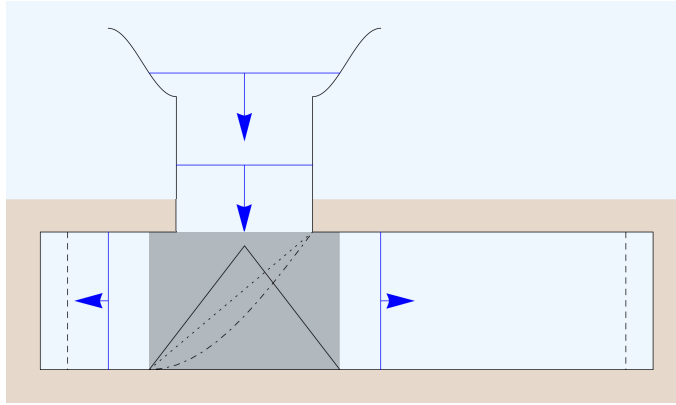


Figure 2.31: Resonance wave tank applications. The shaded gray region shows the region where it is believed a system should be implemented to correct the wave direction from perpendicular to parallel to the resonance wave tank direction. The solid, dotted and dot-dashed lines in these region show concept tested here without clear success.

The main challenge in using this idea of pump is to get the incident wave to split at an off-centered position in the wave rectifier. A top view of the concept is sketched in figure 2.31. Waves enter from the ocean perpendicularly to the resonance tank principal direction. A system must be implemented to get the waves entering the system to split equally or partially to travel in the tank direction. Experimentally, different designs were tested without clear success during this thesis¹⁸ : a) a 90° wedge deflector partially immersed (solid line in the shaded gray region), b) a straight inclined wall (dotted line) and c) a curved wall (dot-dashed line, in figure 2.31). The main critic to the tests being certainly the absence of wave absorber in the experimental setup at the wave generation which limits

¹⁷It corresponds to the sum of the two waves mass transport travelling away from the plunger.

¹⁸ More details on the tests are available in appendix N.

the time of the experiment and the fact that all these proposed designs block the surface and partially the water column (space was left near the sea bed to allow water circulation). In most cases, the tank ended in an undesired 3D sloshing regime and the flow was not unidirectional and uniform under the submerged plate. Another idea which was not tested experimentally is to vary the bathymetry in the shaded region to correct the wave direction using the Snell–Descartes law. This could be a better idea to get the wave energy to split and turn at the entrance of the RWT without obstructing the free surface.

Overall, using this concept to generate current from waves seems complex and thus other designs have to be considered. A simpler idea is to get the waves entering directly in the tank principal direction by one of the extremities. This is the case of waves above submerged plate studied in the next chapter.

Conclusion

In this chapter, a novel kind of Liebau’s pump was presented and studied experimentally, theoretically and numerically. The model proposed, based on simple linear theory, is able to capture the complex non-linear response of this Liebau’s pump. It shows the importance of the wave mass transport in the generation of currents with water waves. The linear potential theory enables to predict the interesting frequency range, while adding dissipation enables to guess the mean flow direction. The model developed for this free-surface Liebau’s pump could be extended to flexible tubes version. The main difference being mostly the surface condition, which is more complex in the case of flexible tube (solid-structure coupled problem). In the next chapter, it is shown that this bio-inspired pump is linked by the physical role of the wave mass transport to another system, which was originally studied in the ocean-engineering field for shore protection: the submerged plate breakwater. In both case, a circulation is observed around a submerged plate.

Chapter 3

Waves above a submerged plate

On présente ici un second exemple, exploitant le transfert de masse entre la couche de surface et l'intérieur du fluide pour la mise en place d'un écoulement moyen. Il s'agit du problème de vagues au dessus d'une plaque submergée. Il a été observé en 1968 par Dick [36] qu'un écoulement se mettait en place autour de la plaque sous l'action des vagues. Ici, le transport de masse est évalué et il est montré qu'il permet seul d'expliquer qualitativement les observations. L'ajout de la dissipation permet de prédire les effets du déferlement mais il manque encore la prise en compte d'autres phénomènes non-linéaires : le transport de masse dans les rouleaux, les efforts sur la plaque et sur la surface libre, les détachements tourbillonnaires... Cet exemple montre cependant directement comment exploiter l'idée de génération de courant pour l'extraction d'énergie des vagues. Le problème de vagues au dessus d'une plaque est simulé en utilisant la méthode SPH.

Abstract

As mentioned in chapter 2, to exploit the mass transport ability to generate currents, one needs to amplify it. It is possible to use the resonance’s properties in a closed pool or tank like in the RWT, but for industrial applications (see discussion in section 2.6) it is difficult to apply the previous idea to ocean wave energy harvesting. Instead, one can use the local change of depth to generate pumping along with pseudo-resonances. As an example, this chapter revisits the five decades old problem of waves above a submerged plate and presents a wave mass transport model to explain the observed circulation. The model is compared to simulations using the SPH method and experiments.

3.1 Introduction: From breakwater studies to a pump

Surprisingly, there is a link between the physics of waves above a submerged plate and the Liebau’s impedance pump. Dick [36] was evaluating the efficiency of submerged permeable breakwater for shore protection when he first observed a strange pumping phenomenon. His experiments consisted of stack nested cylinders with their principal axes parallel to the incident wave direction hold down by a rigid horizontal flat plate. He noticed a pulsating flow under the submerged plate in opposite direction to the incident wave while doing his experiments in a wave flume: a reverse pulsating flow seaward. In his thesis, he gave little explanations about this mean circulation and no actual measurements. He observed this circulation by injecting dye during some of his tests. He sketched the average path lines of the dye (see figure 3.1). These observations led to numerous studies and theoretical works on wave and submerged plate interactions. When looking at this problem, one can see some link to the previous bio-inspired case: the submerged plate and the pumping. The experiment of Dick is actually just the limit case of the previous study with a long tank compared to the submerged plate length and a “pincher” at one extremity. Rather surprisingly, this ocean-engineering breakwater is actually directly linked to the bio-inspired pump of the previous chapter through the wave mass transport properties.

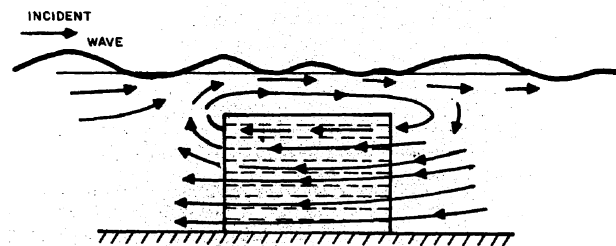


Figure 3.1: Average circulation at breakwater (figure extracted from Dick [36]). The arrow lines represent the path lines of the dye.

Siew and Hurley [147] and then Patarapanich [128] studied the case of long waves above a thin submerged plate theoretically. Patarapanich [128] was mostly investigating the conditions for maximum reflection but yet was the first to propose a theoretical explanation for the observed seaward circulation. He evaluated the flux of energy under the submerged plate and noticed that it was seaward for certain conditions and concluded that a mean circulation should therefore develop around the plate in the same direction as the flux of energy; though he did not comment on what happens outside this range. The link between flux of energy and mean flow is also rather left obscured in his discussion. Experimental observations of the flow around the submerged plate were made by [61–63, 120, 121] for different configurations. Murakami *et al.* [120, 121] studied the cases of horizontal and inclined submerged plate and provided measurements of the velocity around the plate. Brossard *et al.* [16] investigated the effect of the plate depth on the transmission and reflection coefficients, but did not look at the mean circulation. Graw *et al.* [63] led the effort to develop the concept as a wave energy converter (WEC) outlining the benefits of this technique compared to other devices. The key advantages, referring to their studies, are that it does not obstruct the surface, can resist to "killer waves" and is an efficient breakwater. Graw [61, 62] studied the submerged plate both as a wave filter (in the sense of attenuator that absorbs particular wavelength) and as a WEC. Hoeborn [72] proposed also an explanation for the observed circulation using an orbital motion argument. If this model is interesting and can be linked to the present argument through the Lagrangian drift, it is rather left incomplete.

In this chapter, the waves above a submerged plate problem is studied theoretically and numerically. For the first time (to the author's knowledge), a model based on the wave mass transport is proposed and compared to simulations and experimental observations. The model is based on linear potential theory and the case with dissipation is also considered similarly to what is done in the previous chapter. The model is then compared to numerical simulations. The simulations are run using the SPH method (presented in more details in appendix K). The simulations are compared to the experiments of Murakami *et al.* [120] and then used to see the effect of wave amplitude and frequency on the flow rate response. A 3D simulation is also presented as a preliminary investigation for wave energy harvesting.

3.2 Potential model for the waves above a submerged plate

This typical ocean engineering problem is frequently studied in regards of the potential wave theory. Ijima *et al.* [74] was the first to use the present eigenfunction expansions matching method for the case of a thin submerged plate in 1971, and Lui and Iskandarani [100] extended the solution to a thick plate in 1989. The method of matched expansions was applied to a submerged plate in shallow water first by Siew and Hurley [147] and then Patarapanich [128]. Cheong *et al.* [24] proposed a mixed solution between the eigenfunc-

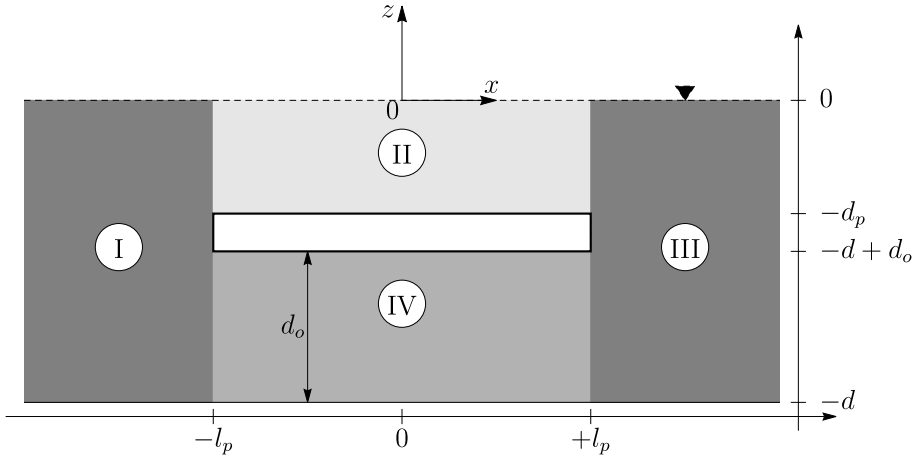


Figure 3.2: Domain decomposition for the waves above a submerged plate problem and notations.

tion expansions method and the long waves matched expansion to alleviate the numerical instabilities they encountered¹. Patarapanich [128] looked at the energy flux under the submerged plate and noticed that for certain frequencies this flux of energy was seaward. He concluded that this was at the origin of the observed circulation of Dick [36]. The long wave approximation is interesting as it enables to give analytical solution to the problem but it is valid only in the limit $d/\lambda \ll 1$.

3.2.1 General equations

In the present study, the eigenfunction expansions (EFE) matching method is applied to the problem of waves above a submerged plate. Consider a fluid of depth d and a submerged plate of length $2l_p$ and thickness t_p immersed d_p under the undisturbed water level leaving a recirculation height $d_o = d - d_p - t_p$. The non-dimensional notations introduced in section 1.2 are now used with the reference depth d of the incident wave. The problem for linear waves to be solved can be written as

$$\left\{ \begin{array}{ll} \Delta \Phi_{\mathbb{C}}^{(1)} = 0, & \text{for } (X, Z) \in \mathcal{D}_f, \text{ (Laplace equation)} \\ \partial_Z \Phi_{\mathbb{C}}^{(1)} = 0, & \text{at } Z = \{-1, D_o - 1\}, X \in]-L_p, L_p[, \text{ (sub. plate impermeability)} \\ \partial_X \Phi_{\mathbb{C}}^{(1)} = 0, & \text{at } X = \pm L_p, Z \in]D_o - 1, -D_p[, \text{ (sub. plate impermeability)} \\ \partial_Z \Phi_{\mathbb{C}}^{(1)} = 0, & \text{at } Z = -1, X \in]-\infty, +\infty[, \text{ (sea bed impermeability)} \\ \partial_Z \Phi_{\mathbb{C}}^{(1)} = \Omega^2 \Phi_{\mathbb{C}}^{(1)}, & \text{at } Z = 0, \text{ (free surface condition)} \end{array} \right. \quad (3.2.1)$$

where $\Phi^{(1)} = \Re \left\{ \Phi_{\mathbb{C}}^{(1)}(X, Z) e^{i\Omega T} \right\}$, \mathcal{D}_f is the fluid domain and all the distance are non-dimensionalized by the water-depth d (see figure 3.2) and $\Omega = \omega \sqrt{d/g}$. The equations are

¹This is probably mostly due to their choice of decomposition in the domain above the submerged plate.

completed by the radiation conditions, which can be written as

$$\left| \partial_X \Phi_C^{(1)} - iK_0 \Phi_C^{(1)} \right| \rightarrow 2 \frac{A\Omega}{\sinh K_0} \cosh [K_0 (Z + 1)], \quad X \rightarrow -\infty, \quad (3.2.2)$$

and

$$\left| \partial_X \Phi_C^{(1)} + iK_0 \Phi_C^{(1)} \right| \rightarrow 0, \quad X \rightarrow +\infty. \quad (3.2.3)$$

Note that this is equivalent to the radiation conditions of eq.1.3.71 for the step in section 1.3.4.3. The fluid domain is now decomposed in 4 rectangular domains (numbered from I to IV as shown in figure 3.2) and a 10-term expansion is used in each of them. This number of terms was found sufficient in the present applications, as computations with a larger number of terms did not exhibit any significant difference in the results².

3.2.2 Wave mass transport above the plate

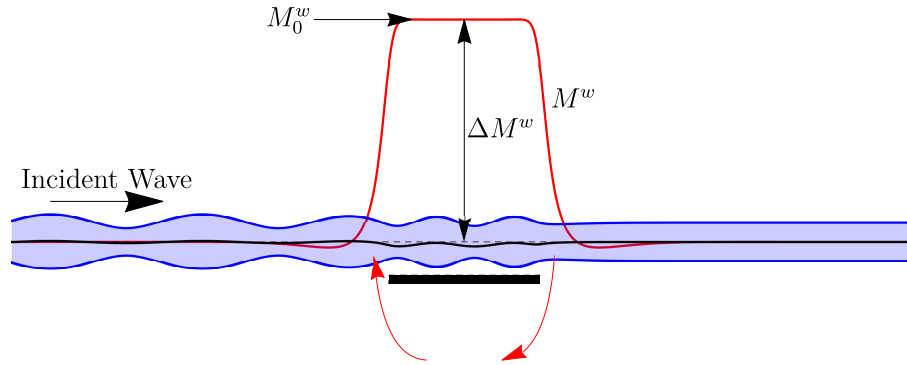


Figure 3.3: Wave mass transport at the origin of wave pumping. For the numerical application $D_p = d_p/d = 1/6$, $L_p = l_p/d = 1$, $T_p = t_p/d = 0.02$, $\Omega = 1.20$ and $a_{inc}/d = 0.1$. The shaded light blue region shows the linear potential predicted surface envelope. The black horizontal dashed line is the undisturbed surface and the solid one the mean water deformation. The red solid line shows the evolution of the wave mass transport.

From the linear theory solution, wave mass transport is evaluated (see eq.1.3.44). Figure 3.3 shows the general shape of the wave mass transport above a submerged plate. One can see that similarly to the wave at a step, the wave mass transport increases above the submerged plate (red solid line). The origin of the circulation observed by Dick [36] seems now clear. It comes from the suction at the leading edge of the plate induced by the wave interaction with the submerged structure. When the plate is “sufficiently” close to the water surface, the suction leads to the observed circulation. The flow under the submerged

²Note however that to reconstruct wave mass transport with good accuracy near the edges of the plate, the number of modes required can exceed 50 modes in each domains.

plate will be at second order the composition of an oscillatory flow (which comes from the linear theory solution) and the mean circulation (which comes from the variation of mass in the surface layer in the potential theory). This leads to a pulse-like flow. If the plate is deeper, the excess of mass in the surface layer could be compensated by suction from above the plate and the mean flow circulation reduced. If the waves reach the breaking threshold one can expect the wave mass transport to be significantly increased by the roller mass transport (see also [33] for a discussion on the surface Lagrangian drift during breaking). For now, the focus is on the effect of the wave frequency on the wave mass transport at the center of the submerged plate (M_0^w) and the wave mass transport jump ($\Delta M^w = M_0^w - M_{\pm\infty}^w$). These two quantities are defined in figure 3.3. The intensity of the oscillations are not discussed for now, but one should keep in mind that the flow oscillates under the submerged plate due to the first order response.

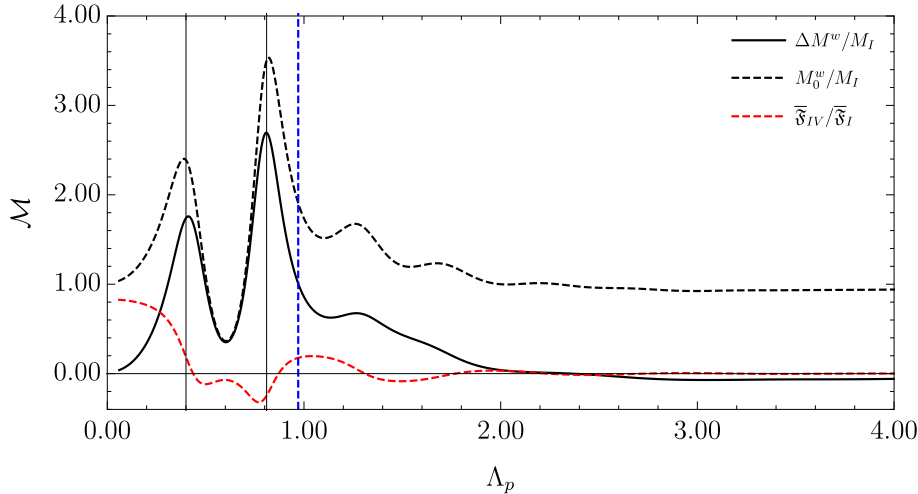


Figure 3.4: Evolution of the wave mass transport and energy flux, according to EFE method, with the non-dimensional length $\Lambda_p = 2l_p/\lambda_p$ and $d_p/d = 1/6$, $l_p/d = 1$, $t_p/d = 0.02$ fixed. The values are non-dimensionalized by the incident wave mass and energy flux. The vertical dashed line shows the configuration of Murakami et al. [120] which is outside the pumping prediction region of Patarapanich [128].

First the plate and its depth are fixed: $d_p/d = 1/6$, $l_p/d = 1$, $t_p/d = 0.02$. This corresponds to the case of a thin plate and for $\Omega = 1.20$, Murakami et al. [120] measured experimentally the velocity under the submerged plate and noticed the pulse flow of interest here³. As in experimental studies, usually $L_p = l_p/d$ and $D_p = d_p/d$ are fixed while the frequency of the waves are varied, in this theoretical description, these parameters are fixed. Patarapanich [128] worked differently as he fixed $d/\lambda \ll 1$ and D_p and then varied the plate length. This is a better strategy for the design of ocean applications as in practice, the parameter

³Note though that the case of Murakami *et al.* involves wave breaking. The effect of wave dissipation is discussed later.

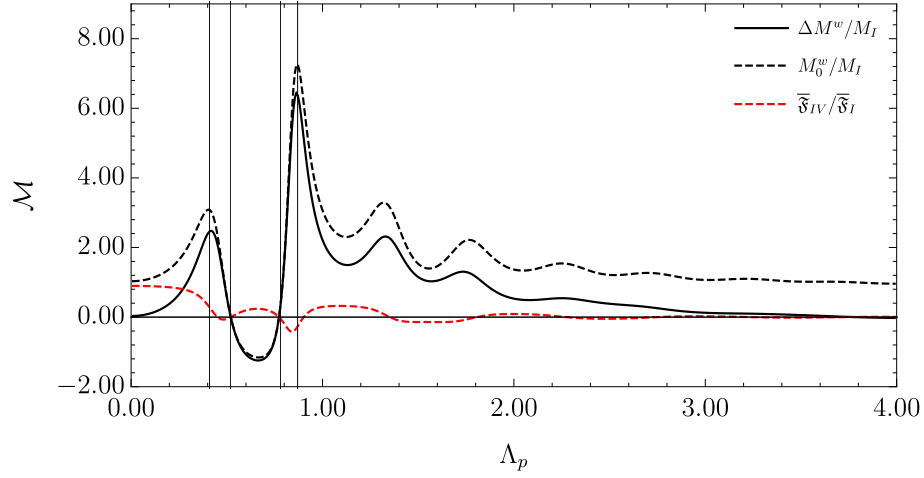


Figure 3.5: Evolution of the wave mass transport and energy flux, according to EFE method, with the non-dimensional length $\Lambda_p = 2l_p/\lambda_p$ and $D_p = d_p/d = 0.1$, $L_p = l_p/d = 1$, $T_p = t_p/d = 0.02$ fixed. The values are non-dimensionalized by the incident wave mass and energy flux. The wave mass transport quantities are negative for $\Lambda_p \in [0.52, 0.78]$.

d/λ (or its range for non-monochromatic waves) is known and then the system should be designed by selecting the proper D_p and L_p for this configuration. That being said, figure 3.4 shows the predicted mass flux quantities along with the energy flux under the submerged plate as a function of the non-dimensional length $\Lambda_p = 2l_p/\lambda_p$, where λ_p is the wavelength measured above the submerged plate using the local linear dispersion relation, using the EFE matching method. The wave mass transport is non-dimensionalized by the incident wave mass transport:

$$M_I = \frac{1}{2} \rho a_{inc}^2 \omega \coth k_0 d, \quad (3.2.4)$$

where a_{inc} is the incident wave height, ω is the incident wave angular frequency and k_0 is the wavenumber associated for the water-depth d . The wave energy flux is similarly non-dimensionalized by the incident energy flux (see eq.1.3.27).

Recall the energy flux was proposed by Patarapanich [128] as a way of predicting this circulation. In the figure 3.4 it is clear that the flux of energy⁴ is not directly linked to the observed pulse flow direction⁵. Similarly to the step, the wave mass transport jump becomes negative before slowly converging toward zero and the wave mass transport at the center of the step tends to the incident wave mass transport M_I as the frequency (here represented by Λ_p) is increased. In other words, for short waves, the jump of mass transport

⁴Note that the energy flux is of the order of 80% when $\Lambda_p \rightarrow 0$ here. Nonetheless, the focus is on the mean flow generation here rather than on the energy flux.

⁵It is even clearer when looking at the wave energy flux in the previous chapter case. One would find that it is positive near the peak of 1.6 Hz while the mean flow is negative.

is reversed and small. The interesting region is in shallow and intermediate waves regime. There, the wave mass transport increases considerably due to the wave interaction with the submerged obstacle. Two maxima are outlined by the vertical lines at $\Lambda_p \approx 0.4$ and $\Lambda \approx 0.81$. This shows that there are special frequencies for the waves above the submerged plate, or pseudo-resonance frequencies. In this configuration (fixed L_p and D_p), the mass transport at the center of the plate is always positive. This is not always the case as illustrated in figure 3.5 for $D_p = 0.1$ and $L_p = 1$. For this case, the wave mass transport at the center and the jump are both negative for $\Lambda_p \in [0.52, 0.78]$. This amounts to saying that the mass transport not only diminishes above the plate but actually that it travels in opposite direction to the incident waves. From an experimental point of view, this will look like waves are travelling against the incident waves above the plate.

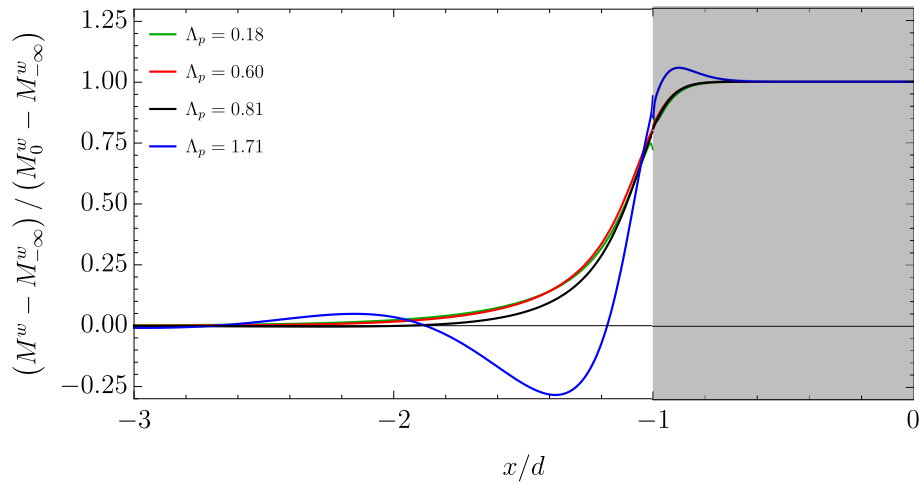
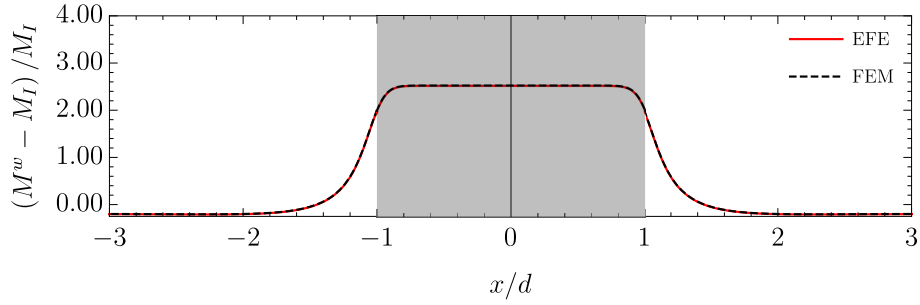


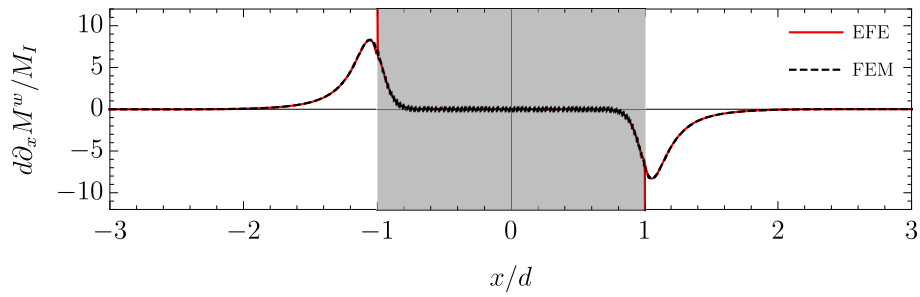
Figure 3.6: Wave mass transport profiles for four characteristic values of Λ_p for $D_p = 1/6$ and $L_p = 1$ fixed. The profiles varies on longer distance outside of the plate domain (shaded gray region). The profile is close to critically damped for the optimal value $\Lambda_p \approx 0.81$. For lower frequency it is damped while for higher frequencies it becomes underdamped and overshoots appear.

The variation of the wave mass transport with the horizontal direction is shown for four representative non-dimensional lengths in figure 3.6 for the configuration $L_p = 1$ and $D_p = 1/6$. The profiles are rescaled to be between 0 and 1. Only half of the profiles are shown as the wave mass transport is symmetric for this non-dissipative case. 50-term expansions are used to get better accuracy at the interface between the two domains. Small discrepancies are visible at the interface for this number of terms. Several comments have to be made about the wave mass transport profile. For high frequency, the profile can become underdamped and over-shoots appear. For lower frequency, the profile is damped. The profile is critically damped for the optimal value $\Lambda_p = 0.81$. The wave mass transport varies on a longer distance outside of the submerged plate domain. This facilitates the suction from under the plate as the maximum of variation is reached before the plate

limiting the suction from above it. This is due to the fact that the distance of variation of the mass transport typically scales like the characteristic distance of influence of evanescent modes, which is $l_d \in [1, 2] d/\pi$.

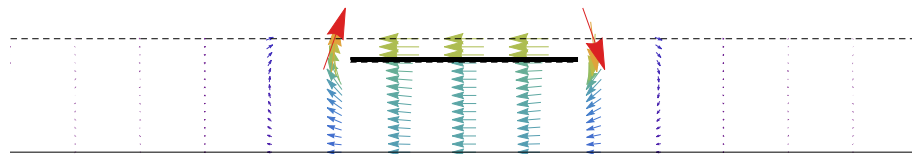


(a) Wave mass transport.

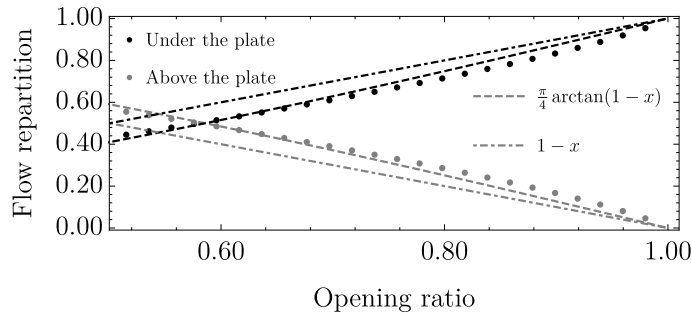


(b) Divergence of the wave mass transport.

Figure 3.7: FEM and EFE wave mass transport and divergence profiles for $d_p/d = 1/6$, $l_p/d = 1$, $t_p/d = 0.01$, and $\Lambda_p = 0.81$. The shaded gray region shows the position of the submerged plate. The divergence is used for the boundary condition for the mean potential flow equations.



(a) Potential mean flow.



(b) Potential flow repartition with opening ratio $1 - d_p / (d - t_p)$.

Figure 3.8: FEM solution for the potential mean flow equations and flow repartition.

To roughly evaluate the ratio of the flow going under the submerged plate, the second order potential mean flow equations are solved numerically assuming no-through flow conditions at the extremities of the numerical domains. This corresponds to a case where no return flow is considered. This way the role of local increase of the wave mass transport is isolated. The Finite Element Method (FEM) of *Mathematica* [75] is used. First the linear problem is solved using the FEM solver. The numerical domain is taken to be equal to 6 times the submerged plate length plus 20 times the maximum characteristic distance of influence of the evanescent modes: $l_t = 12l_p + 20l_d$, where $l_d = 2d/\pi$. The mesh is particularly refined near the edges of the submerged plate and the free surface. Radiation conditions of the form of eq.3.2.2 and 3.2.3 are enforced at the sea- and shore-sides to simulate an infinite tank. To validate the FEM solution, the wave mass transport is measured for $d_p/d = 1/6$, $l_p/d = 1$, $t_p/d = 0.01$, and $\Lambda_p = 0.81$ and compared to the eigenfunction expansion method (EFE). The wave mass transport variation and divergence are shown in figure 3.7. There is a good agreement between the two solutions. For the EFE method, the divergence of the mass transport diverges at the interface between two domains. This is due to the slow convergence of the coefficients with the number of modes⁶.

The divergence of the wave mass transport is used as a boundary condition for the mean velocity potential equations (see section 1.4.1) assuming no through flow at the far boundaries. The obtained velocity field is shown in the top figure of figure 3.8. This velocity field corresponds to the solution in the limit of infinitely small waves, for a flat mean surface and an ideal fluid in potential flow. In general none of these assumptions are verified but this development gives an idea of the penetration of the wave mass transport and what is the maximum depth the plate should be placed at. The ratio of the mass travelling above and under the plate is plotted in the bottom figure of figure 3.8 as a function of the opening ratio $1 - d_p/(d - t_p)$. It corresponds to the part of the section under the plate. In the simulation, the plate depth is varied. The effect of varying the plate thickness is quite similar. One can see that the opening ratio should not be less than 60%. In the limit of thin plate, this means that the plate should not be placed lower than 40% of the water depth.

In experimental cases, the far-field conditions enforce no mean flow in the total cross section. This means that the entire mass flux in the surface layer at the shore-side is compensated by an opposite mean flow in the interior of the fluid domain. This leads to an increase of the mean flow recirculating under the submerged plate. Furthermore, the surface layer and the mean water level set-down above the plate are usually blocking most of the water depth above the submerged plate (as shown in figure 3.3 by the shaded blue area) limiting the return flow above the plate⁷. The relevant parameter to estimate the

⁶The coefficients converge like $N^{-5/3}$ as shown in appendix C and thus the solution diverges when derived twice at the interface.

⁷The surface shear should also be taken into account here.

flow around the plate is then the maximum value reached by the wave mass transport.

In most cases, due to the proximity of the submerged plate with the free surface, dissipation is important in the wave interaction. Two kinds of dissipation are predominant in this problem: the friction on the submerged plate, which will lead to vortex shedding as observed by Poupardin et al. [134] and wave breaking, as reported by Murakami et al. [120] and Carter et al. [22]. In the next subsection, the effect of adding dissipation on the wave mass transport maximum value is discussed. The development is limited to surface dissipation model as presented in section 1.5.3.

3.2.3 Wave mass transport and dissipation

In this part, the effect of the potential wave dissipation model on the mass transport is discussed. As wave breaking is expected to happen above the submerged plate, in the present discussion, the dissipative terms are limited to this region (domain II in figure 3.2). For the sake of simplicity the dissipation is considered constant in this domain. The dissipation is represented by a surface viscosity ν_s and the associated Reynolds number⁸ is $\mathcal{R} = \sqrt{gd_p^3}/\nu_s$. To compare different frequencies, the Reynolds number is scaled by the limit Reynolds number \mathcal{R}_{limit} above the plate (see eq.1.5.26):

$$\mathcal{R}_{limit} = \frac{(K_0^p)^2}{\Omega} \left(\frac{4 \sinh 2K_0^p D_p}{2K_0^p D_p + \sinh 2K_0^p D_p} \right)^{2/3}, \quad (3.2.5)$$

where $D_p = d_p/d$, $K_0^p = k_0^p d$ is the non-dimensional wave number with respect to d , solution of the dispersion relation:

$$\Omega^2 = K^p \tanh K^p D_p. \quad (3.2.6)$$

As explained in chapter 1, this corresponds to the maximum dissipation one can achieve above the submerged plate. Instead of fixing the wave amplitude and evaluating a value of \mathcal{R} to verify a breaking criterium, in this section the dissipation is fixed. This means that the wave dissipation above the plate is considered of the same order for all the frequencies. This choice is made as it is difficult to define here a suitable breaking criterium as the wave travelling seaward and shoreward above the plate can be of drastic different amplitudes. In the case where their amplitudes are close to each other, the breaking criterium should be near the one of a standing wave, and otherwise it should be near the one of a travelling wave. As the goal is not to provide a quantitative model but rather to understand the effect of dissipation above the plate, it seems sufficient to look at the result with fixed

⁸Note that the Reynolds number is evaluated with respect to the water depth d_p while all the other parameters are evaluated with respect to the reference depth d . See nomenclature for details. The Reynolds number defined with respect to d_p (here \mathcal{R}) defers to the one defined with respect to d (call it \mathcal{R}_d) by simply a factor $D_p^{3/2}$: $\mathcal{R} = \mathcal{R}_d D_p^{3/2}$.

dissipation.

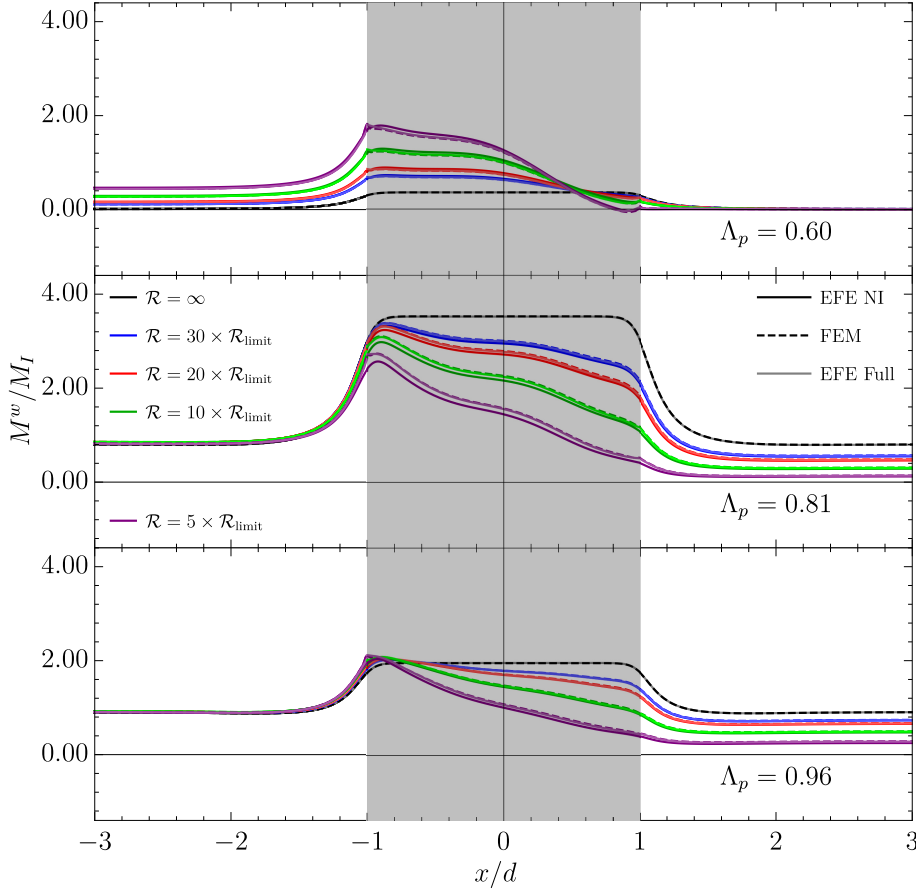


Figure 3.9: Wave mass transport profiles and dissipation for different Λ_p for $L_p = 1$ and $D_p = 1/6$. In the figures, the darker solid lines shows the solution with the EFE NI method (where dissipation is limited to the propagative terms), the dashed line shows the numerical solution using a FEM with a shooting method and the lighter solid line shows the solution found using the EFE with all the dissipative modes. The color lines show different Reynolds numbers defined with respect to the water depth above the plate. The shaded gray region shows the horizontal position of the submerged plate. The three values of Λ_p represent a local minimum, maximum and a value similar to the experimental case of Murakami et al. [120] in the evolution of the wave mass transport with Λ_p in figure 3.4.

For now the configuration is fixed to $D_p = d_p/d = 1/6$ and $L_p = l_p/d = 1$. In this configuration the wave mass transport jump and maximum are always positive in the linear potential theory without dissipation. The system is solved similarly to the previous chapter by limiting the dissipation to the propagative modes (EFE NI). The wave mass transport profiles for different values of the surface viscosity ν_s and different Λ_p are shown in figure 3.9 and compared to the solution found by solving the full dissipation problem

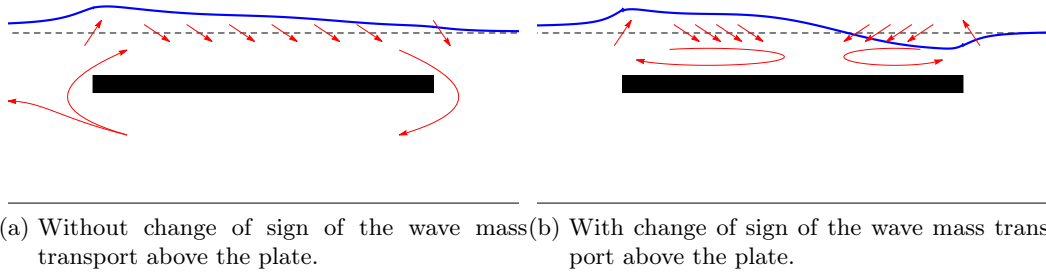


Figure 3.10: Sketch of the two possible kinds of mean flow in the waves above submerged plate problem with dissipation.

with a FEM solver⁹ and the full dissipation eigenfunction expansion matching method (EFE Full)¹⁰. Note that Λ_p is defined based on the wave number without dissipation. The solution limited to the propagative terms provides sufficient accuracy and the same effect. In the rest only the EFE NI is used and discussed. In all the cases, adding dissipation leads to non-symmetric mass transport profiles. It decays above the submerged plate. The maximum of the wave mass transport is reached close to the leading edge of the submerged plate for this configuration. The wave mass transport at the shore-side diminishes with an increase of the dissipation. If one considers that the far field conditions enforced no through flow in the water column (which is the case for an experimental wave flume), this means that all the mass travelling in the surface layer above the plate has to recirculate under it. The important value to estimate the mean flow intensity under the plate is then clearly the maximum wave mass transport reached. This is sketched in figure 3.10-a.

For the three selected values of Λ_p , one can observe three distinct behaviors. For $\Lambda_p = 0.81$, the value is close to the optimal of the potential theory for this configuration and increasing the dissipation leads to a diminution of the maximum wave mass transport value above the plate. Intuitively, when waves start breaking the efficiency drops¹¹. For $\Lambda_p = 0.60$, the value is close to a local minimum of the potential theory. In the present configuration, both the wave mass transport jump and the wave mass transport maximum value predicted by the linear potential theory are positive. An increase of the dissipation leads to an increase of the mass transport maximum above the plate. For this case, wave breaking should lead to an increase of the mean flow efficiency. For the last case, the value is close to the one of the experimental case of Murakami et al. [120] simulated in the next section. An increase of the dissipation leads to a small increase of the maximum of the wave

⁹A shooting method is used to enforce the dissipation at the surface in the FEM solver.

¹⁰This takes significantly longer to be solved. To find the solution with a 10-term (50-term) expansion, one needs about 0.6 s (22 s) for the linear potential solution, 0.6 s (22 s) for the solution with dissipation limited to the propagative terms and 23.5 s (159 s) for the full dissipative solution with dissipation. The solution also requires more modes to be fully converged. While with the limited dissipation model 10-terms expansion is found sufficient, with the full model one needs over 50-terms. There are little differences between the two, not worth the computational effort.

¹¹Roller mass transport is not considered for now.

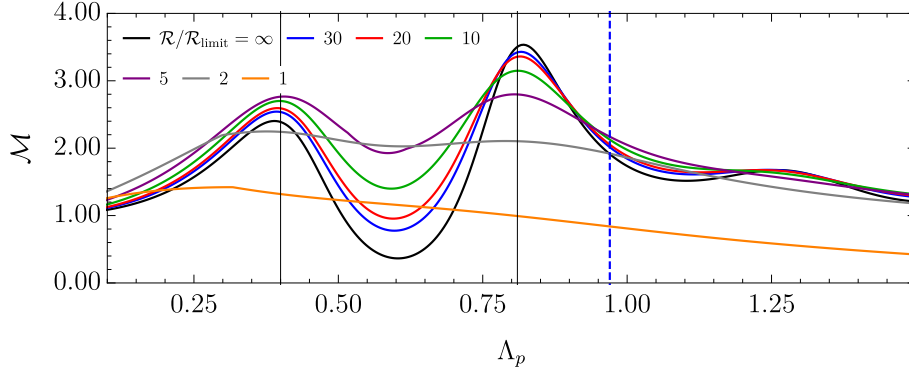


Figure 3.11: Wave mass transport with dissipation for $D_p = 1/6$ and $L_p = 1$ with EFE NI. The color lines show the wave mass transport maximum values above the submerged plate non-dimensionalized by the incident wave mass transport. If the wave mass transport changes sign above the plate, the value is switched to the sum of the two extrema at the seaside and shoreside. Here $\mathcal{M} = M_{max}^w/M_I$, such that the continuous solid black line here is exactly equivalent to the dashed black line in figure 3.4 since $M_{max}^w = M_0^w$. The vertical blue dashed line shows the value of Λ_p for the case of Murakami et al. [120].

mass transport. Overall, an increase of the dissipation tends to uniformize the wave mass transport response: increase the efficiency of minima and reduce the efficiency of maxima. The evolution of the wave mass transport maximum¹² with the parameter Λ_p is shown in figure 3.11. When the dissipation is further increased the efficiency drops uniformly on the entire spectrum.

In all the cases considered so far, the wave mass transport is always positive above the submerged plate. In certain cases, the wave mass transport might change sign above the plate. This is more likely to happen in configurations where the potential wave mass transport without dissipation is negative. Consider now a configuration where $D_p = d_p/d = 0.1$ and $L_p = l_p/d = 1$ and $\Lambda_p = 0.65$. In figure 3.5, the predicted wave mass transport jump and maximum are negative. The circulation is thus expected to be reversed. Adding dissipation leads to a change of sign of the wave mass transport above the plate. Figure 3.12 shows the wave mass transport profiles for this case and different Reynolds number. The extremum value of the wave mass transport at the shoreside does not change drastically with the dissipation. On the contrary at the seaside, as the dissipation is increased, the wave mass transport continues to increase and eventually changes sign. In this case, on top of the plate, the wave mass transported in the surface layer switches direction. Circulation cells can be expected above the plate as sketched in figure 3.10-b. The direction of the flow under the plate will depend on which extremum has the largest absolute value as a first approximation. The intensity of the flow is also penalized. As a rough estimate, one can

¹²The wave mass transport maximum is evaluated by solving the problem with a 10-term expansion and evaluating the mass transport with only the propagative terms, such that in the absence of dissipation its equivalent to M_0^w . It also avoids difficulties when the expansion is not well converged at the interfaces.

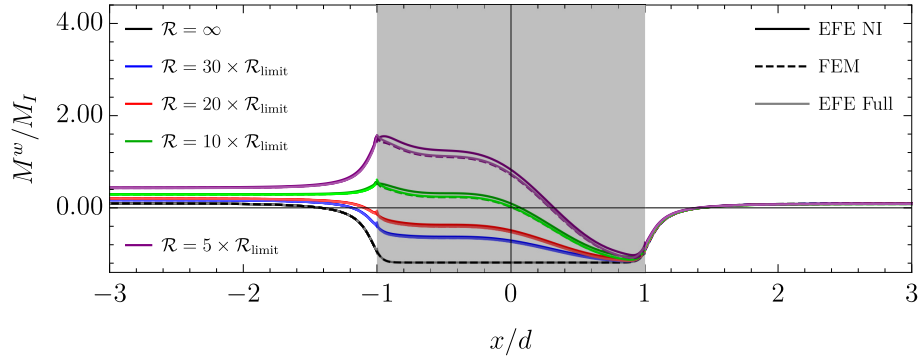


Figure 3.12: Wave mass transport profiles and dissipation for $\Lambda_p = 0.65$ for $L_p = 1$ and $D_p = 0.1$. In this case, the wave mass transport is negative above the plate in the potential theory. In the figures, the darker solid lines shows the solution with the EFE NI method (where dissipation is limited to the propagative terms), the dashed line shows the numerical solution using a FEM with a shooting method and the lighter solid line shows the solution found using the EFE with all the dissipative modes. The color lines show different Reynolds number defined with respect to the water depth above the plate. The shaded gray region shows the the horizontal position of the submerged plate. In this configuration, the wave mass transport changes sign for large dissipation.

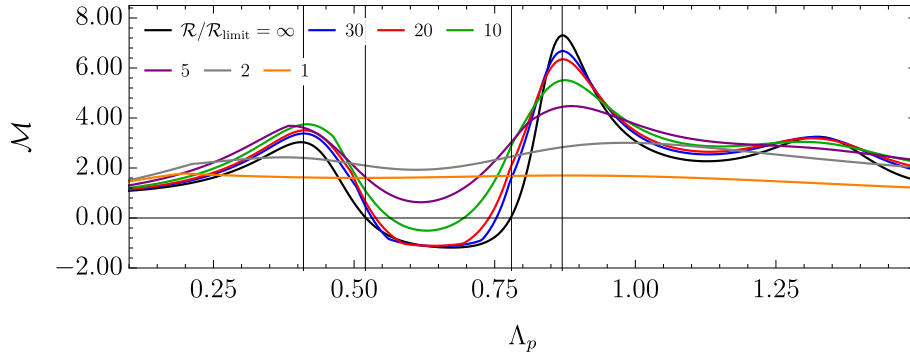


Figure 3.13: Wave mass transport with dissipation for $D_p = 0.1$ and $L_p = 1$ with EFE NI. The color lines show the wave mass transport maximum values above the submerged plate non-dimensionalized by the incident wave mass transport. If the wave mass transport changes sign above the plate, the value is switched to the sum of the two extrema at the seaside and shoreside. Here $\mathcal{M} = M_{max}^w/M_I$, such that the continuous solid black line here is exactly equivalent to the dashed black line in figure 3.4 since $M_{max}^w = M_0^w$. The vertical lines show the maximum and the zero's of the EFE solution without dissipation.

consider that when this happens the intensity of the flow is the sum of the two extrema of the wave mass transport above the plate. Otherwise, the intensity of the flow under the plate scales like the maximum absolute value of the two and the direction is directed by its sign. A positive value of this quantity means that a clockwise circulation is expected (counterclockwise otherwise). The evolution of the wave mass transport maximum with

the parameter Λ_p is shown in figure 3.13. The negative region quickly disappears which means it is in practice unlikely to happen or have significant mean flow.

Note that in this section, the additional mass transport coming from the wave rolling has not been taken into account. In section 3.3.4, it will be proposed as an improvement to the current model. The surface shear stress is also not taken into account as it mostly ensures that the flow coming from the surface layer is pushed in the direction of the wave breaking. The discussion is mostly qualitative.

3.2.4 Oscillations under the submerged plate and dissipation

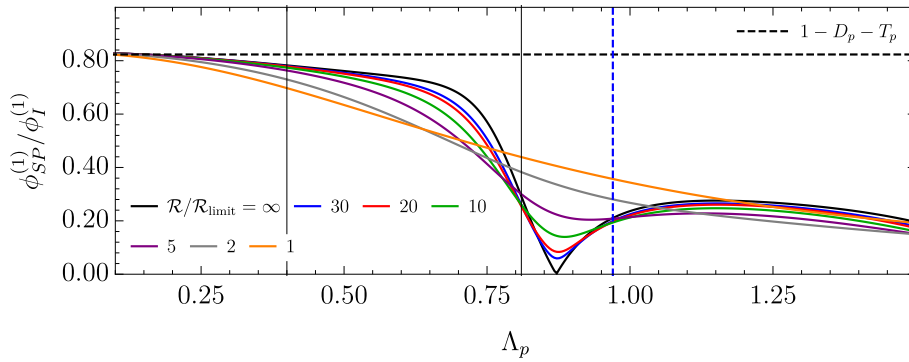


Figure 3.14: Amplitude of oscillations under the submerged plate with dissipation for $D_p = 1/6$ and $L_p = 1$ with EFE NI method. The color lines show the amplitude of oscillations non-dimensionalized by the amplitude of oscillation of the incident wave flow rate on a water column. The horizontal dashed line shows the ratio of the opening height under the submerged plate over the undisturbed water column $d/(d - d_p - t_p)$. The vertical blue dashed line shows the value of Λ_p for the case of Murakami et al. [120].

The dissipation also affects the oscillation amplitude under the submerged plate. Figure 3.14 shows the amplitude of the oscillations of the flow rate under the submerged plate as a function of Λ_p for different \mathcal{R} for $L_p = 1$ and $D_p = 1/6$ non-dimensionalized by the amplitude of the oscillation of the flow rate of the incident wave on a water column:

$$\phi_I^{(1)} = \int_{-d}^0 \partial_x \varphi_{inc}^{(1)} dz = \frac{a_{inc} \omega}{k_0}. \quad (3.2.7)$$

The horizontal dashed line shows the ratio of the opening height under the submerged plate over the undisturbed water column $d/(d - d_p - t_p)$. A value above this line means that the oscillatory flow is amplified by the structure. This can happen theoretically when D_p is small (less than $D_p < 0.1$). Dissipation damps this resonance effect and thus it is not observed in practice. Note that the maximum of the wave mass transport at $\Lambda_p = 0.81$ does not usually match the zero of oscillation (or frozen regime). It depends both on the water depth and plate length.

Adding dissipation makes the frozen regime disappear. Away from this peculiar response, increasing the dissipation leads to a diminution of the non-dimensional amplitude of oscillation. This means that the dimensional amplitude of oscillations increases less fast than linearly with the wave amplitude, while the dimensional mean flow (or wave mass transport) increases faster than quadratically. This is the case for instance for $\Lambda_p \approx 0.60$. The flow under the submerged plate can thus get closer to a pulse flow. The mean flow and oscillations become of the same order. On the other hand, near the maximum $\Lambda_p = 0.81$, the non-dimensional amplitude of oscillations increases with the dissipation while the wave mass transport decreases. The flow under the plate is thus not getting more “rectified”.

In this section, the linear theory showed that wave mass transport is at the origin of the observed circulation and that using a simple submerged structure one can pump with water waves. Note that in this section, the interaction wave tensor is not taken into account and could affect the pumping efficiency as it influences the flow on typical scales of the order of $\lambda_p/2$, where λ_p is the wavelength of waves above the plate. Other effects such as friction on the submerged plate is also neglected and it can amplify the pumping through acoustic streaming phenomenon. The vortex shedding also plays a significant role in the mean flow dynamics [16]. The amplitude of the harmonic modes generated above the plate and downstream of the structure are not negligible for this shallow submergence and may actually have amplitude of the same magnitude as the first harmonic. Their effects on the mean flow have not been taken into account.

The effect of wave breaking is modeled using a simple dissipation potential model and showed that one could expect the response to be quasi-independent of the frequency for large waves where dissipation is strong. In the next section, the model is compared to numerical simulations using the SPH method in 2D and to experiments for both the predictions of the reflection and transmission coefficients and the mean flow under the plate. In the absence of wave breaking, a correction to the dissipation model is proposed. It is based on the dissipation rate in the case of sea-bed dominated friction. In the last section a 3D case is presented.

3.3 2D-SPH simulations

In this section, periodic waves above a submerged plate are simulated using the SPH method and compared to the novel wave mass transport justification for the observed circulation. In the subsection 3.3.1, the numerical wave tank used for the simulations is presented. In subsection 3.3.2, two cases are simulated and compared to the experimental results of Brossard *et al.* [16] for the transmission and reflection coefficients and of Murakami *et al.* [120] for the mean flow under the submerged plate (see also appendix M for an additional validation using new experimental observation). In the latter case,

a boundary layer resolved (BLR) simulation is provided. In subsection 3.3.4, the mean Eulerian mass flux is evaluated and outlines the previously discussed transfer of mass from the interior of the flow to the surface layer at the leading edge of the submerged plate. This suction is due to an increase of the wave mass transport in the surface layer above the submerged plate. Wave height and frequency are varied and the results are compared to the previous model. Details about the SPH numerical methods are provided in appendix K.

3.3.1 SPH numerical wave tank

The experiments of waves above a submerged plate are usually conducted in a wave flume of about 10 m long by 25 cm wide with variable height (see [16, 120, 121, 134], and also appendix M) composed of a piston or flap type wave maker with or without active absorption. A sloping beach composed of absorbing foam is used to passively limit reflection in the last meters (usually about 2 meters) with typical reflection of the order of $\lesssim 10\%$ [139]. The submerged plate is positioned near the center of the tank and spans all its width. This allows a 2D approximation. In the present simulations, a piston-type wave maker with active absorption and a damping sponge layer instead of a sloping beach are used. Figure 3.15 shows a sketch of the numerical wave tank with the notations. In the next paragraph, the numerical absorption method is quickly presented. More details can be found in appendix I and in [20], where an optimization is proposed. The method to absorb the waves at the piston wave maker is also detailed and validated.

Wave Generator

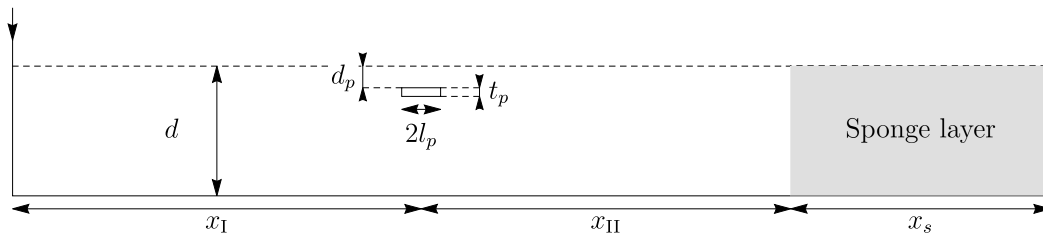


Figure 3.15: Sketch of the numerical wave tank used to simulate waves above a submerged plate: d is the water depth, d_p the submerged plate depth, l_p the half length of the submerged plate and t_p its thickness, which should be at least 4 particle size. The wave generator is placed x_I before the center of the submerged plate and a x_s long sponge layer is used x_{II} behind to limit reflections. The total tank length is $l_{tank} = x_I + x_{II} + x_s$.

3.3.1.1 Wave passive absorption (Sponge layer)

To avoid reflection at the end of the wave tank and limit its length, a passive absorption domain is used (see shaded region in figure 3.15). The principle is quite similar to previous

sponge layer methods [6, 25] but yet is developed in a more physical manner to allow optimization (discussed in appendix I). A damping term of the form $-B(x)\omega\mathbf{u}$ is added to the momentum equation, which is responsible for a kinetic energy dissipation. In the present simulations, the damping term function is of the form:

$$B(x) = \begin{cases} 0 & , x < x_0 \\ B_{\max} \left(1 - \frac{x_{\max}-x}{x_{\max}-x_0}\right)^{n_B} & , x_0 < x < x_{\max} \\ B_{\max} & , x > x_{\max} \end{cases} \quad (3.3.1)$$

where x_0 and x_{\max} are the positions of the beginning and the end of the varying part of the dissipation coefficient, n_B is a power coefficient and B_{\max} is the maximum value of dissipation scalar function and is proportional to the inverse of a time. The advantages of this formulation are that, likewise the one proposed by Altomare *et al.* [6] and Cherfils *et al.* [25], it can be implemented implicitly (there is no limitation on the time step). Optimal values of the coefficients are provided in appendix I. In all the results presented in this paragraph the coefficients are not always at their optimal values, but the reflection from the sponge layer does not alter significantly the results and does not exceed 10% in all the simulations. The lack of table and method to select the proper value led the author to submitting recently a discussion on sponge layer optimization [20].

3.3.1.2 Wave generation and active absorption

In the experimental tanks, a piston or flap wave makers are usually used to generate waves. In the present study, a piston-like wave maker is used similarly to the previous works [6, 25, 37] using the SPH method. Using the linear potential theory and eigenvalue expansion method [12] (see section 1.3.4.1), it is possible to deduce the piston stroke amplitude s_0 required to generate a target wave height $h_{\text{inc}} = 2a_{\text{inc}}$ at a given angular frequency $\omega = 2\pi f_0$:

$$s_0 = h_{\text{inc}} \frac{2k_0 d + \sinh 2k_0 d}{8 \sinh^2 k_0 d}, \quad (3.3.2)$$

where k_0 is the wave number solution of the linear dispersion relation $\omega^2 = gk \tanh kd$. The velocity at the piston is then $u_0(t) = s_0 \omega \sin \omega t$. Note that in Weakly Compressible SPH (WCSPH), it is important to start with a zero initial velocity to avoid acoustic shocks at the initial time, which will perturb the mean flow.

To validate the wave generation, the target wave amplitude h_{inc} is varied in a tank composed of a ‘‘physical’’ part¹³ of length 2 m and a sponge region of length one wavelength. The frequency is fixed to $f_0 = 1.5\text{Hz}$. The particle size, r_{SPH} , is fixed so that $d/r_{\text{SPH}} = 60$. The sponge layer function power is $n_B = 3$ and $B_{\text{mean}} = 0.46$ (see eq.I.3.15). The simulations are ran for 30 seconds of physical time (which takes about 1h30 to run on a single

¹³Physical part means here without fictitious absorption.

GPU's card with the Sphynx code, see appendix K). The surface particle positions are sampled at $dt = T/101$, where $T = 1/f_0$ is the wave period, using Marrone *et al.*'s method [103] with a threshold of 0.55. Figure 3.16 shows the result of the wave height and reflection coefficient using the two-probes method of Goda & Suzuki [59]. Probes are defined as surface interrogation area of length $2r_{SPH}$. The probes are spaced by $0.25 \times \lambda$ and moved along the physical part of the tank starting $0.25 \times \lambda$ away from the wave maker mean position and stopping $0.25 \times \lambda$ before the beginning of the sponge layer. The standard deviation of the reflection is larger for the smallest target wave height due to the relative coarseness. The wave height measure is slightly below the target. This is partially due to the reflection (though it is as desired below 5%), the non-linearity for the highest wave targets, and to the numerical dissipation¹⁴.

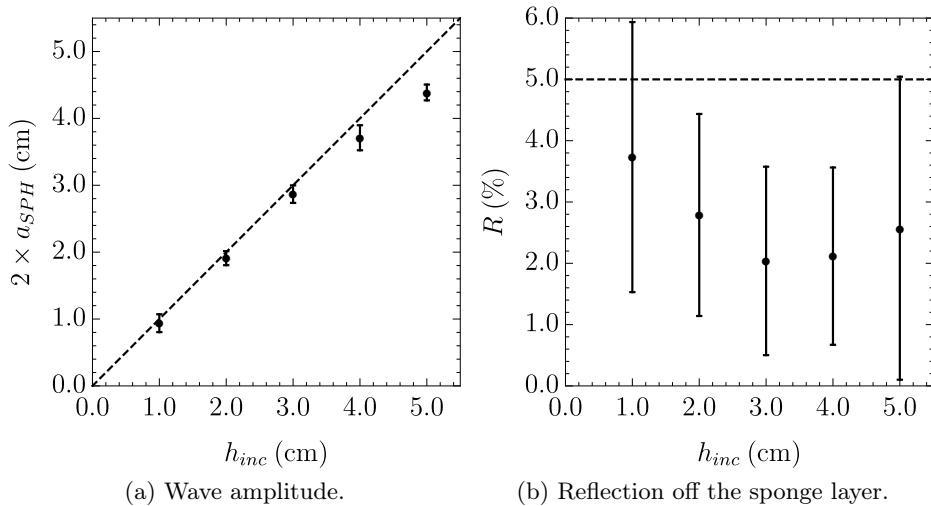


Figure 3.16: Wave generation and reflection in SPH. Simulation in a tank of length $l_t = 2.63$ m, with $f_0 = 1.5$ Hz and a sponge layer of length λ , with $n_B = 3$ and $B_{mean} = 0.45$. The two-probes method of Goda & Suzuki [59] is applied.

When waves interact with structures there are reflections and thus waves travelling back to the piston. In the case of submerged plate, the reflection can be important (of the order of 50% of the incident wave height for the experimental cases of Brossard *et al.* [16]). The waves will then reflect back on the wave maker and perturb the incident wave height. Experimentally it is possible to quickly adjust the wave amplitude by manually varying the piston control till getting the desired wave height (as done in [16, 134] for instance), numerically it is more complex and time consuming as it will require restarting the simulation. Instead, an Active Wave Absorption System (AWAS- η) is implemented as done in [6, 37]. A sketched of the principle of the AWAS- η is shown in figure 3.17. In the present simulations, at each time step, the water elevation at the piston is evaluated.

¹⁴Note also that for the highest amplitude, the mean water level rises in the sponge layer (set-up).

The surface particles up to 0.05λ from the piston are tracked. The surface data are then fitted to a line to extrapolate the measurement of the water elevation at the piston. The instantaneous surface displacement $\eta_{w.m.}$ at the wave maker is then deduced by subtracting the initial water depth. It is compared to the target incident wave $\eta_{inc} = a_{inc} \sin \omega t$. This gives the wave to absorb at the piston to avoid the reflection $\eta_R = \eta_{inc} - \eta_{w.m.}$. The velocity of the piston is corrected to generate the negative reflected wave to cancel the reflection by superposition. One can use the previously developed piston control and this gives:

$$u_R(t) = \eta_R(t)\omega \frac{2k_0d + \sinh 2k_0d}{4 \sinh^2 k_0d}, \quad (3.3.3)$$

referred to as AWAS-mono for monochromatic. In the limit of long waves this leads to the more common control:

$$u_R(t) = \eta_R(t)\sqrt{g/d}, \quad (3.3.4)$$

referred to as AWAS-LW.

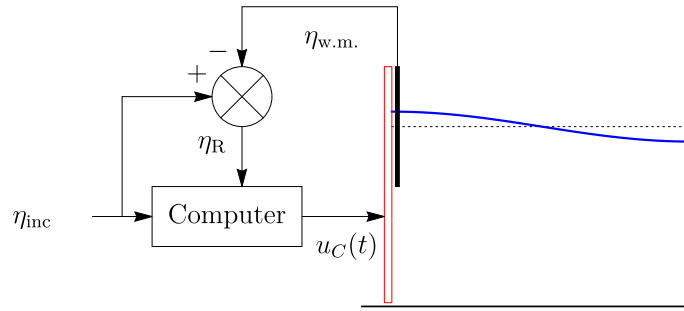


Figure 3.17: Sketch of the AWAS- η principle.

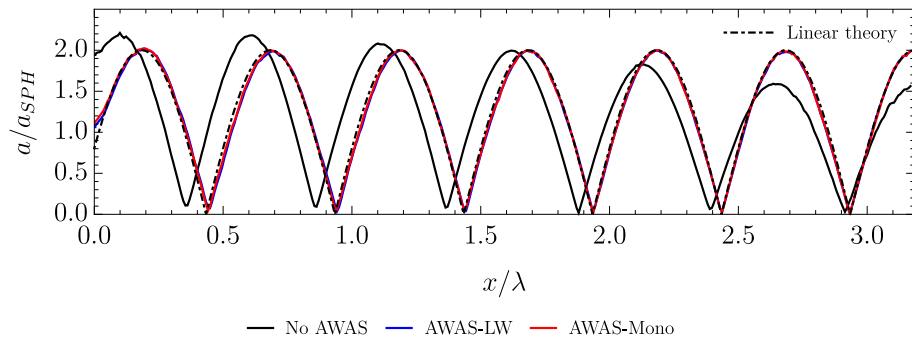


Figure 3.18: Validation AWAS in the SPH simulations: Compared tank without AWAS, with AWAS-LW and AWAS-Mono for $L = 2$ m, $h_{inc} = 2$ cm, $d/r_{SPH} = 60$ and $k_0d = 1.5$ (blue and red curves are almost superimposed).

The latter is more suitable in the case of random waves as it does not require the wave number. In the present study, only monochromatic waves are simulated thus the former seems adapted. The final control of the piston is then $u_C = u_0(t) + u_R(t)$, where $u_0(t)$ is the control with no AWAS. Figure 3.18 shows the linear surface envelope for a tank

without sponge layer and $L = 2$ m, $d = 15$ cm ($x_s = 0$ m) with and without AWAS. The reflection is correctly recovered in both cases. The AWAS-LW works well with a measured linear wave height $2a_{SPH} = 1.95 \pm 0.03$ cm and reflection coefficient of $R = 0.96 \pm 0.02$. Yet the AWAS-Mono provides a better absorption $R = 0.97 \pm 0.02$ but a less good wave height $2a_{SPH} = 1.88 \pm 0.03$ cm.

Note that the accuracy on time is important as it is used to control the piston. Double precision is used in the present SPH method for the time accuracy. In single precision, a Kahan summation or a module of time on a factor of wave period should be performed to avoid error accumulation [69].

3.3.2 Validations

In this section, the simulations of the waves above the submerged plate using the SPH method are compared to two experimental cases to validate the ability of the method to properly capture the physics of the waves interaction with a submerged structure (an additional validation is provided with new experimental data in appendix M). They are also compared to the linear models without and with dissipation. The roller wave mass transport is also considered for the second case.

3.3.2.1 Reflection and transmission coefficients

The first test corresponds to the experimental case of Brossard *et al.* [16], here modeled in 2D. The numerical parameters used are summarized in table 3.1 as *Bros*. The resolution is fixed to $d/r_{SPH} = 80$ and the simulations are ran for 30 seconds or at least 27 wave periods. A simulation takes around 2.5 days to run with *Sphynx* on a single GPU card. In this configuration, note that the parameters $D_p = 0.25$ and $L_p = 0.625$. Thus it is not a surprise that the mean flow is not reported in this study as in the linear theory the wave mass transport jump is not significant enough. The maximum jump in the linear potential theory is less than one (while it is almost three for the case of Murakami *et al.*) and the submergence is important.

The incident wave amplitude, the reflection and transmission coefficients are measured using the two-probes method of Goda & Suzuki [59]. The probe stops $10/\alpha_1$ away from the limits of the domain before and after the submerged plate edges, where α_1 is the first evanescent eigenvalue solution of $\omega^2 = -g\alpha \tan \alpha d$. The results are plotted in figure 3.19 as a function of the non-dimensional length defined in the previous section $\Lambda_p = 2l_p/\lambda_p$. The results of the simulations overestimate the reflection and transmission coefficients leading to less dissipation $\epsilon = 1 - R^2 - T^2$. This is due to the resolution, which affects the results in two ways. First, the simulated submerged plate is thicker than in the experiments ($t_{SPH} = \max\{4r_{SPH}, t_p\} = 1$ cm instead of $t_p = 0.02$ cm). Second, the resolution does not

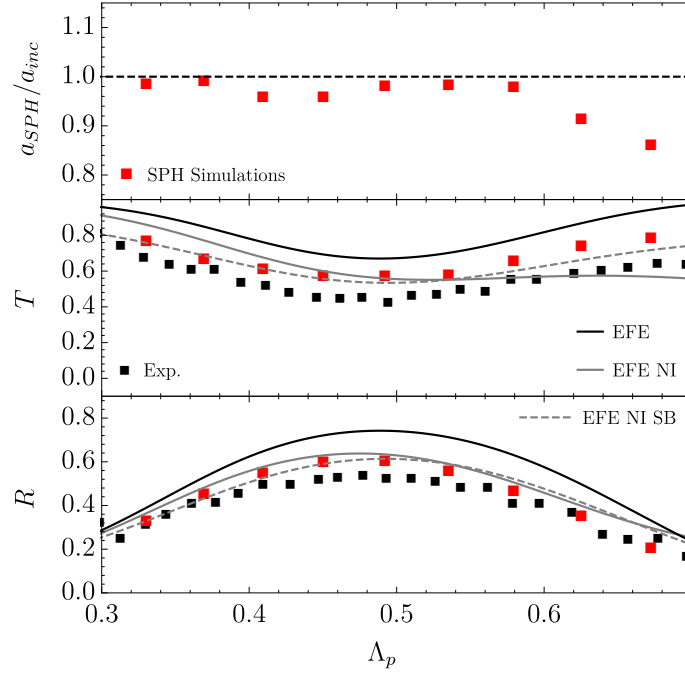


Figure 3.19: Non-dimensional incident wave amplitude, transmission and reflection coefficients in the case of Brossard *et al.* [16]: resolution $d/r_{SPH} = 80$, $t_{SPH} = 1$ cm in the simulations against 3 mm in the experiments. The results are compared to three models: EFE (black solid line), EFE NI with fixed $\nu_{FS} = 3 \times 10^{-3} \text{ m}^2 \cdot \text{s}^{-1}$ (gray solid line) and EFE NI SB with ν_{FS} defined by eq.3.3.6 with $\nu_{SB} = 1 \times 10^{-3} \text{ m}^2 \cdot \text{s}^{-1}$ fixed (gray dashed line).

allow the capture of the boundary layer effects and thus the dissipation due to the vortex shedding at the edges of the plate. To capture vortex shedding, one needs a resolution $r_{SPH} \approx \delta_\nu/3 \approx 0.01$ cm where $r_{SPH} = h_{SPH}/2$ is the particle size and $\delta_\nu = \sqrt{2\nu/\omega}$ is the boundary layer thickness scale and $\nu = 10^{-6} \text{ m}^2 \cdot \text{s}^{-1}$ is the fluid dynamic viscosity. It is not possible to simulate on a single card such a thin case, which requires 1.6×10^8 particles. A solution is to reduce the tank length. Note also that in the experiments, additional dissipation comes from the friction on the lateral side of the tank (3D effects).

Yet the SPH method correctly capture the general frequency response and gives satisfactory results for this case.

Param.	Bros	Mur1	Mur2	Mur3	Mur4
l_{tank}	8 m	8 m	8 m	2.2 m	8 m
x_1	3.15 m	3.15 m	3.15 m	0.75 m	3.15 m
x_s	2 m	2 m	2 m	0.7 m	2 m
d	20 cm	15 cm			
d_p	5 cm	2.5 cm			
l_p	25 cm	30 cm			
t_p	0.2 cm	0.3 cm			
t_{SPH}	1 cm	1 cm	0.5 cm	0.3 cm	1 cm
d/h_{SPH}	40	30	60	150	30
c_{SPH}	14 m/s	12 m/s			
h_{inc}	2 cm	3.54 cm			1.25 - 2.50 cm
f_0	0.9-1.7 Hz	1/0.65 Hz			0.9-1.7 Hz
t_{end}	30 s	30 s	30 s	20 s	30 s
t_{sim}	2.5 days	2 days	20 days	40 days	2 days
N_{part}	2.7×10^5	2.0×10^5	8.0×10^5	1.3×10^6	2.0×10^5

Table 3.1: Simulation parameters for waves above a submerged plate.

The experimental and numerical results can be compared to the models predictions. The results are displayed in solid and dashed lines in figure 3.19. The standard linear theory (EFE) largely overestimates the reflection and transmission coefficients (see black solid lines). It appears that for this case without wave breaking the dissipation is yet important above the plate. The EFE NI model is applied. The value of the dissipation is fixed such that the reflection and transmission coefficient are reasonably close to the SPH simulations for $f_0 = 1.4$ Hz. For the EFE NI, this leads to the relatively large wave Reynolds number $\mathcal{R} \approx 11$ (recall here $\mathcal{R} = \sqrt{gd_p^3}/\nu_s$ and therefore $\nu_s \approx 3 \times 10^{-3} \text{ m}^2 \cdot \text{s}^{-1}$). If a similar dissipation coefficient is used for the other frequency in the EFE NI model the results are not following the points trend for the other Λ_p 's: the transmission is underestimated for larger Λ_p and overestimated for smaller Λ_p ; there is not so much effect on the reflection coefficient on the other hand. The trend discrepancy is due to the model that represents the dissipation when the surface dissipation dominates. As in the present experimental (and numerical) configuration no wave breaking occurs, the dissipation is mostly due here to the friction on the submerged plate. To account for this the wave Reynolds' number needs to be corrected. This is done by comparing the imaginary part of the travelling mode wave number in the case of surface dissipation (see eq.1.5.20) and sea bed dissipation (see appendix H and eq.H.1.8). This yields the wave Reynolds number

$$\mathcal{R}_{FS} = D_p^{3/4} \sqrt{\frac{2\mathcal{R}_{SB}}{\Omega}} K_0^p \sinh 2K_0^p D_p, \quad (3.3.5)$$

where \mathcal{R}_{FS} is the wave Reynolds number at the free surface to have the same dissipation

rate than with sea bed friction with wave Reynolds number \mathcal{R}_{SB} . Recall that $\Omega = \omega\sqrt{d/g}$ in this chapter. In dimensional form, one can show that

$$\nu_{FS} = \frac{\sqrt{\omega\nu_{SB}}}{k_0^p 2^{1/2}} \sinh 2k_0^p d_p, \quad (3.3.6)$$

where again $\mathcal{R}_i = \sqrt{gd_p^3}/\nu_i$ and $i \in \{FS, SB\}$. Using the value $\nu_{FS} = 3 \times 10^{-3} \text{ m}^2 \cdot \text{s}^{-1}$ for $f_0 = 1.4 \text{ Hz}$ yields, $\nu_{SB} = 1 \times 10^{-3} \text{ m}^2 \cdot \text{s}^{-1}$ for this case. Evaluating the dissipation with this fixed value of ν_{SB} in the EFE NI model (called EFE NI SB) leads to the dashed gray line in figure 3.19. The model captures the overall trend on the entire range of data.

3.3.2.2 Flow rate under the submerged plate

The second test corresponds to the experimental case of Murakami *et al.* [120], here also modeled in 2D. The plate length is fixed to $L_p = 1$ and $D_p = 1/6$. The wave period is fixed to $T = 0.65 \text{ s}$ (or $\Lambda_p \approx 0.97$). In their paper, there is an ambiguity on the actual wave height as the authors say (translated from Japanese) that the wave height was $h_{\text{inc}}/\lambda = 0.059$ or $h_{\text{inc}} = 3.54 \text{ cm}$ in the introduction but then mentioned a maximum horizontal velocity at the surface $u_{\text{max}} = a_{\text{inc}}\omega/\tanh k_0 d = 16.47 \text{ cm/s}$, which leads to a wave height of $\approx 3.12 \text{ cm}$. In the present simulations for this case, the target wave height is set to $h_{\text{inc}} = 3.54 \text{ cm}$ and an AWAS-Mono is used.

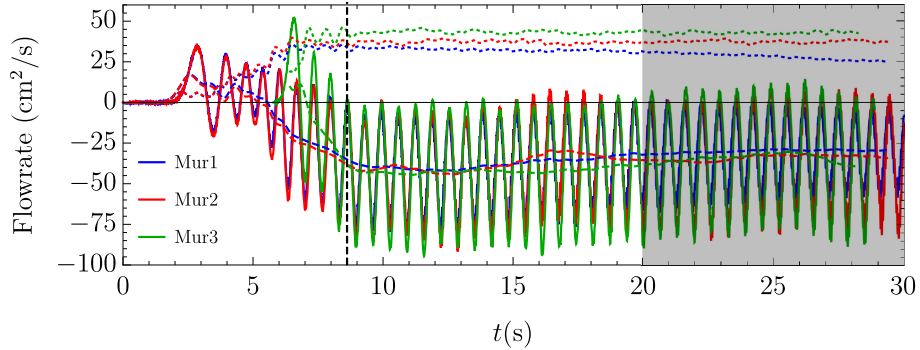


Figure 3.20: Murakami *et al.*'s case. Flow rate under the submerged plate in SPH for the configuration $D_p = 1/6$, $L_p = 1$ and $\Lambda_p \approx 0.96$. Solid (dashed, dotted) lines correspond to $\phi(t)$ ($\bar{\phi}(t)$, $\phi_1(t)$), respectively.

Three resolutions are considered: $d/r_{SPH} = 60$ and 120 with $l_{\text{tank}} = 8 \text{ m}$ and 300 with $l_{\text{tank}} = 2.2 \text{ m}$. Details on the simulation parameters can be found in table 3.1 (Mur1-2-3). The submerged plate thickness is chosen to be $t_{SPH} = \max\{4r_{SPH}, t_p\}$. For the first two cases the submerged plate is thicker than in the experiment. The limitation is due to the fact that a particle on top of the plate should not be able to interact with a particle under the submerged plate. To avoid issue at the edges of the plate no special technique is used beside ensuring that the plate is thick enough. The resolution in the shorter tank (Mur3)

Table 3.2: Simulation and models results for waves above a submerged plate (Murakami *et al.*'s case). EFE NI model uses $\mathcal{R} = 2.2 \times \mathcal{R}_{limit}$ the mean flow is evaluated without and with the roller contribution in the EFE NI.

case	Mur1	Mur2	Mur3	Exp	EFE	EFE NI
$2 \times a_{SPH}$ (cm)	3.03	3.28	3.30	3.54	3.30	3.30
R	0.38	0.41	0.42	≈ 0.4	0.33	0.45
T	0.28	0.23	0.17	≈ 0.2	0.94	0.23
R_{SL}	0.08	0.07	0.05	≈ 0.1	0	0
$\phi^{(0)}$ (cm ² /s)	-33.9 ± 4.5	-33.9 ± 1.6	-34.3 ± 2.1	≈ -37.0	-26.9	-28.5 (-46.2)
$\phi^{(1)}$ (cm ² /s)	30 ± 2.5	37.2 ± 0.8	42.7 ± 0.8	≈ 45.9	33.7	40.5

is chosen in such a way that the boundary layer is resolved. The kinematic viscosity is set to $\nu = 10^{-5} \text{ m}^2 \cdot \text{s}^{-1}$, or ten times the kinematic viscosity of water. With this value, the boundary layer scale is $\delta_\nu = \sqrt{2\nu/\omega} \approx 3r_{SPH}$. The tank length is such that there are a bit more than one wavelength before and after the submerged plate and for the dissipative sponge layer. This represents 1.3 million particles. This case is called boundary layer resolved (BLR). The optimal sponge layer value presented in appendix I is used ($n_B = 3$ and $B_{mean} = 0.45$).

The wave characteristics are measured using the same technique as described before (see table 3.2) on the last 5 wave periods. Note that as the sponge layer is set to the optimal value for the Mur3 case (shortest tank), the reflection from the sponge layer is lower than for the other cases. There is a good agreement with the experiment for all the measured parameters. The experimental data are estimated from the paper graphs when not clearly stated. Note that the transmission coefficient is overestimated as before for the coarsest case.

The flow rate in the experiment is extrapolated from a single probe velocity measurement placed at the mid-point 6 cm under the submerged plate. In the simulations, the instantaneous flow rate, $\phi(t)$, is measured as the average horizontal velocity of all the particles under the submerged plate. Figure 3.20 shows the flow rate measured under the submerged plate as a function of time in this three cases. For the case Mur3, the origin of time is shifted such that the phase matches at the position represented by the vertical black dashed line. The discrepancy for the first waves between the case Mur3 and Mur1-2 comes from the distance between the wave maker and the submerged plate and the fact that the first waves diffuse more for Mur1-2 (the spectrum is extended and the leading wave loses height¹⁵). In all the cases, the flow rate quickly becomes periodically steady under the submerged plate. A pulse flow regime that is quite similar to the one observed in the RWT is observed here. Similarly to the previous chapter, the first harmonic and

¹⁵ See for instance discussion in section 2.4 of [110].

averaged flow rates are measured using a trapezoidal rule integrated on two wave periods:

$$\bar{\phi} = \frac{1}{2T} \int_{t-T}^{t+T} \phi(t) dt, \quad (3.3.7)$$

$$\phi_1 = \frac{1}{T} \left| \int_{t-T}^{t+T} \phi(t) e^{i\omega t} dt \right|. \quad (3.3.8)$$

The values reported in the two last rows of table 3.2 represent the average of the shaded gray window in figure 3.20 where an asymptotic regime is reached. For the case Mur1, the amplitude of oscillation reduces as the time increases. This is thought to be due to the coarseness of this simulation as this effect disappears when the particles are refined (all the other parameters kept fixed). The AWAS does not seem to perform as well for this case. To reduce this bias on the mean flow estimate, the data are averaged on a larger window for this case (starting at 10 seconds, when the maximum absolute mean flow rate is reached approximatively). The amplitude of oscillation is smaller than for the other cases. Yet the mean flow is of the same order. The values are closer to the experimental one for the most refined case for both the amplitude of oscillation and the mean flow. The uncertainties of the mean flow increases with the refinement as vortex shedding starts to affect the results. The effect of the vortex shedding is yet not significant as the value is of the same order for the three refinements and the mean flow is established long before the vortex generated at the surface and at the plate edges reach the domain under the submerged plate. The mean velocity profile is on the other hand largely influence by the vortex dynamics for long time simulations (in agreement with [133, 134]). Figure 3.21 shows the instantaneous vortex fields at the beginning of the pumping near $t \approx 10$ s and later on at $t \approx 25$ s (see figure 3.20 for the evolution of the flow rate with time). The vorticity is non-dimensionalized by the characteristic velocity at the plate and the boundary layer thickness:

$$\varpi_I = \frac{a_{inc}\omega \cosh[k_0(d-d_p)]}{\delta_\nu \sinh k_0 d}, \quad (3.3.9)$$

where recall $\delta_\nu = \sqrt{2\nu/(2\pi f)}$.

The numerical results for the mean and first harmonic flow rates are in good agreement with the experimental data available. For all the parameters refining leads to better results. As in the experiment only a single probe measurement is made available, there is an important uncertainty on the mean flow measurement.

Figure 3.22 shows the horizontal velocity under the submerged plate compared to the data of Murakami *et al.* [120]. In the experiment, the data are sampled at x_I (center of the submerged plate), 6 cm under the submerged plate bottom for 40 seconds and averaged. In the simulations, the mean velocity under the submerged plate is used to remove the bias of the submerged plate thickness and the fluctuation due to vortices travelling under the submerged plate (see figure 3.21 and [134]). The phase is shifted to align with the

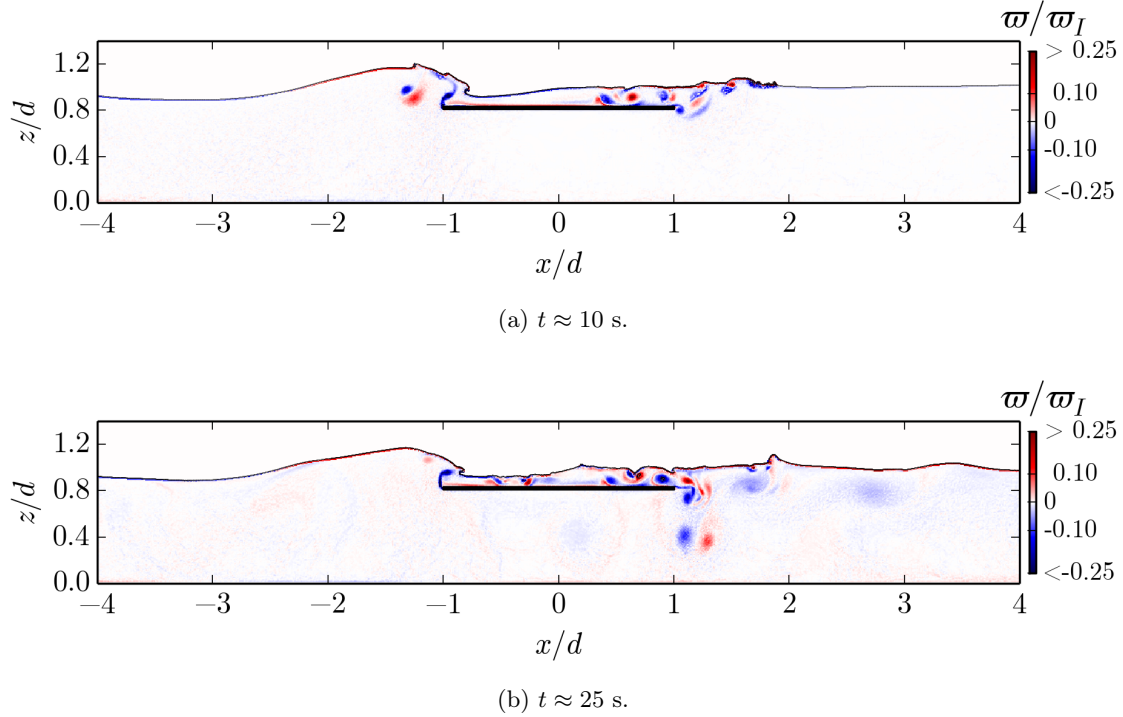


Figure 3.21: Vorticity in SPH simulation of waves above a submerged plate (Murakami *et al.*'s case). The vorticity is non-dimensionalized by the characteristic shear at the submerged plate (eq.3.3.9). The top figure outlines the fact that the vorticity has not had the time to play that the mean flow is already established under the plate at this instant (see figure 3.20). The vortices shed at the trailing edge of the plate starts later on to be advected under the plate.

experiment. The results are in good agreement with the experiment and this validates the simulations.

The experimental and numerical results can be compared to the models predictions. In table 3.2 the last two columns show the different parameters found using the EFE and EFE NI models. Similarly to the case of Brossard *et al.* [16], the EFE overestimates the transmission. Adding dissipation enables to get closer results to the experimental measurements. The dissipation is chosen by trial and errors. The value $\mathcal{R} = 2.2 \times \mathcal{R}_{limit}$ is found to yield good agreement with the experiments. This corresponds to $\nu_{FS} \approx 6.3 \times 10^{-3} \text{ m}^2 \cdot \text{s}^{-1}$. This value is larger than the one used in the previous section as wave breaking is important in the present case. Adding dissipation leads to an increase of the mean flow rate (evaluated as the maximum value of the wave mass transport above the plate) and also an increase of the amplitude of oscillations (see figure 3.14). In the case of EFE NI, the additional wave mass transport coming from the wave breaking roller mass transport is also evaluated. To evaluate this term, it is proposed here to separate the wave amplitude of the shoreward and seaward waves above the plate and use the roller wave

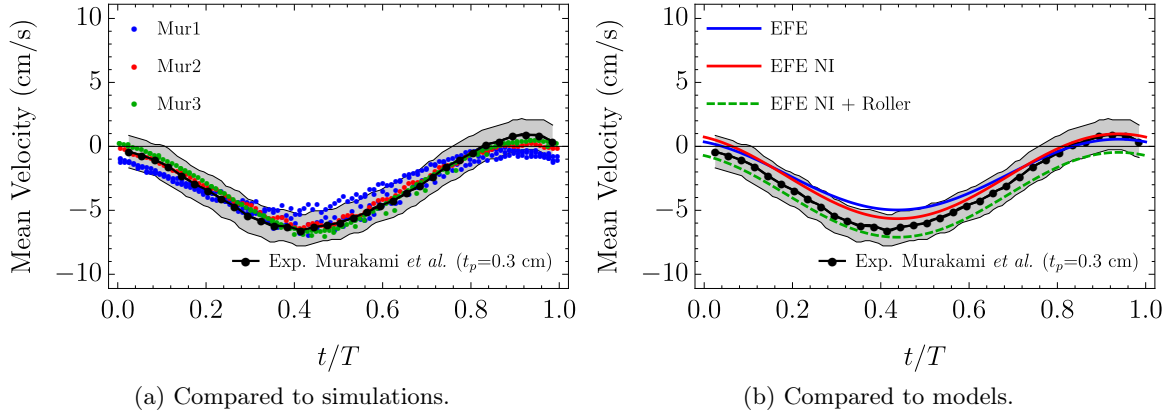


Figure 3.22: Murakami *et al.*'s case. Mean velocity under the submerged plate in the SPH simulations (a) and the linear models (b) compared to the experiment of Murakami *et al.*. Color points correspond to the numerical simulation with three different resolutions using SPH method. Black points correspond to the experimental data of Murakami *et al.*. The experimental data are numerized from the paper of Murakami *et al.* [120]. The shaded region shows the original experiment points size. The blue (red) solid line shows the EFE (EFE NI) model estimates of the mean flow under the plate. The EFE NI is evaluated with $\mathcal{R} = 2.2 \times \mathcal{R}_{limit}$. The green dashed line is the EFE NI with roller mass transport.

mass transport formula of eq.1.5.30 with the estimates of the roller area of Svendsen [151]. It leads to an overestimation of the mean flow rate for this case. The models estimates of the mean velocity under the submerged plate are shown in figure 3.22-b.

In this subsection, the simulations and the models were compared to experimental results with good agreement. Now the simulations and the models are compared on other parameters not available in the literature: the surface amplitude, the set-down and the mean mass flux. The effect of varying the wave amplitude and frequency is then considered.

3.3.3 Wave harmonic amplitude and set-down

From the previous simulations, the surface data are used to extract the wave different harmonics using a standard fast Fourier transform (FFT) method. The probe data on the last 5 wave periods are filtered to find the mean water level, the first and second harmonic. The first harmonic can be compared to the amplitude of the waves in the linear theory without and with dissipation. The second harmonic is the superposition of linked modes (modes that propagates at the same phase velocity than the first harmonic) and free modes, which comes from the wave interaction with the submerged structure. The linear theory can be extended to second order to solve for these modes as done for instance by Touboul and Rey [162]. Here, these two second order modes are not differentiated. Figure 3.23

shows the first harmonic amplitude (solid color lines) and second harmonic (dashed color lines) as a function of the position in the tank. The amplitude are non-dimensionalized by the wave incident amplitude in the simulation (a_{SPH}). The theoretical amplitude is shown in solid black and gray without and with dissipation. The shaded gray region outlines the region above the submerged plate. The vertical green dashed line shows the position of the beginning of the sponge layer for the case Mur3. For the other cases with longer tank, the sponge layer starts at the non-dimensional position 19. The transmission coefficient differs drastically between the simulations and the linear prediction without dissipation. Adding the dissipation enables to get a coefficient of the same order while also improving the match of the phase on the seaside (the gray solid curve is better aligned in both the amplitude and the phase with the SPH simulations). Above the submerged plate, the linear theory with dissipation appears to have the correct slope but does not capture at all the fluctuations. These are due to the violent projections of water occurring during breaking. When looking at the second harmonic amplitude it appears that downstream the amplitude is of the same order than the first order harmonic. This is expected for a case with such a small submergence [16].

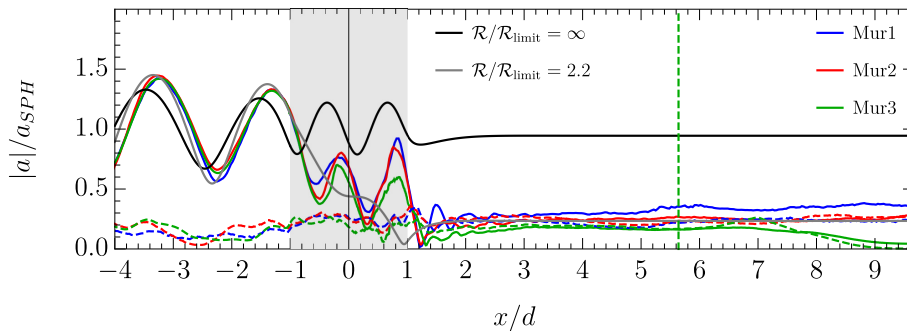


Figure 3.23: Wave harmonic amplitude in the SPH simulations (Murakami *et al.*'s case): first (solid) and second (dashed) harmonics are evaluated at each probe positions spaced by $2 \times r_{SPH}$ in the simulations (different colors) and compared the linear theory prediction without (black) and with (gray) dissipation. The position of the submerged plate is outlined by the shaded gray rectangle. The vertical green dashed line shows the beginning of the sponge layer for Mur3. The sponge layer starts at $x/d = 19$ in the other cases. The entire tank length is shown for the case Mur3.

In figure 3.24, the mean water level is compared to the immersion level of the submerged plate in the simulations. The theoretical mean water levels are also shown and rescaled for this incident wave height (the value $a_{inc} = 3.3$ cm is used). Seaward, the amplitude is similar to the theoretical predictions. Above the plate the mean water level is of about the same magnitude than the linear theory without dissipation (black solid line). The set-down can reach almost 30% of the undisturbed water depth above the plate in the simulations and 12% (5%) in the theory without (with) dissipation. The set-down is 3 to 6 times more

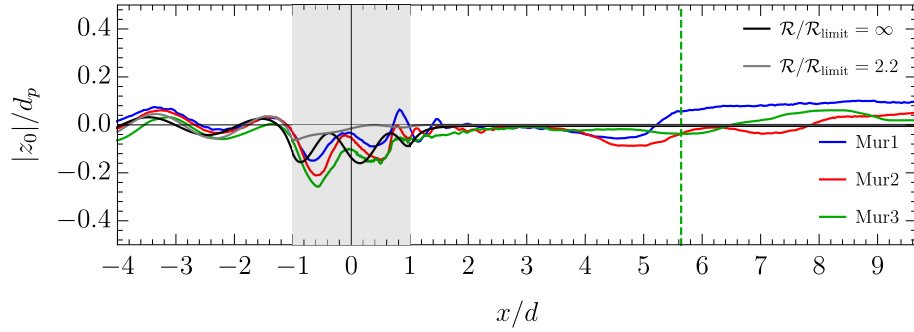


Figure 3.24: Mean water level in the SPH simulations (Murakami *et al.*'s case): mean water level (solid) is evaluated at each probe positions spaced by $2 \times r_{SPH}$ in the simulations (different colors) and compared the linear theory prediction without (black) and with (gray) dissipation. The position of the submerged plate is outlined by the shaded gray rectangle. The vertical green dashed line shows the beginning of the sponge layer for Mur3. The sponge layer starts at $x/l_p = 19$ in the other cases. The entire tank length is shown for the case Mur3.

important than in the theory due to the wave breaking and non-linearities.

As wave breaking occurs above the plate, one should be careful when using the present data in the shaded region. Indeed, the surface elevation at a probe, which corresponds to a spacing of $2 \times r_{SPH}$, is defined as the mean elevation of all the particles in this window. Thus the splashes and the voids are taken into account and alter the apparent instantaneous water elevation at a given probe position. Figure 3.25 shows an example of the instantaneous surface measured by the probes (in red) compared to the actual surface particles positions (black points).

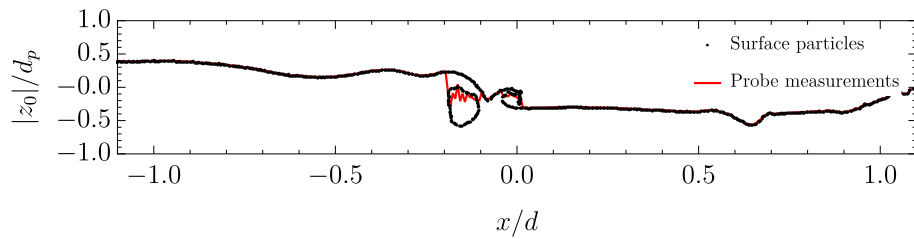


Figure 3.25: Water elevation detection during breaking in the SPH simulations: the black points show the position of surface particles while the red solid line shows the measured water elevation by the surface probes.

3.3.4 Wave mass flux and mass transport

It was shown in the linear potential theory (see section 3.2) that the amount of mass transported by the waves increases in the surface layer at the edge of the submerged plate leading to a fortiori suction of water at the origin of the observed circulation. To illustrate

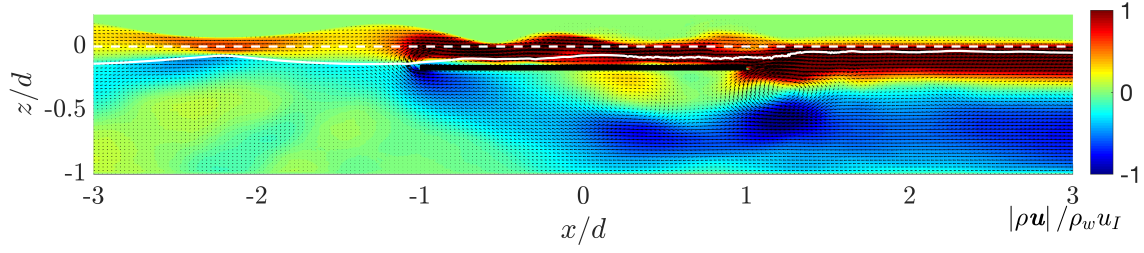


Figure 3.26: Mean mass flux around the submerged plate in the SPH simulation (Murakami *et al.*'s case).

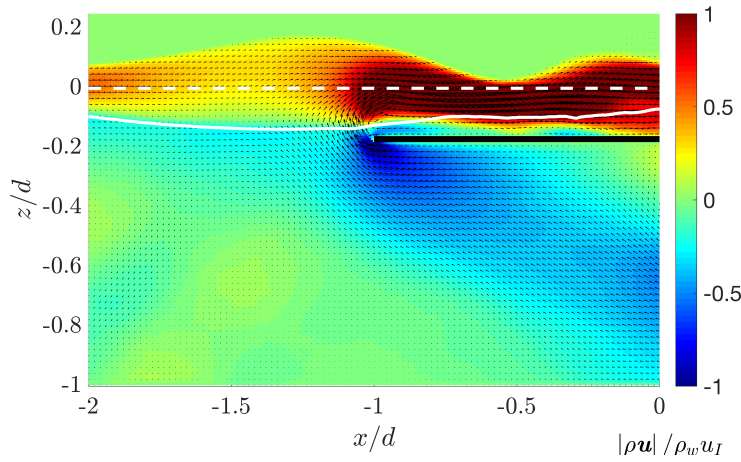


Figure 3.27: Zoom of the mean mass flux around the submerged plate in the SPH simulation (Murakami *et al.*'s case).

this effect and verify that it does appear in the SPH simulations, the mean wave mass flux is evaluated in the SPH simulations. The fluid domain is decomposed in boxes of size $h_{SPH} \times h_{SPH}$ (where $h_{SPH} = 2r_{SPH}$). The mass flux at a given time is defined as the mean value of $\rho_0 \mathbf{u}$ of the particles in this box. The data are averaged on the last 10 wave periods sampled on 101 phases. There are no drastic changes when varying the number of wave period from 10 to 2. In addition, the surface data are used to detect the minimum position of the surface during this time. This defines the surface lower bound of the surface envelope used to evaluate the wave mass transport. Figure 3.26 shows a large view of the Eulerian mean mass flux obtained in the simulation Mur3 and figure 3.27 shows a zoom on the leading edge of the plate. The solid white line shows the lower band of the surface layer while the dashed one shows the undisturbed surface position. The black horizontal plate shows the position of the submerged plate. The velocity is non-dimensionalized by the mean amplitude of the linear horizontal velocity:

$$u_I = \frac{a_{inc}\omega}{k_0 d}. \quad (3.3.10)$$

The color density plot shows the horizontal mass flux. One can see near the seaside edge of the plate ($x/d = -1$) a strong suction toward the surface layer. A recirculation cell is visible under the submerged plate (quite similar to the one observed in the experimental work of Poupardin *et al.* [134]) outlining the importance of the vortex shedding on the mean mass flux under the submerged plate. On the shore side, a recirculation is visible near the trailing edge ($x/d = +1$) of the submerged plate also due to the vortex dynamics. Away from the submerged plate on the shoreside, one can see a strong near surface mean current compensated by a strong submerged current. This can be explained by the fact that the present simulations are, similarly to experiment, in a closed tank. The return flow is surprisingly deeper than in the cases without a plate (see appendix A) where the return flow looks like the predicted mean flow of Gerstner’s waves. This is due to the strong vorticity near the surface generated at the trailing edge of the plate. Thus pass the submerged plate, the vorticity cannot be neglected. Yet, the present focus is on the origin of the circulation. It does seem that the increase of the wave mass transport predicted by the linear theory comes to play. Figures 3.26 and 3.27 show the mean mass flux at the end of the simulation. Figure 3.28 shows the mean mass flux after 5 waves have interacted with the plate. The suction seaside is already clearly established. The flow on the shoreside has not had time yet to spread on the entire tank length. The circulation cell that will be later under the plate is still at the trailing edge of the plate.

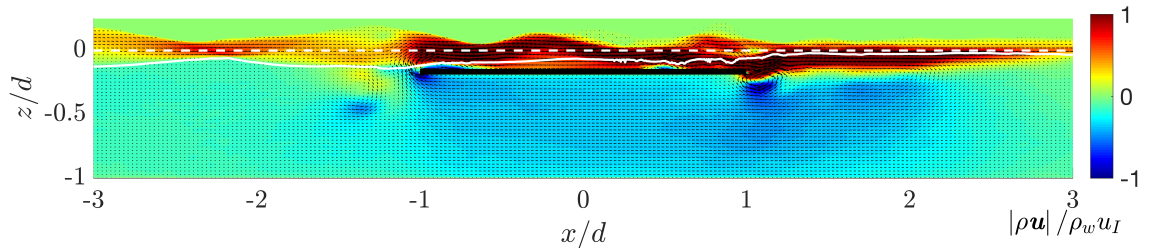


Figure 3.28: Mean mass flux around the submerged plate in SPH simulation after 5 waves (Murakami *et al.*’s case).

Integrating the wave mass flux above the lower bound of the surface envelope yields the numerical wave mass transport. It is compared to the linear theories in figure 3.29. The shaded gray region shows the position of the submerged plate. One can see the predicted increase of the wave mass transport. Note that the increase is about 40% more important at the seaside edge in the simulations than in the linear theories¹⁶. One could get a better estimate by adding the roller wave mass transport. The result is displayed in figure 3.29 in dashed gray. This leads to a better estimation of the wave mass transport maximum value¹⁷. Above the plate the mass transport diminishes due to the non-linearities and

¹⁶Note that in the simulations, the mean mass flux takes also into account the mean velocity, while in the model it is calculated only with the linear wave field. See eq.1.4.12 where the velocity is the total velocity. The mean velocity account for the rolling additional wave mass transport

¹⁷With the chosen dissipation, the slope is well captured at the beginning then the discrepancy between

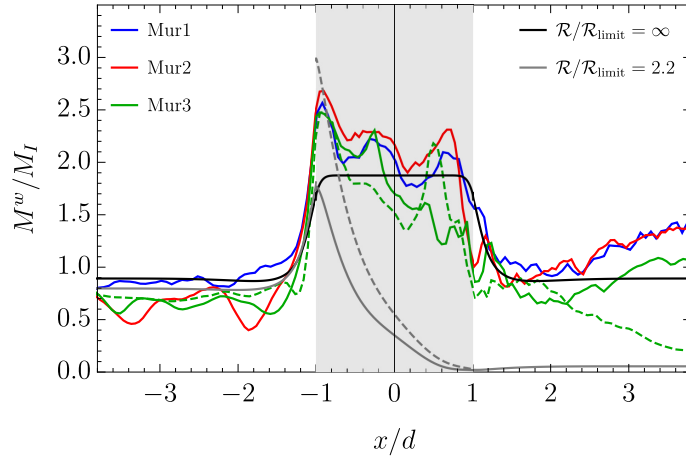


Figure 3.29: Wave mass transport in the surface layer in the SPH simulations and the models for Murakami *et al.*'s case (the SPH simulations in colors for 3 resolutions, linear potential theory without (with) dissipation in black (gray)). The dashed gray curve shows the result while taking into account the roller mass transport. The green dashed line shows the wave mass transport in the case Mur3 after 5 waves.

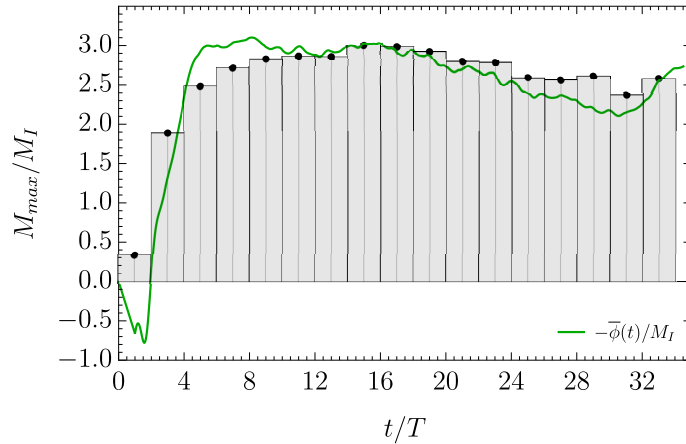


Figure 3.30: Instantaneous wave mass transport maximum and mean flow rate in the SPH simulation (Murakami *et al.*'s case). The bars show the maximum wave mass transport value at the leading edge of the submerged plate integrated on 2 wave periods. The solid line shows the opposite to the instantaneous mean flow rate also evaluated on 2 wave periods.

friction quite similarly to the dissipative linear model. At the shore side, the wave mass transport is larger than expected and actually larger than on the sea side after a long time. This is due to the non-linear modes generated by the plate along with the strong vorticity on that side as it is less pronounced at the early time (see dashed green line). Note that the peak of the wave mass transport is of the order of the mean flow rate under the plate.

the wave mass transport linear model with rolling and the simulation is mostly due to the higher harmonics contribution not accounted for.

This outlines as suggested before that in this closed wave tank case, the flow rate under the submerged plate is dictated by the peak value of the wave mass transport above the plate. Figure 3.30 shows the evolution of the wave mass transport maximum with time. The wave mass flux is evaluated on two wave periods identically to the instantaneous mean mass flux. The opposite of the instantaneous mean mass flux is also shown with the solid green line. There is a clear link between the time evolution of the maximum wave mass transport and the mean flow under the submerged plate for this case. At the early time, the wave mass transport maximum seems to dictate the response. In the next subsection, the wave amplitude and heights are varied and the response is qualitatively compared to the linear theory predictions.

3.3.5 Varying incident wave height and frequency

In this section, the resolution is fixed to $d/r_{SPH} = 60$ and 36 different configurations are simulated for 4 incident wave heights and 9 frequencies (see Mur4 in table 3.1). In all the cases, the mean flow rate under the submerged plate is recorded along with the free-surface. Figure 3.31 shows the measured incident wave height and the non-dimensional flow rate under the submerged plate as a function of the non-dimensional length $\Lambda_p = 2l_p/\lambda_p$ (color points). Additionally, the linear potential prediction and the dissipative models are shown in black and gray. As the color becomes lighter, the dissipation is increased. At first sight, the model correctly captures the trend for the amplitude of oscillations and largely underestimates the mean flow rate. This is mostly due to the fact that the amplification of the wave mass transport due to non-linearities and wave breaking are not accounted for in the present model. The set-down may also play a role as the potential theory predicts larger wave mass jump for lower water depth ratio D_p (see figure 3.5). Adding the roller wave mass transport greatly improve the predictions (see dashed lines in figure 3.31 (c)).

When looking more closely, the dissipation model overestimates the amplitude of oscillation for the largest Λ_p . Additional dissipation can come from the vortex shedding and the friction on the walls under the plates, which are not accounted for. The dissipation model also correctly captures the trend for the mean mass flux. An increase of the dissipation, does lead to an increase of the absolute mean flow rate for $\Lambda_p > 0.9$ as observed in the simulations. When the wave height is increased, thus the dissipation, the amplification plateaued. This is visible in the solid lines which show the maximum of the wave mass transport as previously discussed in section 3.2.3. For $0.65 < \Lambda_p < 0.9$, the model predicts that an increase of the amplitude (or the dissipation), leads to a reduction of the non-dimensional flow rate. This is also observed in the simulations. For the largest amplitude, the non-dimensional mean flow rate is more or less uniform and the value is around -4.0 . In the model a larger dissipation would lead to a global decrease of the mean mass flux, which explains the results of the black triangles (it corresponds to the previous case of

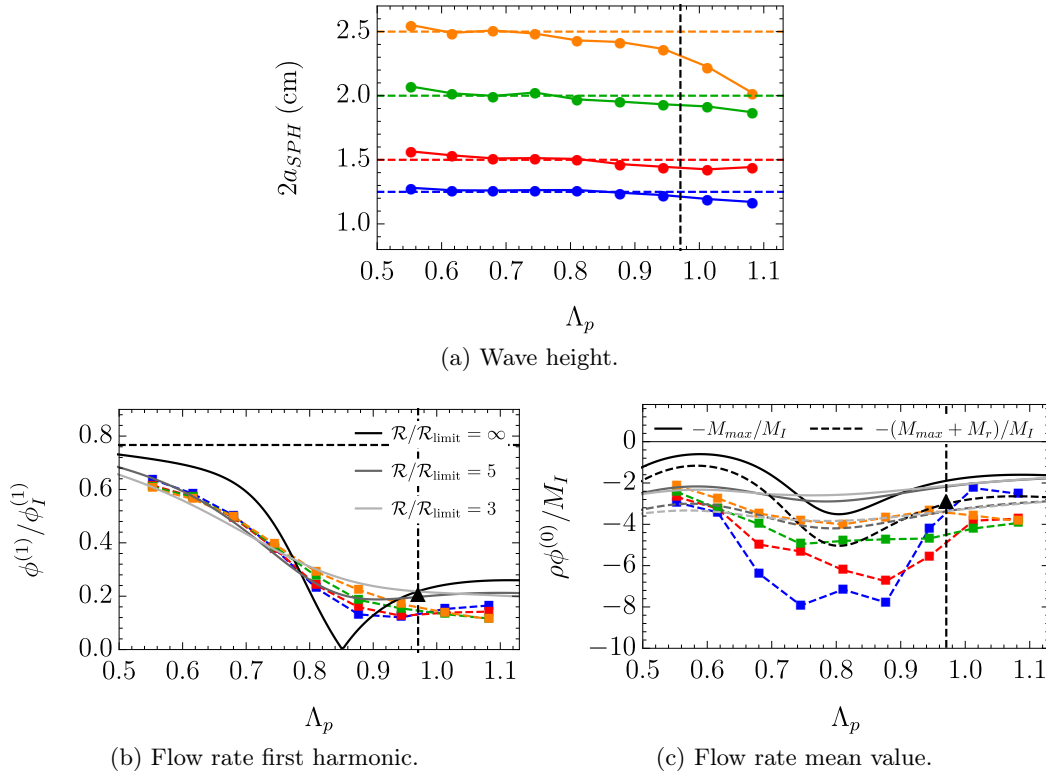


Figure 3.31: Murakami et al.’s configuration with varying incident wave height and frequency. Wave height (a) and non-dimensional first harmonic (b) and mean (c) flow rate under the submerged plate as a function of non-dimensional frequency for different target wave heights (colors correspond to different wave height targets in the SPH simulations, target values are given by the horizontal dashed lines in figure (a), black solid (dashed) curve corresponds to the opposite of linear theory wave mass transport maximum $-M_{max}/M_I$ (with the rolling mass transport $-(M_{max} + M_r)/M_I$), a lighter line corresponds to an increase of the dissipation). The vertical dashed line shows the non-dimensional length and the black triangle the non-dimensional flow rate for the cases Mur1-3, where recall the target wave height is $h_{inc} = 3.54$ cm.

Mur1, where the amplitude is even larger).

Overall, the trend is correctly captured as adding dissipation provides the correct intuitive expectation of the flow amplitude and direction. The model with dissipation only does not however provide quantitative estimates of the mean flow rate. This is principally due to the fact that it is limited for now to the first order and that wave breaking amplifies the mass transport with a roller mass transport term as proposed by Svendsen [151]. This is shown with the dashed lines in figure 3.31¹⁸. In the next section, preliminary results using a 3D SPH code are presented.

¹⁸Further improvement would require taking into account the mean water level above the plate and surface shears.

3.4 3D-SPH simulation

In this section supplementary observations of the circulation are provided using a 3D simulation. These results are preliminary. The goal being in future studies to simulate a turbine under the submerged plate to test energy extraction. The open source-code *GPUSPH* [60] (see also appendix K) is used with dynamic boundary particles. This is known to not correctly capture the boundary layer effects due to improper shear evaluation at the wall¹⁹. The resolution being not fine enough in this 3D case to capture the boundary layer effects, this should not be too much of a concern.

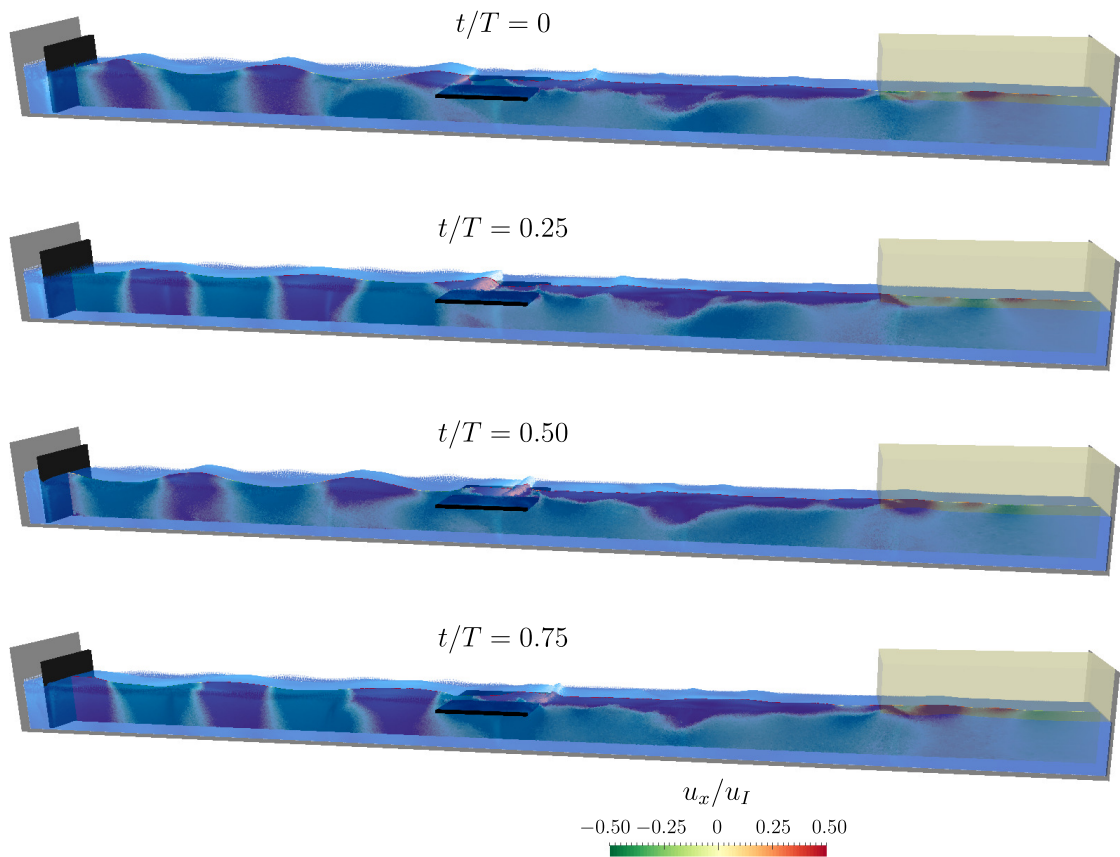


Figure 3.32: 3D SPH simulation of waves above a submerged plate (Murakami et al.’s case) at four instances equally spaced on a wave period (whole tank).

The configuration is similar to the one of the previous sections. The tank length is fixed to $l_t = 3.50$ m and its width to $\ell = 25$ cm. The resolution is fixed to $d/r_{SPH} = 75$ and the smoothing factor $h_{SPH}/r_{SPH} = 1.87643$. The submerged plate is $t_p = 1$ cm thick. The

¹⁹The version of the code at the time of writing present some issues when running on multi-GPUs with the Unified Semi-Analytical Wall boundary conditions (USAW) which are not as significant when using dynamic boundary conditions. This leads to some error when the waves pass from one card to another. This issue should be resolved in the near future.

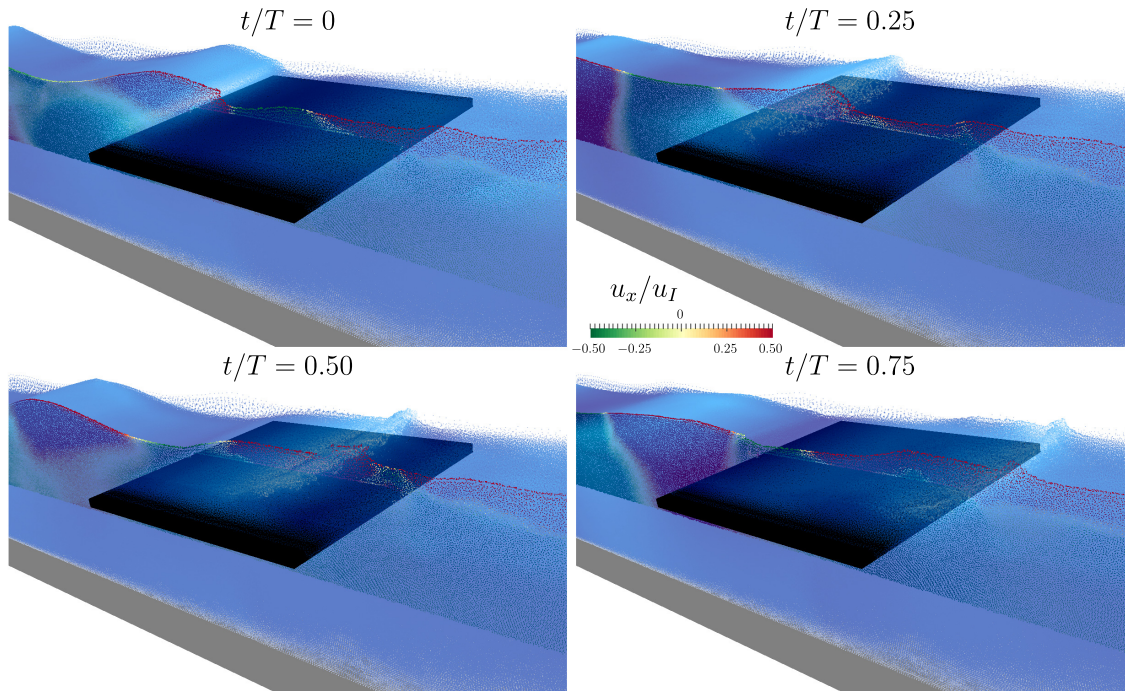


Figure 3.33: 3D SPH simulation of waves above a submerged plate (Murakami et al.’s case) at four instances equally spaced on a wave period (zoom tank).

kinematic viscosity is fixed to $\nu = 10^{-5} \text{ m}^2 \cdot \text{s}^{-1}$ ²⁰. The simulation represents 15.8 millions particles²¹. The simulation is ran on 6 GPUs on EDF’s cluster PORTHOS for 6 days and 23 seconds of physical time is reached. The AWAS- η and sponge layer are implemented similarly than in 2D in the code.

Figure 3.32 shows a global view of the wave tank simulation at different instances. The position of the sponge layer is outlined by shaded box. A “laser” illuminates the center line of the fluid and enables to visualize the horizontal velocity magnitude (red being shoreward and green seaward). Figure 3.33 shows a zoom near the submerged plate.

The flow rate²² is measured similarly to the 2D case on three profiles equally spaced under the submerged plate. The results are shown in figure 3.34. After a transient regime, the flow rates converge to a pulse flow regime. The amplitude of oscillation is $32 \pm 0.2 \text{ cm}^2 \cdot \text{s}^{-1}$ and the mean flow of $-31 \pm 1 \text{ cm}^2 \cdot \text{s}^{-1}$ for the 3 profiles. The results compared well with the case Mur1, which has a similar submerged plate thickness.

Similarly to the 2D case, the surface data are sampled and the first harmonic amplitude of oscillations evaluated. Relatively important dissipation can be seen in this 3D case

²⁰This does not significantly affect the wave dissipation in the simulations. This value is selected as it is intended to reduce the resolution in future work to capture the boundary layer effects using the USAW boundaries when the issue encountered with multi GPU’s simulations on the cluster will be resolved.

²¹To capture the wave boundary layer, one need about 1 billion particles in this 3D case.

²²Formally the flow rate is in $\text{cm}^3 \cdot \text{s}^{-1}$ but to compare to the 2D case results, it is measured on different cross sections and so is in $\text{cm}^2 \cdot \text{s}^{-1}$.

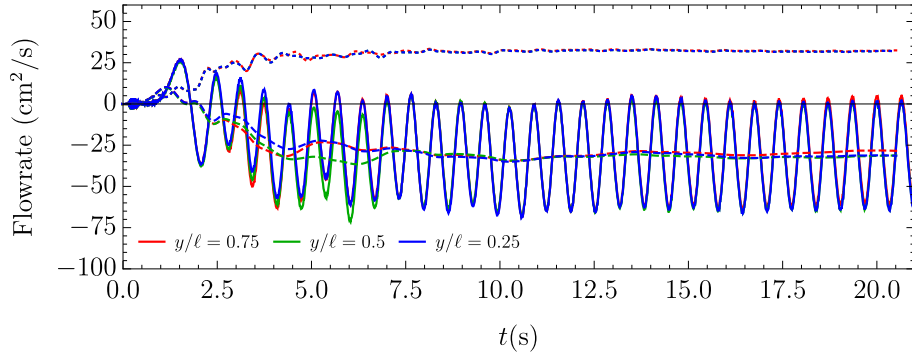


Figure 3.34: Flow rate under the submerged plate in 3D SPH (Murakami et al.'s case). The flow rate is measured similarly to the 2D case on profiles of constant y coordinate equally spaced on the tank length ℓ .

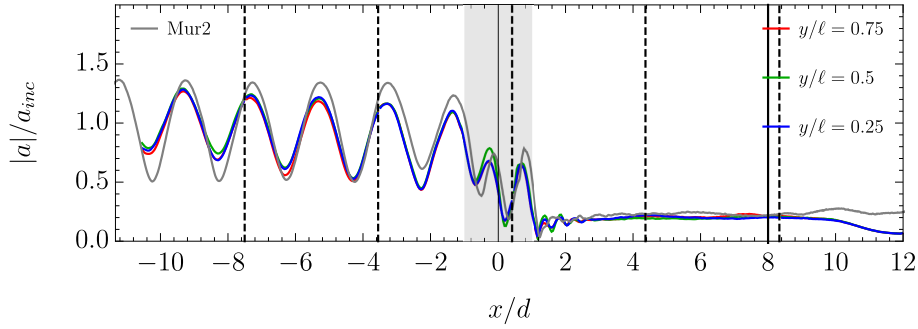


Figure 3.35: Wave amplitude in 3D SPH. The colors show the different profiles lines in the 3D case spaced in the span direction of the waves. The gray solid line shows the result of Mur2 in 2D, where the dissipation is not as pronounced. The dashed vertical lines show the position of the split between the different GPU's. The solid vertical line shows the position of the beginning of the sponge layer. For the 2D case the sponge layer starts at $x/d = 19$. The position of the submerged plate is outlined by the shaded gray region.

compared to the 2D cases (here Mur2 as an example). This is due to the fact that in the current version of the code, renormalization of the SPH operators are not implemented [163]. This should greatly improve the results in future works. The dissipation of the wave during propagation can be evaluated in this 3D case using a Goda & Suzuki [59]. The incident and reflected wave amplitude can then be separated. They are plotted in figure 3.36. First, one can see that the incident wave amplitude at the piston wave maker is close to 1 as requested. The dissipation can be estimated by fitting the curves to $a[1 \pm \alpha(x - x_0)]$ where a is the wave amplitude at the origin x_0 . The plus/minus is for the direction of propagation. In the simulation, the dissipation is found to be $\alpha\lambda \approx 0.17$ for the incident wave and $\alpha\lambda \approx 0.14$ for the reflected wave. In comparison the dissipation due to the viscous dissipation of Lamb [82] is $\alpha\lambda \approx 0.002$ for $\nu = 10^{-6} \text{ m}^2 \cdot \text{s}^{-1}$ and $\alpha\lambda \approx 0.007$ for $\nu = 10^{-5} \text{ m}^2 \cdot \text{s}^{-1}$. There is almost no dissipation in the 2D case.

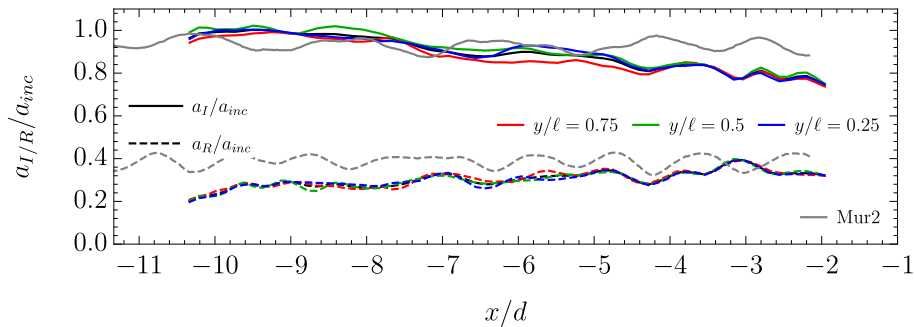


Figure 3.36: Incident and reflected wave amplitude in 3D SPH in the region I before the submerged plate (see figure 3.2). The colors show the different profiles lines in the 3D case spaced in the span direction of the wave. The gray solid line shows the result of Mur2 in 2D, where the dissipation is not as pronounced. The black solid line shows the average of the three 3D profiles used to evaluate the wave dissipation along propagation.

Conclusion

In this chapter, another device enabling the generation of current from water waves was revisited and the origin of the observed circulation explained using the wave mass transport properties. It is shown that the linear theory predicts an increase of the wave mass transport above the submerged plate. This leads to upward suction at the leading edge of the plate. This model is then compared to numerical simulations using the SPH method and validated against experimental data. It correctly predicts the frequency variation (and thus the frequencies of interest). Adding dissipation correctly predicts qualitatively the effect of increasing the wave height and taking into account the roller mass transport improves the quantitative prediction. The focus here was in the well understanding of the origin of the circulation rather than on the efficiency of the device as a wave converter²³. In terms of mean mass flux amplification, the system successfully amplifies the wave mass transported and generates mean flow up to 8 times more important than the incident wave original mass flux in the present simulations. This system shows potential direct applications for wave energy harvesting and current amplifications as well as water cooling and water sport (surfing and skim surfing) using the device as an artificial reef.

²³ At this stage of the study, the efficiency of the system is rather low (less than 6% using the definition of Orer and Ozdamar [124]. Note that this looks only at the kinematic power and does not take into account the mechanical work of the pressure (see dashed red line in figure 3.4)). However Orer and Ozdamar [124] showed that it was possible to increase the efficiency all the way up to 60% in their experiments by reducing the cross section.

Conclusions and future work

Dans cette thèse, on montre comment les vagues, et donc les énergies houlomotrices, peuvent être utilisées pour générer des courants. Le principe est simple et basé sur l'effet de changement brusque de profondeur d'eau qui entraîne dans la théorie linéaire l'augmentation de la dérive (ou transport de masse) dans la couche de surface décrite par la surface libre entre la crête et le creux. Le modèle proposé est simplement basé sur la résolution des équations linéaires avec un modèle de dissipation. Il peut être étendu à d'autres classes de problèmes comme les pompes de Liebau avec des tubes flexibles.

Des améliorations du modèles sont envisageables en s'inspirant d'études d'écoulements moyen près des côtes. Cependant, dans ces derniers, la partie dynamique des vagues est souvent simplifiée ce qui n'est pas directement transposable à la présente étude mais présente une piste intéressante.

L'extension de la présente étude au cas d'ondes polychromatiques à incidences variables est aussi à envisager.

Le présent système et concept est prometteur. Il pourrait être utilisé pour extraire l'énergie des vagues avec une turbine par exemple, ou encore pour des systèmes de refroidissement à eau près des côtes. Il est même envisageable d'étendre l'activité au sport nautique comme le surf et le skim surf en utilisant le système comme un récif artificiel en plus d'un système d'extraction d'énergie.

Wave pumping

The present work shows how water waves can be used to generate mean currents. A simple framework based on the linear potential theory is provided and enables to predict the pumping behavior in the two cases studied in chapters 2 and 3. It is applied to two problems which can be extended to the more general problem sketched in figure 3.37. The principle of the mean flow generation is based on the effect of resonance and abrupt variation of the water depth on the wave mass transport. The wave mass transport corresponds to the mass transported by waves and can be shown to correspond to a flux in the free-surface layer (surface that is not always submerged localised between the trough and the crest) in the Eulerian point of view. The wave mass transport increases in most cases when the water depth decreases. Placing a submerged structure not obstructing all the water depth thus allows to locally amplify the wave mass transport leading to suction and pumping.

This principle is illustrated in two examples studied in this thesis: the resonance wave tank (RWT) and the waves above a submerged plate (WASP) problem. The first one is inspired from the Liebau's pump and requires energy saturation to work. It is studied experimentally and numerically with two methods (VOF and SPH). A model based on linear wave theory and dissipation is developed and is able to predict the pump behavior. The linear potential theory without dissipation enables to predict the important frequencies, *i.e.* the resonance frequencies at which the pump will work, but does not provide further information. Adding dissipation to the model enables to get information on the pumping direction. The model stays rather qualitative but gives a good order of magnitude of the expected flow rate.

The second is inspired from the study of porous breakwaters. Several researchers reported a circulation around (or through) the submerged structure. Here it is shown that the variation of the wave mass transport enables to explain the observed pumping. It is studied numerically using the SPH method and compared to experimental works. Using the linear theory, it is shown that the mass transport increases in general above the submerged structure leading to a local suction (or upwelling) at edge of the plate. Adding dissipation to the model, enables to predict the effect of wave height increase. The model is improved by considering the additional mass transported during breaking in the rollers.

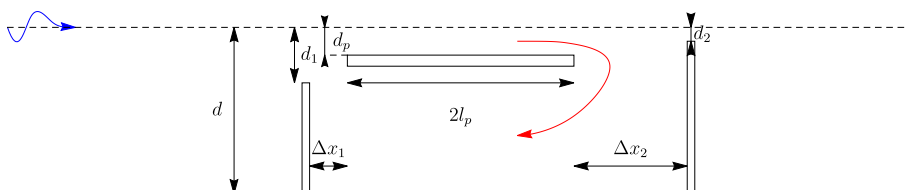


Figure 3.37: Wave energy converter general problem.

Further notes and comments

In this section, future directions and critics of the present work are discussed.

The method used to explain the origin of the circulation in the resonance wave pump is not limited to water waves problem with a free-surface. It could be easily adapted to the flexible tube original Liebau's pump. The main difference between the two problems is the flexible surface condition which is a bit more complex in the case of flexible tubes as both transversal and longitudinal waves exist. The RWT can thus be considered as a simpler problem in the investigation of the origin of pumping in impedance pumps.

In the model proposed here for the RWT and WASP, the estimation of the mean flow was limited to the wave mass transport evaluated from the linear theory and did not take into account the surface friction terms (at the free-surface and also sea-bed) which can lead in certain cases to stronger flow. A more complete modelling of these problems could be inspired by other works on the description of undertow flows for bar evolution in the surf-zone as for instance done in [122]. In this framework, the wave field is used to predict the mean return flow and the water elevation using free-surface and sea bed friction models. In general the wave field equations are rather simple though and limited to the flux of energy with a dissipative term. In the case presented in this thesis, the description is more complex as the wave dynamics cannot be simplified like that. Yet the idea is quite similar somehow. The WASP in particular can be regarded as a way to get the wave return flow away from the free-surface, in addition of an amplification of the mass transported due to the change of depth. The free-surface friction is mostly in the direction of the wave propagation during breaking. In the case of the WASP and RWT, it ensures that the mean flow is pushed in the direction of the waves propagation (which is sketched by down arrows inclined in the wave direction in figure 2.19, 2.20 and 3.10). In other words, the surface friction terms neglected in the present thesis are believed to mostly ensure that there is no return flow above the submerged plate, which was already assumed. Another important effect to take into account, and also modelled in problems such as bar evolution in the surf-zone, is the water set-up and set-down. This is discussed briefly for the WASP case as it is shown that reducing the plate immersion depth could lead to larger mass transport amplification. The two effects, *i.e.* mean water level variation and surface frictions could greatly improve the model.

For the WASP problem, the investigation is limited to the numerical SPH method. It would be interesting to compare the results to other numerical methods. The SPH method also was also used without any turbulence model. The BLR case captures the sea-bed boundary layer but the dissipation due to wave breaking is not fully resolved. A large eddy simulation methods (LES) approach, with sub-particle scaling is implemented in GPUSPH and could be used [31]²⁴. Most of the results are yet based here on 2D simulations with Sphynx and

²⁴ Turbulence models in SPH have been developed for a long time (*e.g.* [47, 142, 164] among others).

LES is not adapted. In the 3D simulations, it was outlined that the method was already too dissipative so adding turbulence will not improve the results. The resolution should first be refined, which would greatly increase the computational time. It is also pointed out that the present method used does not use the renormalization of the SPH operators [163]. This could also greatly improve the results in future works for 3D cases.

The general study was limited also to monochromatic waves with normal incidence to the submerged plate. For the WASP, the incidence angle has been considered in the study of breakwater by Linton and Evans [89]. For the polychromatic case, the linear theory enables to simply evaluate the terms separately but when evaluating the second order terms, low frequency terms will appear (by frequency subtraction) which will perturb the mean flow. This would need to be accounted for in future studies.

For the WASP and RWT, a fixed configuration was considered and the frequency response evaluated. This enabled the description and good understanding of the physics of the wave pumping systems but for real applications this method is reversed. In general, the wave characteristics of a given site for wave harvesting will be known and the system should be designed to be the most efficient for the given site. For the WASP, which is the closest to actual ocean applications, one should thus determine the peak wave frequency of the incident waves (provided by local wave studies or numerical modelling of sea state) and evaluate the depth and length of the submerged plate to get the largest wave mass transport amplification. The depth of the submerged plate should not be smaller than the incident wave height typical size to avoid wave breaking before the plate. The length of the submerged plate should then be chosen to get the maximum linear wave mass transport jump solving the problem with the linear theory.

Concluding remarks

The idea of wave pumping is quite promising and worth studying. It can be used to harness and exploit wave energy. Using the waves above a submerged plate (which is conceptually usable as it is), one can amplify underwater current and thus increase the efficiency of underwater hydro turbines. The system is of course a good breakwater and can be coupled with existing harbour or beach protection programs. The current under the submerged plate can also be used to force the salted water through filters to extract freshwater and be used for desalination. Another direct application, which is particularly promising, is to use the wave pump as a water cooling system in near harbour areas. Interestingly, the artificial reef created by the submerged plate could also be used for water sport activities such as surfing or skim surfing (depending on the water depth) and thus be coupled with tourism activities.

However, the question will arise about how good these models (e.g. the standard k-epsilon model) are to deal with wave propagation.

Bibliography

- [1] Maritime boundaries geodatabase. <http://www.marineregions.org>. Accessed: 2017-11-13.
- [2] International Energy Agency. *Key world energy statistics*. International Energy Agency, 2017.
- [3] G. B. Airy. *Tides and Waves*. William Clowes and Sons, 1845.
- [4] M.-R. Alam. Nonlinear analysis of an actuated seafloor-mounted carpet for a high-performance wave energy extraction. In *Proc. R. Soc. A*, volume 468, pages 3153–3171. The Royal Society, 2012.
- [5] H. Allison. Streaming of fluid under a near-bottom membrane. *Journal of Fluid Mechanics*, 137:385–392, 1983.
- [6] C. Altomare, T. Suzuki, A. Barreiro, and A. J. C. Crespo. Numerical wave dynamics using lagrangian approach: wave generation and passive & active wave absorption. *Proc. 10th SPHERIC International workshop, Parma (Italy), 16-18 June 2015*, 2015.
- [7] C. Altomare, J.M. Domínguez, A. Crespo, J. González-Cao, T. Suzuki, M. Gómez-Gesteira, and P. Troch. Long-crested wave generation and absorption for SPH-based DualSPHysics model. *Coastal Engineering*, 127:37–54, 2017.
- [8] I. Avrahami and M. Gharib. Computational studies of resonance wave pumping in compliant tubes. *Journal of Fluid Mechanics*, 608:139–160, April 2008.
- [9] E. F. Bartholomeusz. The reflexion of long waves at a step. In *Mathematical Proceedings of the Cambridge Philosophical Society*, volume 54, pages 106–118. Cambridge University Press, 1958.
- [10] J. A. Battjes and J.P.F.M. Janssen. Energy loss and set-up due to breaking of random waves. In *Coastal Engineering 1978*, pages 569–587. 1978.
- [11] J. Belden and A. H. Techet. Simultaneous quantitative flow measurement using PIV on both sides of the air–water interface for breaking waves. *Experiments in Fluids*, 50(1):149–161, 2011.

- [12] F. Biesel and F. Suquet. Laboratory wave generating apparatus. *La Houille Blanche*, (2&4):147–165&475–496, 1951.
- [13] F. Brezzi and J. Pitkäranta. On the stabilization of finite element approximations of the stokes equations. In Wolfgang Hackbusch, editor, *Efficient Solutions of Elliptic Systems: Proceedings of a GAMM-Seminar Kiel, January 27 to 29, 1984*, pages 11–19, Wiesbaden, 1984. Vieweg+Teubner Verlag.
- [14] T. T Bringley, S. Childress, N. Vandenberghe, and J. Zhang. An experimental investigation and a simple model of a valveless pump. *Physics of Fluids*, 20(3):033602, 2008.
- [15] A. Brito and J.L. Villate. Annual report. implementing agreement on ocean energy systems-2007. *The Executime Committee of Ocean Energy Systems*, 2007.
- [16] J. Brossard, G. Perret, L. Blonce, and A. Diedhiou. Higher harmonics induced by a submerged horizontal plate and a submerged rectangular step in a wave flume. *Coastal Engineering*, 56(1):11 – 22, 2009.
- [17] R. Carmigniani and D. Violeau. Resonance wave pumping: mean wave mass flux. In *37th IAHR-Congress*, Kuala Lumpur, Malaysia, 2017.
- [18] R. Carmigniani, A. Leroy, A. Joly, and D. Violeau. SPH modeling of resonance wave pumping in closed tank: Parametric study. *Proc. 11th SPHERIC International workshop, Munich (Germany), 14-16 June 2016*, 2016.
- [19] R. Carmigniani, A. Leroy, A. Joly, and D. Violeau. Submerged plate wave energy converter SPH simulations: wave mass transport. *Proc. 12th SPHERIC International workshop, Ourense (Spain), 13-15 June 2017*, 2017.
- [20] R. A Carmigniani and D. Violeau. Optimal sponge layer for water waves numerical models (submitted). *Ocean Engineering*, 2017-18?
- [21] R. A Carmigniani, M. Benoit, D. Violeau, and M. Gharib. Resonance wave pumping with surface waves. *Journal of Fluid Mechanics*, 811:1–36, 2017.
- [22] R. W. Carter, R C. Ertekin, and P. Lin. On the reverse flow beneath a submerged plate due to wave action. In *OMAE2006 25th international conference on offshore mechanics and Arctic engineering. ASME, Hamburg*, pages 595–602, 2006.
- [23] P.G. Chamberlain and D. Porter. On the solution of the dispersion relation for water waves. *Applied Ocean Research*, 21(4):161 – 166, 1999.
- [24] H.-F. Cheong, N. J. Shankar, and S. Nallayarasu. Analysis of submerged platform breakwater by eigenfunction expansion method. *Ocean Engineering*, 23(8):649–666, 1996.

- [25] J.M. Cherfils, L. Blonce, G. Pinon, and E. Rivoalen. Simulation of water wave - coastal structure interactions by smoothed particle hydrodynamics. In *8th Int. Conf. on Hydrodyn.*, Nantes, France, 2008.
- [26] A. Clément. Coupling of two absorbing boundary conditions for 2d time-domain simulations of free surface gravity waves. *Journal of Computational Physics*, 126(1): 139–151, 1996.
- [27] A. A. Clifford. Multivariate error analysis: a handbook of error propagation and calculation in many-parameter systems. 1973.
- [28] A.D.D. Craik. The origins of water wave theory. *Annual review of fluid mechanics*, 36, 2004.
- [29] A.D.D. Craik and S. Leibovich. A rational model for langmuir circulations. *Journal of Fluid Mechanics*, 73(3):401–426, 1976.
- [30] R.A. Dalrymple. Water wave models and wave forces with shear currents. *Coastal and Ocean. Eng. Lab. Univ. of Florida Gainesville, Florida Technical Report No. 20*, 1973.
- [31] R.A. Dalrymple and B.D. Rogers. Numerical modeling of water waves with the sph method. *Coastal engineering*, 53(2):141–147, 2006.
- [32] R. Deigaard. *Mechanics of coastal sediment transport*, volume 3. World Scientific Publishing Co Inc, 1992.
- [33] L. Deike, N. Pizzo, and W. K. Melville. Lagrangian transport by breaking surface waves. *Journal of Fluid Mechanics*, 829:364–391, 2017. doi: 10.1017/jfm.2017.548.
- [34] V.A. Del Grosso and C.W. Mader. Speed of sound in pure water. *the Journal of the Acoustical Society of America*, 52(5B):1442–1446, 1972.
- [35] S. S. Deshpande, L. Anumolu, and M. F. Trujillo. Evaluating the performance of the two-phase flow solver interFoam. *Computational science & discovery*, 5(1):014016, 2012.
- [36] T. M. Dick. *On Solid and permeable submerged plate breakwaters*. PhD thesis, Queen’s University, Kingstson, Ont., 1968.
- [37] E. Didier and M. G. Neves. A semi-infinite numerical wave flume using smoothed particle hydrodynamics. *Int. J. of Offshore and Polar Eng.*, 22(3):193–199, September 2012.
- [38] B. Drew, A. R. Plummer, and M. N. Sahinkaya. A review of wave energy converter technology, 2009.

- [39] J.H. Duncan. An experimental investigation of breaking waves produced by a towed hydrofoil. In *Proceedings of the Royal Society of London A: Mathematical, Physical and Engineering Sciences*, volume 377, pages 331–348. The Royal Society, 1981.
- [40] D. Dutykh. Group and phase velocities in the free-surface visco-potential flow: new kind of boundary layer induced instability. *Physics Letters A*, 373(36):3212–3216, 2009.
- [41] D. Dutykh and F. Dias. Viscous potential free-surface flows in a fluid layer of finite depth. *Comptes Rendus Mathématique*, 345(2):113–118, 2007.
- [42] D. V. Evans and R. Porter. Efficient calculation of hydrodynamic properties of OWC-type devices. *Journal of Offshore Mechanics and Arctic Engineering*, 119(4):210–218, 1997.
- [43] D.V. Evans. A theory for wave-power absorption by oscillating bodies. *Journal of Fluid Mechanics*, 77(1):1–25, 1976.
- [44] A.F. Falcao and P.A. Justino. OWC wave energy devices with air flow control. *Ocean Engineering*, 26(12):1275–1295, 1999.
- [45] J. Falnes. A review of wave-energy extraction. *Marine Structures*, 20(4):185–201, 2007.
- [46] J. D. Fenton. A fifth-order stokes theory for steady waves. *Journal of waterway, port, coastal, and ocean engineering*, 111(2):216–234, 1985.
- [47] M. Ferrand, D.R. Lurence, D. Rogers, D. Violeau, and C. Kassiotis. Unified semi-analytical wall boundary conditions for inviscid, laminar or turbulent flows in the meshless SPH method. *Int. J. Num. Meth. Fluids*, 71(4):446–472, 2011. doi: 10.1002/flid.3666.
- [48] M. C Fishman and K. R Chien. Fashioning the vertebrate heart: earliest embryonic decisions. *Development*, 124(11):2099–2117, 1997.
- [49] A. S Forouhar, M. Liebling, A. Hickerson, A. Nasiraei-Moghaddam, H.-J. Tsai, J. R Hove, S. E Fraser, M. E Dickinson, and M. Gharib. The embryonic vertebrate heart tube is a dynamic suction pump. *Science*, 312(5774):751–753, 2006.
- [50] S. Foteinis and T. Tsoutsos. Strategies to improve sustainability and offset the initial high capital expenditure of wave energy converters (wecs). *Renewable and Sustainable Energy Reviews*, 2016.
- [51] W. Froude. On the rolling of ships. *Trans. Institute of Naval Architects*, 3:45–62, 1862.

- [52] T. Funada and D.D. Joseph. Viscous potential flow analysis of kelvin–helmholtz instability in a channel. *Journal of Fluid Mechanics*, 445:263–283, 2001.
- [53] D. Gaillard. *Wave action in relation to engineering structures*. Number 31. Govt. Print. Off., 1904.
- [54] F. Gerstner. Theorie der wellen. In *Abhand. Kön. Böhmischen Gesel. Wiss.*, Prague, 1802.
- [55] F. Gerstner. Theorie der wellen. *Annalen der Physik*, 32(8):412–445, 1809.
- [56] A. Ghaitanellis, D. Violeau, A. Leroy, A. Joly, and M Ferrand. Application of the unified semi-analytical wall boundary conditions to multi-phase sph. *Proc. 10th SPHERIC International workshop, Parma (Italy), 16-18 June 2015*, pages 333–340, 2015.
- [57] P.S. Girard. Pour divers moyens d’employer les vagues de la mer, comme moteurs. *French Patent, July*, 12:1799, 1799.
- [58] Y. Goda. A synthesis of breaker indices. In *Proceedings of the Japan Society of Civil Engineers*, volume 1970, pages 39–49. Japan Society of Civil Engineers, 1970.
- [59] Y. Goda and T. Suzuki. Estimation of incident and reflected waves in random wave experiments. *Coastal Engineering Proceedings*, 1(15):828–845, 1976.
- [60] GPUSPH.org. Gpusph, Version 5.0. 2017.
- [61] K.-U. Graw. The submerged plate as a wave filter: The stability of the pulsating flow phenomenon. In *Coastal Engineering Proceedings*, volume 1, Venice, Italy, 1992.
- [62] K.-U. Graw. Shore protection and electricity by submerged plate wave energy converter. In *Proc. of the European Wave Energy Symposium*, pages 1–6, Edinburgh, UK, 1993.
- [63] K.-U. Graw and Stieglmeier M. An explanation of wave energy transmission around permeable breakwaters based on turbulence and resonance. In *23rd IAHR-Congress*, pages 1–7, Ottawa, Canada, 1989.
- [64] S. T Grilli and J. Horrillo. Numerical generation and absorption of fully nonlinear periodic waves. *Journal of Engineering Mechanics*, 123(10):1060–1069, 1997.
- [65] K. Gunn and C. Stock-Williams. Quantifying the global wave power resource. *Renewable Energy*, 44(C):296–304, 2012.
- [66] K. Hasselmann. On the mass and momentum transfer between short gravity waves and larger-scale motions. *Journal of Fluid Mechanics*, 50(1):189–205, 1971.

- [67] N.H. Heck and H. Jerry. Service: " velocity of sound in sea water.". *US Coast and Geodetic Survey Special Publication No*, 108.
- [68] T.S. Hedges. An empirical modification to linear wave theory. *Proc. Inst. Civ. Eng*, 61(3):575–579, 1976.
- [69] A. Herault, G. Bilotta, and R. A. Dalrymple. Achieving the best accuracy in an SPH implementation. In *Proceedings of the 9th SPHERIC International Workshop, Paris*, 2014.
- [70] A. I. Hickerson and M. Gharib. On the resonance of pliant tube as a mechanism for valveless pumping. *Journal of Fluid Mechanics*, 555:141–148, January 2006.
- [71] P. Higuera, J. L. Lara, and I. J. Losada. Realistic wave generation and active wave absorption for Navier–Stokes models: Application to OpenFOAM®. *Coastal Engineering*, 71:102–118, 2013.
- [72] G. Hoeborn. *Einfluß einer starren horizontalen getauchten Platte auf Wellen*. PhD thesis, Berg. Univ., Lehr-u. Forschungsgebiet Wasserbau u. Wasserwirtschaft, 1986.
- [73] F. V. Hunt. Resonance versus resonant. *The Journal of the Acoustical Society of America*, 50(2A):435–435, 1971.
- [74] T. Ijima, S. Ozaki, Y. Eguchi, and A. Kobayashi. Breakwater and quay well by horizontal plates. In *Coastal Engineering 1970*, pages 1537–1556. 1970.
- [75] Wolfram Research, Inc. Mathematica, Version 11.0. Champaign, IL, 2017.
- [76] H. Jeffreys. On the formation of water waves by wind. *Proceedings of the Royal Society of London. Series A, Containing Papers of a Mathematical and Physical Character*, 107(742):189–206, 1925.
- [77] D.D. Joseph. Potential flow of viscous fluids: Historical notes. *International Journal of Multiphase Flow*, 32(3):285–310, 2006.
- [78] D.D. Joseph and J. Wang. The dissipation approximation and viscous potential flow. *Journal of Fluid Mechanics*, 505:365–377, 2004.
- [79] J. Kiefer. Sequential minimax search for a maximum. *Proceedings of the American mathematical society*, 4(3):502–506, 1953.
- [80] G.-W. Kim and M.-E. Lee. Damping of water waves over permeable bed of finite depth. *Journal of the Korean Society of Marine Environment & Safety*, 18(3):199–205, 2012.

- [81] J. T. Kirby and R. A. Dalrymple. An approximate model for nonlinear dispersion in monochromatic wave propagation models. *Coastal Engineering*, 9(6):545–561, 1986.
- [82] H. Lamb. *Hydrodynamics*. Cambridge university press, 1932.
- [83] E. M. Lane, J. M. Restrepo, and J. C. McWilliams. Wave–current interaction: A comparison of radiation-stress and vortex-force representations. *Journal of physical oceanography*, 37(5):1122–1141, 2007.
- [84] B. Le Méhauté. Progressive wave absorber. *Journal of Hydraulic Research*, 10(2):153–169, 1972.
- [85] Bernard Le Méhauté. An introduction to hydrodynamics and water waves. *Ocean. Front. Coast. Process*, 1969.
- [86] Y.-H. Li. Equation of state of water and sea water. *Journal of Geophysical Research*, 72(10):2665–2678, 1967.
- [87] G. Liebau. Über ein ventillofes pumpprinzip. *Naturwissenschaften*, 41(14):327–327, 1954.
- [88] G. Liebau. Prinzipien kombinierter ventilloser pumpen, abgeleitet vom menschlichen blutkreislauf. *Naturwissenschaften*, 42(11):339–339, 1955.
- [89] C. M. Linton and D. V. Evans. Trapped modes above a submerged horizontal plate. *The Quarterly Journal of Mechanics and Applied Mathematics*, 44(3):487–506, 1991.
- [90] C. M. Linton and P. McIver. *Handbook of mathematical techniques for wave/structure interactions*. CRC Press, 2001.
- [91] T. C. Lippmann, A. H. Brookins, and E. B. Thornton. Wave energy transformation on natural profiles. *Coastal Engineering*, 27(1):1–20, 1996.
- [92] Y. Liu, X. Niu, and X. Yu. A new predictive formula for inception of regular wave breaking. *Coastal Engineering*, 58(9):877–889, 2011.
- [93] M. S. Longuet-Higgins. Mass transport in water waves. *Philosophical Transactions of the Royal Society of London A: Mathematical, Physical and Engineering Sciences*, 245(903):535–581, 1953.
- [94] M. S. Longuet-Higgins. Longshore currents generated by obliquely incident sea waves: 1. *Journal of geophysical research*, 75(33):6778–6789, 1970.
- [95] M. S. Longuet-Higgins. Peristaltic pumping in water waves. *Journal of Fluid Mechanics*, 137:393–407, 1983.

-
- [96] M. S. Longuet-Higgins and R. W. Stewart. Radiation stress and mass transport in gravity waves, with application to “surf beats”. *Journal of Fluid Mechanics*, 13(4): 481–504, 1962.
- [97] M. S. Longuet-Higgins and R. W. Stewart. Radiation stresses in water waves; a physical discussion, with applications. In *Deep Sea Research and Oceanographic Abstracts*, volume 11, pages 529–562. Elsevier, 1964.
- [98] M. S. Longuet-Higgins and R.W. Stewart. Changes in the form of short gravity waves on long waves and tidal currents. *Journal of Fluid Mechanics*, 8(4):565–583, 1960.
- [99] M. S. Longuet-Higgins and J.S. Turner. An entraining plume model of a spilling breaker. *Journal of Fluid Mechanics*, 63(1):1–20, 1974.
- [100] P. Lui and M. Iskandarani. Hydrodynamic wave forces on submerged horizontal plate. In *Unknown Host Publication Title*. Ottawa, Canada, National Research Council Canada, 1989.
- [101] J. C. Luke. A variational principle for a fluid with a free surface. *Journal of Fluid Mechanics*, 27(2):395–397, 1967.
- [102] R. Luppés, A. E. P. Veldman, and P. R Wellens. Absorbing boundary conditions for wave simulations around offshore structures. In *V European Conference on Computational Fluid Dynamics (ECCOMAS CFD 2010)*, Lisbon, 2010.
- [103] S. Marrone, A. Colagrossi, D. Le Touzé, and G. Graziani. Fast free-surface detection and level-set function definition in SPH solvers. *J. Comput. Phys.*, 229(10):3652–3663, may 2010.
- [104] P. A. Martin. Asymptotic approximations for functions defined by series, with some applications to the theory of guided waves. *IMA journal of applied mathematics*, 54 (2):139–157, 1995.
- [105] H. Martins-Rivas and C. C. Mei. Wave power extraction from an oscillating water column at the tip of a breakwater. *Journal of fluid Mechanics*, 626:395–414, 2009.
- [106] S.R. Massel. Harmonic generation by waves propagating over a submerged step. *Coastal Engineering*, 7(4):357–380, 1983.
- [107] A. Mayrhofer, B. D. Rogers, D. Violeau, and M. Ferrand. Study of differential operators in the context of the semi-analytical wall boundary conditions. *Proc. 7th SPHERIC International workshop, Prato (Italy), 29 May-1 June 2012*, (4), 2012.
- [108] A. Mayrhofer, B. D. Rogers, D. Violeau, and M. Ferrand. Investigation of wall bounded flows using SPH and the unified semi-analytical wall boundary conditions.

- Comp. Ph. Comm.*, 184(11):2515–2527, 2013. ISSN 00104655. doi: 10.1016/j.cpc.2013.07.004.
- [109] C. C. Mei and J. L. Black. Scattering of surface waves by rectangular obstacles in waters of finite depth. *Journal of Fluid Mechanics*, 38(3):499–511, 1969.
- [110] C. C. Mei, M. Stiassnie, and D. K.-P. Yue. *Theory and Applications of Ocean Surface Waves: Part 1: Linear Aspects Part 2: Nonlinear Aspects*. World Scientific, 1989.
- [111] C.C. Mei. The applied dynamics of ocean surface waves, ed. *W. Scientifuc1989, Singapore*.
- [112] J. Meier. *A novel experimental study of a valveless impedance pump for applications at lab-on-chip, microfluidic and biomedical device size scales*. PhD thesis, California Institute of Technology, May 2011.
- [113] A. Miche. Mouvements ondulatoires de la mer en profondeur croissante ou décroissante. Première partie. Mouvements ondulatoires périodiques et cylindriques en profondeur constante. *Annales des Ponts et Chaussées*, Tome 114:42–78, 1944.
- [114] J. H. Michell. XLIV. The highest waves in water. *The London, Edinburgh, and Dublin Philosophical Magazine and Journal of Science*, 36(222):430–437, 1893.
- [115] J. W Miles. On the generation of surface waves by shear flows. *Journal of Fluid Mechanics*, 3(2):185–204, 1957.
- [116] J.H. Milgram. Active water-wave absorbers. *Journal of Fluid Mechanics*, 42(4):845–859, 1970.
- [117] A. Modave, E. Deleersnijder, and E. JM Delhez. On the parameters of absorbing layers for shallow water models. *Ocean Dynamics*, 60(1):65–79, 2010.
- [118] G. Moe and O. Arntsen. Particle velocity distribution in surface waves. In *Coastal Engineering 1996*, pages 565–574. 1997.
- [119] W. H. Munk. The solitary wave theory and its application to surf problems. *Annals of the New York Academy of Sciences*, 51(1):376–424, 1949.
- [120] H. Murakami, Y. Hosoi, Y. Sawamura, and R. Ikeda. Wave induced flow around submerged vertical and horizontal plates. In *Proc. of the 39th Conf. on Coastal Engng.*, pages 571–575, (in Japanese), 1992.
- [121] H. Murakami, S. Itoh, Y. Hosoi, and S. Yoshiyuki. Wave induced flow around submerged sloping plates. In *Coastal Engineering Proceedings*, volume 2, pages 1454–1468, 1994.

- [122] B. A. O'Connor, S. Pan, J. Nicholson, N. MacDonald, and D. A. Huntley. A 2d model of waves and undertow in the surf zone. In *Coastal Engineering 1998*, pages 286–296. 1999.
- [123] OpenFOAM.com. Openfoam, Version 2.2.0. 2013.
- [124] G. Orer and A. Ozdamar. An experimental study on the efficiency of the submerged plate wave energy converter. *Renewable Energy*, 32(8):1317–1327, 2007.
- [125] J. T. Ottesen. Valveless pumping in a fluid-filled closed elastic tube-system: one-dimensional theory with experimental validation. *Journal of mathematical biology*, 46(4):309–332, 2003.
- [126] Y. Ouellet and I. Datta. A survey of wave absorbers. *Journal of Hydraulic Research*, 24(4):265–280, 1986.
- [127] J.-C. Park, M.-H. Kim, and H. Miyata. Fully non-linear free-surface simulations by a 3D viscous numerical wave tank. *International Journal for Numerical Methods in Fluids*, 29(6):685–703, 1999.
- [128] M. Patarapanich. Maximum and zero reflection from submerged plate. *Journal of Waterway, Port, Coastal, and Ocean Engineering*, 110(2):171–181, 1984.
- [129] W.G. Penney and A.T. Price. Part II. Finite periodic stationary gravity waves in a perfect liquid. *Philosophical Transactions of the Royal Society of London A: Mathematical, Physical and Engineering Sciences*, 244(882):254–284, 1952.
- [130] R. Perić and M. Abdel-Maksoud. Reliable damping of free-surface waves in numerical simulations. *Ship Technology Research*, 63(1):1–13, 2016.
- [131] R. Perić and M. Abdel-Maksoud. Analytical prediction of reflection coefficients for wave absorbing layers in flow simulations of free-surface waves. *arXiv preprint arXiv:1705.06940*, 2017.
- [132] O. M. Phillips. On the generation of waves by turbulent wind. *Journal of Fluid Mechanics*, 2(5):417–445, 1957. doi: 10.1017/S0022112057000233.
- [133] G. Pinon, G. Perret, L. Cao, A. Poupardin, J. Brossard, and E. Rivoalen. Vortex kinematics around a submerged plate under water waves. part II: Numerical computations. *European Journal of Mechanics-B/Fluids*, 65:368–383, 2017.
- [134] A. Poupardin, G. Perret, G. Pinon, N. Bourneton, E. Rivoalen, and J. Brossard. Vortex kinematic around a submerged plate under water waves. part I: Experimental analysis. *European Journal of Mechanics - B/Fluids*, 34:47 – 55, 2012.
- [135] N. Ramsing and J. Gundersen. Seawater and gases. *Limnol. Oceanogr*, 37:1307–1312.

- [136] W. Rankine. On the exact form of waves near the surface of deep water. *Philosophical Transactions of the Royal Society of London*, 153:127–138, 1863.
- [137] L. Rayleigh. On the circulation of air observed in kundt's tubes, and on some allied acoustical problems. *Philosophical Transactions of the Royal Society of London*, 175: 1–21, 1884.
- [138] B.G. Reguero, I.J. Losada, and F.J. Méndez. A global wave power resource and its seasonal, interannual and long-term variability. *Applied Energy*, 148:366–380, 2015.
- [139] V. Rey and J. Touboul. Forces and moment on a horizontal plate due to regular and irregular waves in the presence of current. *Applied Ocean Research*, 33(2):88–99, 2011.
- [140] D. Rinderknecht, A. I. Hickerson, and M. Gharib. A valveless micro impedance pump driven by electromagnetic actuation. *Journal of Micromechanics and Microengineering*, 15(4):861, 2005.
- [141] B. Robertson, K. Hall, R. Zytner, and I. Nistor. Breaking waves: Review of characteristic relationships. *Coastal Engineering Journal*, 55(01):1350002, 2013.
- [142] B. D. Rogers and R.A. Dalrymple. Sph modeling of breaking waves. In *Coastal Engineering 2004: (In 4 Volumes)*, pages 415–427. World Scientific, 2005.
- [143] R.C.H. Russell and J.D.C. Osorio. An experimental investigation of drift profiles in a closed channel. *Coastal Engineering Proceedings*, 1(6):10, 1957.
- [144] J. Rytkönen and G. Granholm. Experimental investigation of plunger type wave maker. *Rakenteiden mekaniikka*, 22(3):25–46, 1989.
- [145] S. Saincher and J. Banerjee. Influence of wave breaking on the hydrodynamics of wave energy converters: A review. *Renewable and Sustainable Energy Reviews*, 58: 704–717, 2016.
- [146] H.A. Schäffer and G. Klopman. Review of multidirectional active wave absorption methods. *Journal of waterway, port, coastal, and ocean engineering*, 126(2):88–97, 2000.
- [147] P. F. Siew and D. G. Hurley. Long surface waves incident on a submerged horizontal plate. *Journal of Fluid Mechanics*, 83(01):141, 1977.
- [148] G. G Stokes. On the theory of oscillatory waves. *Trans Cambridge Philos Soc*, 8: 441–473, 1847.
- [149] L.G. Straub, C. E. Bowers, and J.B. Herbich. Laboratory tests of permeable wave absorbers. *Coastal Engineering Proceedings*, 1(6):44, 1957.

-
- [150] R. Stuhlmeier. Gerstner's water wave and mass transport. *Journal of Mathematical Fluid Mechanics*, 17(4):761–767, 2015.
- [151] I. A. Svendsen. Mass flux and undertow in a surf zone. *Coastal Engineering*, 8(4):347–365, 1984.
- [152] K. Takano. Effet de passage de la houle sur un seuil. *La Houille Blanche*, (3), 1960.
- [153] G. Taylor. An experimental study of standing waves. In *Proceedings of the Royal Society of London A: Mathematical, Physical and Engineering Sciences*, volume 218, pages 44–59. The Royal Society, 1953.
- [154] W. Thielicke and E.J. Stamhuis. PIVlab—towards user-friendly, affordable and accurate digital particle image velocimetry in MATLAB. *Journal of Open Research Software*, 2(1), 2014.
- [155] W. Thielicke and E.J. Stamhuis. PIVlab Time-resolved digital particle image velocimetry tool for MATLAB. PIV ver. 1.32, 2014.
- [156] H. Thomann. Simple pumping mechanism in a valveless tube. *Z. Angew. Math. Phys.*, 29:169–177, 1978.
- [157] S. A. Tiedeman, W. Allsop, V. Russo, and A. Brown. A demountable wave absorber for wave flumes and basins. *Coastal Engineering Proceedings*, 1(33):37, 2012.
- [158] S. Timmermann and J. T. Ottesen. Novel characteristics of valveless pumping. *Physics of Fluids*, 21(5):053601, 2009.
- [159] R. Tiron, F. Mallon, F. Dias, and E. G. Reynaud. The challenging life of wave energy devices at sea: A few points to consider. *Renewable and Sustainable Energy Reviews*, 43:1263–1272, 2015.
- [160] H. Titah-Benbouzid and M. Benbouzid. An up-to-date technologies review and evaluation of wave energy converters. *Int. Review of electrical engng-IREE*, 10(1):52–61, 2015.
- [161] J. Tollefson. Power from the oceans: Blue energy. *Nature*, 508:302–304, 2014.
- [162] J. Touboul and V. Rey. Bottom pressure distribution due to wave scattering near a submerged obstacle. *Journal of Fluid Mechanics*, 702:444–459, 2012.
- [163] J. P. Vila. SPH renormalized hybrid methods for conservation laws: applications to free surface flows. *Meshfree methods for partial differential equations II*, pages 207–229, 2005.

- [164] D. Violeau and R. Issa. Numerical modelling of complex turbulent free-surface flows with the SPH method: an overview. *International Journal for Numerical Methods in Fluids*, 53(2):277–304, 2007.
- [165] D. Violeau and B. D. Rogers. Smoothed particle hydrodynamics (SPH) for free-surface flows: past, present and future. *Journal of Hydraulic Research*, 54(1):1–26, 2016.
- [166] Z. Wei and R. A. Dalrymple. SPH modeling of short-crested waves. *Proc. 12th SPHERIC International workshop, Ourense (Spain), 13-15 June 2017*, 2017.
- [167] H. G. Weller, G. Tabor, H. Jasak, and C. Fureby. A tensorial approach to computational continuum mechanics using object-oriented techniques. *Computers in physics*, 12(6):620–631, 1998.
- [168] H. Wendland. Piecewise polynomial, positive definite and compactly supported radial functions of minimal degree. *Advances in Computational Mathematics*, 4(1):389–396, 1995. ISSN 10197168. doi: 10.1007/BF02123482.
- [169] G. B. Whitham. Non-linear dispersion of water waves. *Journal of Fluid Mechanics*, 27(2):399–412, 1967.
- [170] G. B. Whitham. Variational methods and applications to water waves. In *Proceedings of the Royal Society of London A: Mathematical, Physical and Engineering Sciences*, volume 299, pages 6–25. The Royal Society, 1967.
- [171] R. Wiegel and J. Johnson. Elements of wave theory. *Coastal Engineering Proceedings*, 1(1):5–22, 1950.
- [172] V. E. Zakharov. Stability of periodic waves of finite amplitude on the surface of a deep fluid. *Journal of Applied Mechanics and Technical Physics*, 9(2):190–194, 1968.
- [173] Y. H. Zheng, Y. G. You, and Y. M. Shen. On the radiation and diffraction of water waves by a rectangular buoy. *Ocean engineering*, 31(8):1063–1082, 2004.

Appendices

Appendix A

Gerstner's waves

Cette annexe présente la théorie de Gerstner. Cette description des vagues est historiquement la première qui a été proposée. Elle est caractérisée par des trajectoires de particules fermées, contrairement à la théorie d'Airy : il n'y a pas de dérive lagrangienne. Par contre le flux de masse eulérien conserve le même profil dans la couche de surface. Il y a également un écoulement de retour proche de la surface libre. On dérive ici les équations qui décrivent ce genre de vagues, et on évalue le flux moyen de masse. La solution exacte vérifiant les équations d'Euler n'est valide qu'en profondeur infinie. Des simulations utilisant la méthode SPH sont présentées pour évaluer le flux de masse dans la colonne d'eau. On vérifie qu'un tel profil de flux de masse est bien observé dans les simulations.

In this appendix, Gerstner's wave theory is reviewed. The main characteristic of this description of water waves compared to the Airy's waves is that the particle trajectories are closed. Thus there is no Lagrangian drift. A more important feature of interest to us is the absence of mean flow rate over a water column. This is similar to what should be expected for a closed tank. Nonetheless, the wave mass transport in the surface layer M^w is unchanged in between these two theories.

The Gerstner's wave (or trochoidal wave) theory is the first known mathematical description of periodic waves and was developed by Gerstner in the early 19th century [55] (also in 1802 in proceeding of Prague conference [54]) long before the Airy's wave theory [3]. Gerstner concluded that the surface curve is a trochoid. In this appendix, similarly to Froude [51] and Rankine [136], this assumption will be used and the wave characteristics derived: surface profiles, velocity, vorticity, pressure, dispersion relation and mean Eulerian profile. More precisely, it is assumed that the trajectories describe closed ellipses. This appendix summarizes results from several previous studies [51, 53, 54, 118, 136, 150, 171] and is compared to numerical simulations using the SPH method.

The appendix is organized as follows: first the general trochoidal theory is developed for deep water. At first no assumption is made on the water depth and it will appear that the water depth has to be infinite. Case of finite depth is considered by other authors [53] but the condition of incompressibility is not verified as it is shown in this appendix. Second, the mean Eulerian velocity particle velocity is evaluated for regular waves. The profile is compared to the case of Airy waves in deep water. Similarly, there is a forward velocity in the surface layer but a strong negative current in the vicinity of the surface layer. The wave mass transport in the surface layer is evaluated and is similar to the one found in the Airy's wave theory. Third, the results are compared to simulations using SPH method.

A.1 Deep water trochoidal theory

First, no assumption is made on the water depth. It will appear from the derivation of the incompressibility condition that the depth has to be infinite for such a solution to exist. The particle trajectory is assumed to be of the form:

$$x(x_0, z_0, t) = x_0 - a(z_0) \cos(\omega t - kx_0), \quad (\text{A.1.1a})$$

$$z(x_0, z_0, t) = z_0 + b(z_0) \sin(\omega t - kx_0), \quad (\text{A.1.1b})$$

where x_0 and z_0 denotes the center of the trajectory and a , b the principle and secondary axis of the described ellipsoid (there is no reason for now for a and b to be equal). The

trajectories must verify the Euler equations:

$$\frac{\partial u}{\partial x} + \frac{\partial w}{\partial z} = 0, \quad (\text{A.1.2a})$$

$$\frac{Du}{Dt} = -\frac{1}{\rho} \frac{\partial p}{\partial x}, \quad (\text{A.1.2b})$$

$$\frac{Dw}{Dt} = -\frac{1}{\rho} \frac{\partial p}{\partial z} - g \quad (\text{A.1.2c})$$

where D/Dt denotes the Lagrangian derivative. Chain rules are applied to write this equations in terms of Lagrangian derivative only. The velocity is simply

$$u(x_0, z_0, t) = a(z_0) \omega \sin(\omega t - kx_0), \quad (\text{A.1.3a})$$

$$w(x_0, z_0, t) = b(z_0) \omega \cos(\omega t - kx_0). \quad (\text{A.1.3b})$$

To verify the continuity equation, one needs to evaluate the derivative of u and v with respect to the Eulerian coordinates. One can use the following properties

$$\begin{pmatrix} \partial_x u \\ \partial_z u \end{pmatrix} = \begin{pmatrix} \partial_{x_0} x & \partial_{x_0} y \\ \partial_{z_0} x & \partial_{z_0} y \end{pmatrix}^{-1} \cdot \begin{pmatrix} \partial_{x_0} u \\ \partial_{z_0} u \end{pmatrix} \quad (\text{A.1.4})$$

or

$$\begin{pmatrix} \partial_x u \\ \partial_z u \end{pmatrix} = \begin{pmatrix} 1 - ka(z_0) \sin \theta & -kb(z_0) \cos \theta \\ -a'(z_0) \cos \theta & 1 + b'(z_0) \sin \theta \end{pmatrix}^{-1} \cdot \begin{pmatrix} \partial_{x_0} u \\ \partial_{z_0} u \end{pmatrix} \quad (\text{A.1.5})$$

where $\theta = \omega t - kx_0$.

$$\begin{pmatrix} \partial_x u \\ \partial_z u \end{pmatrix} = \frac{1}{\Delta} \begin{pmatrix} 1 + b'(z_0) \sin \theta & kb(z_0) \cos \theta \\ a'(z_0) \cos \theta & 1 - ka(z_0) \sin \theta \end{pmatrix} \cdot \begin{pmatrix} \partial_{x_0} u \\ \partial_{z_0} u \end{pmatrix} \quad (\text{A.1.6})$$

where Δ is the determinant of the matrix and should be non-zero:

$$\Delta = 1 - \{a'(z_0)b(z_0)k \cos^2 \theta + a(z_0)b'(z_0)k \sin^2 \theta\} + \{b'(z_0) - ka(z_0)\} \sin \theta \neq 0. \quad (\text{A.1.7})$$

Using eq.A.1.6, it yields

$$\Delta \partial_x u = -k\omega \cos \theta \{a(z_0) + (a'(z_0)b(z_0) - a(z_0)b'(z_0)) \sin \theta\}. \quad (\text{A.1.8})$$

Identically, it comes

$$\Delta \partial_z w = \omega \cos \theta \{b'(z_0) - k(a'(z_0)b(z_0) - a(z_0)b'(z_0)) \sin \theta\}. \quad (\text{A.1.9})$$

Using the continuity equation, one gets the following conditions on the unknown functions a and b :

$$a(z_0)b'(z_0) = a'(z_0)b(z_0), \quad (\text{A.1.10a})$$

$$b'(z_0) = ka(z_0) \quad (\text{A.1.10b})$$

After simple manipulations, it comes

$$\frac{b''(z_0)}{b'(z_0)} = \frac{b'(z_0)}{b(z_0)} \quad (\text{A.1.11})$$

and thus one can conclude that $a(z_0) = b(z_0) = a_w e^{kz_0}$, where a_w is the wave amplitude. It appears that to respect the incompressibility, infinite water depth has to be considered. Then, the determinant of the Jacobi matrix is a constant of time:

$$\Delta = 1 - a_w^2 k^2 e^{2kz_0}. \quad (\text{A.1.12})$$

The vorticity is evaluated in a similar manner:

$$\varpi = \partial_x w - \partial_z u = \omega \frac{2(ka_w)^2 e^{2kz_0}}{1 - (ka_w)^2 e^{2kz_0}} \neq 0. \quad (\text{A.1.13})$$

It appears that Gerstner's waves are rotational at second order. This does not comply with the general assumption of potential flow usually invoked in wave modeling. The vorticity is concentrated near the surface and is positive. Note this is different from the vorticity at the surface itself which will depend on time.

The dispersion relation is found after evaluating the pressure. Using the momentum equations, it yields:

$$-\frac{1}{\rho} \partial_x p = \frac{Du}{Dt} = a(z_0) \omega^2 \cos \theta, \quad (\text{A.1.14a})$$

$$-\frac{1}{\rho} \partial_z p = \frac{Du}{Dt} + g = g - b(z_0) \omega^2 \sin \theta, \quad (\text{A.1.14b})$$

Using once again the chain rules, the pressure derivatives with respect to the Lagrangian coordinates are found:

$$\frac{1}{\rho} \partial_{x_0} p = a_w e^{kz_0} (gk - \omega^2) \cos \theta, \quad (\text{A.1.15a})$$

$$\frac{1}{\rho} \partial_{z_0} p = -g + (ka_w)^2 \frac{\omega^2}{k} e^{2kz_0} - a_w e^{kz_0} (gk - \omega^2) \sin \theta. \quad (\text{A.1.15b})$$

The pressure is deduced after integration:

$$p(x_0, z_0, t) = -\rho g z_0 - \rho a_w \left(g - \frac{\omega^2}{k} \right) e^{kz_0} \sin \theta + \frac{1}{2} \rho a_w \frac{\omega^2}{k} (ka_w) e^{2kz_0} + P_0, \quad (\text{A.1.16})$$

where P_0 is a constant to determinate. At the free surface, $p(x_0, z_0 = 0, t) = 0$. This leads to:

$$0 = -\rho a_w \left(g - \frac{\omega^2}{k} \right) \sin \theta + \frac{1}{2} \rho a_w \frac{\omega^2}{k} (ka_w) + P_0, \quad (\text{A.1.17})$$

for all values of θ . Hence, the dispersion relation is:

$$\omega^2 = kg, \quad (\text{A.1.18})$$

identically to Airy waves in deep water for $ka_w \ll 1$. Note however that this dispersion relation is independent of the wave steepness, ka_w . In section 1.5.1, it was mentioned that the wave steepness affects the dispersion relation of Airy waves and particularly for deep water waves using eq.1.5.1 in the limit $kd \rightarrow \infty$:

$$\omega^2 = gk(1 + (ka_w)^2). \quad (\text{A.1.19})$$

In summary, in the deep water assumption, the particle motion is given by:

$$x(x_0, z_0, t) = x_0 - a_w e^{kz_0} \cos(\omega t - kx_0), \quad (\text{A.1.20a})$$

$$z(x_0, z_0, t) = z_0 + a_w e^{kz_0} \sin(\omega t - kx_0), \quad (\text{A.1.20b})$$

where k is the wave number and verify the steepness independent dispersion relation:

$$\omega^2 = gk. \quad (\text{A.1.21})$$

The free surface shape is found by definition after evaluating the particle trajectory at $z_0 = 0$:

$$\eta(x, t) = a_w \sin(\omega t - kx_0(x, t)), \quad (\text{A.1.22})$$

and requires to inverse the particle position:

$$x = x_0(x, t) - a_w \cos(\omega t - kx_0(x, t)) \quad (\text{A.1.23})$$

This can be done numerically. Figure A.1 shows the surface profiles for different wave steepness for $\omega = 2\pi$. The limit steepness is $ka_w = 1$ for such waves.

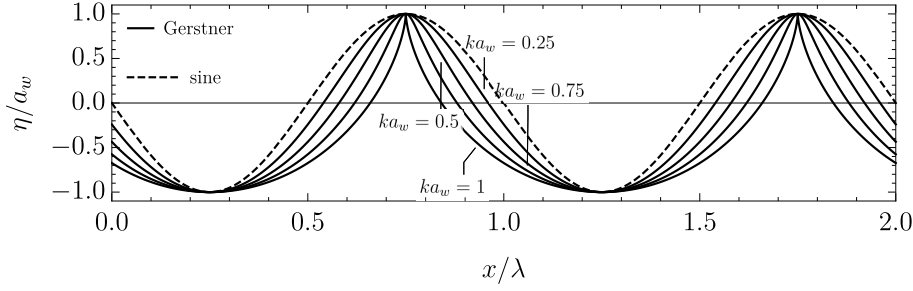


Figure A.1: Free surface profiles of Gerstner's waves of different steepness.

A.2 Mean horizontal Eulerian mass flux of Gerstner's waves

To evaluate the mean horizontal Eulerian mass flux, ρu , it is convenient to work at fixed $x = 0$ without loss of generality and look at the profile as a function of z . The horizontal velocity is given by:

$$u(z, t) = a_w \omega e^{kz_0(z, t)} \sin(\omega t - kx_0(z, t)), \quad (\text{A.2.1})$$

The goal is to express the velocity as a function of z and t only. To do so, consider small steepness and expand near the position $(0, z)$. At first order:

$$u(z, t) = a_w \omega e^{kz} \sin(\omega t), \quad (\text{A.2.2})$$

Identically for the positions:

$$x_0(z, t) = a_w \omega e^{kz} \cos(\omega t), \quad (\text{A.2.3a})$$

$$z_0(z, t) = z - a_w \omega e^{kz} \sin(\omega t). \quad (\text{A.2.3b})$$

Using this to get the second order Eulerian velocity expression:

$$\begin{aligned} u(z, t) &= a_w \omega e^{k\{z - a_w \omega e^{kz} \sin(\omega t)\}} \sin[\omega t - k\{a_w \omega e^{kz} \cos(\omega t)\}] \\ &= a_w \omega e^{kz} (1 - ka_w \omega e^{kz} \sin \omega t) (\sin \omega t - ka_w \omega e^{kz} \cos^2 \omega t) \\ &= a_w \omega e^{kz} \sin \omega t - ka_w^2 \omega e^{2kz}, \end{aligned} \quad (\text{A.2.4})$$

where third order terms are dropped. It is readily seen that in the interior of the fluid (below the surface layer) there is for such waves a negative mass flux in average:

$$\overline{\rho u} = -\rho a_w^2 \omega k e^{2kz}, \quad (\text{A.2.5})$$

while for Airy waves there is no mass flux in the interior of the fluid. In the surface layer, it is necessary to take into account the emergence effects, or the time the point is below the surface. By definition a point is in the water if $z_0 \leq 0$. Evaluating the vertical position

up to the second order, leads to the condition

$$z_0 = z - a_w e^{kz} \sin \omega t + k a_w^2 e^{2kz} \leq 0, \quad (\text{A.2.6})$$

Solving and keeping up to second order terms, yields:

$$\sin \omega t \geq \frac{z + k a_w^2}{a_w (1 + k a_w)} \approx \frac{z}{a_w}. \quad (\text{A.2.7})$$

The mean mass flux is evaluated over the submerged time:

$$\overline{\rho u} = \frac{\rho}{T} \int_0^T \mathcal{I}(t) u(z, t) dt, \quad (\text{A.2.8})$$

where $\mathcal{I}(t)$ is a mask function equal to 1 in water and 0 in air. Using the previous relation:

$$\overline{\rho u} = \frac{\rho}{T} \int_{t_0}^{t_1} u(z, t) dt, \quad (\text{A.2.9})$$

where:

$$t_0 = T \frac{\arcsin\left(\frac{z}{a_w}\right)}{2\pi}, \quad (\text{A.2.10a})$$

$$t_1 = \frac{T}{2} - T \frac{\arcsin\left(\frac{z}{a_w}\right)}{2\pi}. \quad (\text{A.2.10b})$$

Retaining only the lowest order terms:

$$\overline{\rho u}(z) = \begin{cases} -\rho a_w^2 \omega k e^{2kz} & , z < -a_w \\ \rho \frac{a_w \omega}{\pi} e^{kz} \begin{pmatrix} \sqrt{1 - \left(\frac{z}{a_w}\right)^2} \\ -a_w k e^{kz} \arccos\left(\frac{z}{a_w}\right) \end{pmatrix} & , -a_w < z < a_w \end{cases} \quad (\text{A.2.11})$$

For Airy waves, the mean Eulerian mass flux is:

$$\overline{\rho u}_{\text{Airy}}(z) = \begin{cases} 0 & , z < -a_w \\ \rho \frac{a_w \omega}{\pi} e^{kz} \sqrt{1 - \left(\frac{z}{a_w}\right)^2} & , -a_w < z < a_w \end{cases} \quad (\text{A.2.12})$$

In the latter theory, there is no mean mass flux in the interior of the fluid. As $d \rightarrow \infty$, it is difficult to subtract a mean value on the entire water column. The two profiles are displayed in figure A.2.

The wave mass transport in the surface layer is defined by eq.1.3.43 and at second order,

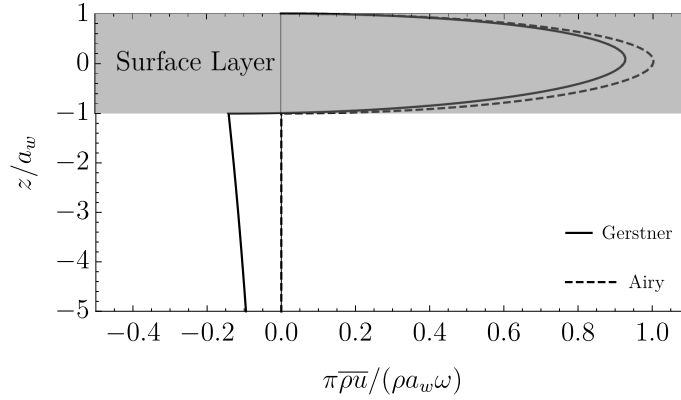


Figure A.2: Mean mass flux Eulerian profiles for Airy and Gerstner's waves (with $ka_w = 0.1$).

it comes for Gerstner's waves:

$$M^w = \frac{1}{2}a^2\omega, \quad (\text{A.2.13})$$

similarly to Airy's wave theory in the limit of deep water waves.

A.3 Compared Mass flux theory and simulations

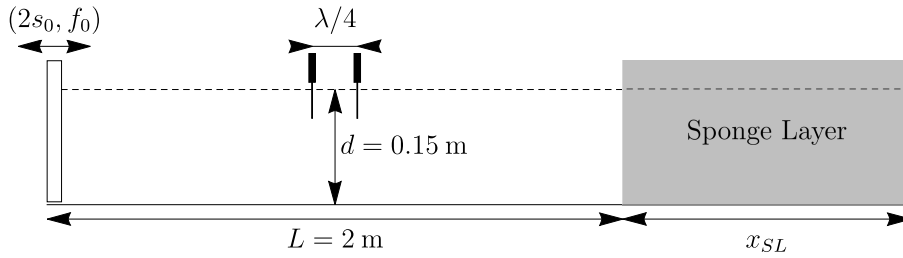


Figure A.3: Numerical wave flumes

In this section, the SPH method presented in appendix K along with the “optimal” sponge layer method developed in appendix I are used to simulate a wave flume of constant water depth $d = 15$ cm. Waves are generated using a piston type wave maker. The target wave amplitude and frequency are $h_{inc} = 2a_{inc} = 2.5$ cm and $f = 1.5$ Hz. The wave flume is composed of 2 meters of physical part¹ and a one wavelength long absorption sponge layer section where a power sponge layer function with $n_B = 3$ and $B_{mean} = 0.45$ (see table I.1 and appendix I for more details about the choice of this sponge layer parameters). The simulation is run for 30 seconds or 45 wave periods for two kernel resolution $h_{SPH} = 2 \times r_{SPH} = 2.5$ mm and $h_{SPH} = 2 \times r_{SPH} = 1.25$ mm (which corresponds to 30 and 60 particles on a water column). Two probes spaced by 0.25λ are placed and centered in the

¹ Physical part means here without fictitious absorption.

physical part of the flume (see figure A.3). The Goda & Suzuki [59] two probes method is applied on sample time of 2 wave periods for both cases. Figure A.4 shows the measured wave reflection coefficient and amplitude with respect to time. The amplitude is slightly below the target wave and the reflection is less than 3% as expected. An asymptotic regime is thus achieved for the wave field.

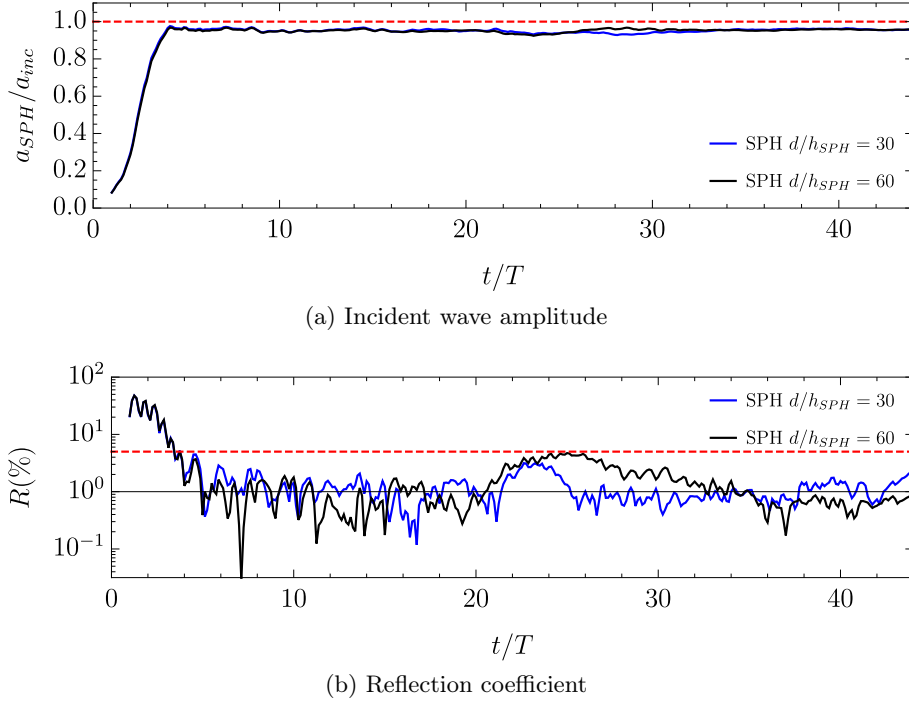


Figure A.4: Incident wave amplitude and reflection coefficient in the SPH wave flume using The Goda & Suzuki [59] two probes method. The reflection is close to the theoretical 2% value (see appendix I).

The mean wave mass flux is measured for these two cases at the centered of the physical tank and plotted in figure A.5 using the 4 last wave periods. No noticeable differences are found when using 1 to 4 wave periods for averaging the profiles. In the figure, two theoretical profiles are shown: the deep water wave theory developed earlier, which is an exact solution of the Euler's equations A.1.2; and the corrected intermediate version, which is:

$$\overline{\rho u}(z) = \begin{cases} -\rho (ka_w)^2 \frac{\omega}{k} \{c^2(z) - 1/2\} & , z < -a_w \\ \rho \frac{a_w \omega}{\pi} c(z) \begin{pmatrix} \sqrt{1 - \left(\frac{z}{a_w}\right)^2} \\ -a_w k s(z) \arccos\left(\frac{z}{a_w}\right) \end{pmatrix} & , -a_w < z < a_w \end{cases}, \quad (\text{A.3.1})$$

where $s(z) = \sinh[k(d+z)] / \sinh kd$ and $c(z) = \cosh[k(d+z)] / \sinh kd$.

The profiles compare well with the Gerstner's wave theory. Of particular interest to the present thesis is the fact that the surface layer flow is quite similar to the Airy wave

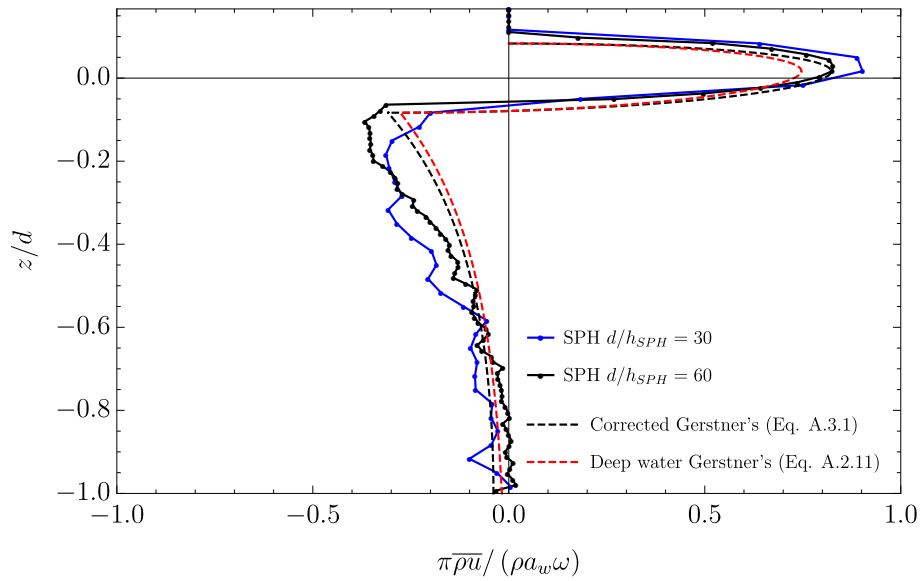


Figure A.5: SPH-simulated Gerstner-like wave profiles compared to the theoretical curves of deep water (see eq.A.2.11) and the corrected intermediate water depth (see eq.A.3.1).

theory. The return flow is located close to the surface in the present simulations, similarly to Gerstner's waves. From the mass transport conservation point of view, it looks like the return flow does not dive deep in the water column. This is a useful information for the design of wave pump systems like the ones studied in the chapters 2 and 3.

Appendix B

Boundary Layers Effects and Wave Mass Transport

Cette annexe présente les effets des vagues sur la couche limite du fond. L'épaisseur de la couche limite est évaluée, et on montre qu'il existe une vitesse de dérive indépendante de la viscosité à la couche limite dans la direction de propagation de la vague. Cela démontre que les efforts de friction peuvent amplifier le transport de masse dans une colonne d'eau.

Inspired by acoustic observations, a phenomenon, called *acoustic streaming*, is also responsible for mass transport and thus worth developing. This effect was first explained theoretically by Rayleigh [137] and extended to water waves propagating in one direction by Longuet-Higgins [93]. In this appendix a review of this phenomena is proposed following the steps of Mei et al. [110] restricted for brevity to a two dimensional case.

To develop this theory, one needs to relax the ideal fluid assumption. It is supposed that the viscous effects are small (or $\mathcal{R} \gg 1$) such that the ideal fluid potential theory developed before is still valid away from the boundaries. The region where this assumption is no more valid is called the *boundary layer* and its thickness is δ_ν in dimensional form and will be noted Δ_ν in non-dimensional form, where the index ν refers to the kinematic viscosity ($\nu = \mu/\rho$). The Navier–Stokes equations with the defined non-dimensional numbers in two dimensions are

$$\begin{cases} \partial_X U + \partial_Z W &= 0, \\ \partial_\tau U + U \partial_X U + W \partial_Z U &= -\partial_X P + \frac{1}{\mathcal{R}} (\partial_{X,X} U + \partial_{Z,Z} U), \\ \partial_\tau W + U \partial_X W + W \partial_Z W &= -\partial_Z P - 1 + \frac{1}{\mathcal{R}} (\partial_{X,X} W + \partial_{Z,Z} W), \end{cases} \quad (\text{B.0.1})$$

where $\mathcal{R} = (gd^3/\nu^2)^{1/2}$ is the wave Reynolds number (defined in section 1.5.3) and $\mathbf{U} = (U, W)$ is the total velocity. From the previous potential analysis (see eq.1.3.4), the velocities near the sea bed are:

$$U|_{BL} \sim A\Omega O(1), \quad W|_{BL} \sim A\Omega O(K\Delta_\nu). \quad (\text{B.0.2})$$

and in the boundary layer the typical scale of variation of the horizontal derivative is $1/K$ (*i.e.* the wavelength) and vertical derivative is Δ_ν (*i.e.* the boundary layer thickness), thus:

$$\frac{1/\mathcal{R}\partial_{Z,Z}U}{\partial_\tau U} \sim O(1), \quad \frac{1/\mathcal{R}\partial_{X,X}U}{\partial_\tau U} \sim O(K\Delta_\nu)^2, \quad \frac{U\partial_X U}{\partial_\tau U} \sim O(KA) = O(\epsilon) \quad (\text{B.0.3})$$

where $\Delta_\nu \propto 1/(\mathcal{R}\Omega)^{1/2}$. It is assumed that $(K\Delta_\nu)^2 \ll \epsilon$, thus the system of eq.B.0.1 can be approximated by:

$$\begin{cases} \partial_X U + \partial_Z W &= 0, \\ \partial_\tau U + U \partial_X U + W \partial_Z U &= -\partial_X P + \frac{1}{\mathcal{R}} \partial_{Z,Z} U, \\ 0 &= -\partial_Z P - 1, \end{cases} \quad (\text{B.0.4})$$

all the terms that are ignored in the last equations are at least of order $K\Delta_\nu$. From the last equation, $P_* = P + Z$ is independent of Z and thus it is equal to its value just outside the boundary layer. Consequently, the boundary layer terms of the Navier–Stokes equation

being negligible just outside it:

$$-\partial_X P_* = -\partial_X P = \partial_T U_I + U_I \partial U_I, \quad (\text{B.0.5})$$

where U_I corresponds to the inviscid velocity at the wall and is deduced from the potential theory. The term $W_I \partial_X U_I$ is dropped as W_I is zero at the sea bed. The horizontal momentum equation of eq.B.0.4 becomes

$$\partial_T U + U \partial_X U + W \partial_Z U = \partial_T U_I + U_I \partial U_I + \frac{1}{\mathcal{R}} \partial_{Z,Z} U, \quad (\text{B.0.6})$$

and U_I is known.

Similarly to the potential theory, the horizontal velocity is expanded in the boundary layer in a perturbation series of $\epsilon = KA$:

$$\mathbf{U} = \mathbf{U}^{(1)} + \mathbf{U}^{(2)} + \dots \quad (\text{B.0.7})$$

where $U^{(1)} = O(\epsilon)$ and $U^{(2)} = O(\epsilon^2)$ and forth and so on. Keeping only the first order terms, the horizontal momentum equation eq.B.0.6 becomes

$$\partial_T U^{(1)} = \partial_T U_I + \frac{1}{\mathcal{R}} \partial_{Z,Z} U^{(1)} \quad (\text{B.0.8})$$

with the boundary conditions

$$\begin{cases} U^{(1)} = 0 & \text{at } Z = -1, \\ U^{(1)} \rightarrow U_I & \text{for } Z + 1 \gg \Delta_\nu. \end{cases} \quad (\text{B.0.9})$$

Assuming that the inviscid velocity is of the general form

$$U_I = \Re \{ U_0(X) e^{i\Omega T} \}, \quad (\text{B.0.10})$$

it is easily found that

$$U^{(1)} = \Re \left\{ U_0(X) \left(1 - e^{-(1+i)\Xi} \right) e^{i(\Omega T - KX)} \right\}, \quad (\text{B.0.11})$$

where $\Xi = (Z + 1) / \Delta_\nu$ and the boundary layer thickness is now known:

$$\Delta_\nu = \sqrt{\frac{2}{\Omega \mathcal{R}}}, \quad \delta_\nu = \sqrt{\frac{2\nu}{\omega}}. \quad (\text{B.0.12})$$

Note that for the case of a forward wave as described by eq.1.3.4, then $U_0 = A\Omega / \sinh K e^{-iKX}$.

Using the continuity equation, the vertical velocity comes

$$W^{(1)} = \Re \left\{ -\partial_X U_0 \Delta_\nu \left[\frac{1-i}{2} \left(e^{-(1+i)\Xi} - 1 \right) + \Xi \right] e^{i(\Omega\mathcal{T} - KX)} \right\}. \quad (\text{B.0.13})$$

For the case of a forward going wave, the coefficient becomes $-\partial_X U_0 \Delta_\nu = iK \Delta_\nu A \Omega / \sinh K e^{-iKX}$. The horizontal velocity profile (eq. B.0.11) correction is plotted in figure B.1 and compared with the complete linear viscous solution of Lamb [82] for the case $\Omega = 1$ and $\mathcal{R} = 10^5$.

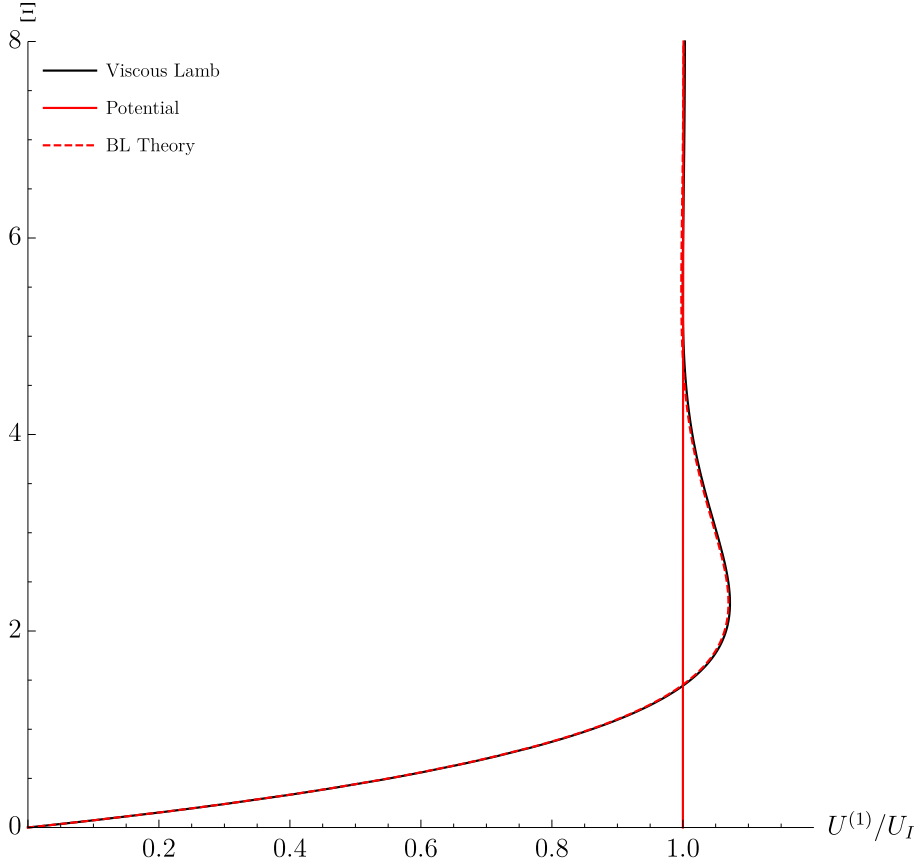


Figure B.1: Boundary layer horizontal velocity profiles in linear waves for $\Omega = 1$ and $\mathcal{R} = 10^5$. The curves show the linear viscous solution of Lamb [82] (see appendix F), the potential theory and the present boundary layer correction. The term in $\exp(i\Omega\mathcal{T} - KX)$ is dropped here and only the amplitude is shown.

Considering now the second order terms in the horizontal momentum equation eq.B.0.6:

$$\partial_{\mathcal{T}} U^{(2)} - \frac{1}{\mathcal{R}} \partial_{Z,Z} U^{(2)} = U_I \partial_X U_I - \left(U^{(1)} \partial_X U^{(1)} + W^{(1)} \partial_Z U^{(1)} \right). \quad (\text{B.0.14})$$

Taking the mean over a wave period:

$$-\frac{1}{\mathcal{R}} \partial_{Z,Z} \overline{U^{(2)}} = \overline{U_I \partial_X U_I} - \left(\partial_X \overline{U^{(1)} U^{(1)}} + \partial_Z \overline{U^{(1)} W^{(1)}} \right), \quad (\text{B.0.15})$$

where the continuity equation is used to rewrite the term in brackets. The terms $\overline{U^{(1)}U^{(1)}}$ and $\overline{U^{(1)}W^{(1)}}$ corresponds to the components of the *Reynolds stress* tensor. The mean flow arises to compensate the pressure fluctuation of the inviscid solution (first term of the right-hand side) and the Reynolds stress friction at the sea bed. Eq. B.0.15 is solved straightforwardly with the boundary conditions:

$$\begin{cases} \overline{U^{(2)}} = 0, & z = 0, \\ \partial_z \overline{U^{(2)}} \rightarrow 0, & Z + 1 \gg \Delta_\nu, \end{cases} \quad (\text{B.0.16})$$

which corresponds to a no-slip condition at the sea bed and no stress outside the boundary layer. The mean flow is then:

$$\overline{U^{(2)}} = \Re \left\{ -\frac{U_0 \partial_X U_0^*}{4\Omega} \left[3(1+i) - (1-i)e^{-2\Xi} - 2(1+3i)e^{-(1+i)\Xi} + 2ie^{-(1-i)\Xi} + 2\Xi(1-i)e^{-(1+i)\Xi} \right] \right\}. \quad (\text{B.0.17})$$

Note that at the end of the boundary layer:

$$\overline{U^{(2)}} \xrightarrow{\Xi \rightarrow \infty} \Re \left\{ -3 \frac{U_0 \partial_X U_0^*}{4\Omega} (1+i) \right\}, \quad (\text{B.0.18})$$

and is independent of the viscosity. In the case of a forward going wave:

$$\overline{U^{(2)}} \xrightarrow{\Xi \rightarrow \infty} \frac{3}{4} \frac{A\Omega}{\sinh^2 K} KA. \quad (\text{B.0.19})$$

This development shows how the sea bed viscous boundary layer effects generate a mean velocity of magnitude independent of the viscosity. To workout the effect on the interior of the flow, it requires to proceed to the same evaluation near the free surface.

In the case of Allison's peristaltic pump [5], Longuet-Higgins [95] argued that the streaming velocity is the same for the two boundary layers of the tube. Thus if one assumes a uniform flow in the core (or interior) of the fluid, it comes that the total wave mass transport is increased by $3/4A^2\Omega/K$ and thus it is amplified by a factor of $5/2$. The take-home message is that the mass transport can be amplified by taking into account frictional effects.

Appendix C

Solver *Mathematica* waves generated by plunger

Dans cette annexe, on donne à titre d'exemple un code pour résoudre un problème en utilisant la méthode des expansions (EFE). La solution est codée dans le langage de Mathematica. On vérifie ainsi la vitesse de convergence des coefficients prédite au chapitre 1.

In this appendix, the code to solve the plunger problem of section 1.3.4.2 using eigenfunction expansion (EFE) method is provided for *Mathematica* version 11.0.1.0.

C.1 Linear dispersion relation for waves

First this part of the code provides a calculation of the dispersion relations for linear waves.

Mathematica Session

```

In[1]:= Precision[12/10];
In[2]:= MAXITER = 106;
In[3]:= TH_ERROR = 10-16;
In[4]:= dispPotEval[Ω_, k_] := k * Tanh[k] - Ω2 (*Compute the dispersion relation Error*)
In[5]:= newtRaphPot[Ω_, xguess_] :=
  (*Newton Raphson of the dispersion relation,
  loop till MAXIT or below Threshold TH_ERROR*)
  FixedPointList[(((Ω2 + #2 Sech[#]2)/(# * Sech[#]2 +
  Tanh[#]))N)&, xguess, MAXIT,
  SameTest -> (Abs[#1 - #2] < TH_ERROR&)]
In[6]:= DispPotNR[Ω_] :=
  (*Solver for the propagating mode,
  INPUT:
  Ω : Non-dimensional angular frequency
  OUTPUT:
  {kres, Error} : Non-dimensional real wave number and Error
  *)
  - Module[{kres, xguess, ν, disp, k, kx, ky, min, list},
    ν = Ω2;
    disp = Abs[(k * Tanh[k] - Ω2)2] /. k -> (kx + I * ky);
    xguess =
    ν(1 - 4 * (15 - (15 + 30ν + 30ν2 + 5ν3 - 10ν4 + 2ν5)Exp[-2ν])/
    (15 * (2 * ν + Sinh[2 * ν] - 4(1 - (ν + 1)Exp[-2ν])))-1/4 // N;
    list = newtRaphPot[Ω, xguess];
    kres = list[[-1]] // N;
    {kres, dispPotEval[Ω, kres]}
  ]
In[7]:= dispPotEvNR[Ω_, n_] :=
  (*Solver for the Evanescent modes,
  INPUT:
  Ω : Non-dimensional angular frequency
  n : Number of evanescent modes seeked
  OUTPUT:
  {kres, Error} : Table of non-dimensional imaginary wave number and Error
  *)
  Module[{kres, xguess, ν, disp, k, kx, ky, min, list},
    ν = Ω2;
    disp = Abs[(k * Tanh[k] - Ω2)2] /. k -> (kx + I * ky);
    xguess = n * Π - Π/2Tanh[(2 * ν)/(n * Π2)] // N;
    list = newtRaphPot[Ω, -I * xguess];
    kres = list[[-1]] // N;
    {kres, dispPotEval[Ω, kres]}
  ]
In[8]:= DispPotAllNR[Ω_, ntot_] :=
  (*Wave modes constructor,
  INPUT:
  Ω : Non-dimensional angular frequency
  n : Number of evanescent modes seeked
  OUTPUT:
  {kres, Error} : Table of non-dimensional wave number and associated Error,
  the modes are ranked in importance order
  *)
  Module[{list, i = 1},
    list = DispPotNR[Ω];
    While[i < ntot,
      AppendTo[list, DispPotEvNR[Ω, i]];
      i = i + 1;];
    list
  ]
In[9]:= KTab[Sigma_, N_] := DispPotAllNR[Sigma, N][[; ; , 1]]
    
```

C.2 Projection Calculations

In this part of the code, the projections of the eigenfunctions are pre-calculated analytically.

Mathematica Session

```
In[10]:= FnFn[k_] :=
(*Projection of the Modes <cosh[k(1 + Z)] cosh[k(1 + Z)]>_1^0,
INPUT:
k : Wave number
OUTPUT:
res : result of the projection,
*)
(2k + Sinh[2k])/(4k)
In[11]:= PnPn[B_, ZA_, ZB_] :=
(*Projection of the Modes <cos[k(1 + Z)] cos[k(1 + Z)]>_ZA^ZB,
INPUT:
B : Wave number
ZA, ZB : borns of the integral
OUTPUT:
res : result of the projection,
*)
(2B(-ZA + ZB) - Sin[2B(1 + ZA)] + Sin[2B(1 + ZB)])/(4B)
In[12]:= Fn1[k_, ZA_, ZB_] :=
(*Projection of the Mode with unity <cosh[k(1 + Z)]|1>_ZA^ZB,
INPUT:
k : Wave number
ZA, ZB : borns of the integral
OUTPUT:
res : result of the projection,
*)
(-Sinh[k(1 + ZA)] + Sinh[k(1 + ZB)])/k
In[13]:= FnPn[k_, B_, ZA_, ZB_] :=
(*Projection of the Mode with unity <cosh[k(1 + Z)] cos[B(1 + Z)]>_ZA^ZB,
INPUT:
k : Wave number for the cosh
B : Wave number for the cos
ZA, ZB : borns of the integral
OUTPUT:
res : result of the projection,
1/(B^2 + k^2)(-BCosh[k(1 + ZA)]Sin[B(1 + ZA)] +
BCosh[k(1 + ZB)]Sin[B(1 + ZB)] -
kCos[B(1 + ZA)]Sinh[k(1 + ZA)] +
kCos[B(1 + ZB)]Sinh[k(1 + ZB)])
```

C.3 Solver

This function construct the system of equation and solve the problem of the wave generated by a plunger.

```
In[14]:= Clear[$Cp, $JI, $eq, X, Z]
In[15]:= SolvePlunger[sigma_, L_, Dp_, Nm_] :=
(*
Solve the problem of wave generation by an oscillating plunger:
INPUT:
sigma : Non-dimensional angulkar frequency,
sigma = omega*sqrt[d/g]
L: Non-dimensional half length of the plunger,
L = l/d
Dp: Non-dimensional draft,
Dp=dp/d
Nm: number of modes in the expansion,
OUTPUT:
Ainf : Wave size at infinity,
JI[[n]]: list coefficients of Phi1,
```

```

Cp[[n]]: list coefficients of Phi2,
Phi1(X,Z): scalar velocity potential in domain I,
Phi2(X,Z): scalar velocity potential in domain II,
U1(X,Z): horizontal velocity in domain I,
U2(X,Z): horizontal velocity in domain II,
V1(X,Z): vertical velocity in domain I,
V2(X,Z): vertical velocity in domain II,
*)
Module[{Cp, JI, eqTab, Ktab, Btab, i, j, sol, Phi1, Phi2, U1, U2, V1, V2, Ainf},
Cp = Table[Unique[$Cp], {i, 1, Nm}];
JI = Table[Unique[$JI], {i, 1, Nm}];
eqTab = Table[Unique[$eq], {i, 1, 2Nm}];
Ktab = KTab[sigma, Nm];
Btab = Table[{(j - 1) * Pi}/(1 - Dp), {j, 1, Nm}];
(*Velocity Projections of eq.1.3.66*)
For[i = 1, i <= Nm,
eqTab[[i]] =
- I * Ktab[[i]] * Cp[[i]] * FnFn[Ktab[[i]]] ==
(-L)/(1 - Dp) * Fn1[Ktab[[i]], -1, -Dp] +
Sum[JI[[j]](1 - Exp[-2 * Btab[[j]] * L]) * Btab[[j]] *
FnPn[Ktab[[i]], Btab[[j]], -1, -Dp], {j, 2, Nm}];
i = i + 1;
];
(*Scalar Projections of eq.1.3.67*)
eqTab[[1 + Nm]] =
Sum[Cp[[j]] * Fn1[Ktab[[j]], -1, -Dp], {j, 1, Nm}] ==
1/(2(1 - Dp))(-1/3)(-1 + Dp)^3 + (-1 + Dp)L^2 + JI[[1]] * (1 - Dp);
For[i = 2, i <= Nm,
eqTab[[i + Nm]] =
Sum[Cp[[j]] * FnPn[Ktab[[j]], Btab[[i]], -1, -Dp], {j, 1, Nm}] ==
JI[[i]] * (1 + Exp[-2 * Btab[[i]] * L]) * PnPn[Btab[[i]], -1, -Dp] +
1/(2(1 - Dp))(1/Btab[[i]]^3(-2Btab[[i]](-1 + Dp)Cos[Btab[[i]] - Btab[[i]]Dp] +
(-2 + Btab[[i]]^2((-1 + Dp)^2 - L^2))Sin[Btab[[i]] - Btab[[i]]Dp));
i = i + 1;
];
(*Numerical solver*)
sol = NSolve[eqTab, Join[Cp, JI], WorkingPrecision -> 100][[1]];
(*Reconstruction of the solution Phi1 and Phi2*)
Phi1 = ((Z + 1)^2 - X^2)/(2(1 - Dp)) + JI[[1]] +
Sum[JI[[j]] * (Exp[-Btab[[j]] * (X + L)] + Exp[Btab[[j]] * (X - L)]) *
Cos[Btab[[j]](Z + 1)], {j, 2, Nm}];
Phi2 = Sum[Cp[[j]] * Exp[-I * Ktab[[j]] * (X - L)] * Cosh[Ktab[[j]](Z + 1)], {j, 1, Nm}];
(*Reconstruction of the velocity U1 and U2*)
U1 = -X/(1 - Dp) +
Sum[Btab[[j]] * JI[[j]] * (-Exp[-Btab[[j]] * (X + L)] + Exp[Btab[[j]] * (X - L)]) *
Cos[Btab[[j]](Z + 1)], {j, 2, Nm}];
U2 = Sum[-I * Ktab[[j]] * Cp[[j]] * Exp[-I * Ktab[[j]] * (X - L)] *
Cosh[Ktab[[j]](Z + 1)], {j, 1, Nm}];
(*Reconstruction of the velocity V1 and V2*)
V1 = (Z + 1)/(1 - Dp) +
Sum[-Btab[[j]] * JI[[j]] * (Exp[-Btab[[j]] * (X + L)] + Exp[Btab[[j]] * (X - L)]) *
Sin[Btab[[j]](Z + 1)], {j, 2, Nm}];
V2 = Sum[Ktab[[j]] * Cp[[j]] * Exp[-I * Ktab[[j]] * (X - L)] *
Sinh[Ktab[[j]](Z + 1)], {j, 1, Nm}];
(*Wave size at infinity*)
Ainf = -I * Cp[[1]]/sigma * Ktab[[1]] * Sinh[Ktab[[1]]];
(*OUTPUT:*)
{Ainf, JI, Cp, Phi1, Phi2, U1, U2, V1, V2} /. sol
]

```

C.4 Convergence tests

Convergence tests are performed with intermediate $\Omega = 1$, $L = 1$ and $D_p = 1$.

C.4.1 Convergence of the wave amplitude

In this first convergence, the number of modes is increased and the wave amplitude is monitored. Figure 1.17 shows the error on the wave amplitude as a function of the number of modes. The reference value is taken with 500 modes. It is found that the amplitude converges as $N^{-5/3}$. This does not come as a surprised as the influence of the evanescent modes should decay as $N^{-5/3}$ (see eq.1.3.69). This is checked in the next convergence test.

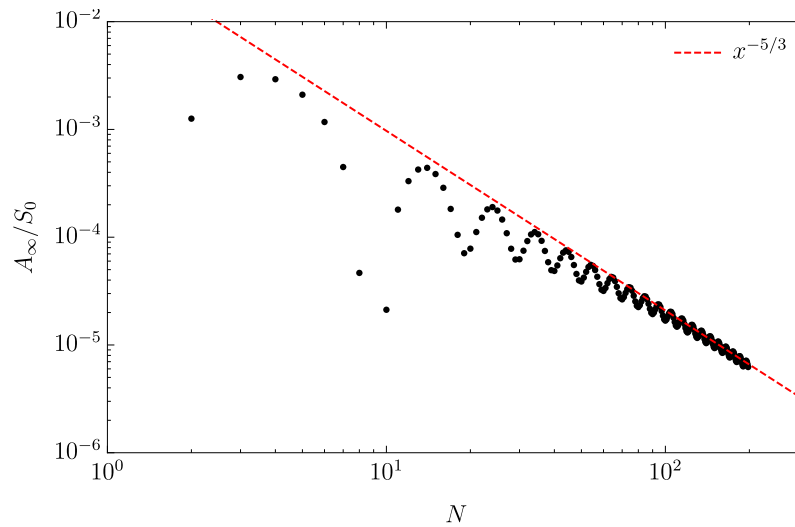


Figure C.1: Error wave amplitude generated by a plunger: the point corresponds to the results found with SolvePlunger and the dashed curve shows the convergence speed of 5/3. Results are for $\Omega = 1$, $L = 1$ and $D_p = 0.1$.

C.4.2 Decay of the coefficients absolute value

Eq.1.3.69 predicts that the coefficients should decay as $N^{-5/3}$. This is indeed the case as shown in figures C.2 and C.3. For the coefficients J_n a small increase is observed for the last modes. This increase is due to the error on the last modes and diminishes when the number of modes is increased. This is visible in the figure between the case with 50 modes and 200 modes. The error "bump" travels down.

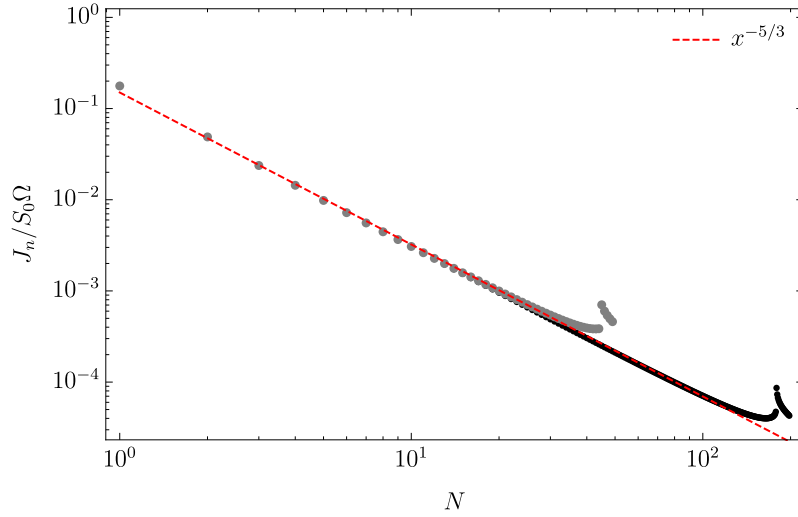


Figure C.2: Coefficients J_n of the wave generated by a plunger for two resolutions $N = 50$ (in gray) and $N = 200$. The decay predicted in eq.1.3.69 is verified. Results are for $\Omega = 1$, $L = 1$ and $D_p = 0.1$.

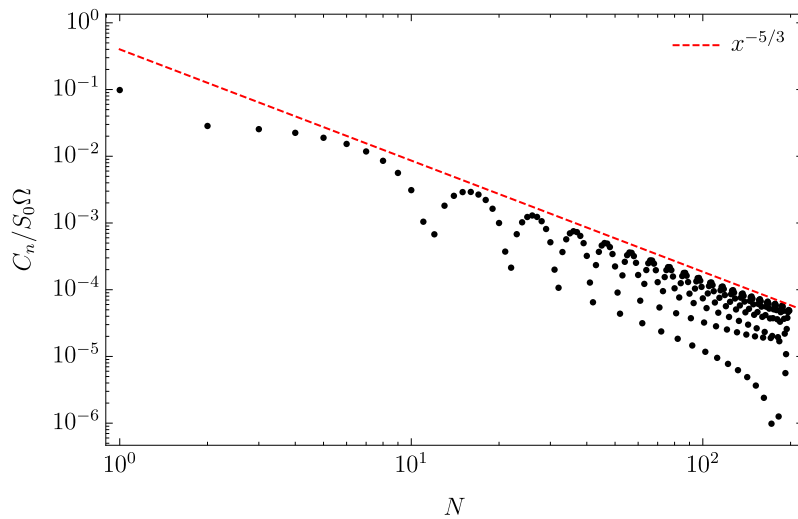


Figure C.3: Coefficients C_n of the wave generated by a plunger for two resolutions $N = 50$ (in gray) and $N = 200$. The decay predicted in eq.1.3.69 is verified. Results are for $\Omega = 1$, $L = 1$ and $D_p = 0.1$.

Appendix D

Proof of mean flow kinematic boundary condition

Dans cette annexe, on donne la démonstration complète de la condition cinématique à la surface pour l'écoulement moyen, eq. [1.4.13](#).

This appendix provides a proof of the mean flow kinematic condition of eq.1.4.13. The proof is done in 2D but can be easily extended to 3D.

To find this boundary condition, first note that:

$$f(x) = f(a) + \int_a^x f'(t) dt. \quad (D.0.1)$$

Further suppose that the velocity can be continued analytically to the mean surface even for $\eta' < 0$. Then, one can write the boundary condition in the kinematic boundary condition in this form:

$$\frac{\partial \bar{\eta}}{\partial t} + \frac{\partial \eta'}{\partial t} + \left(\frac{\partial \bar{\eta}}{\partial x} + \frac{\partial \eta'}{\partial x} \right) \left(\bar{u}|_{\bar{\eta}} + u'|_{\bar{\eta}} + \int_{\bar{\eta}}^{\eta} \frac{\partial u}{\partial z} dz \right) - \left(\bar{w}|_{\bar{\eta}} + w'|_{\bar{\eta}} + \int_{\bar{\eta}}^{\eta} \frac{\partial w}{\partial z} dz \right) = 0, \quad (D.0.2)$$

where $\eta = \bar{\eta} + \eta'$. Time averaging and eliminating rapidly oscillating zero averaged terms, yields

$$\frac{\partial \bar{\eta}}{\partial t} + \frac{\partial \bar{\eta}}{\partial x} \overline{u'|_{\bar{\eta}}} - \bar{w}|_{\bar{\eta}} + \frac{\partial \eta'}{\partial x} \overline{u'|_{\bar{\eta}}} + \frac{\partial \eta}{\partial x} \overline{\int_{\bar{\eta}}^{\eta} \frac{\partial u}{\partial z} dz} - \overline{\int_{\bar{\eta}}^{\eta} \frac{\partial w}{\partial z} dz} = 0. \quad (D.0.3)$$

The three first terms correspond to the left hand side of the final results and the last three need to be worked on a bit more. Using the incompressibility equation on the last term, it becomes

$$\frac{\partial \bar{\eta}}{\partial t} + \frac{\partial \bar{\eta}}{\partial x} \overline{u}|_{\bar{\eta}} - \bar{w}|_{\bar{\eta}} + \frac{\partial \eta'}{\partial x} \overline{u'|_{\bar{\eta}}} + \frac{\partial \eta}{\partial x} \overline{\int_{\bar{\eta}}^{\eta} \frac{\partial u}{\partial z} dz} + \overline{\int_{\bar{\eta}}^{\eta} \frac{\partial u}{\partial x} dz} = 0. \quad (D.0.4)$$

Then, using the Leibniz'rule:

$$\overline{\int_{\bar{\eta}}^{\eta} \frac{\partial u}{\partial x} dz} = \frac{\partial}{\partial x} \overline{\int_{\bar{\eta}}^{\eta} u dz} - \frac{\partial \eta}{\partial x} \overline{u|_{\eta}} + \frac{\partial \bar{\eta}}{\partial x} \overline{u|_{\bar{\eta}}}, \quad (D.0.5)$$

one can expand the last term and rewrite the equation in this form

$$\frac{\partial \bar{\eta}}{\partial t} + \frac{\partial \bar{\eta}}{\partial x} \overline{u}|_{\bar{\eta}} - \bar{w}|_{\bar{\eta}} + \frac{\partial}{\partial x} \overline{\int_{\bar{\eta}}^{\eta} u dz} + \frac{\partial \eta}{\partial x} \overline{\int_{\bar{\eta}}^{\eta} \frac{\partial u}{\partial z} dz} + \frac{\partial \eta'}{\partial x} \overline{u'|_{\bar{\eta}}} - \frac{\partial \eta}{\partial x} \overline{u|_{\eta}} + \frac{\partial \bar{\eta}}{\partial x} \overline{u|_{\bar{\eta}}} = 0. \quad (D.0.6)$$

Then it is left to show that:

$$\frac{\partial \eta}{\partial x} \overline{\int_{\bar{\eta}}^{\eta} \frac{\partial u}{\partial z} dz} + \frac{\partial \eta'}{\partial x} \overline{u'|_{\bar{\eta}}} - \frac{\partial \eta}{\partial x} \overline{u|_{\eta}} + \frac{\partial \bar{\eta}}{\partial x} \overline{u|_{\bar{\eta}}} = 0. \quad (D.0.7)$$

After basic algebra, and using the averaging property:

$$\overline{\frac{\partial \eta'}{\partial x} u' |_{\bar{\eta}}} = \overline{\frac{\partial \eta'}{\partial x} u' |_{\bar{\eta}}} + \overline{\frac{\partial \eta'}{\partial x} \bar{u} |_{\bar{\eta}}} = \overline{\frac{\partial \eta'}{\partial x} (u' + \bar{u}) |_{\bar{\eta}}} = \overline{\frac{\partial \eta'}{\partial x} u |_{\bar{\eta}}} \quad (\text{D.0.8})$$

$$\overline{\frac{\partial \eta'}{\partial x} u' |_{\bar{\eta}}} + \overline{\frac{\partial \bar{\eta}}{\partial x} u |_{\bar{\eta}}} = \overline{\frac{\partial \eta'}{\partial x} u |_{\bar{\eta}}} + \overline{\frac{\partial \bar{\eta}}{\partial x} u |_{\bar{\eta}}} = \overline{\frac{\partial \eta}{\partial x} u |_{\bar{\eta}}} \quad (\text{D.0.9})$$

it comes

$$\overline{\frac{\partial \eta'}{\partial x} u' |_{\bar{\eta}}} + \overline{\frac{\partial \bar{\eta}}{\partial x} u |_{\bar{\eta}}} - \overline{\frac{\partial \eta}{\partial x} u |_{\eta}} = \overline{\frac{\partial \eta}{\partial x} u |_{\bar{\eta}}} - \overline{\frac{\partial \eta}{\partial x} u |_{\eta}} = -\overline{\frac{\partial \eta}{\partial x} \int_{\bar{\eta}}^{\eta} \frac{\partial u}{\partial z} dz}, \quad (\text{D.0.10})$$

it yields the result of eq. 1.4.13:

$$\frac{\partial \bar{\eta}}{\partial t} + \frac{\partial \bar{\eta}}{\partial x} \bar{u} |_{\bar{\eta}} - \bar{w} |_{\bar{\eta}} = -\frac{\partial}{\partial x} \overline{\int_{\bar{\eta}}^{\eta} u dz}. \quad (\text{D.0.11})$$

Appendix E

Higher orders Stokes waves theory and Non-linear dispersion relation

Cette annexe présente la dérivation de l'équation de dispersion non-linéaire à partir de l'expansion au troisième ordre de la théorie de Stokes des vagues.

This appendix looks at higher order term of the Stokes waves theory. First the second order equations are considered and the focus is on the oscillatory terms. Then, the third order terms of the potential system of equations 1.2.8 are developed. The non-linear dispersion relation is deduced.

E.1 Second order wave theory

Keeping the second order terms in the system of equations 1.2.8 leads to the second order system:

$$\left\{ \begin{array}{ll} \Delta\Phi^{(2)}(X, Z, \mathcal{T}) = 0 & (X, Z) \in]-\infty, +\infty[\times]-1, 0[, \\ \partial_{\mathcal{T}, \mathcal{T}}\Phi^{(2)} + \partial_Z\Phi^{(2)} = -\tilde{Z}^{(1)}\partial_Z(\partial_{\mathcal{T}, \mathcal{T}}\Phi^{(1)} + \partial_Z\Phi^{(1)}) & \text{on } Z = 0, \\ & -\partial_t(|\mathbf{U}^{(1)}|^2) \\ \partial_t\Phi^{(2)} + \tilde{Z}^{(2)} = -\tilde{Z}^{(1)}\partial_{\mathcal{T}, Z}\Phi^{(1)} - \frac{1}{2}|\mathbf{U}^{(1)}|^2 & \text{on } Z = 0, \\ \partial_z\Phi^{(1)} = 0 & \text{on } Z = -1, \end{array} \right. \quad (\text{E.1.1})$$

where the first order terms act like source terms on the second order solution. The multiplication of first order terms leads to constant and second harmonic terms. Thus, one should look for solution of the form:

$$\Phi^{(2)}(X, Z, \mathcal{T}) = \Re \left\{ F_2(Z)e^{2i(\Omega\mathcal{T}-KX)} \right\} + F_0(Z), \quad (\text{E.1.2})$$

where the second term in the left hand side is the mean Eulerian velocity potential: $\Phi^{(2,0)} = F_0(z)$ and is a second order term. Identically for the free surface position it comes:

$$\tilde{Z}^{(2)}(X, \mathcal{T}) = \Re \left\{ A_2 e^{2i(\Omega\mathcal{T}-KX)} \right\} + \tilde{Z}^{(2,0)}, \quad (\text{E.1.3})$$

where $\tilde{Z}^{(2,0)}$ corresponds to the variation of the mean water depth due to the wave field. Note that $\Phi^{(2,0)}$ and $\tilde{Z}^{(2,0)}$ are independent of X here due to the fact that a linear potential approach for a forward wave with no dissipation is considered. In the cases with dissipation there will also depend on the horizontal position. After simple algebra, one finds:

$$\left\{ \begin{array}{l} A_2 = KA^2 \frac{3 - \tanh K^2}{4 \tanh K^3} \\ F_2(z) = \frac{3}{8} \frac{iA\Omega}{K \sinh K^4} AK \cosh [2K(1 + Z)] \end{array} \right. \quad (\text{E.1.4})$$

It appears that the small parameter in the development is $\epsilon = KA$ and the development is valid as long as:

$$KA^2 \frac{3 - \tanh K^2}{4 \tanh K^3} \ll A \quad (\text{E.1.5})$$

which leads to the general Ursell number

$$\mathcal{U}_r = KA \frac{3 - \tanh K^2}{4 \tanh K^3}, \quad (\text{E.1.6})$$

and in the limit $K \rightarrow 0$ (long waves) the more common Ursell number:

$$\mathcal{U}_r = \frac{3}{4} \frac{A}{K^2}, \quad (\text{E.1.7})$$

or in the dimensional form $\mathcal{U}_r = a/(k^2 d^3)$, where the 3/4 coefficient is dropped. For short waves ($K \rightarrow \infty$), the Ursell number is simply $\mathcal{U}_r \approx KA/2 \propto \epsilon$, thus the approximation is always valid as long as $\epsilon \ll 1$.

The second order contribution to the static pressure can be evaluated using the Bernoulli's equation eq.1.2.2 expanded to the second order. It comes:

$$P_*^{(2)} = P_2 + Z = -\partial_{\mathcal{T}} \Phi^{(2)} - \frac{1}{2} \left| \mathbf{U}^{(1)} \right|^2 \quad (\text{E.1.8})$$

After a bit of algebra, the following expression is found:

$$P_*^{(2)} = \Re \left\{ \frac{AK}{8 \sinh 2K} A \left(\frac{3 \cosh [2K(1+Z)]}{\sinh K^2} - 1 \right) e^{2i(\Omega\mathcal{T} - KX)} \right\} \quad (\text{E.1.9})$$

The expression of the surface displacement can also be found using the static pressure P_* and the Taylor expansion of the surface static pressure condition:

$$P_* = \tilde{Z}, \text{ at } Z = \tilde{Z}, \quad (\text{E.1.10})$$

and thus at the second order, the expression reads:

$$P_*^{(2)} + \tilde{Z}^{(1)} \partial_Z P_*^{(1)} = \tilde{Z}^{(2)}. \quad (\text{E.1.11})$$

This expression enable to reconstruct the free surface from the static pressure at the second order.

It is important to note that up to the second order theory the dispersion relation is unchanged. To find the first non-linear effect one needs to consider the third order terms in the potential theory.

E.2 Third order wave theory

$$\left\{ \begin{array}{l} \Delta\Phi^{(3)}(X, Z, \mathcal{T}) = 0, (X, Z) \in]-\infty, +\infty[\times]-1, 0[, \\ \partial_{\mathcal{T}, \mathcal{T}}\Phi^{(3)} + \partial_Z\Phi^{(3)} = -\tilde{Z}^{(1)}\partial_Z(\partial_{\mathcal{T}}\Phi^{(2)} + \partial_Z\Phi^{(2)}) - \tilde{Z}^{(3)}\partial_Z(\partial_{\mathcal{T}, \mathcal{T}}\Phi^{(1)}\partial_Z\Phi^{(1)}) \\ \quad - 2\partial_{\mathcal{T}}(\mathbf{U}^{(1)} \cdot \mathbf{U}^{(2)}) - \frac{1}{2}(\tilde{Z}^{(1)})^2\partial_{Z, Z}(\partial_{\mathcal{T}, \mathcal{T}}\Phi^{(1)}\partial_Z\Phi^{(1)}) \\ \quad - \tilde{Z}^{(1)}\partial_{\mathcal{T}, Z}(|\mathbf{U}^{(1)}|^2) - \frac{1}{2}\mathbf{U}^{(1)} \cdot \nabla(|\mathbf{U}^{(1)}|^2), \text{ on } Z = 0, \\ \partial_{\mathcal{T}}\Phi^{(3)} + \tilde{Z}^{(3)} = -\tilde{Z}^{(1)}\partial_{\mathcal{T}, Z}\Phi^{(2)} - \tilde{Z}^{(3)}\partial_{\mathcal{T}, Z}\Phi^{(1)} - \mathbf{U}^{(1)} \cdot \mathbf{U}^{(2)} \\ \quad - \frac{1}{2}(\tilde{Z}^{(1)})^2\partial_{\mathcal{T}, Z, Z}\Phi^{(1)} - \frac{1}{2}\tilde{Z}^{(3)}\partial_Z(|\mathbf{U}^{(1)}|^2), \text{ on } Z = 0, \\ \partial_z\Phi^{(3)} = 0, \text{ on } Z = -1. \end{array} \right. \quad (\text{E.2.1})$$

The second and first order terms multiplications generate first and third order harmonics. The first order harmonic leads to secular terms as the left hand side of the second equation in the system E.2.1 is identical to the linear theory but the left hand side is not zero anymore. This means that the linear dispersion relation 1.3.5 is no longer valid. After basic algebra, the second order dispersion relation is found:

$$\Omega^2 = K \tanh K \left\{ 1 + K^2 A^2 \frac{9 - 10 \tanh K^2 + 9 \tanh K^4}{8 \tanh K^4} \right\} \quad (\text{E.2.2})$$

Whitham [169] proposed a variational approach to derive this non-linear dispersion relation. This method is elegant but could not be applied to the cases with dissipation. Note however that it is possible to do so using the fact that the system of equation can be reduced to the variational form of Luke [101]:

$$\delta \int \int L \, dx \, dt = 0, \quad (\text{E.2.3})$$

$$L = \int_{-1}^{\eta} \left\{ \partial_t \varphi + \frac{1}{2} |\nabla \varphi|^2 + gz \right\} dz. \quad (\text{E.2.4})$$

E.3 Approximation of the non-linear dispersion relation

One can assume that $K = K_0 + K_2 + \text{h.o.t.}$ where K_0 is solution to the linear dispersion relation:

$$\Omega^2 = K_0 \tanh K_0 \quad (\text{E.3.1})$$

and K_2 is a second order term and $K_2 \propto \epsilon^2$. Injecting the development of K into the non-linear dispersion relation eq.E.2.2 and expanding with respect to ϵ , the second order terms yield the effect of non-linearity on the wave number:

$$K_2 = -K_0^3 A^2 \frac{16 \cosh K_0 \cosh 3K_0 + \cosh 5K_0}{8 \sinh K_0^3 (2K_0 + \sinh 2K_0)}. \quad (\text{E.3.2})$$

It appears that the non-linearity will lead to a reduction of the wave number (or equivalently an increase of the wavelength). Another interpretation of this result is that the phase wave speed ($c_\varphi = \Omega/K$) is increased by non-linearity. In the limit of long waves ($K_0 \rightarrow 0$) the non linear contribution reduces to:

$$K_2 \approx -\frac{9A^2}{16K_0} \tag{E.3.3}$$

while for short waves ($K_0 \rightarrow \infty$), it yields:

$$K_2 \approx -K_0^3 A^2 \tag{E.3.4}$$

Hence for long waves this is valid only if $U_r \epsilon \ll 1$ (as pointed out by Kirby and Dalrymple [81]). This illustrates another way of defining the Ursell number. Figure E.1 shows the effect of non-linearity on the wave number for three distinct values of Ω corresponding to long, intermediate and short waves compared with the expansion approximation.

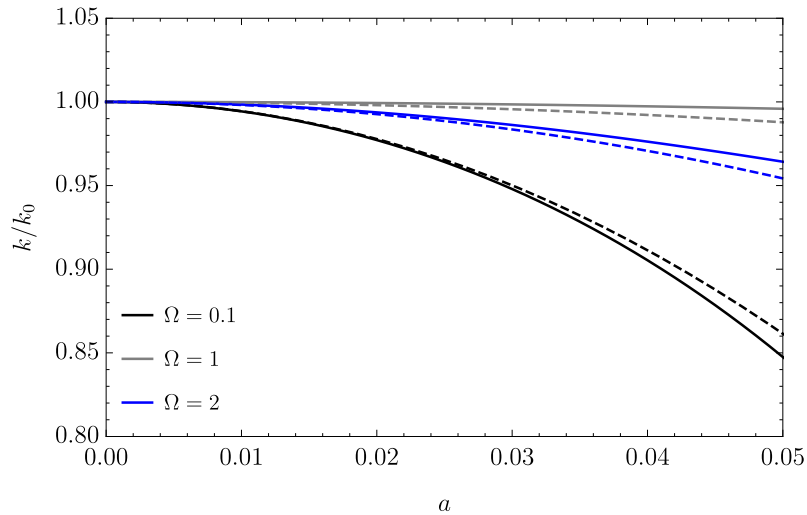


Figure E.1: Non linearity effect on the wave number for short, intermediate and long waves ($\Omega = \{2, 1, 0.1\}$ respectively). The dashed lines show the approximation of eq.E.3.2.

Appendix F

Lamb's viscous waves

Cette annexe présente une théorie de vagues visqueuses à partir des équations de Navier–Stokes linéarisées. On dérive l'équation de dispersion. Elle sera comparée à d'autres modèles visqueux de vagues dans les annexes suivantes.

In this appendix the solution of the viscous waves of Lamb [82] is derived. In particular, this appendix outlines the horizontal profile of the first harmonic solution and the solution is compared to the boundary layer correction developed in section B. The equations are derived in the limit of creeping flow, *i.e.* in the limit in which the wave amplitude is much smaller than the free-surface boundary layer. The original derivation was done by Lamb [82] for infinite water depth. Lamb [82] used a Helmholtz-Leray decomposition (see article 349 in [82]). Here, the derivation is done in a more general manner and for finite depth.

The flow is considered two dimensional. The problem of eq.1.1.18 is linearized and for brevity the index (1) is dropped. The non-dimensional notations defined in section 1.2 are used. The flow verifies the general linearized Navier–Stokes equations written using the non-dimensional notations of chapter 1:

$$\begin{cases} \partial_X U + \partial_Z W = 0, \\ \partial_{\mathcal{T}} U = -\partial_X P + \frac{1}{\mathcal{R}} (\partial_{X,X} U + \partial_{Z,Z} U), \\ \partial_{\mathcal{T}} W = -\partial_Z P - 1 + \frac{1}{\mathcal{R}} (\partial_{X,X} W + \partial_{Z,Z} W), \end{cases} \quad (\text{F.0.1})$$

with the boundary conditions:

$$\mathbf{U} = \mathbf{0}, \quad \text{at } Z = -1, \quad (\text{F.0.2})$$

and at the free-surface, the kinematic boundary condition:

$$\partial_{\mathcal{T}} \tilde{Z} = V, \quad \text{at } Z = 0, \quad (\text{F.0.3})$$

and the dynamic boundary condition:

$$\begin{aligned} P - \frac{2}{\mathcal{R}} \partial_Z W &= 0, \quad \text{at } Z = \tilde{Z}, \\ \frac{1}{\mathcal{R}} (\partial_Z U + \partial_X W) &= 0, \quad \text{at } Z = 0 \end{aligned} \quad (\text{F.0.4})$$

F.1 Solution for a wave

The solutions are assumed separable, periodic in time and in the x direction (up to a dissipation term), which amounts to saying

$$\begin{pmatrix} U \\ W \\ P_* \end{pmatrix} = \Re \left\{ \begin{pmatrix} F_U(Z) \\ F_W(Z) \\ F_P(Z) \end{pmatrix} e^{i(\Omega\mathcal{T} - KX)} \right\}. \quad (\text{F.1.1})$$

Substituting the form of the solution in the continuity equation yields:

$$F_U = -i \frac{F'_W(Z)}{K}, \quad (\text{F.1.2})$$

where the prime indicates here the differentiation with respect to the vertical coordinate. Injecting this expression in the horizontal momentum equation yields:

$$F_P = -\frac{i\Omega}{K^2} F'_W \left(1 - i\frac{K^2}{\Omega\mathcal{R}} \right) + \frac{1}{\mathcal{R}K^2} F_W^{(iii)}, \quad (\text{F.1.3})$$

and the index (iii) denotes the third order differentiation. Substituting the expression of F_P and F_U in the last momentum equation yields a fourth-order equation for F_W , which can be written after some algebra:

$$F_W^{(iv)} - (K^2 + \mathcal{L}^2) F_W^{(ii)} + K^2 \mathcal{L}^2 F_W = 0, \quad (\text{F.1.4})$$

where:

$$\mathcal{L}^2 = K^2 + i\Omega\mathcal{R}. \quad (\text{F.1.5})$$

Note that in the limit $\mathcal{R} \rightarrow \infty$ the system readily yields the equation:

$$F_W^{(2)} - K^2 F_W = 0, \quad (\text{F.1.6})$$

which is equivalent to the one found starting from the potential assumption.

One can show that the differential equation eq.F.1.4 assumes solutions of the form:

$$F_W(Z) = C_1 \sinh [K(1+Z)] + C_2 \cosh [K(1+Z)] + C_3 e^{\mathcal{L}Z} + C_4 e^{-\mathcal{L}(Z+1)}, \quad (\text{F.1.7})$$

where $\{C_i\}_{i \in \llbracket 1,4 \rrbracket}$ are constants that will be determined up to a coefficient (the wave amplitude) by enforcing the boundary conditions. There are 5 unknowns (the 4 coefficients C_i and the wavenumber) and the boundary conditions yields the 5 following conditions to verify:

$$\begin{cases} C_2 + C_3 e^{-\mathcal{L}} + C_4 = 0, \\ C_1 + C_3 \frac{\mathcal{L}}{K} e^{-\mathcal{L}} - C_4 \frac{\mathcal{L}}{K} = 0, \\ C_1 \sinh K + C_2 \cosh K + C_3 + C_4 e^{-\mathcal{L}} = i\Omega A, \\ (C_1 \cosh K + C_2 \sinh K) \frac{K^2 + \mathcal{L}^2}{K\mathcal{R}} - 2\frac{\mathcal{L}}{\mathcal{R}} (C_3 - C_4 e^{-\mathcal{L}}) = A, \\ 2K^2 (C_1 \sinh K + C_2 \cosh K) + (K^2 + \mathcal{L}^2) (C_3 + C_4 e^{-\mathcal{L}}) = 0. \end{cases} \quad (\text{F.1.8})$$

The fourth equation is used to derive the dispersion relation. Using the four other ones yields the values of C_i as functions of A the wave amplitude:

$$C_1 = i \frac{A\Omega}{\mathcal{L}^2 - K^2} \frac{K^2 + \mathcal{L}^2 - 2K^2\mathcal{B}}{\sinh K - \mathcal{B} \frac{K}{\mathcal{L}} \sinh \mathcal{L}}, \quad (\text{F.1.9})$$

$$C_2 = -i \frac{K}{\mathcal{L}} \frac{A\Omega}{\mathcal{L}^2 - K^2} \frac{(K^2 + \mathcal{L}^2) \tanh \mathcal{L} - 2K\mathcal{L}\mathcal{B} \tanh K}{\sinh K - \mathcal{B} \frac{K}{\mathcal{L}} \sinh \mathcal{L}}, \quad (\text{F.1.10})$$

$$C_3 = -i \frac{K(1 + \tanh \mathcal{L})}{2\mathcal{L}} \frac{A\Omega}{\mathcal{L}^2 - K^2} \frac{(K^2 + \mathcal{L}^2) e^{-\mathcal{L}} - 2KL \cosh K \left(\frac{K}{\mathcal{L}} - \tanh K\right)}{\sinh K - \mathcal{B} \frac{K}{\mathcal{L}} \sinh \mathcal{L}}, \quad (\text{F.1.11})$$

$$C_4 = i \frac{K(1 + \tanh \mathcal{L})}{2\mathcal{L}} \frac{A\Omega}{\mathcal{L}^2 - K^2} \frac{(K^2 + \mathcal{L}^2) - 2KL \cosh K e^{-\mathcal{L}} \left(\frac{K}{\mathcal{L}} + \tanh K\right)}{\sinh K - \mathcal{B} \frac{K}{\mathcal{L}} \sinh \mathcal{L}}, \quad (\text{F.1.12})$$

where:

$$\mathcal{B} = \frac{\cosh K}{\cosh \mathcal{L}}. \quad (\text{F.1.13})$$

F.2 Dispersion relation and approximation

Finally, injecting the results in the last boundary conditions of eq.F.1.8 and after some algebra, the dispersion relation comes:

$$-\frac{1}{\Omega^2} + \frac{\coth K}{K} \mathcal{Q} - \frac{\mathcal{L} \coth \mathcal{L}}{K} \frac{\mathcal{L}}{K} (\mathcal{Q} - 1)^2 - \frac{\left\{ \mathcal{Q} \text{csch} K - (\mathcal{Q} - 1) \frac{\mathcal{L}}{K} \text{csch} \mathcal{L} \right\}^2}{K \coth K - \mathcal{L} \coth \mathcal{L}} = 0, \quad (\text{F.2.1})$$

where:

$$\mathcal{Q} = 1 - i \frac{2K^2}{\Omega \mathcal{R}}, \quad (\text{F.2.2})$$

and \mathcal{L} is given by eq.F.1.5. Note that at the limit $\mathcal{R} \rightarrow \infty$ the dispersion readily simplifies to the linear dispersion relation of eq.1.3.5.

Consider the limit $\mathcal{R} \gg 1$, and expand $K = K_0 + K_1 + K_2 + \dots$ where $K_2 \ll K_1 \ll K_0$, it comes:

$$K_1 = (1 - i) \sqrt{\frac{2}{\Omega \mathcal{R}}} \frac{K_0^2}{2K_0 + \sinh 2K_0}, \quad (\text{F.2.3})$$

where K_0 is solution to the undisturbed dispersion relation. This is the same result as found in the viscous potential model of Dutykh and Dias [41] (see eq.H.1.8). At the next order the correction is:

$$K_2 = iK_0^3 \frac{2}{\Omega \mathcal{R}} \frac{2 \sinh 2K_0 + \coth K_0}{\sinh 2K_0 + 2K_0} \quad (\text{F.2.4})$$

Appendix G

Potential flow of viscous fluid

Dans cette annexe, un modèle d'écoulement potentiel visqueux est présenté. L'écoulement est supposé parfaitement potentiel et la viscosité n'intervient que sur la condition à la surface. On trouve une équation de dispersion équivalente à celle utilisée dans le corps de la thèse. Elle est comparée aux autres modèles des annexes suivantes.

The potential flow of viscous fluid (PVF) is considered as discussed by Funada and Joseph [52], Joseph and Wang [78]. In this model, the flow is still considered as potential and the effect of viscosity thus only appears on the free surface boundary condition. It is different from the viscous potential flow (VPF) description developed by Dutykh and Dias [41], where the equations are corrected to take into account the effect of vorticity and thus are closer to the description of viscous waves of Lamb [82]. These two cases are discussed in appendix H and F, respectively¹.

In the present description, the flow is supposed to be potential and viscous. That is $\mathbf{u} = \nabla\varphi$ but $\mu \neq 0$. In particular the viscous stress is:

$$\bar{\tau} = 2\mu\nabla \otimes \nabla\varphi. \quad (\text{G.0.1})$$

The only difference with the previous linear potential description of an ideal fluid is the dynamic boundary condition (see eq.1.1.16), which becomes for a potential flow²

$$p - 2\mu\partial_{z,z}\varphi = 0. \quad (\text{G.0.2})$$

Using the previously defined non-dimensional notations, the system to solve becomes

$$\begin{cases} \Delta\Phi = 0 & (X, Y, Z) \in]-\infty, +\infty[^2 \times]-1, \tilde{Z}[, \\ \partial_{\mathcal{T}}\Phi + \tilde{Z} + \frac{2}{\mathcal{R}}\partial_{Z,Z}\Phi = 0 & \text{on } Z = 0, \\ \partial_{\mathcal{T}}\tilde{Z} = \partial_Z\Phi & \text{on } Z = 0, \\ \partial_Z\Phi = 0 & \text{on } Z = -1, \end{cases} \quad (\text{G.0.3})$$

where \mathcal{R} is a Reynolds number:

$$\mathcal{R} = \sqrt{\frac{gd^3}{\nu^2}} \quad (\text{G.0.4})$$

One can write a boundary condition that depends only on the scalar potential at the free surface of the form

$$\partial_{\mathcal{T},\mathcal{T}}\Phi + \partial_Z\Phi + \frac{2}{\mathcal{R}}\partial_{Z,Z}\mathcal{T}\Phi = 0, \quad \text{on } Z = 0. \quad (\text{G.0.5})$$

Then, it yields the new function $F^{(1)}$ defined similarly to eq.1.3.4

$$F^{(1)}(Z) = \frac{iA\Omega}{K \sinh K} \cosh [K(1 + Z)], \quad (\text{G.0.6})$$

¹The PVF presents the advantage of keeping all the description simple and potential, while the modes in the viscous potential flow are more complex to enumerate and in the case of large dissipation new propagative modes appear.

²It reduces to the normal stress balance as shown by Joseph and Wang [78].

and the dispersion relation eq.1.3.5 becomes

$$\Omega^2 \left(1 - i \frac{2K^2}{\Omega \mathcal{R}} \right) = K \tanh K, \quad (\text{G.0.7})$$

or in dimensional form:

$$\omega^2 \left(1 - i \frac{2\nu k^2}{\omega} \right) = gk \tanh kd. \quad (\text{G.0.8})$$

The dispersion relation is this similar to the one of potential wave dissipation proposed in section 1.5.3. The main difference concerns the boundary condition at the interface between two domains. The condition should then be the continuity of the normal velocity and the normal stress to verify mass and momentum conservation. The vertical velocity is thus not ensure to be continuous and shear can be expected, this will break the condition of no vorticity. This justifies why this model of dissipation was not considered in the present thesis.

Appendix H

Viscous potential flow

Dans cette annexe, les effets de la vorticit  et de la viscosit  sont pris en compte pour aboutir   une description potentielle corrig e. On trouve une nouvelle forme de l' quation de dispersion. Toutes les  quations de dispersions sont alors compar es. Contrairement   la description dite de Lamb, toutes les autres pr esentent un nombre de Reynolds critique   partir duquel la dissipation diminue.

This appendix looks at the effect of vorticity and dissipation on the potential description. The results are based on the paper of Dutykh and Dias [41].

In this potential description proposed by Dutykh and Dias [41], the potential equations are corrected to take into account the general linear dissipative effects. The main difference with the potential flow of viscous fluid approach (see section 1.5.3) is that the equations are derived from the Helmholtz-Leray decomposition and take into account the vorticity in the boundary layers (at the sea-bed and at the free-surface). It is derived for creeping flow. Compared to the solution of Lamb [82], it looks only at the potential part.

Firstly the equations of motion are given based on [41] and written then for the case of an infinite wave train. In particular, the sea bed boundary condition is evaluated in the approximation of long time for an oscillatory flow. The dispersion relation is derived and the solutions discussed. The dispersion is rather complex and this is illustrated in the case of $\Omega = 1$ by looking at the solutions as a function of the dissipation. New modes are outlined. Secondly, the case with slip condition at the sea bed is considered.

H.1 Case of no-slip condition:

The new set of viscous potential free-surface flow equations given by Dutykh and Dias [41] are

$$\left\{ \begin{array}{ll} \Delta\varphi(x, y, z, t) = 0 & (x, y, z) \in]-\infty, +\infty[^2 \times]-d, \eta[, \\ \partial_t\varphi + g\eta + \frac{1}{2}|\nabla\varphi|^2 = -2\nu\partial_{z,z}\varphi & \text{on } z = \eta(x, y, t), \\ \partial_t\eta + \nabla\varphi \cdot \nabla\eta = \partial_z\varphi + 2\nu\Delta\eta & \text{on } z = \eta(x, y, t), \\ \partial_z\varphi = -\sqrt{\frac{\nu}{\pi}} \int_0^t \frac{\partial_{z,z}\varphi}{\sqrt{t-\tau}} d\tau & \text{on } z = -d. \end{array} \right. \quad (\text{H.1.1})$$

The first boundary condition is exactly the one used in the previous section. The free-surface kinematic condition has a new term which comes from the rotational part of the general kinematic boundary condition and was used in the thesis model. The sea bed is also modified and an Abel's integral equation appears, which for oscillatory flow leads to an error function:

$$\int_0^t \frac{e^{i\omega\tau}}{\sqrt{t-\tau}} d\tau = \sqrt{\frac{\pi}{i\omega}} \text{Erf}(\sqrt{i\omega t}) e^{i\omega t}. \quad (\text{H.1.2})$$

As the interest here is an infinite wave train, the limit of $t \rightarrow \infty$ is considered and the sea bed boundary condition simplifies to

$$\partial_z\varphi = \frac{1-i}{2}\delta_\nu\partial_{z,z}\varphi \quad \text{on } z = -d, \quad (\text{H.1.3})$$

where recall $\delta_\nu = \sqrt{2\nu/\omega}$ is the boundary layer thickness at the sea bed.

In non-dimensional form the linearized system is simply

$$\begin{cases} \Delta\Phi = 0 & (X, Y, Z) \in]-\infty, +\infty[^2 \times]-1, \tilde{Z}[, \\ \partial_{\mathcal{T}}\Phi + \tilde{Z} + \frac{2}{\mathcal{R}}\partial_{Z,Z}\Phi = 0 & \text{on } Z = 0, \\ \partial_{\mathcal{T}}\tilde{Z} - \frac{2}{\mathcal{R}}\Delta\tilde{Z} = \partial_Z\Phi & \text{on } Z = 0, \\ \partial_Z\Phi = \frac{-1}{\sqrt{i\mathcal{R}\Omega}}\partial_{Z,Z}\Phi & \text{on } Z = -1. \end{cases} \quad (\text{H.1.4})$$

Similarly to the linear potential case without dissipation, one can write a condition that depends only on the scalar potential:

$$\partial_{\mathcal{T},\mathcal{T}}\Phi + \partial_Z\Phi + \frac{4}{\mathcal{R}}\partial_{Z,Z,\mathcal{T}}\Phi + \frac{4}{\mathcal{R}^2}\partial_{Z,Z,Z}\Phi = 0, \quad \text{on } Z = 0, \quad (\text{H.1.5})$$

Note the difference with the previous boundary equation for potential flow of viscous fluid eq.G.0.5 (in particular the factor 4 on the third term instead of 2). After some algebra, this set of equation yields

$$F^{(1)}(Z) = \frac{iA\Omega(1 - i2K^2/(\Omega\mathcal{R}))}{K \sinh K - K^2/\sqrt{i\Omega\mathcal{R}}} \left\{ \cosh [K(1 + Z)] - \frac{1}{\sqrt{i\Omega\mathcal{R}}} K \sinh [K(1 + Z)] \right\}, \quad (\text{H.1.6})$$

and the a new dispersion relation is:

$$\Omega^2 \left(1 - i\frac{2K^2}{\Omega\mathcal{R}} \right)^2 \left\{ 1 - \frac{K \tanh K}{\sqrt{i\Omega\mathcal{R}}} \right\} = K \tanh K - \frac{K^2}{\sqrt{i\Omega\mathcal{R}}}. \quad (\text{H.1.7})$$

Some comments have to be made on this dispersion relation. First, this equation is similar to the one derived by Dutykh [40]. The symmetry of the solutions with respect to the origin is conserved, which amounts to saying that if K is solution $-K$ is also solution. The terms in $\sqrt{\mathcal{R}}$ comes from the sea bed boundary friction, while the others are due to the free-surface boundary layer. The issue with this dispersion relation is that, up to the author's knowledge, the form of all the solutions are not known. If it is clear that the solutions of the undamped dispersion relation will have at least one equivalent damped mode, the fact that there is no other mode is not certain and actually wrong. Figure H.1 shows the trajectories of the modes found numerically for the case $\Omega = 1$. The modes are initialized for a value of $\mathcal{R} \approx 0.5$ by manually searching the zero in the complex plane. The blue points in figure H.1 shows the initial value found and used. From there, the Reynolds' number is varied (increased and diminished). The arrows show the direction of increasing viscosity (*i.e.* reducing \mathcal{R}). As the viscosity is set back to zero, it appears that all the mode trajectories traced by black arrows go back to a solution of the regular linear dispersion relation. Three new modes are identified in red. In particular in the right panel of the complex plane, the red arrow shows a new propagative mode which for strong dissipation is of the same order of magnitude but different from the mode originating from the regular travelling mode (red point near $K \approx 1.2$). Similarly on the left panel the lowest

red arrow shows a mode travelling in the opposite direction with small dissipation. At a Reynolds value $\mathcal{R} = 0.5$ there are thus three main modes: $K \approx 0.285 - i0.275$ (which comes from the original travelling mode $K \approx 1.2$), and two new modes $K \approx 0.427 - i0.455$ and $K \approx -0.818 - i0.446$. The order of the imaginary part is similar meaning these two new modes shall not be disregarded as they will persist in space on similar distances¹.

In the limit of small viscosity (*i.e.* $\mathcal{R} \rightarrow \infty$), these new modes are negligible (large imaginary part) and one can show that the original modes can be approximated by:

$$K \approx K_0 \left\{ 1 + (1 - i) \sqrt{\frac{2}{\Omega \mathcal{R}}} \frac{K_0}{2K_0 + \sinh 2K_0} \right\}, \quad (\text{H.1.8})$$

where K_0 is the solution of the undamped linear dispersion relation eq.1.3.5. Compared to eq.1.5.20, this leads to both dissipation and variation of apparent wavelength. This correction is in $\mathcal{R}^{-1/2}$ instead of \mathcal{R}^{-1} . The dissipation is thus mostly due to friction at the sea bed. As the goal is to use these models to mimic the wave breaking dissipation in the theoretical part, it appears to the author that this complete dispersion relation is probably not well adapted. Another argument against using this kind of dissipation is the complexity of the function $F^{(1)}$, given by eq.H.1.6, it generates and the absence of well documented approximative solutions of the dispersion relation for all \mathcal{R} .

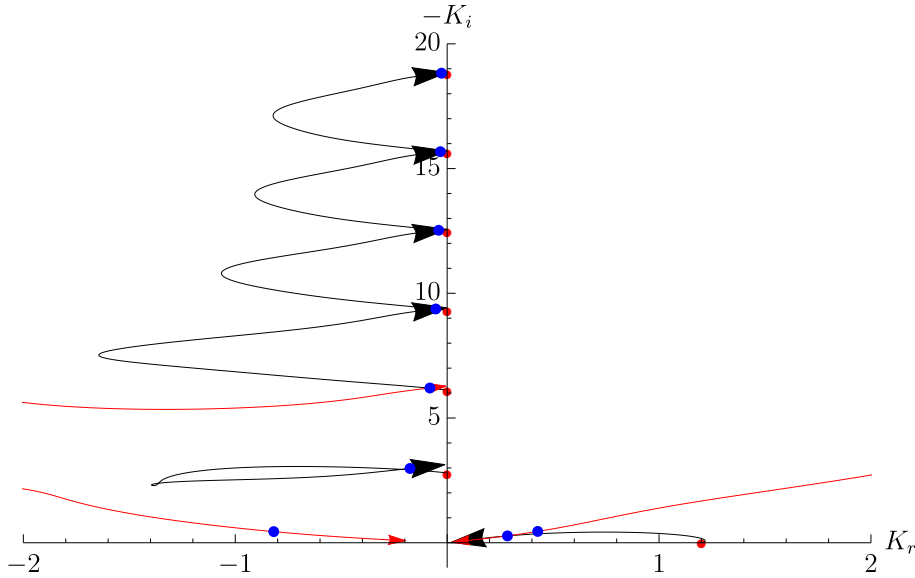


Figure H.1: Trajectories of the wavenumber with viscosity for $\Omega = 1$ for the dispersion relation eq.H.1.7. The arrows indicate the trajectories of the wavenumbers starting from the inviscid potential solutions (red points) and increasing the viscosity (*i.e.* reducing \mathcal{R}).

¹For a case where this could happen, one could consider a silicon oil of viscosity $\nu \approx 6.3 \times 10^{-3} \text{ m}^2 \cdot \text{s}^{-1}$ in a bath with a depth of 1cm, and waves generated at a frequency of 5 Hz

H.2 Case of slip condition:

Neglecting the sea bed friction does not alleviate the problem completely. It is proposed to consider the correction at the free-surface only and ignore the sea bed friction for now. The system of equations is then:

$$\begin{cases} \Delta\Phi = 0 & (X, Y, Z) \in]-\infty, +\infty[^2 \times]-1, \tilde{Z}[, \\ \partial_{\mathcal{T}}\Phi + \tilde{Z} + \frac{2}{\mathcal{R}}\partial_{Z,Z}\Phi = 0 & \text{on } Z = 0, \\ \partial_{\mathcal{T}}\tilde{Z} - \frac{2}{\mathcal{R}}\Delta\tilde{Z} = \partial_Z\Phi & \text{on } Z = 0, \\ \partial_Z\Phi = 0 & \text{on } Z = -1. \end{cases} \quad (\text{H.2.1})$$

The function $F^{(1)}$ is now:

$$F^{(1)}(Z) = \frac{iA\Omega}{K \sinh K} \left(1 - i\frac{2K^2}{\Omega\mathcal{R}} \right) \cosh [K(1 + Z)], \quad (\text{H.2.2})$$

and the dispersion relation is simply:

$$\Omega^2 \left(1 - i\frac{2K^2}{\Omega\mathcal{R}} \right)^2 = K \tanh K, \quad (\text{H.2.3})$$

where the only difference now with the dispersion relation of potential flow of a viscous fluid eq.G.0.8 is the power two coefficient on the bracket of the left hand side. In the limit of small viscosity (*i.e.* $\mathcal{R} \rightarrow \infty$), it comes:

$$K \approx K_0 \left(1 - i\frac{4K_0^2}{\Omega\mathcal{R}} \frac{\sinh 2K_0}{2K_0 + \sinh 2K_0} \right), \quad (\text{H.2.4})$$

where there is a factor two difference with the expression of eq.H.2.4. The origin of this difference is the effect of surface boundary layer on the kinematic boundary condition. Note also that the characteristic time of dissipation is readily found to be twice the one of eq.1.5.22 in agreement with the calculation of Lamb [82]. Yet the solution of the dispersion relation in this form is till not clearly known. Using the same method as described before, it appears that from this dispersion relation, there still are more than one main mode for large dissipation (see figure H.2).

H.3 Discussions

In this appendix dispersions relation for the viscous potential flow of Dutykh and Dias [41] in the case of slip and no-slip boundary conditions were derived. It was shown that new modes appear. As the value of K is going to zero for large dissipation, the dispersion relations can be seen as a sixth order polynomial in the case of eq.H.1.4 and fourth order

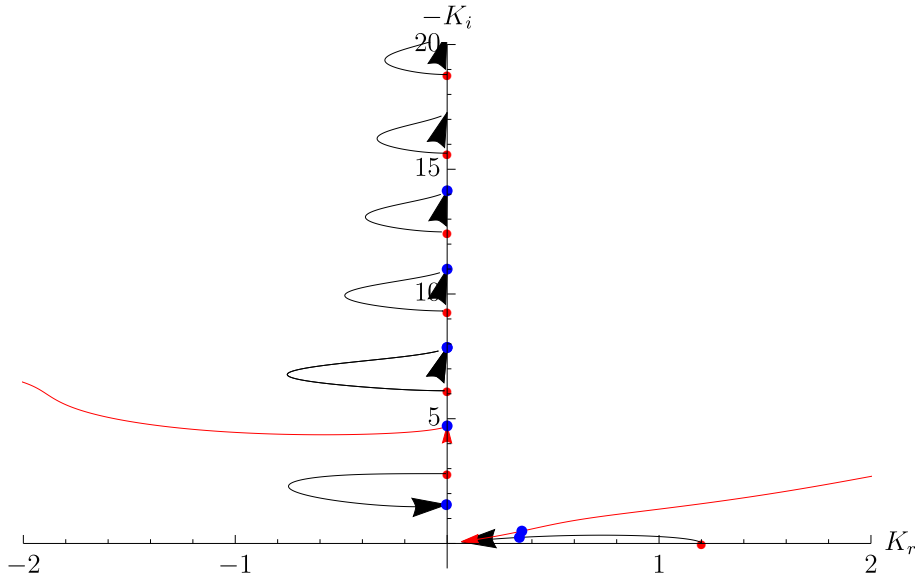


Figure H.2: Trajectories of the wavenumber with viscosity for $\Omega = 1$ for the dispersion relation eq.H.2.3. The arrows indicate the trajectories of the wavenumber starting from the inviscid potential solutions (red points) and increasing the viscosity (*i.e.* reducing \mathcal{R}).

in the case of eq.H.2.1. It is thus not so surprising that there are 3 modes (symmetric with respect to the origin) and 2 modes in these cases. The dominant mode (in the sense of the one with the lowest dissipation) can be traced back to the original travelling mode.

It is interesting to look at the real part and imaginary part of the dominant wave number as a function of the dissipation and compare the four viscous models: the potential flow of viscous fluid (or the potential wave dissipation model of section 1.5.3 as they have the exact same dispersion relation), the viscous potential model with slip and no-slip boundary conditions of Dutykh and Dias [41] and the complete viscous model of Lamb [82]. The results are shown for $\Omega = 1$ in figure H.3 and figure H.4 for the real and imaginary part respectively. Looking at the real part (or apparent wave number), the viscosity has a weak effect till a critical value of about $\mathcal{R} = 10^2$. Then the real part dramatically decreases to zero. The different models have similar behaviours past this threshold. Note that the potential flow of viscous fluid is shifted. This is due to the factor 2 difference due to the missing power of 2 on the bracket term. Before this threshold, the models of Lamb and Dutykh with no-slip have the same behaviour.

For the imaginary part, it is seen that the dissipation is mostly due to sea bed friction at first as the slip model dissipates way less than the model of Lamb and the one with no-slip. The potential flow of viscous fluid one is shifted compared to the viscous potential with slip by a factor 2. As the viscosity is increased in all cases the dissipation increases till reaching a critical maximum value. In the case of Lamb, then the dissipation plateaus. In the other case, the dissipation drops. This happens for \mathcal{R} near 0.2 so for larger viscosity

than the breakdown in the real part. Overall, it appears that the potential flow of viscous fluid does not perform that differently from the one of Dutykh with slip condition. It is mainly shifted by a factor 2 in \mathcal{R} .

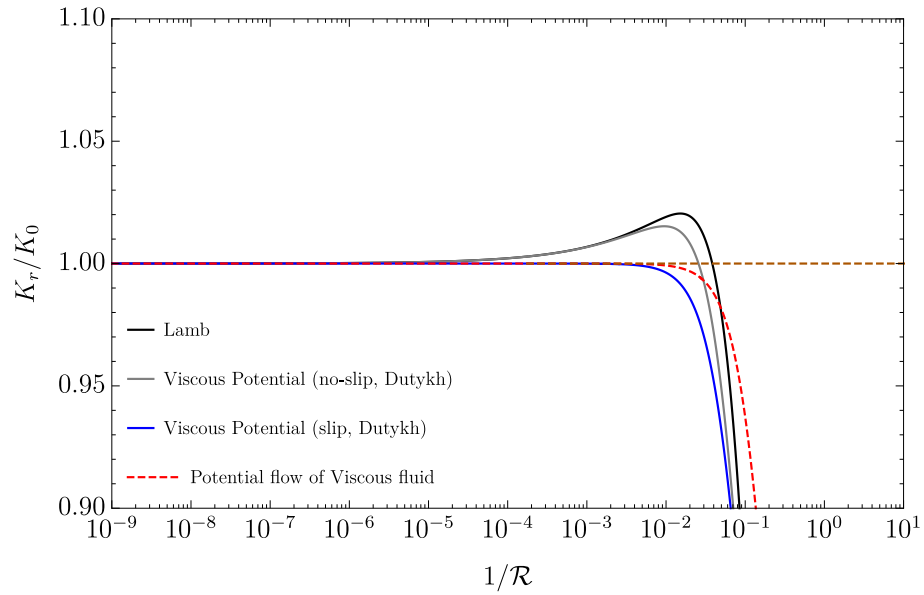


Figure H.3: Effect of viscous dissipation on the real part of the wavenumber for $\Omega = 1$ for the different viscous models. The dashed brown line corresponds to no modification of wavelength.

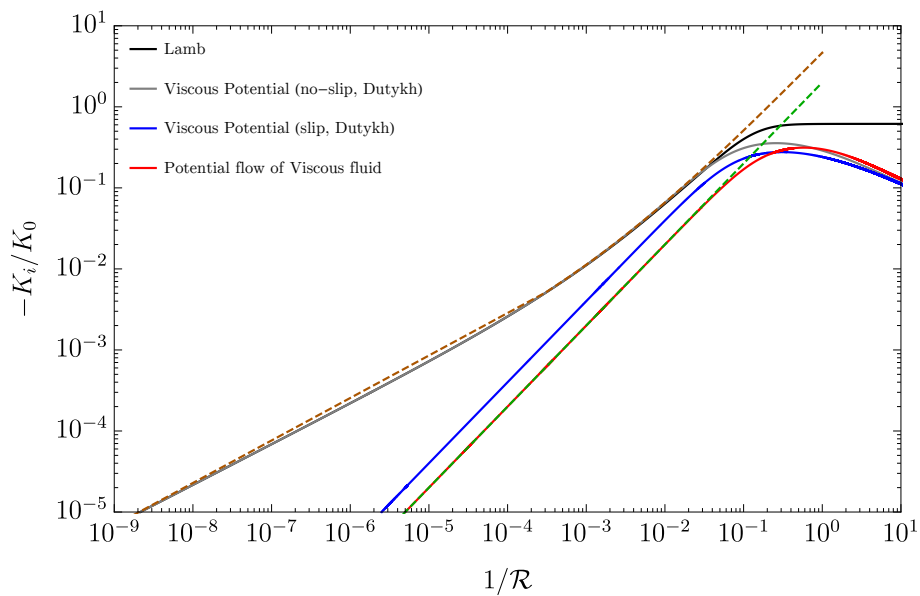


Figure H.4: Effect of viscous dissipation on the imaginary part of the wavenumber for $\Omega = 1$ for the different viscous models. The dashed brown and green lines show the first order approximations for the dispersion of Lamb (and Dutykh with no-slip) and the potential flow of viscous fluid, respectively. In the case of Lamb, the dissipation increases till reaching a threshold value. In the other cases the dissipation reaches a maximum then decreases. The potential flow of viscous fluid is shifted by a factor two compared to the model of Dutykh with slip. It also has a larger maximum than the one of Dutykh with slip.

Appendix I

Optimal Sponge Layer for water waves numerical models

Cette annexe présente la version en cours de révision d'un article soumis pour publication sur l'absorption de vagues dans les méthodes numériques. Il est montré qu'il est possible de prédire "l'efficacité" de la zone d'absorption à faible coût en résolvant un système d'équations linéarisé. On fournit des tables des valeurs des coefficients conseillés pour avoir moins de 5% de réflexion due à la zone d'absorption. Les tables s'arrêtent à une fréquence adimensionnelle égale à 2, étant donné que les valeurs n'évoluent quasiment plus pour des fréquences plus élevées.

This appendix is the submitted version of the paper on Optimal sponge layer for numerical simulations [20] after first review.

The lack of rules to select the proper parameters for absorbing layer led to the study of the sponge layer linear equations. We present the system of linear equations to be solved to evaluate the reflection coefficient at a sponge layer boundary. The case of 2D waves is discussed in details and different sponge layer functions are proposed. The linear system is solved using the finite element method (FEM) at low computational cost compared to the target simulations. This method should enable the design of efficient sponge layer for any full Navier–Stokes solvers. The linear model results solved with a FEM solver are compared here to SPH simulations with good agreement. The linear model is then used to determine the reflection coefficient for different power sponge functions, length and dissipation coefficient using the FEM solver.

The linear model solved by a simple FEM solver can be used to evaluate the suitable dissipation coefficients for waves ranging from shallow to deep water for a given sponge layer length. The coefficient depends on the non-dimensional frequency for $\Omega = \omega\sqrt{d/g} < 2$. A table of suitable parameters for different sponge layer functions is provided over a large range of non-dimensional frequency and sponge layer length. A 3D application of waves is also presented with 45° incidence angle.

I.1 Introduction

The study of water waves problem in open ocean is a challenge for the design and optimisation of various ocean and coastal engineering problems (coastal defence works, oil platforms, ship, wave energy converters, etc.). Experimentally, these problems are studied in finite length facilities and waves are absorbed using most popularly beach like passive absorption regions [16, 84, 126, 134, 149, 157] or active absorbers (at the wave generator called Active Wave Absorber Systems, AWAS, [116, 146]). Numerically, the models are limited by computational cost. Thus, the strategy is to simulate the waves in the smallest possible domain to capture all the desired physics (with the desired accuracy to capture for instance the radiation but also in some cases the induced currents) and let the waves exit the domain without reflecting on the boundaries.

There exists different strategies to absorb waves in simulations: a Sommerfeld condition [26, 71, 102] and a fictitious force (or momentum source term) to absorb the waves are the most popular [26, 64, 127, 130]. Different forms of the forces have been investigated: fictitious pressure correction based on the vertical velocity [26, 64], or a volume force [127, 130]. The latter is the simplest absorption to implement. It consists in adding fictitious dissipative forces to the governing equations. One can for instance add viscous forces by increasing the viscosity of the fluid to absorb the waves. This requires to implement

implicit viscous forces to avoid penalty on the time step and can be a challenge in certain numerical methods. A simpler idea is to add linear dissipative forces of the form of:

$$\rho \mathbf{f}_{SL} = -\rho \beta \mathbf{u}, \quad (\text{I.1.1})$$

in the absorbing region, where ρ is the density, β is called the sponge layer function and \mathbf{u} is the velocity vector. The sponge layer function can be characterised by its mean value in the sponge layer β_{mean} , or the dimensional sponge layer strength, and its length x_{SL} .

This fictitious force can be straightforwardly implemented implicitly, thus has no effect on the time step of the original method. The region of absorption has many names in the literature: sponge or absorbing layers [6, 7, 117], damping zones [6], numerical beaches [26] to cite a few. In this paper it will be referred to as sponge layer. The cost of the method is then directly linked to the length of this absorbing layer, x_{SL} and the efficiency to the value of the sponge layer strength, β_{mean} . A sponge layer is said to be efficient if the reflection coefficient is smaller than a threshold value (here 5%). It is not rare to proceed by trials and errors to find the best coefficient and waste precious computational time. Perić & Abdel-Maksoud [130] first proposed a scaling law to select the length and coefficient based on numerical trials. Their scaling is valid in the limit of deep water waves for which the dispersion relation is linear. In this limit, they found that the strength $\beta_{mean} \propto \omega$ and $x_{SL} \propto \lambda$, where λ is the wavelength of the incident wave to absorb. This is verified in the present paper in the limit of deep water and the results are extended to shallow and intermediate waves where the strength, β_{mean} is no more simply proportional to ω because of the non-linearity of the dispersion relation for water waves.

Perić & Abdel-Maksoud [131] recently proposed a pseudo-analytical model to estimate the sponge layer response with rather good agreement with their simulations in the limit of deep water waves. Their model predicted correctly the reflection coefficient and optimal sponge layer strength for a given sponge layer function and length with sufficient accuracy for many practical purposes in the limit of deep water waves. However, when the sponge layer source terms had a vertical component some discrepancies were observed for larger than optimal sponge layer strength. Their method enables nonetheless the prediction of optimal sponge layer strengths with sufficient accuracy for deep water waves. Le Méhauté [84] proposed the design of permeable beaches in experimental tank with a similar model. Nevertheless, most experimental and actual application tests are in intermediate and even shallow water: waves above a submerged plate [19, 63, 120, 134], mean current induced by short crested waves [166], long shore currents [94] to cite a few. Modave *et al.* [117] investigated the choice of the absorption parameters for shallow waters and show the importance of parameter β_{mean} and its space dependance on the absorption efficiency. The present study aims to provide a method to simply predict the optimal coefficients for the entire wave spectrum (from shallow to deep water waves). It is therefore important to use

non-dimensional notations to make the results universal. Based on Le Méhauté [85] wave diagram, we define the non-dimensional frequency $\Omega = \omega\sqrt{d/g}$. The goal of the present paper is to provide the values of the sponge layer strength $B_{mean} = \beta_{mean}/\omega = \mathcal{F}(\Omega)$, where $\mathcal{F} \propto 1$ when $\Omega \gg 1$ (deep water limit) for a given sponge layer function and sponge layer length $x_{SL} \propto \lambda$.

In this paper, the general wave equations are derived with fictitious linear wave absorption forces. Compared to the potential wave theory it appears that no general Bernoulli's equation can be derived. The case of monochromatic waves is then considered. Writing the equation in terms of the pressure leads to a Laplace's equation with a redefined gradient operator. This equation is discussed in the case of two dimensional water waves. The case of variable β with space is investigated and the solutions of the equations are compared to simulations of the full Navier–Stokes equations for weakly-compressible fluid with the Smoothed Particle Hydrodynamics (SPH) method as an example. Sponge layer optimal coefficients are evaluated for various sponge layer functions and sponge layer length using the linear model presented here with a Golden section search algorithm. The tables provided can be used for the design of efficient wave absorptions sponge layer for any numerical models. In the last section, a three-dimensional configuration is considered to check the ability of the results to absorb waves with an incident angle.

I.2 Waves absorption by energy penalisation: General formulation

I.2.1 Equations of motions and Bernoulli's equations

The motion of an ideal homogenous incompressible fluid of depth $d(x, y)$ with a free surface $z = \zeta(x, y, t)$ is governed by the Euler equations with boundary conditions:

$$\left\{ \begin{array}{ll} \nabla \cdot \mathbf{u} = 0, & -d \leq z \leq \zeta \\ \partial_t \mathbf{u} + (\mathbf{u} \cdot \nabla) \mathbf{u} + \frac{1}{\rho} \nabla p - \mathbf{f}_{SL} = 0, & -d \leq z \leq \zeta \\ p - \rho g \zeta = p_{atm}, & \text{at } z = \zeta \\ \partial_t \zeta + \mathbf{u} \cdot \nabla \zeta - w = 0, & \text{at } z = \zeta \\ \mathbf{u} \cdot \nabla d + w = 0, & \text{at } z = -d \end{array} \right. \quad (\text{I.2.1})$$

with appropriate conditions on the lateral boundaries, where $\mathbf{u} = \{u, v, w\}$ is the velocity vector, g denotes the gravitational acceleration, p the kinematic pressure minus the equilibrium pressure $-\rho g z$ and \mathbf{f}_{SL} is the fictitious damping force used in the sponge layer. In this paper, the dissipation is applied to all directions. From now on, it will be considered that:

$$\mathbf{f}_{SL} = -\beta(x, y)\mathbf{u}. \quad (\text{I.2.2})$$

Note that the study is limited to function that depends only on the horizontal coordinates (x and y). A standard approximation in water waves problem is to consider the flow irrotational and thus potential:

$$\mathbf{u} = \nabla\varphi, \tag{I.2.3}$$

where φ is the scalar velocity potential. In the absence of fictitious forces ($\mathbf{f}_{SL} = \mathbf{0}$), the Bernoulli's equation can then be derived and links the scalar velocity to the pressure allowing to write the well known potential wave theory equations. The general Bernoulli's equation reads:

$$\partial_t\varphi + \frac{1}{2}|\mathbf{u}|^2 + \frac{1}{\rho}p = 0, \quad \forall \mathbf{x}. \tag{I.2.4}$$

Nonetheless adding the sponge layer dissipation term does not allow the derivation of the Bernoulli's equation everywhere in the fluid anymore for all the cases. It is possible though to derive a modified Bernoulli's equation in the case of constant dissipation $\beta = \beta_0$:

$$\partial_t\varphi + \frac{1}{2}|\mathbf{u}|^2 + \frac{1}{\rho}p + \beta_0\varphi = 0, \quad \forall \mathbf{x} \tag{I.2.5}$$

as done by Le Méhauté [84] while studying the design of porous absorbing beaches for experimental implementation. It appears then that the potential flow approximation is not proper for this case. Using a perturbation method and redefining the gradient operator, it is yet possible to write the problem similarly to the well known linear potential theory in the form of a Laplace's equation with proper boundary conditions.

I.2.2 Perturbation method and sponge layer equations

Consider a monochromatic wave train. Similarly to water wave problems, the solution is expanded near an undisturbed configuration and using complex notation:

$$\begin{pmatrix} \mathbf{u} \\ p \\ \zeta \end{pmatrix} = \Re \left\{ \epsilon \begin{pmatrix} \mathbf{u}^{(1)} \\ p^{(1)} \\ \zeta^{(1)} \end{pmatrix} e^{i\omega t} + \epsilon^2 \left[\begin{pmatrix} \mathbf{u}^{(0)} \\ p^{(0)} \\ \zeta^{(0)} \end{pmatrix} + \begin{pmatrix} \mathbf{u}^{(2)} \\ p^{(2)} \\ \zeta^{(2)} \end{pmatrix} e^{2i\omega t} \right] + 0(\epsilon^3) \right\}, \tag{I.2.6}$$

where ϵ is a small parameter, ω is the angular wave frequency. The superscripts (k) refer to the expansion terms, (0) being the time independent induced terms, (1) the first harmonic and so on.

Retaining only first order terms in the momentum equation (second line of eq.I.2.1) leads to:

$$\mathbf{u}^{(1)} = -\frac{\nabla}{(i\omega + \beta)} \frac{1}{\rho} p^{(1)}. \tag{I.2.7}$$

Thus the velocity is still directly linked to the pressure but not through a simple gradient as it is the case for the linear potential wave theory. It is clear also from this development

that the term β can be linked to the wave angular frequency ω . A new gradient operator is defined as:

$$\mathbf{grad} = \frac{\nabla}{(1 - iB)}, \quad (\text{I.2.8})$$

where the nabla operator refers to the regular gradient and $B = \beta/\omega$. Injecting into the continuity equation (first line of eq.I.2.1) yields a modified Laplace equation for the pressure. The general problem to be solved to evaluate the efficiency of the sponge layer is then:

$$\begin{cases} i\omega (1 - i\beta/\omega) \Delta p^{(1)} - \nabla p^{(1)} \text{ot} \nabla \beta = 0, & -d \leq z \leq 0, \\ \partial_z p^{(1)} - p^{(1)} (1 - i\beta/\omega) \omega^2/g = 0, & \text{at } z = 0, \\ \nabla p^{(1)} \text{ot} \nabla d + \partial_z p^{(1)} = 0, & \text{at } z = -d, \end{cases} \quad (\text{I.2.9})$$

with adequate lateral boundary conditions. The free surface can be reconstructed using:

$$\zeta^{(1)} = \frac{p^{(1)}}{\rho g}, \text{ at } z = 0. \quad (\text{I.2.10})$$

Note that the first equation is a Laplace's equation with the newly defined gradient operator and can be written:

$$\nabla \cdot \mathbf{grad} \{ p^{(1)} \} = 0. \quad (\text{I.2.11})$$

Using this set of equations, the efficiency of the sponge layer is found by evaluating the reflection coefficient upstream of the sponge layer. The value found corresponds to the first order reflection coefficient. In experimental works it is common to evaluate the reflection and transmission coefficients using the two probes method of Goda & Suzuki [59] or a single moving probe method [16]. In all cases, a Fast Fourier Transform (FFT) is done to extract the first harmonic and thus only the first order coefficients are evaluated. This justifies the limitation to the first order theory in the evaluation of the efficiency of the sponge layer. Note that the linear reflection coefficient cannot be directly evaluated from the surface envelope due to non-linearities. For instance, free-modes can induce envelope oscillations which are different from reflection. Another example is the surface envelope of a non-linear wave reflection at a wall, for which second order terms lead to non-zero surface oscillations at the linear nodes.

The equations eq.I.2.9 are written in a general manner in 3D with variable depth d . This enables the extension of the present study to the evaluation of combined inclined beaches and simple sponge layer. In the next section, the study is limited to two dimensions and constant water depth.

I.3 Two dimensional applications with constant depth

In this section, it is first assumed that flow is two dimensional (*i.e.* we assume the flow to be invariant through y translations with zero y velocity component) and the water depth, d , is constant.

I.3.1 Linear two dimensional equations and sponge layer functions

The sponge layer function is written:

$$\beta(x) = \omega B(x) \quad (\text{I.3.1})$$

where B is a non-dimensional shape function and is zero in the *physical part* of the tank (here *physical part* means the part of the tank where no fictitious forces are added) and strictly positive in the absorbing part (or sponge layer). The system of equations of eq.I.2.9 now reads in 2D:

$$\begin{cases} (1 - iB) \Delta p^{(1)} + i\partial_x p^{(1)} \partial_x B = 0, & -d \leq z \leq 0, \\ \partial_z p^{(1)} - p^{(1)} (1 - iB) \omega^2/g = 0, & \text{at } z = 0, \\ \partial_z p^{(1)} = 0, & \text{at } z = -d. \end{cases} \quad (\text{I.3.2})$$

The velocity and surface elevation are reconstructed using:

$$\mathbf{u}^{(1)} = -\mathbf{grad} \left(\frac{p^{(1)}}{i\rho\omega} \right), \quad (\text{I.3.3})$$

$$\zeta^{(1)} = \frac{p^{(1)}}{\rho g}, \text{ at } z = 0. \quad (\text{I.3.4})$$

In the above equations, the Laplace and gradient operators are two-dimensional (*i.e.* the (x, z) plane, z denoting the vertical coordinate).

It is convenient to work with non-dimensional equations from now on such that the results found in the present paper can be straightforwardly applied to other cases. Define the following non-dimensional parameters:

$$(X, Z) = (x, z)/d, \quad \mathcal{T} = t\sqrt{g/d}, \quad K = kd, \quad \Omega = \omega\sqrt{d/g}, \quad P = p^{(1)}/(\rho g d). \quad (\text{I.3.5})$$

Note that in the paper all capital letters refer to non-dimensional parameters. The system of equations reads:

$$\begin{cases} (1 - iB) \Delta P + i\partial_X P \partial_X B = 0, & -1 \leq Z \leq 0, \\ \partial_Z P - P (1 - iB) \Omega^2 = 0, & \text{at } Z = 0, \\ \partial_Z P = 0, & \text{at } Z = -1. \end{cases} \quad (\text{I.3.6})$$

The non-dimensional velocity and surface elevation are reconstructed using:

$$\mathbf{U}^{(1)} = -\mathbf{Grad}(\Phi), \quad (\text{I.3.7})$$

$$\tilde{Z}^{(1)} = P, \text{ at } Z = 0. \quad (\text{I.3.8})$$

where the scalar velocity potential Φ is:

$$\Phi = -\frac{P}{i\Omega}. \quad (\text{I.3.9})$$

I.3.2 Sponge layer functions

We consider the case of continuous sponge functions. Different form of sponge functions are proposed based on the literature. The linear sponge layer model (eq.I.3.6 or eq.I.3.2) developed in the previous section can then be solved using a FEM solver to evaluate the reflection coefficient. The case of power sponge layer is then studied in details and the FEM based solutions compared to numerical simulations obtained using the SPH method. The linear sponge layer model solved with FEM can be used to find the optimal coefficient for a given sponge layer length.

In the literature, different types of sponge layer functions are considered. In this paper, we define three general sponge layer functions:

1. the power sponge layer[6]:

$$B(X) = B_{max} \left(\frac{X - X_0}{X_{max} - X_0} \right)^{n_B} \mathcal{H}(X - X_0) \quad (\text{I.3.10})$$

2. the trigonometric sponge layer[25]:

$$B(X) = B_{max} \sin^{n_B} \left(\frac{\pi}{2} \frac{X - X_0}{X_{max} - X_0} \right) \mathcal{H}(X - X_0) \quad (\text{I.3.11})$$

3. the exponential sponge layer[131]:

$$B(X) = B_{max} \left(\frac{e^{\left(\frac{X-X_0}{X_{max}-X_0}\right)^{n_B}} - 1}{e - 1} \right) \mathcal{H}(X - X_0) \quad (\text{I.3.12})$$

where in all the cases $n_B > 0$, B_{max} is the maximum value of the sponge layer coefficient at the end of the sponge layer domain X_{max} , X_0 denotes the beginning of the sponge layer region and \mathcal{H} is the Heaviside function. Figure I.1 shows different sponge layer function profiles. It appears that the slope is more gentle near the beginning of the sponge layer as the power coefficient, n_B is increased. The trigonometric sponge layer presents the

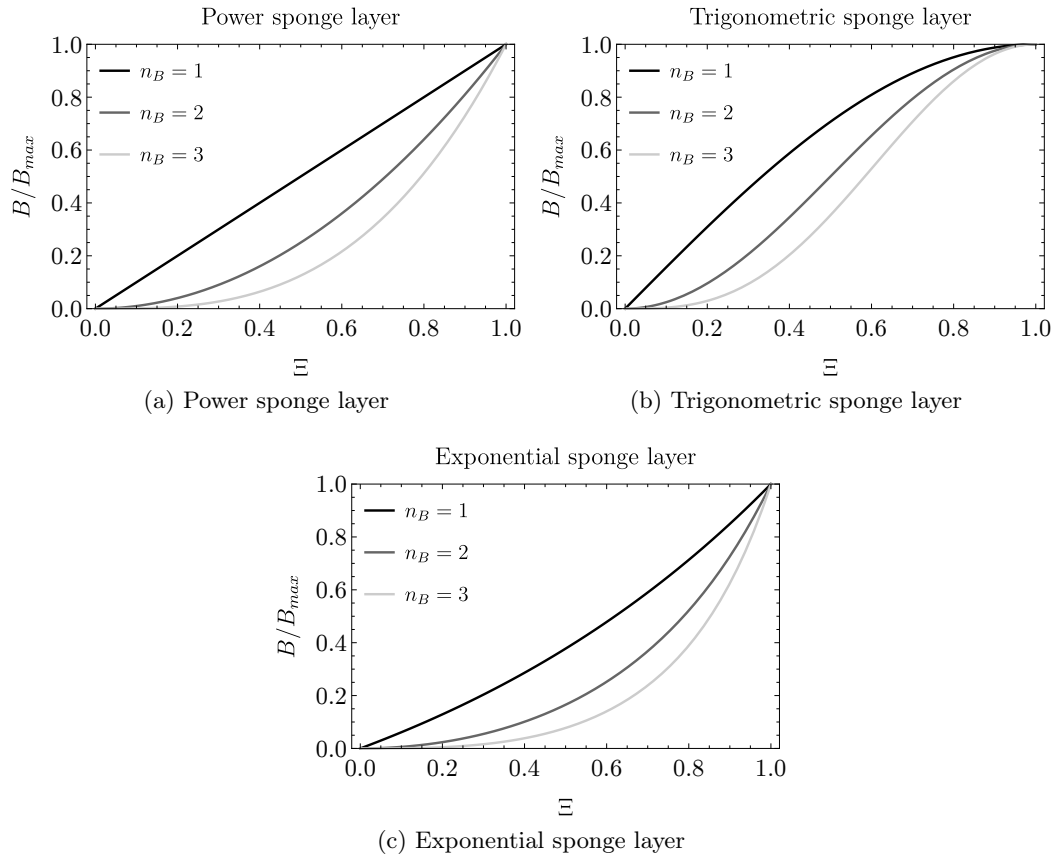


Figure I.1: Different type of sponge layer functions in the absorbing domain ($\Xi = (X - X_0)/(X_{max} - X_0)$). The different colours denote different power coefficients n_B .

characteristic of having a gentle slope toward the end of the sponge layer domain too, at the cost of higher slope within the main part of the sponge. In the next section, the power sponge layer is primarily used as it is simpler to define the mean value of B in the sponge layer $B_{mean} = B_{max}/(n_B + 1)$ and it has been used before for SPH simulations by previous authors [6] with rather good results. Here the goal is to provide a method to evaluate the suitable parameters for the sponge layer so the function in itself is not important. All the sponge layer functions are considered in the section I.3.4 where suitable absorption parameters are provided for numerical modelling.

I.3.3 Finite element solver and SPH model

The system eq.I.3.6 (or eq.I.3.2) can be easily solved using a commercial finite element solver. In this paper, the NDSolve function of Mathematica is used to solve the linear system at low cost to find the reflection coefficient for different sponge layer parameters (see convergence study in I.5). A single CPU is used to run the Mathematica code and

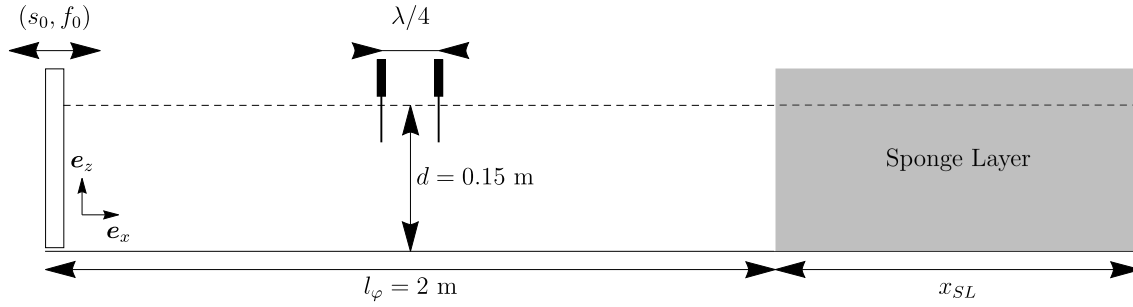


Figure I.2: Sketch of the wave flume.

it takes about 0.5 second to solve the linear problem. For this optimisation problem, the following numerical configuration is considered: a physical domain of length $l_\varphi = 2$ m and water depth $d = 0.15$ m where no dissipation is added and a sponge layer of variable length, $x_{SL} = (X_{max} - X_0)d$ (see figure I.2). The frequency is fixed to $f_0 = 1.5$ Hz (this configuration corresponds to $\Omega \approx 1.17$) and the waves are considered to be generated using a piston type wave maker. In the linear theory approximation, this is equivalent to a Neumann boundary condition on the horizontal velocity at the mean piston position. The piston stroke amplitude can be linked to the target incident wave amplitude by:

$$s_0 = a_{\text{inc}} \frac{2kd + \sinh 2kd}{4 \sinh^2 kd}, \quad (\text{I.3.13})$$

where a_{inc} is the target wave amplitude in the absence of reflection. Since the theory is for linear waves, the wave amplitude is a scaling parameters. The results are compared to numerical simulations obtained using the Smoothed Particle Hydrodynamic (SPH) method (see Violeau and Rogers (2015) [165] for a description of the method, and the K for a short presentation of the model used here and how to implement the fictitious absorption). The SPH simulations are run on a single GPU card (GeForce GTX TITAN Black) and takes about 6 hours. For the SPH simulations, the wave amplitude is first fixed to $a_{\text{inc}} = 1$ cm and the skewness is $kax_{\text{inc}} \approx 0.1$. The simulations are ran with a fixed particle size r_0 such that $d/r_0 = 60$ and for 35 waves periods. The waves can travel about 10 times the entire tank length. The surface particle positions are sampled at $\delta t = T/101$, where $T = 1/f_0$ is the wave period, using Marrone *et al.*'s method [103] with a threshold of 0.55. Figure I.3 shows the instantaneous horizontal velocity at the end of the simulation for the case $x_{SL} = 2\lambda$ with $n_B = 3$, $B_{max} = 0.5$. The surface particles are outlined in black.

To check that an asymptotic regime is reached, the Goda & Suzuki [59] two probes method is applied on sample time of 2 wave periods at different instance for a tank with a power sponge layer of length $x_{SL} = 2\lambda$ with $n_B = 3$, $B_{max} = 0.5$. The method uses a FFT to evaluate the amplitudes of the incident wave, a_I (travelling away of the wave maker, shoreward) and the reflected wave, a_R (travelling toward the wave maker, seaward). The reflection coefficient is found by evaluating $R = a_R/a_I$. More details on the method can

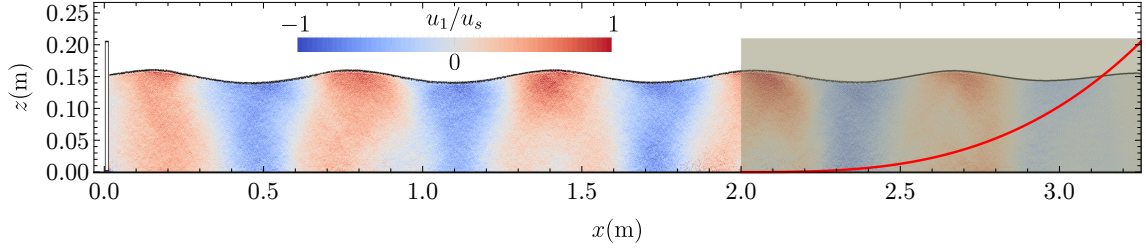


Figure I.3: Instantaneous velocity field in the SPH simulation for $x_{SL} = 2\lambda$ with $n_B = 3$, $B_{max} = 0.5$. The shaded region shows the sponge layer domain. The density plot shows the horizontal velocity rescaled by the linear surface velocity $u_s = a_{inc}\omega \coth kd$. The red line shows the shape of the sponge layer used.

be found in [59]. The probes are spaced by a quarter of wavelength and centred in the physical part of tank (see figure I.2). Figure I.4 shows the measured reflection coefficient and incident wave amplitude with time. An asymptotic regime is reached after 20 wave periods. Note that from now, $X_{SL} = x_{SL}/\lambda$ is the non-dimensional sponge layer length and is compared to the wavelength (instead of the undisturbed water depth d as in Section I.3.1).

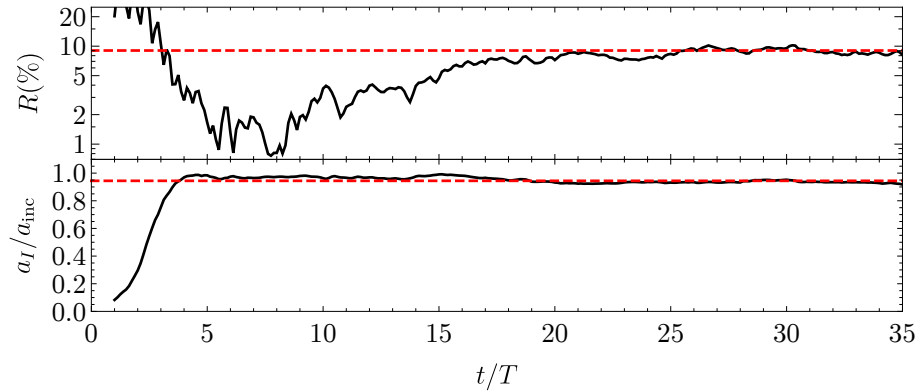


Figure I.4: SPH simulations (black solid lines) time evolution of the reflection and incident wave amplitude measured using Goda & Suzuki two probes method at the centre of the physical tank for $n_B = 3$, $B_{max} = 0.5$ and $x_{SL} = 2\lambda$. The red dashed lines show the linear sponge layer model solution of eq.I.3.2 found using the FEM.

To see the influence of B_{max} on the reflection coefficient, figure I.5 shows the surface envelope over the last 5 wave periods for three cases with a power sponge layer of length $x_{SL} = 2\lambda$ with $n_B = 3$, $B_{max} = \{0.5, 5, 32\}$. For the first case, clear reflections are visible and outlined in the envelope by the red lines which are spaced by half a wavelength. On the other hand, for the case $B_{max} = 5$ the envelope shows small fluctuations. These fluctuations are not due to reflections but to combinations of different wavelength waves. The piston generates also free modes of higher order. In this case the reflection is not as high as it might appear from this graph. To capture only the first harmonic terms, a Fast

Fourier Transform with time of the different probes position is performed. The amplitude of the first harmonic is displayed in figure I.6 for the three cases (this is different from the envelope amplitude). The amplitude is non-dimensionalised by the incident wave amplitude. The results are compared to the linear sponge layer model (red dashed lines) with good agreement. For the last case with the largest value of $B_{max} = 32$, the surface shows again reflection characteristics.

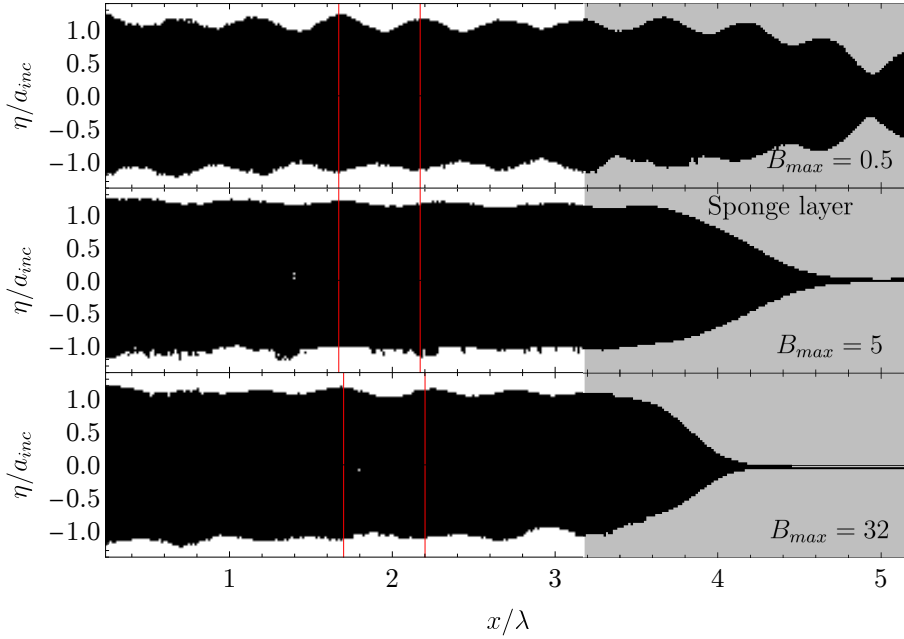


Figure I.5: SPH simulations surface envelope for a power sponge layer of length $x_{SL} = 2\lambda$ with $n_B = 3$, $B_{max} = \{0.5, 5, 32\}$.

Figure I.7 shows the influence of the value of mean sponge layer strength in the sponge layer on the reflection coefficient for different power sponge layer functions compared to the theory. The mean sponge layer strength is defined as:

$$B_{mean} = \frac{1}{x_{SL}} \int_{x_0}^{x_{max}} B(x) dx. \quad (I.3.14)$$

For power sponge layers it comes:

$$B_{mean} = \frac{B_{max}}{n_B + 1}. \quad (I.3.15)$$

The choice of this non-dimensional parameter is such that the minimum of the sponge layer theoretical reflection are aligned.

First notice that in the simulations the reflection coefficient plateaus to a threshold value of 1-2%. This is partially due to the particle size used here and other non-linear effects not accounted for in the simplified linear sponge layer model. The simulations then follows

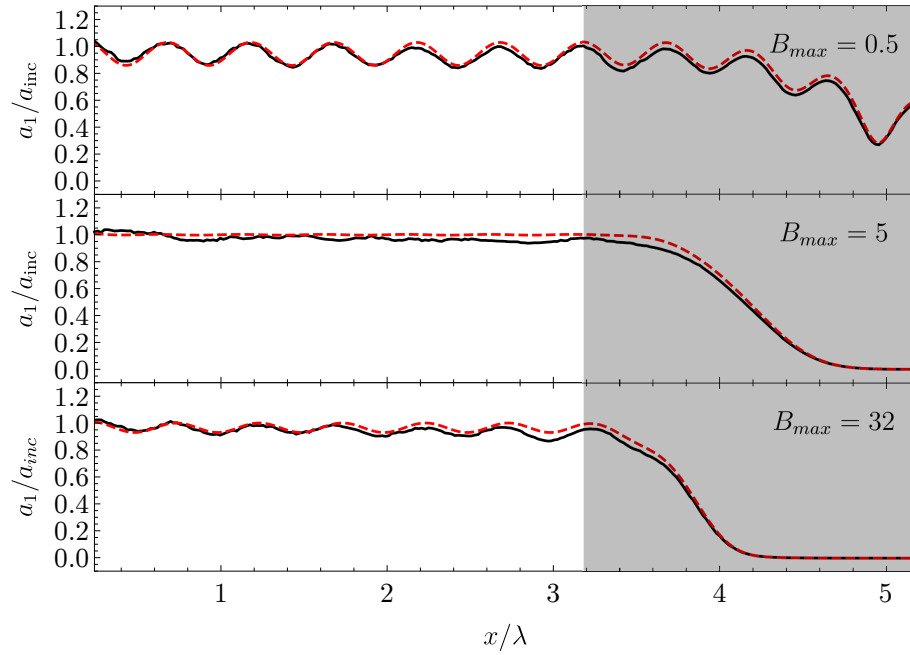


Figure I.6: SPH simulations surface first harmonic amplitude for a power sponge layer of length $x_{SL} = 2\lambda$ with $n_B = 3$, $B_{max} = \{0.5, 5, 32\}$. The red dashed lines show the linear sponge layer model eq.I.3.2 solved with FEM.

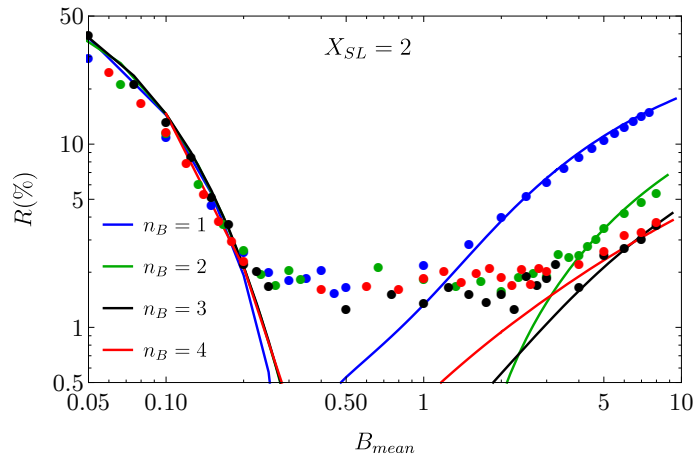


Figure I.7: Reflection coefficient measured from SPH simulations (symbols) for different power sponge layer functions compared to the present linear sponge layer model of eq.I.3.2 solved with FEM (continuous lines). The sponge layer length is fixed to $x_{SL} = 2\lambda$.

the theory trend when the reflection increases again above this threshold value. The linear theory correctly predicts the position of the minimum and the influence of the B_{mean} and n_B on this large range of values. For the cases $n_B = 3$ or 4 , the value of B_{mean} can be set anywhere between 0.2 and 6 and the reflection will be lower than $\approx 3\%$. This large range of acceptable values outlines the fact that the sponge layer is probably larger than

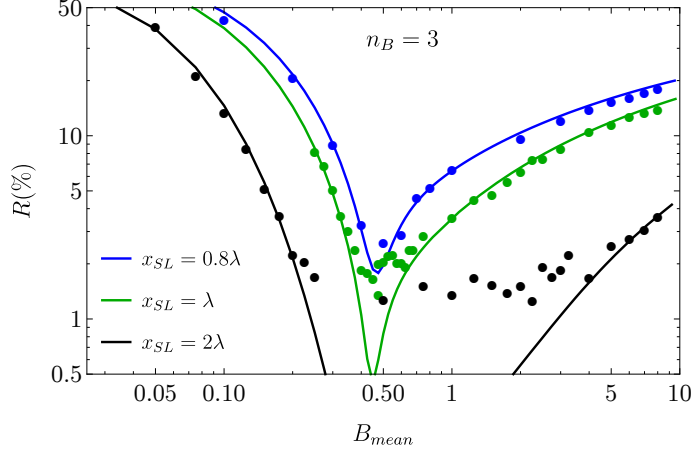


Figure I.8: Reflection coefficient measured from SPH simulations (symbols) for different sponge layer lengths using the power sponge layer with $n_B = 3$, compared to the present linear sponge layer model of eq.I.3.2 solved with FEM (continuous lines).

it could be for this power function. Using the theory, one can show that it is possible to reduce significantly the sponge layer length while keeping the same absorption efficiency (absorption efficiency means here small reflection coefficient). The value $n_B = 3$ is fixed and the sponge layer length is varied in this second test. Figure I.8 shows the influence of the sponge layer length on the results compared to the theory. We see that with a sponge layer as small as 0.8λ it is possible to have a reflection coefficient as small as 2%. This is enough for numerical simulations compared to experimental wave fume where the reflection is estimated to be around 5%. The drawback is that the range of values of B_{mean} for which the reflection is small, is narrower. This justifies the importance of using the linear theory equations derived earlier to find this optimal prior to running the full Navier–Stokes numerical model.

I.3.4 Sponge layer prediction and optimal for fixed Ω

As an application example, the previous case (with $\Omega \approx 1.17$ fixed) is now studied using the FEM based solution of the linear theory to seek the optimal sponge layer strength (B_{mean}) for a given sponge layer length (X_{SL} , non-dimensionalised by the incident wavelength) and for power sponge layer type functions. We chose to work with the sponge layer as there is a simple relationship between the mean value of the sponge layer strength and its maximum. A similar method can be used for other type of sponge functions.

Figure I.9 shows the reflection of the sponge layer contour plot obtained for 4 different values of n_B for the power sponge layer function. The red contours outline the limit for 1% and 2% reflections. For $n_B = 1$ to have a reflection of less than 5% (about the numerical accuracy), the smallest theoretical sponge layer length is $\approx 0.5\lambda$ and $B_{mean} \in [0.51, 0.81]$

and for 2% $B_{mean} \in [0.58, 0.68]$. The minimum reflection for this length of sponge layer is found at $B_{mean} \approx 0.62$ with a theoretical reflection of the order of 0.8%. The value are found using a Golden section-search algorithm [79] (assuming unimodal behaviour). Yet this small reflection range is also limited in terms of sponge layer length. One can see that increasing the sponge layer length for B_{mean} can lead to larger reflection coefficient for this case. The present linear theory shows that it is possible to use as small as 0.5λ long sponge layer for this case. To verify this result found using the present linear model, simulations are run with $x_{SL} = 0.5\lambda$ using the SPH method. The results are shown in figure I.10.

For larger n_B , the minimum sponge length to reach the 5% and 2% thresholds increases. For $n_B = 3$, at $X_{SL} = 0.5$ the minimum reflections is 13% for $B_{mean} \approx 0.69$. One needs to have about $X_{SL} \approx 0.7$ to reach less than 5% reflection with $B_{mean} \approx 0.5$ and $X_{SL} \approx 0.8$ to get less than 2% with $B_{mean} \approx 0.46$. For $n_B = 4$, the minimum length is 0.9 ($B_{mean} \approx 0.41$) and 1.0 ($B_{mean} \approx 0.4$), respectively.

The contour plots of figure I.9 provide important informations. For efficient absorptions, one wants to have the smallest possible sponge layer but also the one that absorbs efficiently all the (free and linked) modes due to non-linearities and scattering. For instance, if one chooses a sponge layer with a linear sponge layer function ($n_B = 1$) of non-dimensional length $X_{SL} = 0.5$ with $B_{mean} = 0.6$, then the second harmonic will see a sponge layer equal to its wavelength and the free mode of about 1.8 time its wavelength. Though the absorption of the second harmonic requires to develop the theory to the next order, the free-mode absorption follows the same theory. The sponge layer efficiency for the free-mode can therefore be inferred from the contour plots of figure I.9. The apparent B_{mean} will be half the one of the first harmonic thus 0.3 for the free mode (see green diamond point). It is for this case still in the acceptable range of 5%. Yet it is clear that the higher frequency free-modes will be less efficiently absorbed as the apparent B_{mean} diminishes. The green point in figure I.9 shows this case example for $n_B = 1$. A good strategy is thus to select a value near the upper bound of the interval of interest to have the best absorption of higher modes. Note though that usually these modes have smaller amplitudes or also dissipate faster due to viscous dissipation, wave breaking and so on. Table I.1 shows the confidence intervals for a reflection of 5% and the minimum of reflection in this range. The data outlined in red shows the cases where the minimum is below 2%. The results of the table are also displayed in the contour plots. The blue points show the range of 5% while the white line shows the minimum path once the 5% threshold is reached and the white diamonds the minimum values listed in table I.1.

So far the angular frequency was fixed to $\Omega \approx 1.17$. We showed that it was possible to use the linear theory and a simple FEM solver to predict the optimal absorption conditions. It is found that one can have a sponge layer as small as 0.5λ for this case. Due to the non-linearity of the dispersion relation, one cannot use directly the optimal value found

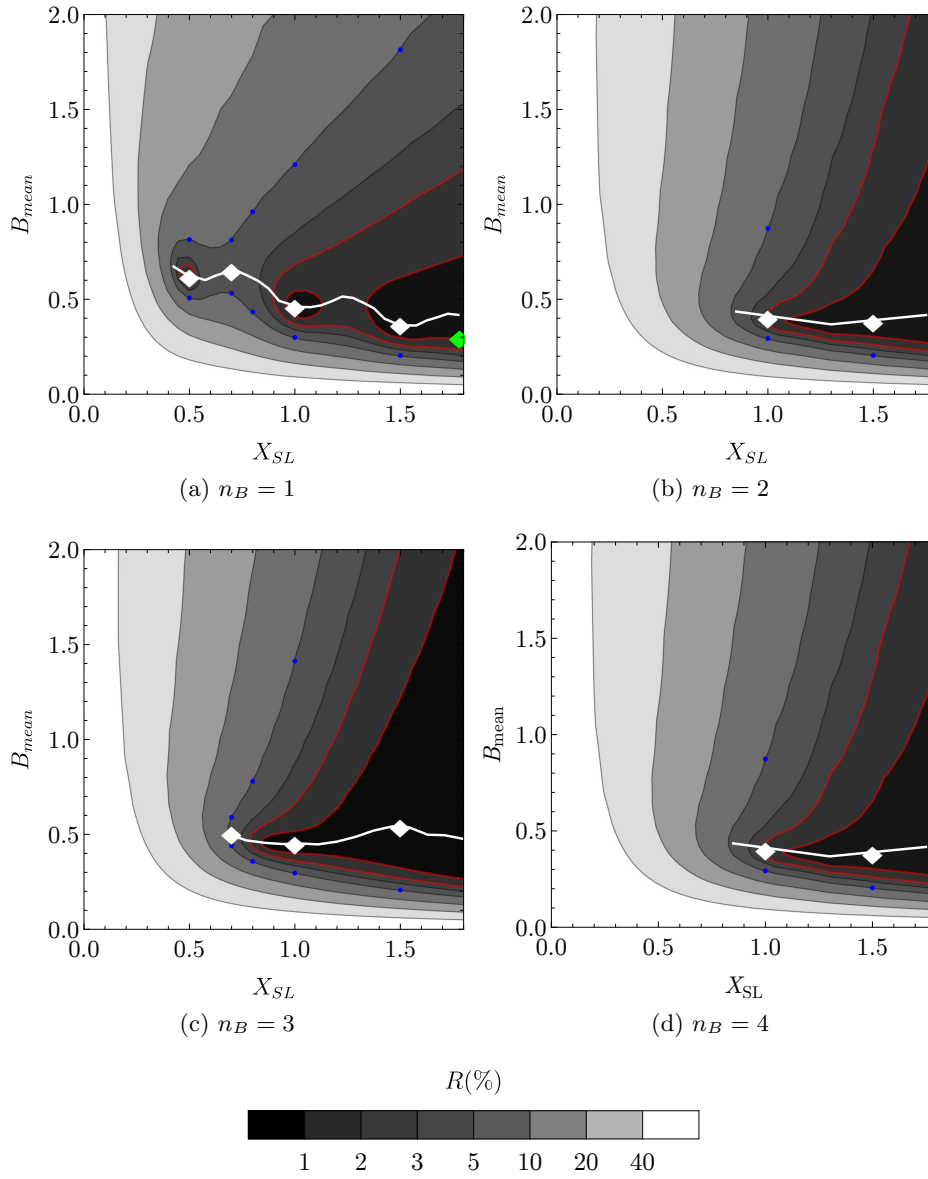


Figure I.9: Reflection coefficient contour plot obtained with FEM for different n_B values for power sponge layer for $\Omega \approx 1.17$. The red contours outline the iso reflection of 1% and 2%. The blue points show the value obtains for a threshold of 5% using the Golden section search algorithm and the white line the minimum reflection starting once the reflection is below 5%. The green point in the first figure shows the expected reflection for the first free mode for a sponge layer of non-dimensional length 0.5 and $B_{mean} = 0.6$ for the dominant first harmonic.

for $\Omega \approx 1.17$ for other wave angular frequencies.

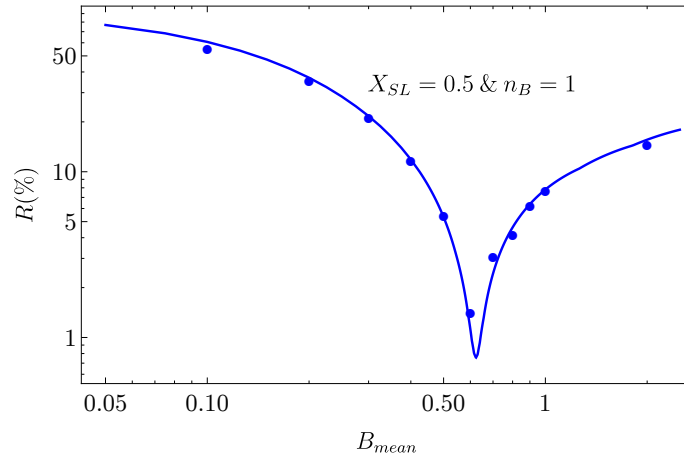


Figure I.10: Reflection coefficient measured from SPH simulations (symbols) for a sponge layer of length $x_{SL} = 0.5\lambda$ with $n_B = 1$, compared to the present linear sponge layer model of eq.I.3.2 solved with FEM (continuous line).

		X_{SL}			
		0.5	0.7	1	1.5
n_B	1	0.51- 0.62 -0.81	0.53-0.65-0.81	0.30- 0.46 -1.20	0.21- 0.36 -1.80
	2	N/A	0.40- 0.53 -0.88	0.31- 0.57 -1.67	0.21- 0.77 -3.76
	3	N/A	0.44-0.51-0.58	0.30- 0.45 -1.41	0.21- 0.54 -4.72
	4	N/A	N/A	0.30- 0.40 -0.87	0.21- 0.38 -4.25

Table I.1: Predicted power sponge layers range of B_{mean} to get less than 5% reflection for different wave length (extremes value) and value at which the minimum is reached (center). The number in red shows minimum for which the predicted reflection is below 2%.

I.3.5 Sponge layer prediction as a function of Ω

In this subsection, we fix the water depth and the sponge layer length to $x_{SL} = \lambda(\omega, d)$, where the brackets outline the fact that the wavelength is a function of the frequency and depth. A power sponge layer is used with $n_B = 3$ and a sponge layer mean coefficient $B_{mean} = 0.36$. This value corresponds to an optimal sponge layer strength in the limit of deep water waves (see figure I.12 commented in the next paragraph). The wave angular frequency is varied. The reflection coefficients measured in the simulations are displayed in figure I.11 in gray as a function of the non-dimensional angular frequency, Ω . The SPH simulations (gray symbols) are compared to the linear theory results found using the FEM solver (solid gray line). It is clear that the ability of the sponge layer to absorb the wave depends on the wave frequency. This is due to the non-linear form of the dispersion relation. The difference of trend between the SPH simulations and the linear model as Ω increases (slightly increasing reflection) is believed to be due to the relative coarseness (the particle size is fixed and the wavelength diminishes), the increasing non-linearities

(the wave amplitude is fixed here) and the increasing numerical dissipation in the wave propagation. An improvement in the SPH simulations would be to reduce the particle size as the wave frequency is increased and use renormalisation operators as done in [163]. This is outside the scope of the present study.

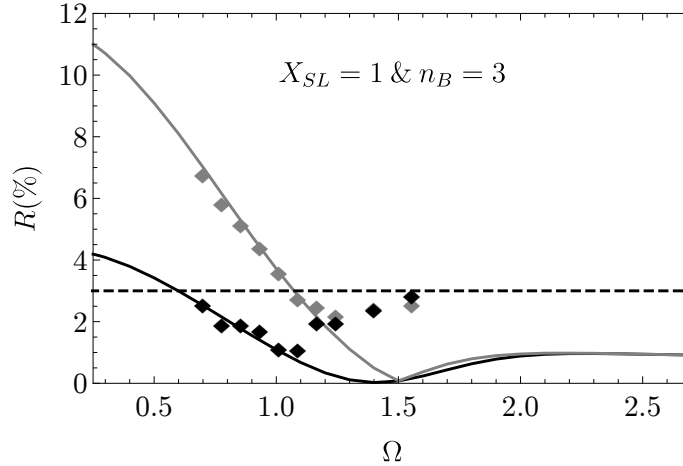


Figure I.11: Effect of varying the angular frequency and sponge layer strength on the reflection coefficient for a power sponge layer with $n_B = 3$ and $X_{SL} = 1$. Compared SPH-based simulation (symbols) and FEM-based solutions of the linear theory (solid lines) results of the reflection coefficient for a fixed $B_{mean} = 0.36$ (in gray) and for the optimal value of B_{mean} found using the Golden section search algorithm and the FEM solver (in black). Figure I.12 shows the optimal sponge layer strength values as a function of Ω for the black points and line.

Using the Golden section search algorithm and the FEM solver, we show in figure I.12 the evolution of the optimal B_{mean} with Ω for the power sponge layer for $n_B = 3$ and $X_{SL} = 1$. It appears clearly in this graph that B_{mean} is a constant in the limit of deep water waves consistently with the results of [130, 131]. This optimal value was used to generate the gray data in figure I.11. For $\Omega < 2$, the optimal is no more a constant referring to the linear model. The optimal value of B_{mean} increases as Ω diminishes. In figure I.11, the reflection coefficient found for this optimal values using the SPH method and the FEM solver are displayed in black. With the optimal value we are able to keep the reflection coefficient below 3% (dashed line) on the entire spectrum tested here. This illustrates the importance of knowing the proper B_{mean} as a function of Ω . Note that the reflection coefficient still increases as Ω diminishes in the linear sponge layer model with optimal absorption. To get a constant reflection coefficient one would probably need to increase the sponge layer length to wavelength ratio as Ω diminishes. In the present study, we limit ourself to finding the optimal value for a given sponge layer length to wavelength ratio (here $X_{SL} = 1$) and wave angular frequency.

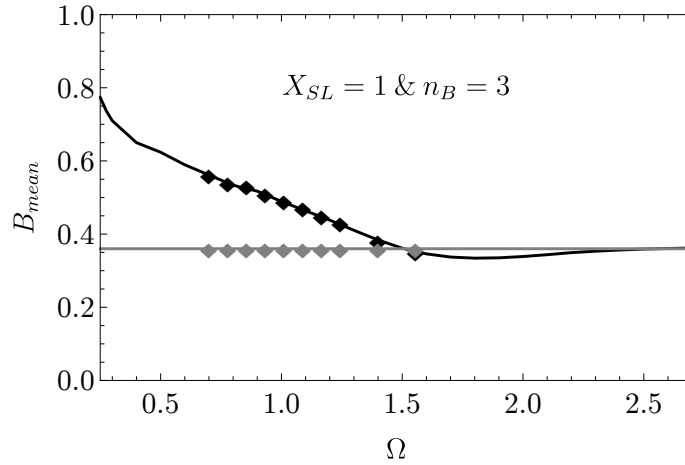


Figure I.12: Evolution of the optimal value of B_{mean} with the angular frequency Ω for power sponge function with $n_B = 3$ and $X_{SL} = 1$. The black line is found using the Golden section search algorithm to find the minimum of reflection. The gray horizontal line shows the value found in the limit of deep water waves. The diamonds show the value used in the SPH simulations. The reflection coefficients are plotted in figure I.11.

Finally, the table I.2 provides values of B_{mean} for which the reflection is minimum for different values of Ω and different sponge layer functions. The values are listed if below 5% and in red if below 2%. The results are obtained using the Golden section search algorithm [79]. The table stops at $\Omega = 2.0$ as for larger values the variations are not significant and B_{mean} is approximatively a constant consistently with the results of [130, 131]. Solving the present linear problem and search for the optimal for a given Ω is cheap in computational time and can save precious computational efforts. In the present case, FEM solver takes about a 0.5 seconds to solve the linear equations and the Golden section search takes about a minute to find the optimal value. On the other hand, the SPH solver needs about 6 hours to reach an asymptotic regime.

I.4 3D application

To show that the results found in 2D can be directly applied to 3D, consider a wave flume of length $l_\varphi = 2$ m and $\ell = 25$ cm wide, with an inclined sponge layer boundary of $\theta = 45^\circ$ incidence. The simulations are ran using the *GPUSPH* open-source solver [60] with USAW boundary conditions (see appendix K). The particle size, r_0 , is fixed such that $d/r_0 \approx 30$. There are 1.25 millions particules in the tank. The simulations is ran on 4 GPU's (NVIDIA GK110GL Quadro K5200) for 15 seconds of physical times (taking 48 hours of simulation time).

The waves are generated using a piston wave maker. The water depth is still 15 cm and the

		Ω		0.1	0.25	0.5	0.75	0.9	1.0	1.1	1.5	1.75	> 2.0	
		n_B	X_{SL}											
Power	1	0.5		N/A	N/A	N/A	0.71	0.67	0.65	0.64	0.56	0.54	0.54	
		0.7		N/A	N/A	N/A	N/A	N/A	N/A	0.67	0.58	0.54	0.55	
		1.0		0.59	0.58	0.56	0.53	0.50	0.49	0.47	0.43	0.43	0.45	
	2	0.7		N/A	N/A	N/A	0.63	0.59	0.58	0.55	0.45	0.42	0.43	
		1.0		0.87	0.85	0.80	0.71	0.67	0.64	0.60	0.48	0.46	0.47	
	3	0.7		0.68	0.67	0.65	0.60	0.57	0.54	0.53	0.41	0.39	0.40	
1.0			0.91	0.78	0.63	0.55	0.52	0.49	0.46	0.36	0.34	0.34		
Exp.	1	0.5		0.81	0.80	0.78	0.74	0.70	0.68	0.66	0.56	0.54	0.54	
		1.0		0.66	0.65	0.63	0.59	0.56	0.53	0.52	0.46	0.47	0.49	
	2	0.7		0.74	0.73	0.69	0.65	0.62	0.60	0.57	0.44	0.42	0.42	
		1.0		1.01	0.99	0.88	0.75	0.65	0.61	0.57	0.41	0.38	0.39	
	Trig.	1	0.5		N/A	N/A	N/A	N/A	0.64	0.63	0.61	0.56	0.54	0.55
			1.0		0.55	0.54	0.53	0.49	0.47	0.46	0.45	0.41	0.41	0.42
2	1.0		0.71	0.70	0.66	0.63	0.59	0.56	0.55	0.48	0.46	0.47		

Table I.2: Table values of B_{mean} for different sponge layer functions with minimum reflection. The values are listed if the predicted reflection is below 5% and in red if below 2%. The results are found using the Golden section search algorithm.

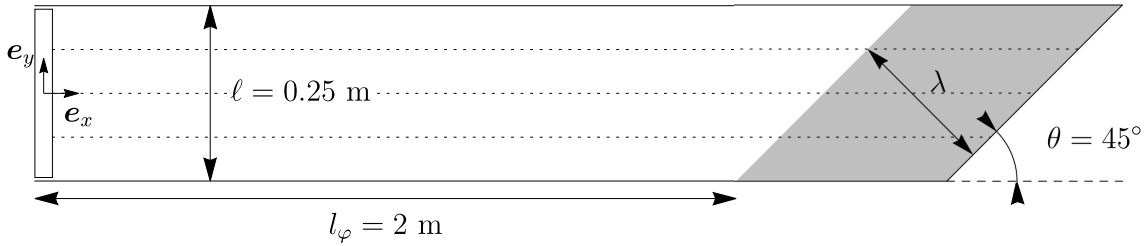


Figure I.13: Top view of the 3D SPH numerical wave flume. The shaded gray region represent the sponge layer. The dotted line shows the sampled line for the water surface elevation.

frequency 1.5 Hz, thus $\Omega \approx 1.17$. The waves have a 45° incident angle with the sponge layer. The sponge layer is designed to absorb most efficiently the waves perpendicular to it with a power sponge layer function optimised for $X_{SL} = 1$, for $n_B = 3$ we set $B_{mean} = 0.45$ (see table I.1). A top view of the simulated tank is shown in figure I.13. Figure I.14 shows the instantaneous horizontal velocity field at the end of the simulation. The surface is sampled on 3 lines perpendicular to the wave crest evenly spaced (at the middle and quarter widths from the lateral walls). The amplitude of the first harmonic and the phase are plotted along these three lines in figure I.15. First, it is noticed that in 3D the dissipation is important in the physical part. This is due to additional numerical dissipation along with physical friction on the lateral walls. The wavenumber of the generated waves is $k \approx 9.54 \text{ m}^{-1}$ instead of $k_0 = 10.0 \text{ m}^{-1}$ of the linear theory. The discrepancy can originate from the difficulty of filling the tank using our current software which leads to a diminution of the

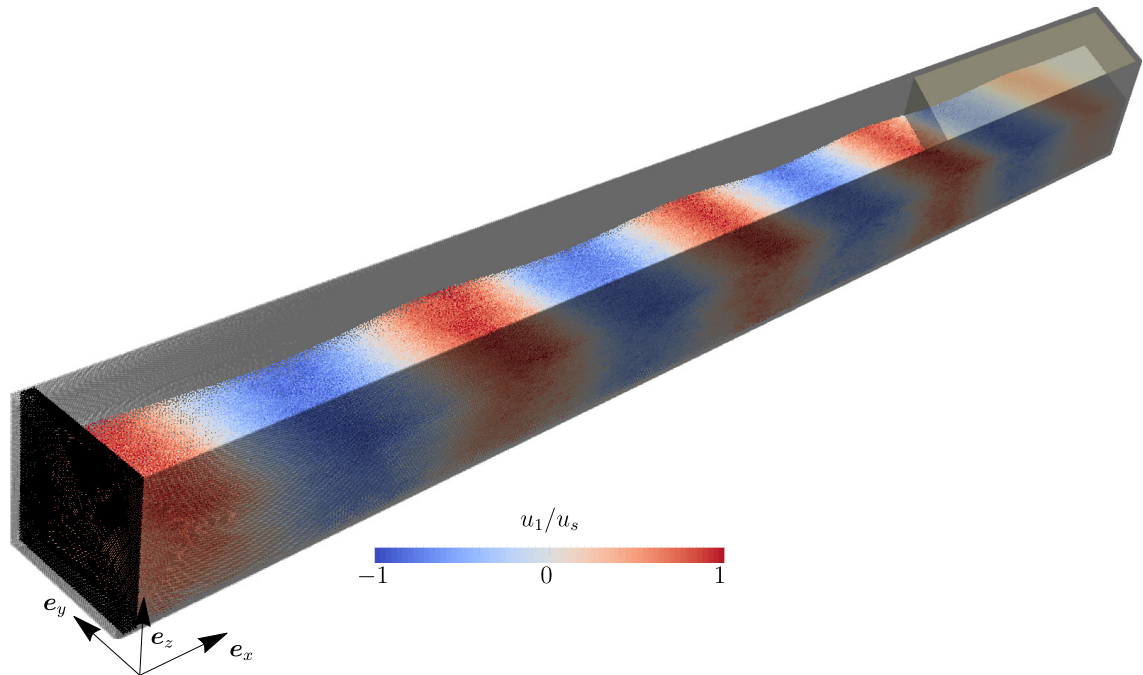


Figure I.14: 3D SPH simulation wave tank at the end of the simulation. The shaded region shows the sponge layer domain. The density plot shows the horizontal velocity rescaled by the linear surface velocity $u_s = a_{inc}\omega \coth kd$.

water-depth after particle rearrangement along with the increased friction at the lateral walls. No apparent reflection patterns are visible in the amplitude graph. As the sponge layer is inclined with the incident waves one might expect a modification of the incidence angle in the sponge layer and this is visible in the phase plot where the different profiles are out-of-phased in the sponge layer.

I.5 Conclusion

In this paper, the sponge layer equations are derived and perturbation method is applied for monochromatic waves. A linear theory sponge layer pressure equation is found and can be easily solved using FEM solver. It predicts accurately the reflection coefficient as confirmed using a SPH Navier–Stokes solver.

The case of 2 dimensional waves is considered. We show that the model can be used to predict accurately the optimal reflection coefficient. Using a Golden search algorithm we are able to provide the optimal absorption parameters for a given sponge layer function shape and length at low computational cost. We verified that the optimal sponge layer strength is a constant for deep water waves ($\Omega > 2$) and varies for intermediate depth waves. Tables of optimal absorptions are provided other a range of non-dimensional wave angular frequencies where the coefficient varies for various sponge layer functions found in

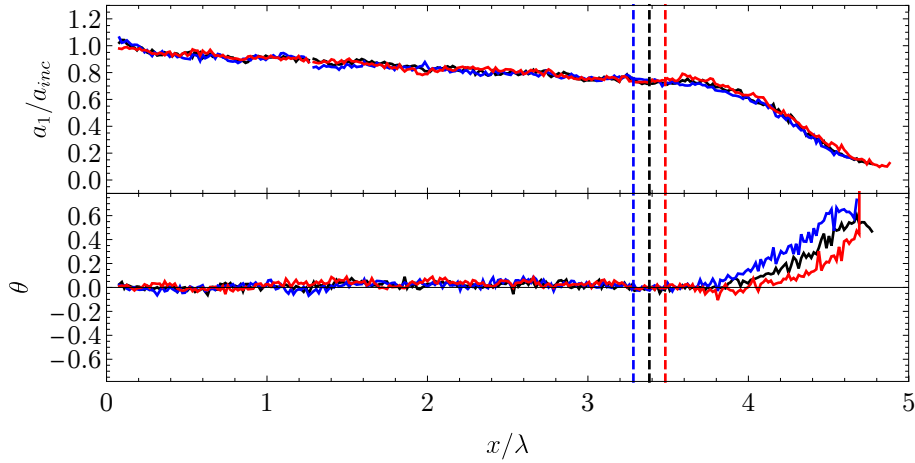


Figure I.15: 3D SPH simulation wave amplitude and phase along the lines $y = \{1/4, 1/2, 3/4\} \ell$ in blue, black and red respectively (see dashed lines in figure I.13). The phase is evaluated using the measured wavenumber $k = 9.54 \text{ m}^{-1}$ different from the theoretical one $k_0 = 10.0 \text{ m}^{-1}$. The vertical color lines show the beginning of the sponge layer at the different positions. The amplitude and phase are identical in the physical part.

the literature.

A 3D application, with the *GPUSPH* open-source solver [60], is presented with this choice of parameters. The sponge layer works as expected. A change of incident angle is observed in the sponge layer.

The authors outline the simplicity of solving the linear theory sponge layer problem which can be done before running a full Navier–Stokes simulation to select the proper form and value of the sponge layer function. The results match our simulations as long as the reflection is above a numerical threshold of 1-2% which is satisfactory for numerical simulations of water wave problems. The linear theory can also be used to assess the efficiency of sponge layer used in previous paper where the authors frequently omit providing this essential information. Furthermore, this can be also used to design a sponge layer such that the reflection coefficient matches the one of experimental investigations if provided.

FEM Solver: mesh and convergence

The linear problem of eq.I.3.6 (or eq.I.3.2) is solved using the FEM solver embodied in Mathematica[75]: *NDSolve*. The mesh is constructed using *ToBoundaryMesh* function first to correctly capture the edges, then the *ToElementMesh* function is used to mesh the interior. The mesh is refined near the free surface such that the area of a cell is 100 times smaller for cells above the mid water depth. The refinement is defined as the root square of the cells near the surface. Figure I.16 shows a mesh for a resolution $dx = \lambda/50$ (thus

$dx \approx \lambda/5$ at the sea bed).

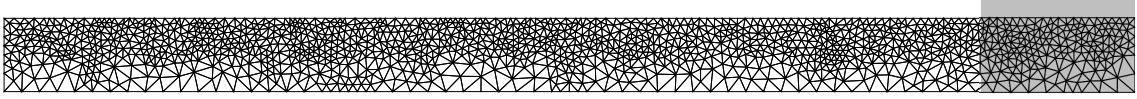


Figure I.16: Example of mesh used in the FEM for $dx = \lambda/50$. The mesh is refined near the free surface.

The resolution is first varied for a fixed value of the dissipation coefficient. A power sponge layer of length 2λ with $n_B = 3$ and $B_{max} = 0.5$ is used here (this corresponds to the configuration in the top graph of figures I.5 and I.6). The reflection coefficient is measured near the center of the physical part of the tank using the formula:

$$R = \frac{|\tilde{Z}_{max}| - |\tilde{Z}_{min}|}{|\tilde{Z}_{max}| + |\tilde{Z}_{min}|}. \quad (\text{I.5.1})$$

The error corresponds to the relative difference between the most refined simulations (here $dx/\lambda = 10^{-3}$). The expected reflection is about 9.03%. The results converges as seen in figure I.17. The vertical dashed line shows the resolution selected to evaluate the contour profiles.

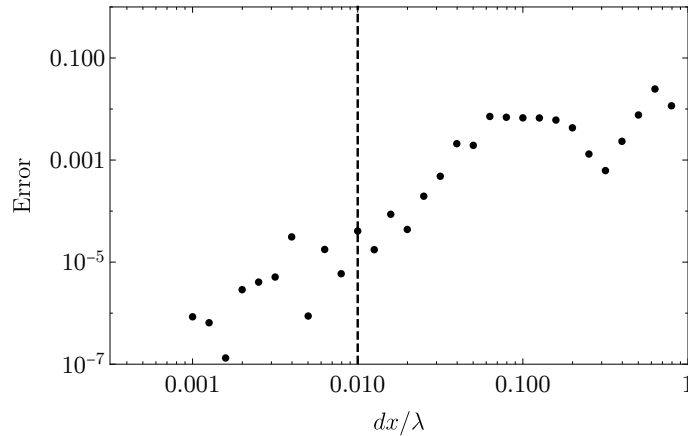


Figure I.17: Convergence test: error on the value of the reflection coefficient for power sponge layer with $n_B = 3$ and $B_{max} = 0.5$. The dashed line shows the resolution used for the contour plots.

To see the effect of the grid size on the variation of the damping coefficient, a convergence test is performed for power sponge layer of length 2λ with $n_B = 3$ with variable damping coefficient B_{mean} . The results are shown in figure I.18. Away from the minimum region, the curve converges rapidly. The resolution of the red curve is used to construct the contour plots.

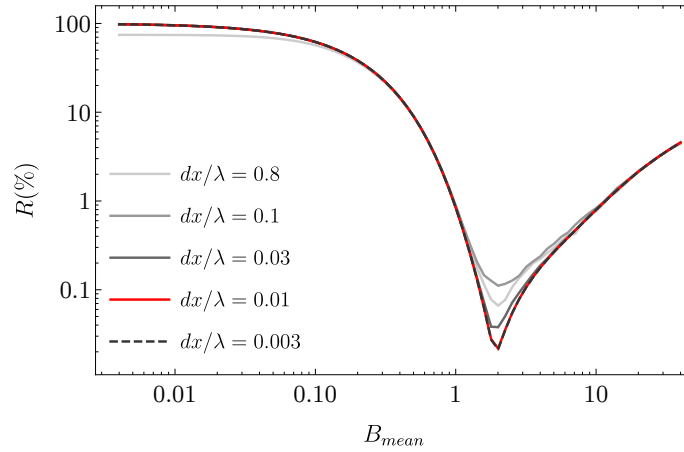


Figure I.18: Convergence test: reflection coefficient for power sponge layer with $n_B = 3$ as a function of B_{mean} for different mesh resolution. The red curve shows the resolution used for the contour plots.

Appendix J

Dissipation above a shelf

Cette annexe présente l'étude de l'impact de vagues monochromatiques sur une marche. Au-dessus de la marche, on suppose que l'écoulement est dissipé. On évalue le saut du transport de masse pour les différents modèles.

In this appendix, the simple example of wave at a step is considered with dissipation above the shelf and simplifications are proposed.

Consider a similar case to the one described in the section 1.3.4.3. In addition, to model the wave breaking at the shelf, dissipation is added in the shallower region. This is thus valid only in the case of intermediate water depth above the plate ($\Omega\sqrt{D_s} < 1.7$), since otherwise the waves would also break before the shelf and dissipation should be considered there too. In this example, the dissipation is still considered only above the shelf and this even in the deep water regime. This enables to see what is the proper way of simplifying the model with dissipation (called EFE Full).

The solution is supposed to be of the form:

$$\begin{aligned}\Phi_{\text{C,I}}^{(1)} &= \frac{iA\Omega}{K_0 \sinh K_0} e^{-iKX} \cosh [K_0 (Z + 1)] + \\ &\quad \sum_{n \in \mathbb{N}} C_n^- e^{iK_n X} \cosh [K_n (Z + 1)], \quad \text{for } X < 0 \\ \Phi_{\text{C,II}}^{(1)} &= \sum_{n \in \mathbb{N}} C_n^+ e^{-iK_n^{s,\mathcal{R}} X} \cosh [K_n^{s,\mathcal{R}} (Z + D_s)], \quad \text{for } X > 0\end{aligned}\quad (\text{J.0.1})$$

where now $K_n^{s,\mathcal{R}}$ are solution of the dissipative dispersion relation eq.1.5.18, which for this water depth becomes:

$$\Omega^2 \left\{ 1 - i \frac{2 (K^{s,\mathcal{R}})^2}{\Omega \mathcal{R}} \right\} = K^{s,\mathcal{R}} \tanh K^{s,\mathcal{R}} D_s, \quad (\text{J.0.2})$$

and can be brought back to its original form after defining $\Omega_s = \Omega\sqrt{D_s}$ and $\mathcal{R}_s = \mathcal{R}D_s^{3/2}$ and $K = K^{s,\mathcal{R}}D_s$. The boundary conditions at the interface between the two domains are unchanged. The convergence is not ensured by the Sturm–Louville theorem due to the complex coefficient at the free surface boundary condition (see eq.1.5.16). Numerically, it is found that the solution converges but rather slowly. As an illustration, figure J.1 shows the evolution of the first parameter C_0^- as a function of the number of modes for $D_s = 1/3$ and $\Omega = 0.25$ and 3.0 and $\mathcal{R} = \mathcal{R}_{limit}^s$, where:

$$\mathcal{R}_{limit}^s = \frac{K_0^s}{\Omega} \left(\frac{4 \sinh 2K_0^s D_s}{2K_0^s D_s + \sinh 2K_0^s D_s} \right)^{2/3}, \quad (\text{J.0.3})$$

is the limit Reynolds number in the shallower part¹ and K_0^s is solution of the dispersion relation:

$$\Omega^2 = K_0^s \tanh K_0^s D_s. \quad (\text{J.0.4})$$

The evolution of the parameter is compared to the case without dissipation and to two simplified models where the effect of the dissipation is limited to the propagative term only. In the first simplified model, the eigenfunctions are kept identical to the potential

¹Note that it is also possible to define the reference depth as d_s but it seems more natural to keep d fix and vary the shelf depth.

domain without dissipation and the dissipation only affects the term $e^{-iK_0^s X}$ where K_0^s is modified by its dissipative value $K_0^{s,\mathcal{R}}$ (called EFE NI for not incompressible as this term does not then verify the Laplace equation):

$$\Phi_{\mathbb{C},\text{II}}^{(1),NI} = C_0^+ e^{-iK_0^{s,\mathcal{R}} X} \cosh [K_0^s (Z + D_s)] + \sum_{n \in \mathbb{N}^*} C_n^+ e^{-iK_n^s X} \cosh [K_n^s (Z + D_s)]. \quad (\text{J.0.5})$$

This modification was proposed in the study of waves above a permeable bed by Kim and Lee [80].

In the second simplified model, the eigenfunction associated with this mode is also modified to $\cosh [K_0^{s,\mathcal{R}} (Z + D_s)]$, and thus this mode now also verify the incompressibility and is called hereafter EFE Limited:

$$\Phi_{\mathbb{C},\text{II}}^{(1),NI} = C_0^+ e^{-iK_0^{s,\mathcal{R}} X} \cosh [K_0^{s,\mathcal{R}} (Z + D_s)] + \sum_{n \in \mathbb{N}^*} C_n^+ e^{-iK_n^s X} \cosh [K_n^s (Z + D_s)]. \quad (\text{J.0.6})$$

The drawbacks of this correction is that the first mode is not orthogonal to the other ones and as they do not verify the same surface condition (or equivalently the same dispersion relation) if the continuity of the scalar and the velocity are enforced at the interface between the two domains the velocity diverges at the intersection at $Z = 0^-$. On the other hand, far from the matching interface, the solution then verifies the desired set of equations.

It appears that the solution converges for the full dissipative model (EFE Full) but at lower rate compared to the other models. The solution oscillates around its final value for the case $\Omega = 0.25$ while it converges without oscillations for the higher frequency case. The simplified models all converge fast to their asymptotic values. As in the rest, the attention is on the wave mass transport; the mass transport jump is measured for the different models. To have a consistent definition between the different models, the wave mass transport is evaluated in each domain at the interface as the value of the propagative terms limited expansion in the domain. In other words, in the domain of water depth D_s , the expansion is limited to the first term C_0^+ .

To estimate the wave mass transport jump asymptotic value with a reasonable number of modes in the EFE Full version, it is proposed to evaluate the solution from 5 to 10 terms (sufficient for the other models) and evaluate the final result as the mean of the two extrema found. For the low frequencies, this enables to limit the error coming from the oscillations around the asymptotic value. For high frequencies, the result is closer to the absolute maximum. In all the other models, a 10-term expansion is used.

The wave mass transport jump frequency response with fix $\mathcal{R}/\mathcal{R}_{limit}$ values are shown

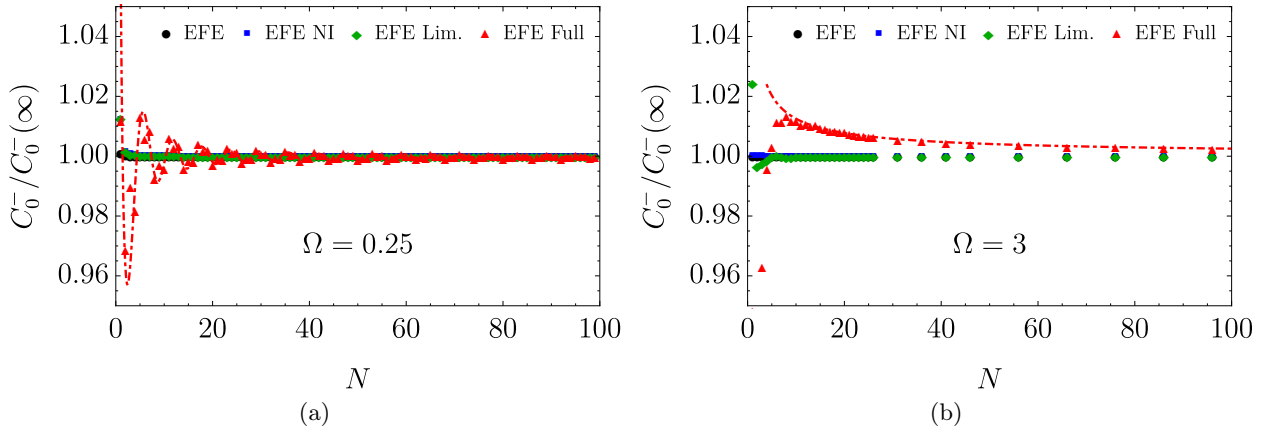


Figure J.1: Convergence of the dissipative models for wave at a step for two distinct frequencies. The solution appears to converge in all cases. For the EFE Full model, the convergence is slower. It oscillates around its asymptotic value for the case $\Omega = 0.25$ and converges slowly for the case $\Omega = 3$. The rate of convergence is estimated to be approximately $N^{-1.4}$ for $\Omega = 0.25$ and $N^{-0.6}$ for the case $\Omega = 3$. For the other models, the convergence is in $N^{-5/3}$ as shown in appendix C. Note that the models do not converge all to the same results. The values are divided by the results of the most refined simulation in each model.

in figure J.2. They are less data points for the EFE Full as the computational time is significantly more important. For a 10-term expansion, in this simple two domains case, one needs 0.6 seconds to compute the solution with the EFE, EFE NI and EFE Limited models, while it needs 30 seconds for the EFE Full and the solution is not fully converged. At $\mathcal{R} = 5 \times \mathcal{R}_{limit}$, the curves are more or less superimposed. For the case $\mathcal{R} = 2 \times \mathcal{R}_{limit}$, the EFE Limited overestimates the reduction of jump at the low frequencies while it has a similar behaviour for high frequencies. The EFE NI, behaves similarly to the EFE Full for low frequencies but does not capture any change of behaviour at high frequencies. Note that at high frequency the EFE Full and EFE Limited show a non-zero jump. This might be surprising at the first sight one would expect the effect of the step to be insignificant in the deep water case. Yet here, dissipation is forced over the step. For the case $\mathcal{R} = 1 \times \mathcal{R}_{limit}$, the results are similar to the previous case. The EFE Limited captures correctly the dynamics but overestimates the effect on the entire spectrum. It appears in this example that both simplified models carry informations about the frequency response with dissipation. The EFE NI is more accurate in the region where wave breaking is likely to happen. The EFE Full is unfortunately too computationally expensive and cannot be used reliably. This justifies the use of the EFE NI model in all the rest of the thesis.

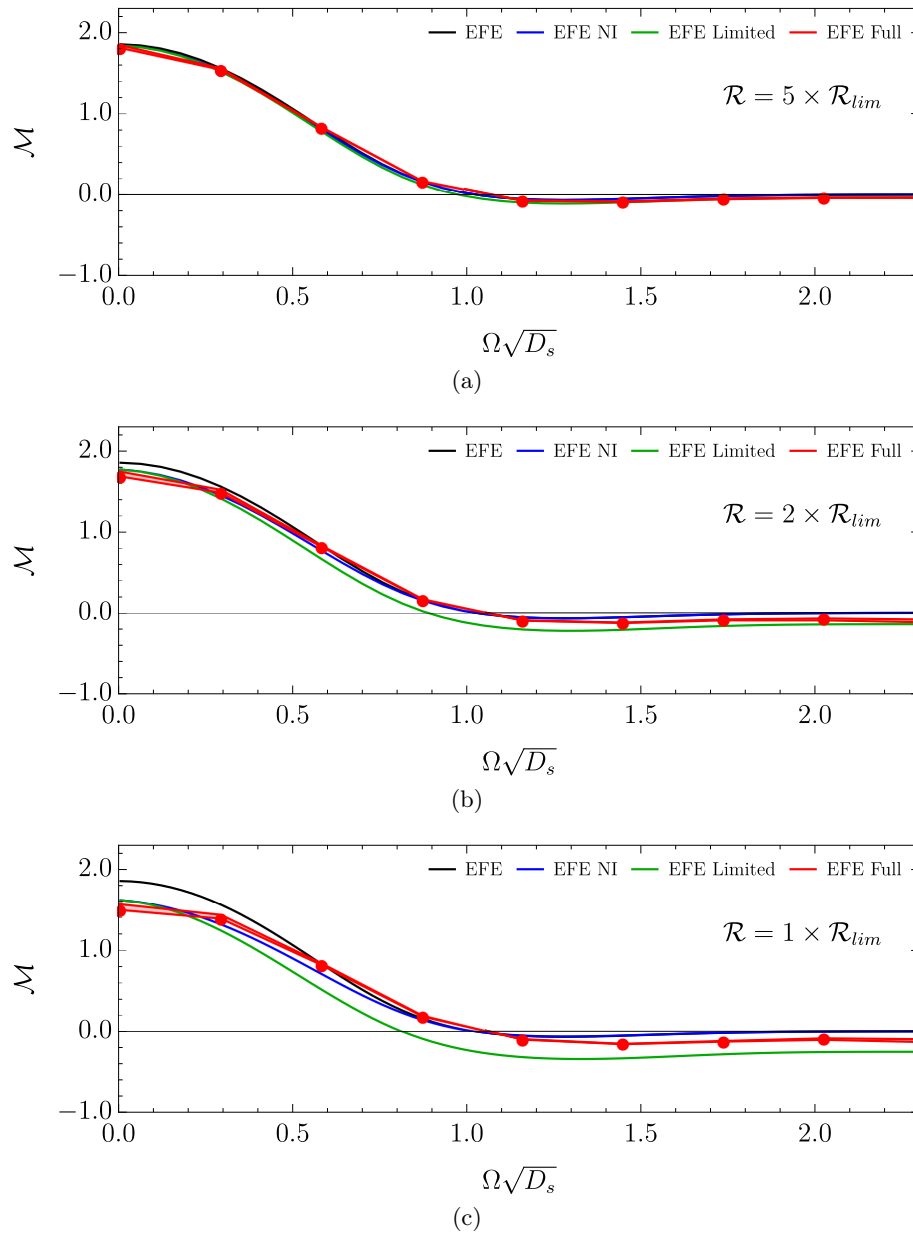


Figure J.2: Wave mass transport jump above the shelf and dissipative models.

Appendix K

Smoothed Particle Hydrodynamics

Cette annexe présente sommairement la méthode SPH utilisée dans les simulations, ainsi que les codes retenus pour cela.

In the present study, a weakly compressible smoothed particle hydrodynamics method (WCSPH) is used to solve the Navier-Stokes equation (*Sphynx* solver in 2D and *GPUSPH* open-source solve in 3D [60]). The equations are:

$$\frac{d}{dt} \begin{pmatrix} \rho \\ \mathbf{u} \end{pmatrix} = \begin{pmatrix} -\rho \nabla \cdot \mathbf{u} \\ \frac{1}{\rho} (\mathbf{g} + \nabla \cdot \bar{\sigma}) \end{pmatrix}, \quad (\text{K.0.1})$$

where $\mathbf{g} = -g\mathbf{e}_z$ is the gravitational acceleration ($g = 9.81 \text{ m.s}^{-2}$), and $\bar{\sigma}$ is the stress tensor:

$$\bar{\sigma} = -p\bar{\mathbf{I}} + \mu (\nabla \mathbf{u} + \nabla \mathbf{u}^T). \quad (\text{K.0.2})$$

In order to close this system of equations, an equation of state is defined to relate the pressure and the density [86]:

$$p = \frac{\rho_0 c_{SPH}^2}{\zeta} \left[\left(\frac{\rho}{\rho_0} \right)^\zeta - 1 \right], \quad (\text{K.0.3})$$

where ρ_0 is the reference density, c_{SPH} is the numerical speed of sound and ζ is the adiabatic index equals to 7 for water. In the present simulations, the speed of sound is fixed to $c_{SPH} \approx 10\sqrt{gd_{\max}}$, where d_{\max} is the maximum water depth, which ensures that the flow is close to incompressible. SPH method is used to solve this problem. The fluid is decomposed in particles, which represents material points of fixed mass m and initial size at rest $r_{SPH} = h_{SPH}/2$ (for example $a \in \mathcal{P}$ in Fig. K.1).

A function f evaluated at a position a is given by

$$[f]_a = \frac{1}{\gamma_a} \sum_{b \in \mathcal{P}} V_b f_b W_{ab}, \quad (\text{K.0.4})$$

where \mathcal{P} is the set of all particles, V_b denotes the volume of the particle b , $W_{ab} = W(|\mathbf{r}_a - \mathbf{r}_b|)$ the kernel function as a function of the distance between the particle b and the position a , which is the quintic polynomial by Wendland [168]. In 2D, it is:

$$W_{2D}(r) = \begin{cases} \frac{\alpha}{(2h_{SPH})^2} \left(1 - \frac{r}{2h_{SPH}}\right)^4 \left(1 + 2\frac{r}{h_{SPH}}\right) & , r < 2h_{SPH} \\ 0 & , r \geq 2h_{SPH} \end{cases} \quad (\text{K.0.5})$$

with $\alpha = 7/\pi$ and $h_{SPH} = 2 \times r_{SPH}$ is the smoothing length in 2D. In 2D, it is:

$$W_{3D}(r) = \begin{cases} \frac{\alpha}{(2h_{SPH})^3} \left(1 - \frac{r}{2h_{SPH}}\right)^4 \left(1 + 2\frac{r}{h_{SPH}}\right) & , r < 2h_{SPH} \\ 0 & , r \geq 2h_{SPH} \end{cases} \quad (\text{K.0.6})$$

where $\alpha = 21/2\pi$, $h_{SPH} = 1.87643 \times r_{SPH}$ ¹.

¹The value is chosen here to minimize the error of approximation of the unity integral on a unigrid

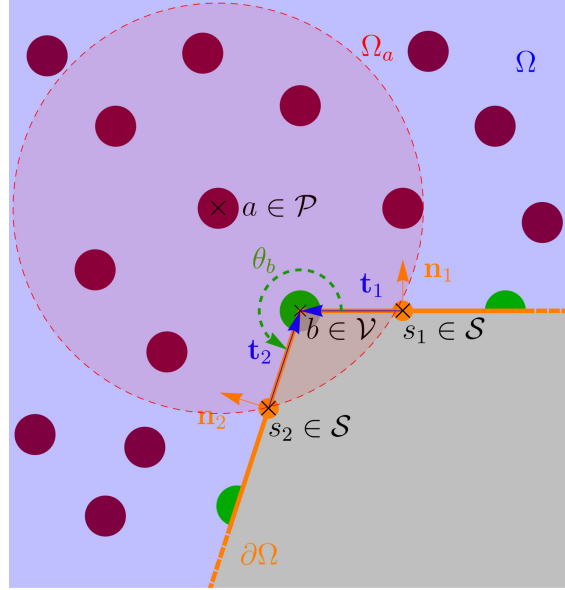


Figure K.1: Sketch of a fluid portion (Ω , shaded blue domain) near a solid boundary ($\partial\Omega$, orange lines and the solid domain shaded in gray) with: a fluid particle $a \in \mathcal{P}$ and its kernel compact support Ω_a truncated by the boundary, a vertex particle $b \in \mathcal{V}$ and its opening angle θ_b , the two connected segments $s_i \in \mathcal{S}$ at the vertex particle b .

In the USAW (Unified Semi-Analytical Wall boundary conditions) SPH variant, a kernel wall renormalisation factor γ_a is defined:

$$\gamma_a = \int_{\Omega} W(|\mathbf{r}_a - \mathbf{r}_b|) d\mathbf{r}_b, \quad (\text{K.0.7})$$

where Ω is the fluid domain, which takes into account the fact that the kernel of a particle is truncated near a boundary. It is possible to analytically evaluate this integral in 2D [47], but in the present study the value is computed throughout a governing equation:

$$\frac{d\gamma_a}{dt} = \mathbf{v}_a^R \cdot \nabla \gamma_a, \quad (\text{K.0.8})$$

where \mathbf{v}_a^R is the relative velocity to the rigid boundary and $\nabla \gamma_a$ is given by a surface integral:

$$\nabla \gamma_a = \int_{\partial\Omega} W(|\mathbf{r}_a - \mathbf{r}'|) \mathbf{n} d\mathbf{r}', \quad (\text{K.0.9})$$

with \mathbf{n} the inward oriented unit normal. The boundaries in 2D are divided in straight segments (\mathcal{S}) linked by vertex particles (\mathcal{V}) of mass a fraction θ of the reference mass m . The fraction, or opening angle, θ_b of the vertex particle b represents the interior opening angle of the two connected segments at this particle (see Fig. K.1) and can be evaluated

particle repartition: $\sum_{i,j} W(\mathbf{r}_{i,j}) \approx 1$

using:

$$\theta_b = \pi + \text{sign} [(\mathbf{t}_1 + \mathbf{t}_2) \cdot (\mathbf{n}_1 + \mathbf{n}_2)] \arccos (\mathbf{n}_1 \cdot \mathbf{n}_2), \quad (\text{K.0.10})$$

where \mathbf{t}_i and \mathbf{n}_i are the tangent and the inward normal vector of the two connected segments, respectively.

The gradient and divergence standard SPH operators are given with USAW boundary terms by:

$$\begin{aligned} \mathbf{G}_a^\gamma(f) = \frac{\rho_a}{\gamma_a} \sum_{b \in \mathcal{P} \cup \mathcal{V}} m_b \left(\frac{f_a}{\rho_a^2} + \frac{f_b}{\rho_b^2} \right) \nabla W_{ab} \\ - \frac{\rho_a}{\gamma_a} \sum_{s \in \mathcal{S}} \rho_s \left(\frac{f_s}{\rho_s^2} + \frac{f_a}{\rho_a^2} \right) \nabla \gamma_{as}, \end{aligned} \quad (\text{K.0.11})$$

$$\begin{aligned} D_a^\gamma(\mathbf{B}) = -\frac{1}{\gamma_a \rho_a} \sum_{b \in \mathcal{P} \cup \mathcal{V}} m_b (\mathbf{B}_a - \mathbf{B}_b) \cdot \nabla W_{ab} \\ + \frac{1}{\gamma_a \rho_a} \sum_{s \in \mathcal{S}} \rho_s (\mathbf{B}_a - \mathbf{B}_s) \cdot \nabla \gamma_{as}, \end{aligned} \quad (\text{K.0.12})$$

where $\nabla \gamma_{as}$ is the integral of the kernel on a boundary segment. Furthermore the USAW variant of the SPH Laplacian is defined as:

$$\begin{aligned} \mathbf{L}_a^\gamma(f, A) = \frac{\rho_a}{\gamma_a} \sum_{b \in \mathcal{P} \cup \mathcal{V}} m_b \frac{4f_a f_b}{f_a + f_b} \frac{A_a - A_b}{r_{ab}^2} \mathbf{r}_{ab} \cdot \nabla W_{ab} \\ - \frac{1}{\gamma_a} \sum_{s \in \mathcal{S}} (f_s \nabla A_s + f_a \nabla A_a) \cdot \nabla \gamma_{as}, \end{aligned} \quad (\text{K.0.13})$$

where $r_{ab} = \|\mathbf{r}_a - \mathbf{r}_b\|$.

The symplectic time integration scheme used is:

$$\begin{cases} \mathbf{u}_a^{n+1} = \mathbf{u}_a^n + \left(\frac{-1}{\rho_a^n} \mathbf{G}_a^\gamma(p^n) + \frac{\mu}{\rho_a^n} \mathbf{L}_a^\gamma(1, \mathbf{u}^n) + \mathbf{g} \right) \delta t, \\ \mathbf{r}_a^{n+1} = \mathbf{r}_a^n + \mathbf{u}_a^{n+1} \delta t, \\ \gamma_a^{n+1} = \gamma_a^n + \sum_{s \in \mathcal{S}} (\mathbf{u}_a^n - \mathbf{u}_s^n) \cdot \nabla \gamma_{as} \delta t, \\ \rho_a^{n+1} = \frac{1}{\gamma_a^{n+1}} \left(\gamma_a^n \rho_a^n + \sum_{b \in \mathcal{P}} m_b (W_{ab}^{n+1} - W_{ab}^n) \right) - \delta t D_B \Delta^n, \end{cases} \quad (\text{K.0.14})$$

where the index n denotes the time iteration, $\mu = 10^{-3} \text{ m}^2/\text{s}$ is the kinematic molecular viscosity, $\delta t = C^{h,0} h_{SPH} / c_{SPH}$, with $C^{h,0} = 0.1$ in all the numerical applications, $D_B = 0.1$ is the Brezzi and Pitkäranta diffusion coefficient and:

$$\Delta^n = -\rho_a^n \left(L_a^\gamma \{ \delta t, \mathbf{g}, \mathbf{r}_b^n \} - L_a^\gamma \left\{ \frac{\delta t}{\rho_b^n}, p_b^n \right\} \right), \quad (\text{K.0.15})$$

as shown in [13, 56]. This additional term acts like a diffusive terms in the continuity equation and helps limit acoustic discrepancy in the pressure terms. The pressure at the boundaries are interpolated from the fluid:

$$p_w = \frac{\sum_{b \in \mathcal{P}} p_b V_b W_{wb} + \sum_{b \in \mathcal{P}} \rho_b \mathbf{g} \cdot \mathbf{r}_{wb} V_b W_{wb}}{\sum_{b \in \mathcal{P}} V_b W_{wb}}. \quad (\text{K.0.16})$$

The acceleration of the wall is not taken into account as it is always small compared to the gravity acceleration term (at most 10%). More details about the USAW variant of the WCSPH method and its implementation can be found in the papers by Ferrand *et al.*[47] and Mayrhofer *et al.* [107, 108]. In the sponge layer domain the velocity update is changed to:

$$\mathbf{u}_a^{n+1} = \frac{\mathbf{u}_a^{*n+1}}{1 + \beta \delta t}, \quad (\text{K.0.17})$$

where \mathbf{u}_a^{*n+1} corresponds to the right-hand side of the first equation in the system eq.K.0.14 and $\beta = B(x)\omega$ is the damping parameter.

Simulations in 2D are run using a single GPU card (GeForce GTX TITAN Black) while 3D applications are ran on multi-GPU's on a cluster (42 cards NVIDIA GK110GL Quadro K5200).

Appendix L

Error calculation and Raw data

Cette annexe présente les détails des calculs d'erreur dans les expériences du chapitre 2, ainsi que les tableaux des données expérimentales.

This appendix is organized as follows: firstly the error calculation for the flow rates characteristics are detailed (this text is directly extracted from the paper of Carmigniani et al. [21]), secondly table of the raw data of the chapter 2 are given.

L.1 Error Calculation

The calculation of errors in the present study is done using the propagation of error formula. Consider for example the calculated parameter $\mathcal{F}(x_1, x_2, \dots, x_n)$ where $\{x_i\}_{i=1,2,\dots,n}$ are some parameters with uncertainties $\{\sigma_{x_i}\}_{i=1,2,\dots,n}$ known or calculated previously. Then the uncertainty on \mathcal{F} can be estimated¹ by [27]:

$$\sigma_{\mathcal{F}}^2 = \sum_{i=1}^n \sigma_{x_i}^2 \left| \frac{\partial \mathcal{F}}{\partial x_i} \right|^2. \quad (\text{L.1.1})$$

To measure the flow rate under the submerged plate, PIV data are used. This provides a matrix of pixel per frame velocities with uncertainties estimated to $\sigma_{\text{PIV}} = 0.25$ pixel per frame (sub-pixel accuracy is used). The dimensional velocity is then calculated using the formula:

$$\mathbf{u} = \mathbf{u}_{\text{PIV}} \frac{sc}{\delta t}, \quad (\text{L.1.2})$$

where \mathbf{u}_{PIV} is the velocity in pixel per frame, sc is the scaling in cm per pixel and δt the time stepping in seconds per frame. Typical values with uncertainties are given in table L.1. To calculate the instantaneous flow rate under the submerged plate at a given PIV grid position, a trapezoidal rule is used:

$$\phi(x_{i_x}, t) = \int_W u_x dz \approx \sum_{i_z=1}^{n_z} \frac{u_x(i_x, i_j + 1) + u_x(i_x, i_j)}{2} \delta z. \quad (\text{L.1.3})$$

This yields n_x (of the order of 10) values of the flow rate with uncertainties calculated by the eq. L.1.1. The value of instantaneous flow rate is then averaged on the n_x profiles:

$$\phi(t) = \frac{1}{n_x} \sum_{i_x=1 \dots n_x} \phi(x_{i_x}, t). \quad (\text{L.1.4})$$

The uncertainty on $\phi(t)$ is then estimated by:

$$\sigma_{\phi(t)}^2 = \frac{\sum n_x \sigma_{\phi_{i_x}}^2}{n_x} + \left(\sigma_{\phi(t)}^{\text{std}} \right)^2, \quad (\text{L.1.5})$$

where the first term corresponds to the propagation of error of the averaging and the second one to the standard deviation of the measurement of the n_x profiles. The second

¹ Assuming independent variables.

Symbol	Description	values
σ_{PIV}	Uncertainty on the PIV velocity	0.25 pixel/frame
σ_{sc}	Uncertainty on the scaling	$3 - 5 \times 10^{-4}$ cm/pixel
$\sigma_{\delta t}$	Uncertainty on the time step	60 μs /frame
$\sigma_{\phi(t)}$	Uncertainty on the instantaneous flow rate	0.35-0.44 $\text{cm}^2 \cdot \text{s}^{-1}$

Table L.1: Estimated uncertainties ranges.

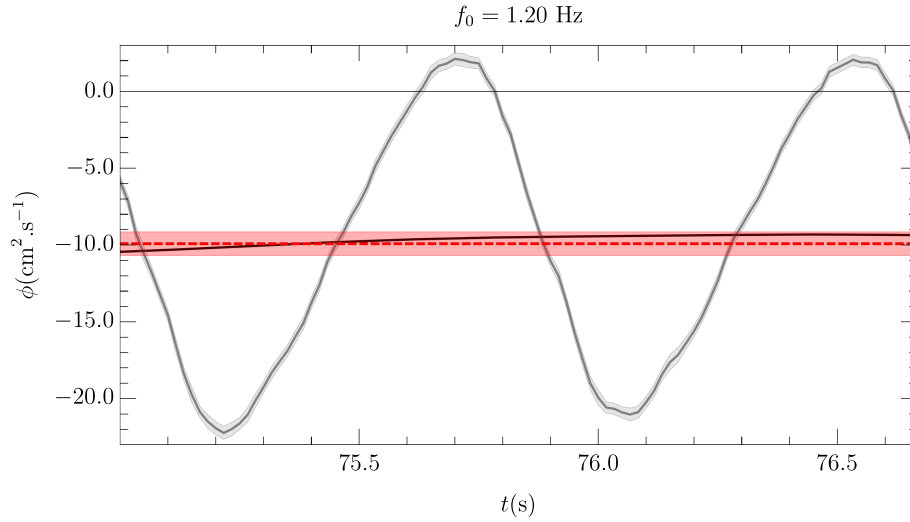


Figure L.1: Instantaneous flow rate with uncertainties. The grey curve shows the flow rate $\phi(t)$ with the instantaneous uncertainties shaded in light grey. The red dashed curve is the asymptotic bulk flow rate with the uncertainties shaded in light red. The black solid curve is the instantaneous bulk flow.

term captures partially additional errors such as misalignment of the laser and camera with the flow. Figure L.1 shows the instantaneous flow rate plus-minus the standard deviation estimated for the case $f_0 = 1.2$ Hz with the estimated uncertainty defined above.

The uncertainties on the instantaneous mean and first harmonic flow rate are evaluated in a similar manner. The asymptotic values are calculated by averaging the instantaneous ones on the last 20 seconds and the uncertainty is evaluated through a quadrature sum of the propagated error on this time sample and the standard deviation. For instance, the uncertainty for $\phi^{(0)}$ is evaluated as:

$$\sigma_{\phi^{(0)}}^2 = \frac{\left(\sigma_{\phi(t)}^{\max}\right)^2}{t_{\text{sample}} \cdot f_0} + \left(\sigma_{\phi(t)}^{\text{std}}\right)^2, \quad (\text{L.1.6})$$

where $t_{\text{sample}} \cdot f_0$ is approximatively the number of periods in the time sample. On top of this analysis, it is roughly estimated that the uncertainty threshold is $0.45 \text{ cm}^2 \cdot \text{s}^{-1}$. This estimated value is found by resetting the tank (moving the plunger and resetting it and emptying the tank and refilling it) 3 times and collecting the data. The results for

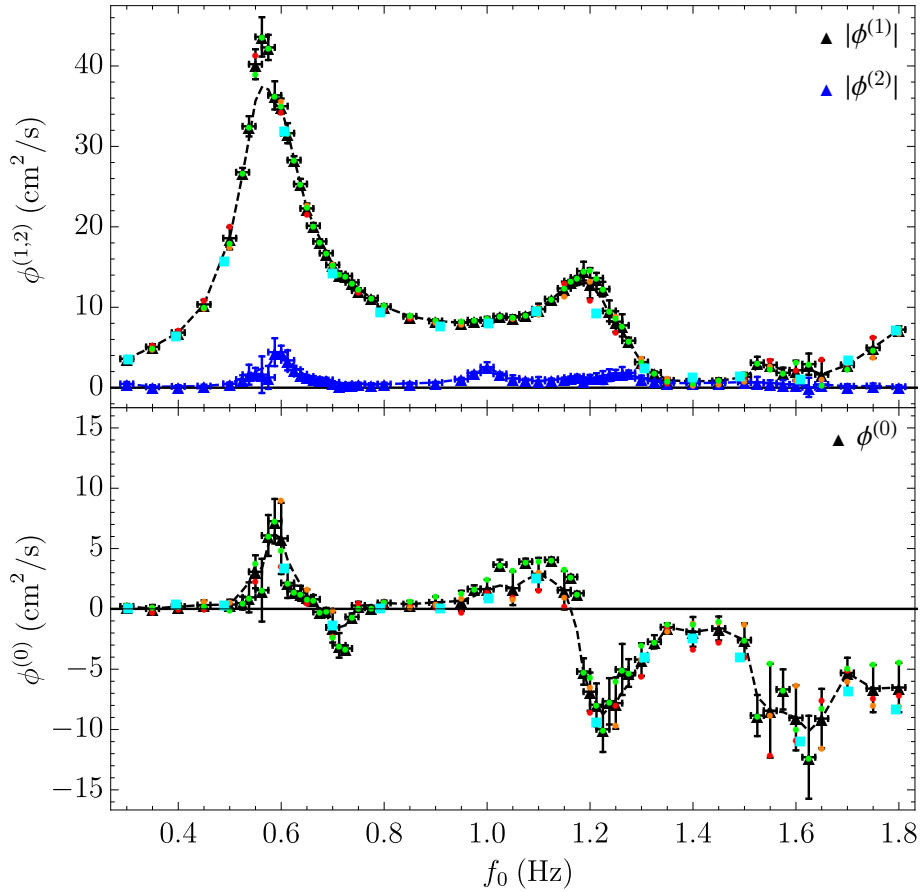


Figure L.2: Mean, first and second harmonic flow rate as a function of frequency with $2l_p = 10.5 \pm 0.05$ cm and a fixed stroke amplitude $S_0 = 0.69$ cm. The black points show the average of three independent experiments. The black dashed line is the mean of the three experiments linear interpolation functions. The experiment is reproducible (the color circles points show the three distinct experiments and the cyan squares the case of no modulation for different duty cycles (experiment DS1); for the latter the plunger position is slightly different).

the asymptotic bulk flow are shown in figure L.2. The dashed line shows the mean of these three different experiments with roughly same configuration. It is observed a good agreement between the different measures. The repeatability is really good near the peak at 1.2 Hz in particular. Some deviations are visible and are due to slight change in the plunger position and water depth leading to change in the resonance frequencies. The peak values are correctly captured in all the cases. The threshold of the error is estimated as the third quantile² of the uncertainties of these three independent experiments.

L.2 Data tables

In this section, the summary of all the experimental results are given in the form of tables. The errors are estimated using the previous defined formula. In the case of a single formula the threshold defined in the previous paragraph is used. Note that this is justified by the fact that from the repeatability experiments of the first configuration (Experiment 1 to 3) the third quantile of the uncertainties is found to be of the order of $0.45 \text{ cm}^2 \cdot \text{s}^{-1}$. In the case of a single experimental set, one should not expect the error to be less than this threshold.

case	Experiment A	Experiment B
l_t	$77.4 \pm 0.1 \text{ cm}$	$77.4 \pm 0.1 \text{ cm}$
d	$3.5 \pm 0.05 \text{ cm}$	$3.5 \pm 0.05 \text{ cm}$
d_{tot}	$10.8 \pm 0.05 \text{ cm}$	$10.8 \pm 0.05 \text{ cm}$
d_o	$6.2 \pm 0.1 \text{ cm}$	$6.2 \pm 0.1 \text{ cm}$
$\delta_{R/L}$	$3.0 \pm 0.05 \text{ cm}$	$3.0 \pm 0.05 \text{ cm}$
S_0	$0.69 \pm 0.05 \text{ cm}$	$\{0.34, 0.45, 0.69, 1.16\} \text{ cm}$
f_0	$0.3 - 1.8 \text{ Hz}$	$0.3 - 1.8 \text{ Hz}$
l_c	$18.7 \pm 0.1 \text{ cm}$	$18.7 \pm 0.1 \text{ cm}$
$2l_p$	$10.5 \pm 0.05 \text{ cm}$	$10.5 \pm 0.05 \text{ cm}$
t_p	$2.54 \pm 0.1 \text{ cm}$	$2.54 \pm 0.1 \text{ cm}$

Table L.2: Experimental configurations A to B.

case	Experiment C	Experiment D	Experiment E
l_t	$77.4 \pm 0.1 \text{ cm}$	$77.4 \pm 0.1 \text{ cm}$	$77.4 \pm 0.1 \text{ cm}$
d	$3.5 \pm 0.05 \text{ cm}$	$(2.1, 3.5, 5.5, 6.9) \pm 0.05 \text{ cm}$	$3.5 \pm 0.05 \text{ cm}$
d_{tot}	$10.8 \pm 0.05 \text{ cm}$	$10.8 \pm 0.05 \text{ cm}$	$10.8 \pm 0.05 \text{ cm}$
d_o	$6.2 \pm 0.1 \text{ cm}$	$6.2 \pm 0.1 \text{ cm}$	$(2.1, 4.0, 6.2) \pm 0.1 \text{ cm}$
$\delta_{R/L}$	$3.0 \pm 0.05 \text{ cm}$	$3.0 \pm 0.05 \text{ cm}$	$3.0 \pm 0.05 \text{ cm}$
S_0	$\{0.69, 1.16\} \text{ cm}$	$\{0.69, 1.16\} \text{ cm}$	$\{0.69, 1.16\} \text{ cm}$
f_0	$0.3 - 1.8 \text{ Hz}$	$0.3 - 1.8 \text{ Hz}$	$0.3 - 1.8 \text{ Hz}$
l_c	$18.7 \pm 0.1 \text{ cm}$	$18.7 \pm 0.1 \text{ cm}$	$18.7 \pm 0.1 \text{ cm}$
$2l_p$	$\{5.7, 10.5, 14.8, 19.9\} \pm 0.05 \text{ cm}$	$10.5 \pm 0.05 \text{ cm}$	$10.5 \pm 0.05 \text{ cm}$
t_p	$2.54 \pm 0.1 \text{ cm}$	$2.54 \pm 0.1 \text{ cm}$	$2.54 \pm 0.1 \text{ cm}$

Table L.3: Experimental configurations C to E.

² The third quantile corresponds roughly to $\mu - 0.43\sigma$ for a normal distribution. The probability of having an error below this value is less than 33% and is considered unacceptable.

f_0 (Hz)	$\phi^{(0)}$ ($\text{cm}^2 \cdot \text{s}^{-1}$)	$ \phi^{(1)} $ ($\text{cm}^2 \cdot \text{s}^{-1}$)	f_0 (Hz)	$\phi^{(0)}$ ($\text{cm}^2 \cdot \text{s}^{-1}$)	$ \phi^{(1)} $ ($\text{cm}^2 \cdot \text{s}^{-1}$)
0.300	0.20 ± 0.19	3.59 ± 0.17	1.025	3.67 ± 0.41	8.91 ± 0.18
0.350	0.02 ± 0.30	5.07 ± 0.34	1.050	1.71 ± 1.40	8.75 ± 0.27
0.400	0.20 ± 0.24	6.85 ± 0.32	1.075	3.92 ± 0.25	9.10 ± 0.12
0.450	0.32 ± 0.39	10.35 ± 0.58	1.100	2.90 ± 1.32	9.75 ± 0.69
0.500	0.36 ± 0.40	18.58 ± 1.39	1.125	4.07 ± 0.19	11.02 ± 0.15
0.525	0.48 ± 0.53	26.78 ± 0.54	1.150	1.55 ± 1.59	12.34 ± 0.85
0.538	0.95 ± 1.24	32.50 ± 1.26	1.163	2.64 ± 0.17	13.25 ± 0.15
0.550	3.08 ± 1.37	40.21 ± 1.86	1.175	1.29 ± 0.14	13.70 ± 0.19
0.563	1.55 ± 2.60	43.62 ± 2.44	1.188	-5.19 ± 1.09	14.49 ± 1.17
0.575	6.08 ± 1.69	42.30 ± 1.56	1.200	-6.86 ± 1.58	12.99 ± 1.89
0.588	7.27 ± 1.84	36.34 ± 1.75	1.213	-7.95 ± 1.77	13.62 ± 0.65
0.600	5.84 ± 2.95	35.00 ± 0.95	1.225	-9.98 ± 1.88	12.26 ± 0.90
0.613	2.15 ± 1.25	31.64 ± 1.25	1.238	-7.66 ± 1.92	9.55 ± 1.30
0.625	1.45 ± 0.49	28.29 ± 0.49	1.250	-7.81 ± 2.13	8.21 ± 1.29
0.638	1.29 ± 0.62	25.32 ± 0.64	1.263	-5.02 ± 2.12	7.75 ± 1.38
0.650	1.01 ± 0.60	22.28 ± 0.61	1.275	-5.31 ± 1.15	5.85 ± 0.38
0.663	0.79 ± 0.35	20.13 ± 0.35	1.300	-4.20 ± 1.35	3.19 ± 0.54
0.675	-0.25 ± 0.24	18.19 ± 0.26	1.325	-2.72 ± 0.54	1.90 ± 0.12
0.688	-0.16 ± 0.24	16.73 ± 0.26	1.350	-1.51 ± 0.32	0.91 ± 0.30
0.700	-1.54 ± 1.25	15.27 ± 0.17	1.400	-1.90 ± 1.23	0.80 ± 0.57
0.713	-3.02 ± 1.02	14.11 ± 0.34	1.450	-1.62 ± 0.99	0.84 ± 0.34
0.725	-3.28 ± 0.25	13.89 ± 0.26	1.500	-2.59 ± 1.38	1.35 ± 0.49
0.738	-0.66 ± 0.28	13.10 ± 0.22	1.525	-8.84 ± 1.70	3.11 ± 0.74
0.750	0.28 ± 0.31	12.07 ± 0.29	1.550	-8.44 ± 3.89	2.83 ± 0.66
0.775	0.10 ± 0.17	11.15 ± 0.17	1.575	-6.68 ± 1.66	1.86 ± 0.63
0.800	0.49 ± 0.20	10.08 ± 0.31	1.600	-9.03 ± 2.70	2.16 ± 1.20
0.850	0.39 ± 0.27	8.88 ± 0.18	1.625	-12.30 ± 3.44	2.93 ± 1.32
0.900	0.54 ± 0.48	8.30 ± 0.19	1.650	-9.09 ± 2.46	1.65 ± 1.76
0.950	0.66 ± 0.84	8.08 ± 0.23	1.700	-5.31 ± 1.26	2.84 ± 0.54
0.975	1.64 ± 0.31	8.39 ± 0.12	1.750	-6.61 ± 1.96	4.96 ± 1.29
1.000	1.64 ± 0.79	8.40 ± 0.40	1.800	-6.52 ± 2.05	7.23 ± 0.41

Table L.4: Raw data Experiment A.

s_0 (cm)	0.34		0.45		0.69		1.16	
f_0 (Hz)	$\phi^{(0)}$	$\phi^{(1)}$	$\phi^{(0)}$	$\phi^{(1)}$	$\phi^{(0)}$	$\phi^{(1)}$	$\phi^{(0)}$	$\phi^{(1)}$
0.300	-0.05 ± 0.23	2.01 ± 0.23	-0.05 ± 0.29	2.23 ± 0.29	0.20 ± 0.45	3.85 ± 0.45	0.28 ± 0.76	7.40 ± 0.76
0.350	0.12 ± 0.23	2.93 ± 0.23	-0.02 ± 0.29	3.21 ± 0.29	-0.27 ± 0.45	5.78 ± 0.45	0.30 ± 0.76	9.45 ± 0.76
0.400	0.08 ± 0.23	1.26 ± 0.23	0.15 ± 0.29	4.98 ± 0.29	-0.02 ± 0.45	7.67 ± 0.45	-0.01 ± 0.76	13.40 ± 0.76
0.450	0.28 ± 0.23	6.05 ± 0.23	0.15 ± 0.29	7.72 ± 0.29	-0.00 ± 0.45	11.75 ± 0.45	0.31 ± 0.76	20.42 ± 0.76
0.500	0.40 ± 0.23	11.06 ± 0.23	0.39 ± 0.29	14.06 ± 0.29	0.60 ± 0.45	21.55 ± 0.45	5.11 ± 0.96	36.02 ± 0.94
0.550	1.61 ± 0.23	31.85 ± 0.23	3.64 ± 0.64	36.49 ± 0.58	2.46 ± 0.62	44.30 ± 0.61	5.87 ± 2.35	58.03 ± 1.30
0.600	1.91 ± 0.23	28.47 ± 0.23	3.25 ± 0.65	33.73 ± 0.52	3.86 ± 0.84	36.74 ± 0.66	2.31 ± 1.07	43.90 ± 1.02
0.650	0.03 ± 0.23	13.58 ± 0.23	0.75 ± 0.29	16.65 ± 0.29	0.57 ± 0.45	23.13 ± 0.45	0.73 ± 0.76	32.65 ± 0.76
0.700	-0.57 ± 0.23	9.06 ± 0.23	-0.83 ± 0.29	10.87 ± 0.29	-2.39 ± 0.45	16.25 ± 0.45	-7.51 ± 0.83	24.49 ± 0.76
0.750	-0.43 ± 0.23	7.02 ± 0.23	-0.29 ± 0.29	8.54 ± 0.29	0.54 ± 0.45	12.71 ± 0.45	0.04 ± 0.76	20.35 ± 0.76
0.800	-0.41 ± 0.23	5.75 ± 0.23	-0.15 ± 0.29	7.44 ± 0.29	0.32 ± 0.45	10.43 ± 0.45	1.59 ± 0.76	18.29 ± 0.76
0.850	-0.61 ± 0.23	5.14 ± 0.23	-0.70 ± 0.29	6.58 ± 0.29	0.34 ± 0.45	9.32 ± 0.45	0.95 ± 0.76	16.68 ± 0.76
0.900	-0.78 ± 0.23	4.79 ± 0.23	-0.92 ± 0.29	6.06 ± 0.29	0.15 ± 0.45	8.75 ± 0.45	1.08 ± 0.76	15.87 ± 0.76
0.950	-0.93 ± 0.23	4.66 ± 0.23	-0.42 ± 0.29	5.95 ± 0.29	-0.31 ± 0.45	8.58 ± 0.45	0.72 ± 0.77	15.55 ± 0.76
1.000	-1.13 ± 0.23	4.78 ± 0.23	-1.01 ± 0.29	6.06 ± 0.29	1.48 ± 0.45	9.07 ± 0.45	-1.25 ± 1.07	15.62 ± 0.76
1.050	-0.71 ± 0.23	5.34 ± 0.23	0.29 ± 0.29	6.80 ± 0.29	1.11 ± 0.84	9.33 ± 0.60	2.28 ± 0.76	15.51 ± 0.76
1.100	-1.22 ± 0.23	6.23 ± 0.23	-0.89 ± 0.29	7.73 ± 0.29	1.75 ± 0.45	10.81 ± 0.45	0.10 ± 0.76	16.46 ± 0.76
1.150	-2.30 ± 0.23	9.75 ± 0.23	-1.61 ± 0.29	11.14 ± 0.29	0.31 ± 0.45	14.03 ± 0.45	-9.98 ± 1.08	19.49 ± 0.76
1.200	-3.90 ± 0.30	7.07 ± 0.23	-4.28 ± 0.45	8.80 ± 0.31	-9.20 ± 0.75	11.76 ± 0.59	-26.86 ± 5.91	20.24 ± 1.62
1.250	-1.38 ± 0.23	3.13 ± 0.23	-4.62 ± 0.29	4.52 ± 0.29	-8.46 ± 0.76	7.43 ± 0.50	-20.74 ± 2.74	12.15 ± 1.05
1.300	-0.04 ± 0.23	0.81 ± 0.23	-0.76 ± 0.29	1.07 ± 0.29	-5.96 ± 0.98	2.82 ± 0.45	-8.77 ± 0.79	8.30 ± 0.76
1.350	-0.08 ± 0.23	0.27 ± 0.23	-0.41 ± 0.29	0.36 ± 0.29	-1.56 ± 0.45	0.67 ± 0.45	-9.03 ± 1.01	5.11 ± 0.76
1.400	-0.21 ± 0.23	0.12 ± 0.23	-1.35 ± 0.29	0.34 ± 0.29	-3.57 ± 0.50	1.53 ± 0.45	-10.58 ± 1.83	4.32 ± 0.84
1.450	-0.74 ± 0.23	0.09 ± 0.23	-1.83 ± 0.29	0.36 ± 0.29	-2.97 ± 0.45	1.12 ± 0.45	-11.53 ± 1.34	4.57 ± 0.76
1.500	-1.22 ± 0.23	0.09 ± 0.23	-1.32 ± 0.29	0.30 ± 0.29	-4.20 ± 0.47	1.48 ± 0.45	-17.48 ± 2.51	8.01 ± 1.00
1.550	-0.54 ± 0.23	1.02 ± 0.41	-1.26 ± 0.29	0.67 ± 0.29	-13.00 ± 1.39	3.73 ± 0.60	-29.77 ± 4.48	9.11 ± 1.59
1.600	-3.84 ± 0.64	2.42 ± 0.35	-9.77 ± 1.76	1.85 ± 0.31	-11.68 ± 1.29	2.37 ± 0.56	-18.97 ± 3.31	5.39 ± 0.93
1.650	-2.59 ± 0.23	4.08 ± 0.23	-4.88 ± 0.88	4.16 ± 0.42	-8.15 ± 1.21	3.80 ± 0.48	-17.83 ± 1.67	1.66 ± 0.86
1.700	-3.79 ± 0.30	4.48 ± 0.26	-4.26 ± 0.73	4.62 ± 0.30	-5.43 ± 3.00	3.26 ± 0.62	-20.34 ± 4.29	1.32 ± 1.20
1.750	-0.19 ± 0.23	4.65 ± 0.23	-2.44 ± 0.37	5.63 ± 0.29	-7.95 ± 0.66	6.74 ± 0.50	-20.08 ± 3.28	5.03 ± 1.07
1.800	-0.98 ± 0.23	5.01 ± 0.23	-2.41 ± 0.29	5.97 ± 0.29	-7.61 ± 0.98	7.95 ± 0.45	-16.04 ± 1.96	9.16 ± 0.76

Table L.5: Raw data Experiment B: vary the stroke amplitude.

$2l_p$ (cm)	5.7	10.5	14.8	19.9
f_0 (Hz)	$\phi^{(0)}$			
0.300	-0.06 ± 0.45	0.19 ± 0.45	-0.11 ± 0.45	0.05 ± 0.45
0.350	-0.08 ± 0.45	-0.25 ± 0.45	-0.27 ± 0.45	-0.41 ± 0.45
0.400	0.29 ± 0.45	-0.02 ± 0.45	-0.22 ± 0.45	-0.20 ± 0.45
0.450	0.23 ± 0.45	-0.01 ± 0.45	0.11 ± 0.45	-0.11 ± 0.45
0.500	0.44 ± 0.45	0.56 ± 0.45	0.29 ± 0.45	0.32 ± 0.45
0.550	3.52 ± 0.45	2.30 ± 0.58	0.41 ± 0.45	1.40 ± 0.45
0.600	0.59 ± 0.45	3.60 ± 0.79	0.61 ± 0.79	1.47 ± 0.52
0.650	0.40 ± 0.45	0.53 ± 0.45	1.07 ± 1.09	5.72 ± 0.97
0.700	0.54 ± 0.45	-2.22 ± 0.45	0.01 ± 0.82	0.86 ± 0.52
0.750	1.18 ± 0.45	0.49 ± 0.45	-0.93 ± 0.45	0.11 ± 0.45
0.800	1.39 ± 0.45	0.30 ± 0.45	2.04 ± 0.45	2.51 ± 0.45
0.850	0.92 ± 0.45	0.32 ± 0.45	1.69 ± 0.45	3.75 ± 0.45
0.900	0.93 ± 0.45	0.14 ± 0.45	1.37 ± 0.45	3.21 ± 0.45
0.950	0.99 ± 0.45	-0.27 ± 0.45	1.43 ± 0.45	4.19 ± 0.53
1.000	1.78 ± 0.45	1.38 ± 0.45	1.37 ± 0.56	5.30 ± 0.71
1.050	1.75 ± 0.45	1.03 ± 0.78	1.29 ± 0.45	5.41 ± 0.85
1.100	0.53 ± 0.45	1.61 ± 0.45	1.13 ± 0.45	4.80 ± 0.77
1.150	-4.39 ± 0.55	0.29 ± 0.45	2.71 ± 0.60	6.40 ± 1.64
1.200	-5.05 ± 0.74	-8.55 ± 0.72	2.87 ± 0.60	5.39 ± 0.62
1.250	-1.99 ± 0.45	-7.90 ± 0.72	-5.75 ± 0.49	-8.77 ± 0.80
1.300	-0.31 ± 0.45	-5.54 ± 0.91	-8.00 ± 0.82	-5.74 ± 0.60
1.350	-0.77 ± 0.45	-1.46 ± 0.45	-7.45 ± 0.53	-4.57 ± 0.59
1.400	-0.79 ± 0.45	-3.31 ± 0.48	-3.41 ± 0.45	-0.74 ± 0.45
1.450	-1.59 ± 0.45	-2.76 ± 0.45	0.66 ± 0.45	0.90 ± 0.45
1.500	-2.69 ± 0.45	-3.94 ± 0.45	1.62 ± 0.45	1.80 ± 0.79
1.550	-2.90 ± 0.45	-12.06 ± 1.28	0.25 ± 0.45	10.77 ± 2.13
1.600	-6.02 ± 0.60	-10.84 ± 1.23	3.06 ± 0.45	2.09 ± 0.52
1.650	-2.53 ± 0.45	-7.56 ± 1.10	-20.02 ± 3.32	-2.60 ± 0.45
1.700	-3.18 ± 1.18	-5.05 ± 2.78	-13.92 ± 2.70	-14.84 ± 2.36
1.750	-2.68 ± 0.45	-7.36 ± 0.61	-11.54 ± 1.26	-7.89 ± 1.76
1.800	-0.51 ± 0.45	-7.08 ± 0.91	-14.64 ± 1.31	-21.47 ± 5.15

Table L.6: Raw data Experiment C: vary the plunger length, $s_0 = 0.69$ cm.

$2l_p$ (cm)	5.7	10.5	14.8	19.9
f_0 (Hz)	$\phi^{(0)}$			
0.300	0.34 ± 0.45	0.24 ± 0.45	0.29 ± 0.45	0.32 ± 0.45
0.350	0.41 ± 0.45	0.25 ± 0.45	0.14 ± 0.45	0.01 ± 0.45
0.400	0.44 ± 0.45	-0.02 ± 0.45	0.32 ± 0.45	0.68 ± 0.45
0.450	0.19 ± 0.45	0.25 ± 0.45	0.49 ± 0.45	0.01 ± 0.45
0.500	0.94 ± 0.45	4.31 ± 0.82	0.38 ± 0.45	0.90 ± 0.45
0.550	8.45 ± 0.85	5.02 ± 1.99	1.86 ± 0.84	1.35 ± 1.31
0.600	2.69 ± 0.45	1.95 ± 0.93	2.69 ± 1.26	3.20 ± 0.99
0.650	0.32 ± 0.45	0.61 ± 0.45	1.55 ± 1.06	3.45 ± 1.71
0.700	-2.21 ± 0.45	-6.39 ± 0.68	1.56 ± 0.45	-0.54 ± 0.65
0.750	1.95 ± 0.45	0.03 ± 0.45	3.60 ± 0.45	0.50 ± 0.45
0.800	1.12 ± 0.45	1.35 ± 0.45	2.58 ± 0.45	2.92 ± 0.62
0.850	0.91 ± 0.45	0.82 ± 0.45	2.90 ± 0.45	3.64 ± 0.80
0.900	2.03 ± 0.45	0.92 ± 0.45	2.35 ± 0.45	4.22 ± 1.25
0.950	2.85 ± 0.67	0.59 ± 0.65	2.76 ± 0.45	3.95 ± 0.77
1.000	2.54 ± 0.51	-1.09 ± 0.91	1.93 ± 0.45	6.15 ± 0.81
1.050	1.10 ± 0.45	1.93 ± 0.45	1.04 ± 0.45	2.85 ± 0.45
1.100	1.00 ± 0.45	0.08 ± 0.45	0.51 ± 0.65	1.36 ± 0.45
1.150	-7.90 ± 1.02	-8.52 ± 0.92	-0.96 ± 0.45	-1.88 ± 0.45
1.200	-14.74 ± 2.25	-23.12 ± 4.99	-13.19 ± 1.36	-6.88 ± 0.59
1.250	-5.99 ± 0.68	-17.75 ± 2.35	-18.33 ± 2.09	-13.19 ± 1.60
1.300	-4.43 ± 0.76	-7.51 ± 0.68	-10.71 ± 2.20	-15.60 ± 2.23
1.350	-3.11 ± 0.45	-7.70 ± 0.86	-9.44 ± 0.64	-14.99 ± 2.64
1.400	-2.53 ± 0.59	-9.06 ± 1.55	-10.86 ± 1.38	-12.82 ± 2.87
1.450	-9.37 ± 1.69	-9.89 ± 1.17	-8.81 ± 1.73	-10.96 ± 1.96
1.500	-7.48 ± 1.00	-15.05 ± 2.12	-15.68 ± 1.99	-13.27 ± 1.42
1.550	-7.53 ± 0.75	-25.65 ± 3.83	-23.98 ± 3.34	-8.19 ± 0.87
1.600	-7.05 ± 1.34	-16.33 ± 2.82	-28.63 ± 4.83	-18.81 ± 3.03
1.650	-3.87 ± 1.32	-15.38 ± 1.40	-25.93 ± 3.97	-21.39 ± 3.19
1.700	-4.58 ± 1.38	-17.54 ± 3.71	-21.74 ± 5.66	-21.26 ± 4.99
1.750	-3.58 ± 0.57	-17.23 ± 2.79	-25.16 ± 3.21	-25.37 ± 4.07
1.800	-1.90 ± 0.74	-13.78 ± 1.67	-21.97 ± 3.81	

Table L.7: Raw data Experiment C: vary the plunger length, $s_0 = 1.16$ cm.

Appendix M

Experiment of WASP at Le Havre

Cette annexe présente un nouveau cas de validation des vagues au dessus d'une plaque immergée. Les expériences ont été réalisées en collaboration avec l'Université du Havre. On compare le débit sous la plaque et le coefficient de réflexion à une simulation fine avec la méthode SPH. On y met en évidence une résonance de surface dans la simulation, qui ne perturbe pas significativement l'écoulement. Cette résonance semble être due à la position du batteur.

In this appendix another validation case of the WASP is presented. The experiments were conducted in Le Havre with the kind help of Dr. Gaële Peret and the case is simulated using the SPH method with Sphynx in 2D.

The appendix is organized as follows: firstly the experimental protocol is presented; secondly the PIV measurements and probes data are commented; finally the case is simulated using the SPH method. In this case, the simulation results are limited to the BLR case. The flow rate is in good agreement with the experiment. Yet a strange behavior, which did not happen in the simulations reported in the chapter 3 is observed in this simulation. It seems to be a resonance between the piston and the submerged plate.

M.1 Experimental protocol

The experiment is conducted in the same tank as the one used in Poupardin et al. [134] and Brossard et al. [16] at the Université du Havre. The tank is $l_t = 10\text{m}$ long, $l_w = 0.30\text{m}$ wide and $l_h = 0.30\text{m}$ high wave flume (see figure M.1). The water depth is fixed to $d = 0.15\text{m}$. A submerged plate $2l_p = 0.25\text{m}$ long and $t_p = 0.003\text{m}$ thick spans all the tank length and is positioned about one meter before the beginning of the sloping beach used to limit wave reflection at the end of the tank (of the order of 5%) and $d_p = 2.5\text{cm}$ under the undisturbed water surface. The tank has clamps along its two lateral sides enabling to increase the pressure on the submerged plate. No noticeable displacement of the plate is observed while running the experiment. Poupardin et al. [134] measured the displacement to be less than $0.0183 \pm 9 \times 10^{-4}\text{cm}$ in their experiments.

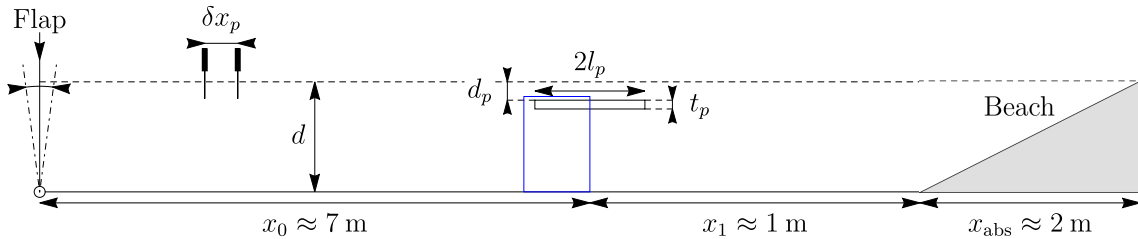


Figure M.1: Sketch of the experimental tank with notation. The submerged plate is intentionally placed close to the beach to have the longest possible distance to the wave maker. The submerged plate is $2l_p = 0.25\text{m}$ long and $t_p = 0.003\text{m}$ thick and spanned all the tank width ($l_w = 0.30\text{m}$). The blue rectangle outlines the position of the PIV window. The probes approximative positions are also shown.

The waves are generated at the far opposite end of the tank using a flap wave maker. It does not absorb the wave reflected at the plate; therefore for long runs the amplitude of the wave is not known prior to running the experiment as it is the complex superposition of multiple wave reflections between the wave maker and the plate. The frequency is fixed

to $f_0 = 1.4$ Hz in all the rest. During approximately 15 seconds after the first waves reach the plate, the incident waves at the plate are not influenced by the reflection at the wave maker.

The two-probes method of Goda & Suzuki [59] is applied to measure the wave height and reflection coefficient. Two resistive probes are held fixed at the center of the tank and spaced by $\delta x_p = 0.145$ m. For this frequency and water depth, the linear theory predicts a wavelength of $\lambda \approx 0.70$ m and therefore the spacing is about $0.21 \times \lambda$ in the good range of validity of the method. The sampling frequency of the two probes is fixed to $f_s = 150$ Hz. The water is seeded with spherical polyamid particles of typical diameter $20\mu\text{m}$ and density $1.1\text{g} \cdot \text{cm}^{-3}$. A 120 mJ YAG pulse laser is used to illuminate the fluid under the submerged plate close to the leading edge (or seaside) at the centerline of the tank width. The two pulses flash at interval $\delta t_l = 10$ ms with a frequency of $f_l = 15$ Hz. The particle motion is recorded using a 1600×1200 pixels CCD camera synchronized with the laser pulses. The region of PIV measurement is outlined in figure M.1.

M.2 Experimental results

Using the instantaneous probe data, the incident and reflected wave amplitudes are measured. The results are displayed in figure M.2. The origin of time is arbitrary here and does not correspond to the start of the wave maker. At first, the incident wave amplitude is zero (tank at rest). At $t_0 = 0$ s, the leading wave reaches the probes position. The incident wave amplitude measured by the probes increases till reaching a first asymptotic regime with a wave amplitude $a_I = 14.0 \pm 0.2$ mm at $t_1 = 4.7$ s. The amplitude reached corresponds to the wave amplitude in the absence of reflection from the flap. This regime lasts till the first waves travel from the probes to the plate, reflect and travel back to the flap and reflect and back to the probe. Then the amplitude of the incident wave height changes as visible at the end of the time sample. It will eventually reach another asymptotic regime. Here, the reflection at the flap leads to constructive addition (the amplitude increases). The reflected wave amplitude (in red) reaches also an asymptotic regime at $t_2 = 13.6$ s. The time gap between t_1 and t_2 gives an idea of the distance of the probe to the plate. There is a time lapse of about 15 seconds during which the waves reaching the plate are not influenced by the reflection at the wave maker. This should be long enough to observe the rise of the flow rate to an asymptotic regime.

The flow rate under the submerged plate is measured and displayed in figure M.3. The origin of time is also arbitrary here as the wave maker, the probes and the camera are not synchronized. Figure M.3 shows the instantaneous (mean, first harmonic) flow rate in solid black (red, blue). The light color line shows the standard deviation of the mean and first harmonic. Similarly to the probe data, there exists a time window of about 15

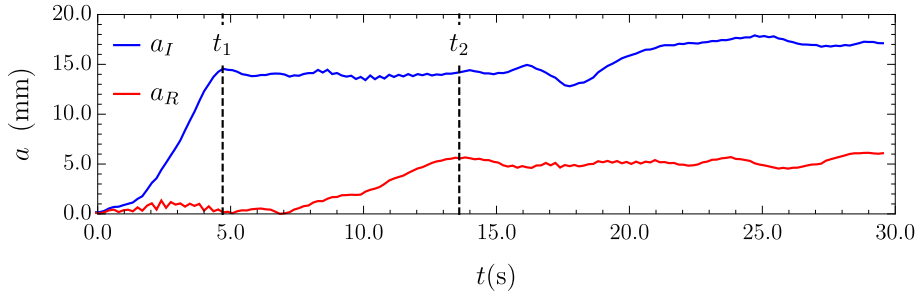


Figure M.2: Experimental time evolution incident (blue) and reflected (red) wave amplitude measured using Goda & Suzuki [59] two-probes method. The vertical dashed lines outline the moment the asymptotic regime is reached for the incident and reflected wave amplitudes.

seconds where the data are not affected by the reflection of the waves on the wave maker and the flow rate is rather two dimensional under the submerged plate. The flow rate amplitude increases at first and reaches an asymptotic regime at $\tau_1 = 7.8$ s. The mean flow rate reaches also its asymptotic regime around this time. For the first couple of waves, the frequency spectrum has spread due to the fact the tank was at rest at first (see for instance the discussion in section 2.4 of [110]). The time required to pass this transient regime mostly depends on the distance between the flap and the plate. It is basically the time the wave train needs to fully reach the plate. In the shaded gray time window, the asymptotic regime is reached and unperturbed by the reflections at the wave maker. The asymptotic values of the mean flow rate and first harmonic can be defined in this time region. It is measured that $\phi^{(0)} = -24.9 \pm 1.3$ cm²/s and $\phi^{(1)} = 51.0 \pm 0.7$ cm²/s. Afterward, the flow appears not to be two-dimensional anymore as it clearly appears when looking at the lighter blue lines pass 15 seconds. This effect is observed to start when the leading reflected waves at the flap reach the plate.

M.3 Numerical simulations

The configuration of the experiment is simulated using the Sphynx code in a tank of length $l_t = 2.7$ m with $r_{SPH}/d = 300$ (BLR, with 1.6 million particles on a single GPU). The plate is positioned at $x_0 = 1$ m of the wave maker. The wave maker is implemented with AWAS in the simulations allowing to shorten the tank. The wave height target is set to $2 \times a_{inc} = 27.8$ mm. An optimal sponge layer as defined in appendix I is used (power sponge layer with $n_B = 4$, $B_{mean} = 0.45$ is found to have a suitable absorption). The wave parameters obtained in the simulations are compared to the experimental one in table M.1. There is a good agreement with experiment.

The flow rate measured in the simulation is compared to the experimental results in figure M.4. The origin of time is shifted for the simulation such that the phase matches at

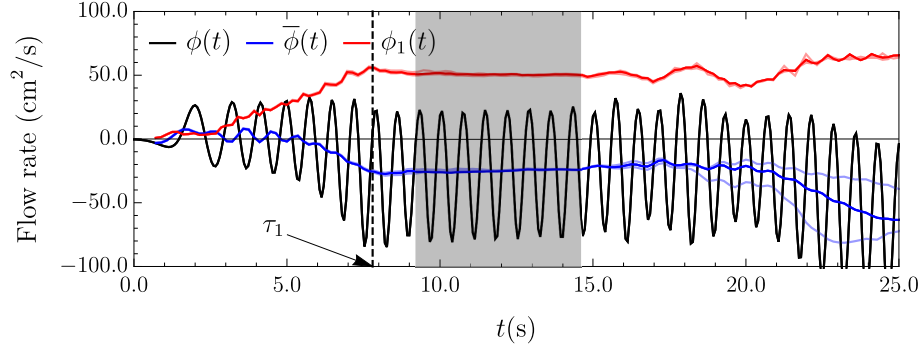


Figure M.3: Experimental time evolution of the flow rate under the plate. The black (blue, red) solid line shows the instantaneous (mean, first harmonic) flow rate. The lighter color lines show the standard deviation on the different vertical profiles of the PIV window. The shaded gray region shows the asymptotic regime of interest. The mean flow rate $\phi^{(0)} = -24.9 \pm 1.3 \text{ cm}^2/\text{s}$ and the first harmonic flow rate is $\phi^{(1)} = 51.0 \pm 0.7 \text{ cm}^2/\text{s}$ in this time window.

Table M.1: Simulation results for waves above a submerged plate case compared to the experimental data.

case	SPH	Exp
$2 \times a_{\text{SPH}}(\text{cm})$	2.7 ± 0.1	2.8 ± 0.4
R	0.33 ± 0.01	0.28 ± 0.11
T	0.24 ± 0.01	N/A
R_{SL}	0.08 ± 0.02	N/A
$\phi^{(0)} (\text{cm}^2/\text{s})$	-26.7 ± 0.3	-24.9 ± 1.3
$\phi^{(1)} (\text{cm}^2/\text{s})$	52.5 ± 0.2	51.0 ± 0.7

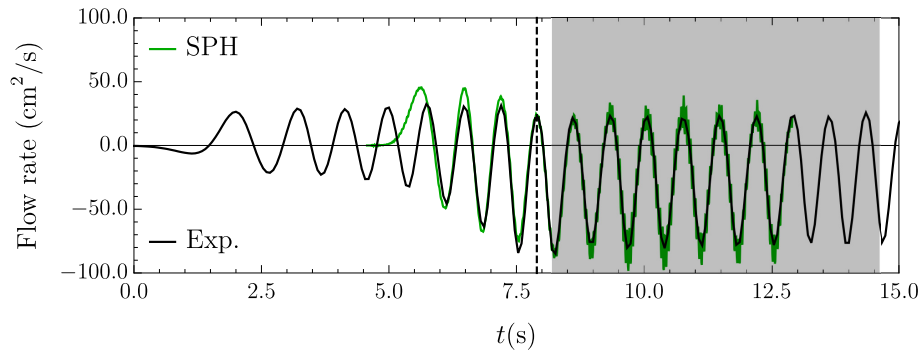


Figure M.4: Compared SPH and experimental flow rate.

the position depicted by the vertical black dashed line. The difference in the transient regime has already been mentioned and linked to the tank length difference between the simulation and experiment. The asymptotic regime is quantitatively similar to the one found in the experiment. In the SPH simulation, it is found $\phi^{(0)} = -26.7 \pm 0.3 \text{ cm}^2/\text{s}$ and

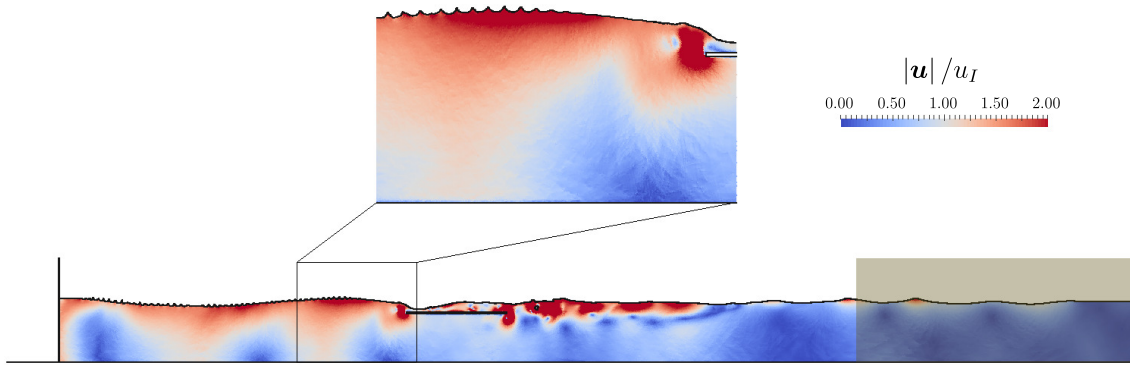


Figure M.5: Velocity magnitude in the SPH simulations. Small wavelength perturbations are visible riding on top of the long wavelength. These small waves are probably due to a resonance between the piston and the plate. The shaded region at the end shows the sponge layer.

$\phi^{(1)} = 52.5 \pm 0.2 \text{ cm}^2/\text{s}$. In both case, the simulation results are slightly stronger than in the experiment. The time resolution of the experiment being coarse (15 Hz), this is acceptable. This provides a supplementary validation with an actual flow rate experimental evaluation.

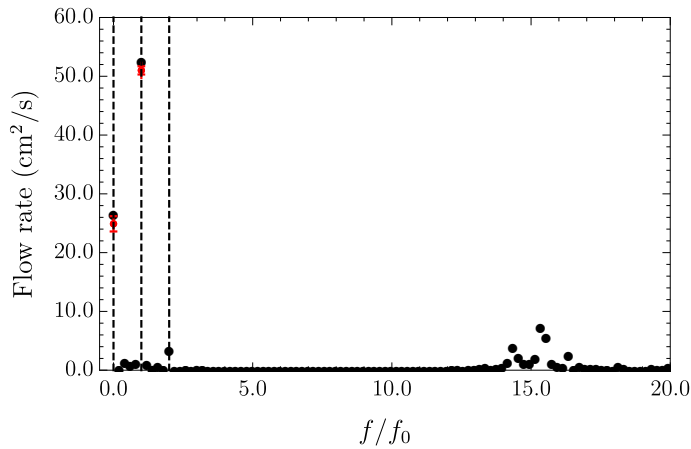


Figure M.6: FFT of the SPH simulation flow rate. The red point shows the experimental results for the mean and first harmonic flow rate. High frequency fluctuations are visible close to $15 \times f_0$ and are linked to the small wavelength waves visible in figure M.5.

Nonetheless a strange behavior the author wants to report appears in this simulation. It is visible when looking at the flow rate. The simulation flow rate is “noisy” and has rapid fluctuation in the asymptotic regime. This appears to be due to a sort of resonance between the plate and wave maker that is encountered when setting the distance, x_0 , to close to a wavelength harmonic ($n\lambda$ or $(2n + 1)/2\lambda$ where $n \in \mathbb{N}$). It is clearly visible when looking at the free surface where small waves can be seen riding on the long wavelength (see figure M.5). This effect did not occur in the simulations reported in chapter 3. It was observed

in other simulation configurations tested but not reported in the present manuscript. The wavelength of these small waves is estimated to be around ≈ 0.013 m and their frequency $\approx 15 \times 1.4$ Hz in the present simulations. Their wavelength is 26 times longer than the particle size, therefore they are well captured at this resolution. These waves affect the flow rate under the submerged plate by inducing rapid fluctuation around the principle modes. Figure M.6 shows the FFT of the flow rate in the SPH simulation. High frequency oscillations modes are visible near the 15th harmonic. Their effect on the mean flow rate is expected to be small, thus they are not a concern.

Appendix N

Experimental trials of 3D RWT

Cette annexe présente des essais d'applications d'un canal à résonance en forme de "T". On essaye de faire rentrer des vagues de façon orthogonale au canal et de corriger leur direction de propagation avec des déflecteurs en surface. On présente différents prototypes qui ont été testés mais qui n'ont fourni aucun résultat quantitatif.

This appendix details the experiment attempted in 3D of the RWT experiment. No quantitative measurements are reported here as they are not considered of good enough quality. This appendix just reports unsuccessful trials and comments which the author hope would help potential researchers or entrepreneurs interested in the concept.

The goal was to see if the concept of RWT was applicable to ocean water waves. The challenge is to get incident waves from the ocean entering at an off-centered position perpendicular to the wave tank and make them turn to be in the RWT direction. This splits the wave energy in two. The general idea is sketched in figure 2.31 in section 2.6.

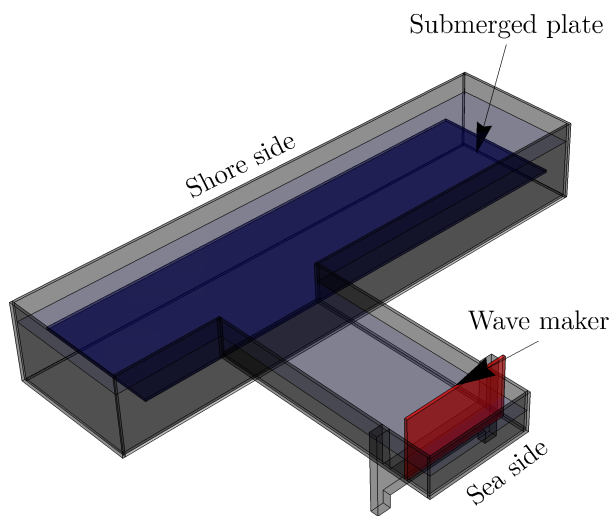


Figure N.1: 3D RWT experimental setup. In the experiment, the submerged plate is the same as the one used in the chapter 2. The T-section is 20 cm wide. The water depth above the plate was about 4 cm. The wave are generated using a flap wave maker controlled by a stepper motor.

A 3D sketch of the tank used for these trials is shown in figure N.1. Different system were tested to correct the wave direction.

A 90° wedge deflector was first tested (see figure N.2). The wedge is held by a frame which allows vertical translation such that the space left between the lower part of the wedge and the submerged plate can be varied. This seemed at first to be a promising idea. Unfortunately, the flow becomes quickly 3D after some wave periods under the submerged plate. In some cases the flow under the plate could stream in opposite direction on the shore and sea side. It is probably because the wave maker was not equipped with AWAS and thus after some waves the tank ends up in a 3D standing wave configuration. Other

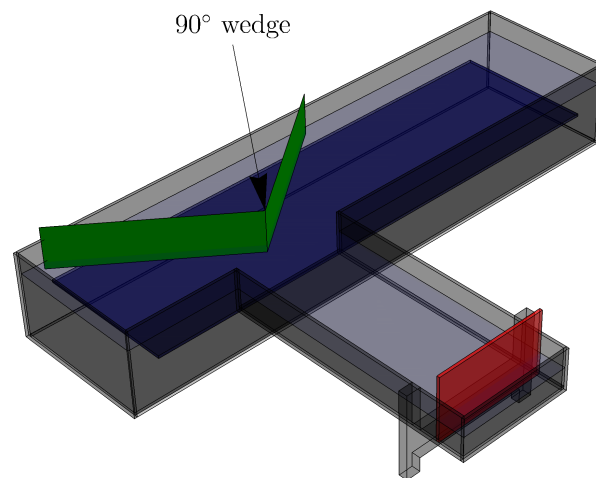


Figure N.2: 90° wedge deflector.

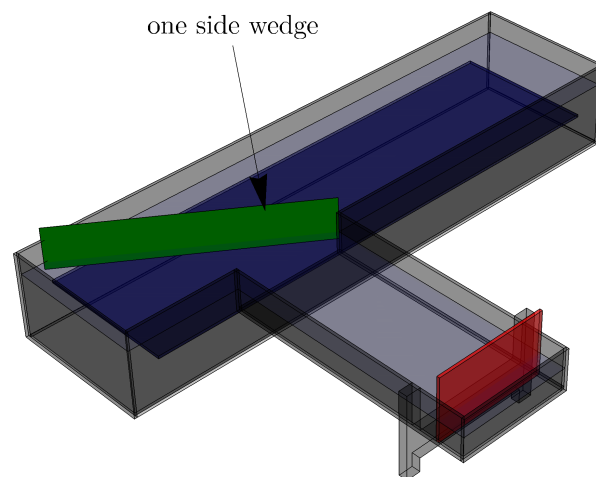


Figure N.3: Straight inclined wall.

concepts were tested with one side wedge: a straight and curved one as shown in figure N.3 and N.4. Once more, the flow was 3D under the plate and 3D standing waves developed in the tank.

Main two critics on these experimental tests are: 1) the wave maker should be implemented

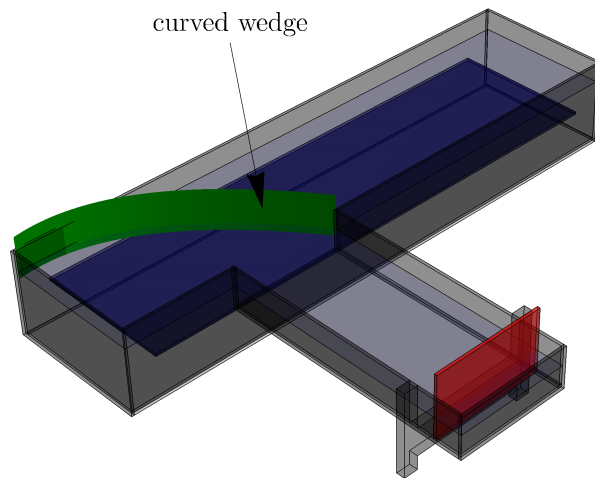


Figure N.4: Curved wall.

with AWAS to represent indeed an open ocean, 2) the deflectors always block the surface while the flow comes from the wave mass transport and thus this system block it forcing the mean flow to dive at the deflector. An interesting idea to test would be one with a varying bathymetry near the T-shape entrance to correct the wave direction. The “hill” will make the wave turn faster without blocking the surface layer.